Background estimation, search for heavy resonances and off-shell Higgs boson signal strength measurement in the 4 lepton final state with the ATLAS detector

Panagiotis Bellos

A thesis submitted in fulfillment of the requirements for the degree of Doctor of Philosophy (Ph.D.)

National and Kapodistrian
UNIVERSITY OF ATHENS

School of Science, Faculty of Physics
Department of Nuclear and Particle Physics

Athens, July 2020

Background estimation, search for heavy resonances and off-shell Higgs boson signal strength measurement in the 4 lepton final state with the ATLAS detector

Panagiotis Bellos

Advisory Committee:
Dimitrios Fassouliotis, Associate Professor, NK University of Athens (Thesis Supervisor)
Christine Kourkoumelis, Professor, NK University of Athens
Konstantinos Nikolopoulos, Professor, University of Birmingham

Exam Committee:
Dimitrios Fassouliotis, Associate Professor, NK University of Athens
Christine Kourkoumelis, Professor, NK University of Athens
Konstantinos Nikolopoulos, Professor, University of Birmingham
Konstantinos Vellidis, Associate Professor, NK University of Athens
Vasileios Spanos, Associate Professor, NK University of Athens
Theodoros Alexopoulos, Professor, National Technical University of Athens
Theodoros Geralis, Researcher A', NCSR Demokritos

"Podrán cortar todas las flores, pero no podrán detener la primavera"

Pablo Neruda

Περίληψη

Εισαγωγή

Το 2012 η ανακάλυψη του μποζονίου Higgs επαλήθευσε την πρόβλεψη των Englert, Brout, Higgs και επιβεβαίωσε το Καθιερωμένο Πρότυπο (ΚΠ), την θεωρία η οποία περγράφει τα στοιχειώδη σωμάτια και τις αλληλεπιδράσεις τους. Η ανακάλυψη επετεύχθη από τα δύο μεγάλα πειράματα, ATLAS και CMS, αναλύοντας δεδομένα απο συγκρούσεις πρωτονίων στον LHC στο CERN. Καθώς με το μποζόνιο Higgs ολοκληρώθηκε η αναζήτηση των σωματιδίων τα οποία προβλέπονται από το ΚΠ, η έρευνα εστιάζεται πλεόν στην μέλετη των ιδιοτήτων του, καθώς και στην αναζήτηση σωματιδίων τα οποία προβλέπονται απο θεωρίες Πέραν του ΚΠ (ΠΚΠ).

Κατά την 2η περίοδο λειτουργίας του LHC, τα έτη 2015-2018, σε ενέργεια κέντρου μάζας 13 TeV, συλλέχθησαν δεδομένα τα οποία αντιστοιχούν σε ολοκληρωμένη φωτεινότητα περίπου 140 fb^{-1}. Η παρούσα διατριβή συνέβαλε στην αναλύση αυτων των δεδόμενων για την διεξαγωγή 3 μελετών σχετικά με το μποζόνιο Higgs . Στο πλαίσιο της διατριβής μια άκομα μελέτη διεξήχθη, αλλά με προσομοιωμένα δεδομένα. Σε αυτήν, εξετάστηκε η προοπτική βελτίωσης της αναγνώρισης ηλεκτρονίων από τον ανιχνευτή μετά την αναβάθμισή του, κατά την διάρκεια της 2ης φάσης αναβάθμισης. Η διατριβή διαρθρώνεται ως εξής, στο 1ο και 2ο κεφάλαιο περιγράφονται εν συντομία η θεωρία του ΚΠ και ο ανιχνευτής ATLAS . Στο 3ο κεφάλαιο παρουσιάζεται η μελέτη για την αναγνώριση ηλεκτρονίων. Και ακολουθούν οι 3 μελέτες σχετικά με το μποζόνιο Higgs , η εκτίμηση του υποβάθρου στο 4ο κεφάλαιο, η αναζήτηση νέων μποζονίων στο 5ο και η μέτρηση του πλάτους διάσπασης στο 6ο.

Το Καθιερωμένο Πρότυπο

Το ΚΠ είναι η θεωρία η οποία περιγράφει τα στοιχειώδη σωματίδια και τις αλληλεπιδράσεις τους. Τα στοιχειώδη σωματίδια χωρίζονται σε 3 κατηγορίες σύμφωνα με το spin τους. Τα φερμιόνια, τα οποία είναι τα σωματίδια που απαρτίζουν την ύλη, έχουν ημιακέραιο spin 1/2, ενώ τα μποζόνια τα οποία είναι τα σωματίδια φορείς των αλληλεπιδράσεων έχουν ακέραιο spin 1. Τέλος το σωματίδιο Higgs, το οποίο είναι κι αυτό μποζόνιο, έχοντας spin 0, είναι υπεύθυνο για τον μηχανισμό ο οποίος προσδίδει μάζα σε όλα τα σωματίδια.

Στο πλαίσιο της Κβαντικής Θεωρίας Πεδίου (ΚΘΠ) τα σωματίδια περιγράφονται σαν διεγερμένες καταστάσεις των αντίστοιχων πεδίων. Τα πεδία αυτά μπορούν να προκύψουν μέσω του Λαγκραντζιανού φορμαλισμού. Για τα ελεύθερα πεδία οι Λαγκραντζιάνες αποτελλούνται από έναν όρο μάζας και έναν κινητικό όρο, σε αναλογία με την κλασσική μηχανική. Οι αλλήλεπιδράσεις των σωματιδίων εισάγονται μέσω επιπλέον όρων στις Λαγκραντζιανές. Σε μια θεωρία βαθμίδας, όπως το ΚΠ, οι επιπλέον αυτοί όροι προκύπτουν από την απαίτηση η Λαγκραντζιανή να είναι αναλλοίωτη υπό τον μετασχηματισμό συμμετρίας που υπακούει η συγκεκριμένη αλληλεπίδραση. Κατ΄ αυτόν τον τρόπο αναδύεται η Κβαντική Ηλεκτροδυναμική (ΚΗΔ) και η Κβαντική Χρωμοδυναμική (ΚΧΔ), οι οποίες περιγράφουν την ηλεκτομαγνητική και την ισχυρή πυρηνική αλληλεπίδραση αντίστοιχα. Ο παραπάνω μηχανισμός είναι εφικτός μόνο όσο τα μπόζονια φορείς της αλληλεπίδρασης είναι άμαζα.

Στην περίπτωση της ασθενούς πυρηνικής αλληλεπίδρασης αυτό δεν ισχύει κάθως τα W και Z έχουν μάζα. Για να διατηρηθεί η αναλλοιότητα της Λαγκρατζιανής, παρουσία μποζονίων με μάζα, απαιτείται η εισαγωγή ενός επιπλέον βαθμώτου πεδίου το οποίο συζευγνύεται με τα μποζόνια. Στο πλαίσιο του μηχανισμού Higgs, το πεδίο αυτό απαιτείται να είναι μιγαδικό, έχοντας ένα κύκλο από εκφυλισμένα ελάχιστα (χαρακτηριστικό σχήμα μεξικάνικου καπέλου). Το πέδιο αναπτύσεται γύρω από ένα από τα ελάχιστα, σε μια διαδικάσια που λέγεται αυθόρμητη ρήξης της συμμετρίας. Οι επιπλέον βαθμοί ελευθερίας, γνωστοί ως μποζόνια Goldstone, μπορούν να απαλλοιφούν με την κατάλληλη επιλογή βαθμίδας. Για την περιγραφή της ενοποιημένης ηλεκτρασθενούς αλληλεπίδρασης απαιτείται ένα 2 διαστάσεων μιγάδικο πέδιο. Στην συνέχεια ο μηχανισμός Higgs μπορεί να γενικευτεί ώστε να προσδώσει μάζα και στα φερμιόνια. Τέλος κάποιες θεώριες πέραν του ΚΠ, η πιο γνωστή εκ των οποίων είναι το μοντέλο 2HDM, προβλεπουν επιπλέον μποζόνια Higgs μέσω της εισαγωγής πιο γενικευμένων δυναμικών.

Στον LHC το μποζόνιο Higgs μπορεί να δημιουργηθεί από τις συγκρούσεις πρωτονίων με 4 βασικές διαδικασίες. Η σημαντικότερη από αυτές τις διαδικασίες είναι η σύντηξη γκλουονίων (ggF) και η συνολική ενεργός διατομή ειναι περίπου 55 fb. Στην σύνεχεια μπορεί να διασπαστεί επίσης με 4 βασικούς τρόπους. Η περίπτωση διάσπασης σε 2 μπόζονια Z, ένα εκ των οποίων είναι δυνητικό, τα όποια με την σειρά τους διασπόνται σε ζεύγη ηλεκτονίων ή μιονίων έχει αξιοσημείωτο ενδιαφέρον, κάθως μπορεί να ανιχνευτεί και μελετηθεί πολύ αποδοτικά.

Τα προηγούμενα χρόνια πλήθος μελέτων σχετικά με τις ιδιότητες του μποζονίου Higgs δημοσιεύτηκε. Οι μελέτες αυτές αφορούσαν την μέτρηση της μάζας, του spin, της ομοτιμίας, των ενεργών διατομών, των σταθερών σύζευξης καθως και του πλάτους διάσπασης. Δεν παρατηρήθηκε κάποια σημαντική απόκλιση από τις προβλέψεις του ΚΠ. Το πλάτος διάσπασης μετρήθηκε με μια καινοτόμο έμμεση μέθοδο, κάθως απεθείας μέτρησή του δεν είναι εφικτή, αφού η προβλεπόμενη από το ΚΠ τιμή είναι 3 τάξεις μεγέθους μικρότερη από την διακριτική ικανότητα του ανιχνευτή. Η έμμεση αυτή μέθοδος ουσιαστικά βασίζεται στην μέτρηση του λόγου των on και off-shell ενεργών διατομών.

Το πείραμα ATLAS

Το πείραμα ATLAS (A Toroidal LHC ApparatuS) είναι εγκαταστημένο στον μεγάλο επιταχυντή αδρονίων LHC (Large Hadron Collider) στο CERN (Conseil Européen pour la Recherche Nucléaire). Ο LHC αποτελείται από δύο κυκλικούς δακτυλίους μέσα στους οποίους επιταχύνονται δέσμες πρωτονίων. Οι δέσμες συγκρούονται στο κέντρο του ATLAS δημιουργώντας πλήθος σωματιδίων, τα οποία καταγράφει ο ανιχνευτής.

Ο ATLAS αποτελείται από 3 βασικά συστήματα ανιχνευτών, των εσωτερικό ανιχνευτή τροχιών ID (Inner Detector) , τα καλορίμετρα και το φασματόμετρο μιονίων MS (Muon Spectrometer). Βασικός σκοπός του ID είναι η ανακατασκευή τροχιών φορτισμένων σωματιδίων κοντά στο σημείο σύγκρουσης των δεσμών. Το καλορίμετρα μετρούν την ενέργεια των σωματιδίων που αλληλεπιδρούν με το υλικό τους. Τέλος το MS ανακατασκευάζει τις τροχίες των μιονίων. Παράλληλα λειτουργεί και ένα σύστημα σκανδαλισμού που επιλέγει τα ενδιαφέροντα γεγονότα, ενώ η ανακατασκευή των σωματιδίων επιτυγχάνεται με το λογισμικό Athena.

Ο εσωτερικός ανιχνευτής είναι σχεδιασμένος να παρέχει ερμητική κάλυψη για αναγνώριση τροχιών κοντά στο σημείο σύγκρουσης των δεσμών. Έχει εξαιρετική διακριτική ικανότητα στην εγκάρσια ορμή, και μπορεί να ανακατασκευάσει τόσο τις πρωτεύουσες όσο και τις δευτερεύουσες κορυφές πάνω από ένα κατώφλι εγκάρσιας ορμής, σε περιοχή ψευδοωκύτητας < 2.5. Αποτελείται από 3 υποσυστήματα τον Pixel Detector, τον Semiconductor Tracker και τον Transition Radiation Tracker . Το 2014 εγκαταστάθηκε ένα 4ο υποσύστημα, το Insertable B-Layer, το οποίο παρέχει πληροφορία ακόμα πιο κοντά στις δέσμες. Ο ID βρίσκεται στο εσωτερικό ενός σωληνοειδούς μαγνήτη πεδίου 2 T.

Ο κύριος σκοπός των καλοριμέτρων σε έναν επιταχυντή αδρονίων είναι η ακριβής μέτρηση της ενέργειας και της θέσης φωτονίων και ηλεκτρονίων ή μέτρηση της ενέργειας και της κατεύθυνσης των πιδάκων (jets) καθώς και της ελλείπουσας εγκάρσιας ορμής. Ο ATLAS έχει 2 καλορίμετρα, το ηλεκτρομαγνητικό και το αδρονικό, τα οποία καλυπτουν ψευδοωκύτητα μέχρι και 4.9. Το ηλεκτρομαγνητικό είναι βασισμένο στην τεχνολογία υγρού αργού, ενώ το αδρονικό χρησιμοποιεί και την τεχνολογία σπινθιριζόντων πλακιδίων.

Τέλος το φασματόμετρο μιονίων βρίσκεται στο εξώτερο μέρος του ανιχνευτή. Είναι σχεδιασμένο να ανιχνεύει φορτισμένα σωματίδια, τα οποία διαπερνούν τα καλορίμετρα, μετρώντας την ορμή τους σε περιοχή ψευδοωκύτητας μεχρι 2.7, ενώ παράλληλα προσφέρει και σκανδαλισμό. Το φασματόμετρο επίσης αντιστοιχίζει τις τροχιές που ανιχνεύει με αυτές από τον εσωτερικό ανιχνευτή. Αποτελείται από 4 τεχνολογίες, Monitored Drift Tubes, Cathode Strip Chambers, Resistive Plate Chambers και Thin Gap Chambers και περιβάλλεται από ένα σύστημα τοροειδών μαγνητών.

Κατά την πρώτη φάση αναβαθμισής του ανιχνευτή ATLAS θα αντικατασταθεί ο εσωτερικός τροχός του MS με το New Small Wheel, ενώ κατά την δέυτερη θα αντικατασταθεί ο εσωτερικός ανιχνευτής από τον New Inner Tracker (ITk) . Μέχρι το τέλος της λειτουργίας του ο ATLAS αναμένεται να συλλέξει ολοκληρωμένη φωτεινότητα τουλάχιστον 3000 fb^{-1}.

Αναγνώριση ηλεκτρονίων στην εμπρόσθια περιοχή

Τα ηλεκτρόνια περνώντας μέσα από το ηλεκτρομαγνητικό καλορίμετρο εναποθέτουν ενέργεια στα κελιά του, δημιουργώντας συσσωματώματα από γειτονικά κελιά με εναποθετημένη ενέργεια (clusters). Τα αδρόνια εναποθέτουν επίσης ενέργεια στο ηλεκτρομαγνητικό καλορίμετρο, σχηματίζοντας clusters διαφορετικής δομής εν γένει. Η αναγώριση των ηλεκτρονίων επιτυγχάνεται λαμβάνοντας υπ΄ όψιν το σχήμα των clusters καθώς και πληροφορία τροχιάς από τον ID. Ο παρών ID καλύπτει περιοχή ψευδοωκυτητάς έως 2.5, ενώ το καλορίμετρο μέχρι 4.9. Πέραν της περιοχής κάλυψης του ID η αναγνώριση βασίζεται μόνο στα clusters. Ο καινούργιος ITk θα καλύπτει ψευδοωκυτητα μέχρι 4.0 και θα είναι έτσι για πρώτη φορά εφικτή η ανακατασκευή τροχιών στην περιοχή 2.5–4.0. Αυτό αναμένεται να βελτιώσει σημαντικά την αναγνώριση των ηλεκτρονίων στην συγκεκριμένη περιοχή.

Για την μελέτη χρησιμοποιήθηκαν προσομοιωμένα γεγονότα MC (Monte Carlo) . Τα γεγονότα αυτά είναι 4 ειδών. Γεγονότα με μεμονωμένα ηλεκτρόνια, γεγονότα με μεμονωμένα ηλεκτρονία παρουσία pile-up , γεγονότα με πολλαπλά jets παρουσία pile-up και τέλος γεγονότα με ένα μποζόνιο Z το οποίο διασπάται σε 2 ηλεκτρόνια.

Αρχικά αντιστοιχίζεται κάθε cluster στο ηλεκτρομαγνητικό καλορίμετρο με την πλησιέστερη γωνιακά τροχιά από τον ITk. Από την μελέτη της απόστασης cluster-τροχιάς, για όλα τα MC γεγονότα, είναι φανερό ότι τα προερχόμενα από ηλεκτρόνια clusters έχουν εγγύτερα τροχιές από ότι αυτά τα οποία προέρχονται από υπόβαθρο (jets ή pile-up). Αξιοποιώντας αυτήν την παρατήρηση μπορούν να εφαρμοστούν κριτήρια στην γωνιακή απόσταση μεταξύ τροχιάς και cluster . Τα κριτήρια εφαρμόζονται για κάθε γωνιακή συντεταγμένη (η,φ) ξεχωριστά. Η εφαρμογή τους μπορεί να απορρίψει τουλάχιστον 60% από το υπόβαθρο με απώλεια απόδοσης περίπου 7%.

Στην συνέχεια αξιοποιούνται κάποιες μεταβλητές οι οποίες περιγράφουν το σχήμα των clusters. 8 τέτοιες μεταβλητές συνδυάστηκαν σε 3 πολυπαραγοντικές μεθόδους, μέθοδο Fischer, Δέντρο Αποφάσεων (BDT) και Νευρωνικό Δίκτυο (NN). Οι 3 μέθοδοι συγκρίθηκαν με βάση την απόδοση σαν συνάρτηση της απόρριψης υποβάθρου. Οι δύο μέθοδοι μηχανικής εκμάθησης, NN και BDT, είχαν παραπλήσια απόδοση, πολύ καλύτερη από αυτήν της μεθόδου Fischer. Τελικά επιλέχθηκε το NN για την συνέχεια της μελέτης. Με βάση την διακρίνουσα την οποία επιστρέφει το NN και τα κριτήρια γωνιακής απόστασης cluster-τροχιάς ορίζονται 3 working points για τα ηλεκτρόνια με απόδοση 70, 80 και 90% (tight, medium, loose αντίστοιχα). Για το ενδιάμεσο wp η απόρριψη υποβάθρου φτάνει το 99%.

Τέλος μελετήθηκαν 2 ακόμα μεταβλητές οι οποίες θα μπορούσαν να βελτιώσουν περαιτέρω την αναγνώριση. Η μεταβλητή της απομόνωσης τροχιάς φαίνεται να έχει μεγάλη προοπτική, ενώ η μεταβλήτη παραμέτρου κρούσης στον z άξονα δεν μπορεί να συμβάλει. Ένα επιπλεόν κριτήριο στην απομόνωση μπορεί να απορρίψει ακόμα 40% από το υπόβαθρο με απώλεια απόδοσης 5%.

Η απόδοση και η απόρριψη υποβάθρου υπολογίστηκαν εν τέλει σαν συνάρτηση κάποιων σημαντικών μεταβλητών, όπως η εγκάρσια ορμή, η ψευδοωκύτητα και ο αριθμός ανακατασκευασμένων κορυφών.

$H \to 4l$ επιλογή γεγονότων και εκτίμηση υποβάθρου

Η τελική κατάσταση 4 λεπτονίων έχει αρκέτα υπόβαθρα. Τα πιο σημαντικά από αυτα μπορούν να απορριφθούν σε πολύ μεγάλο βαθμό μέσω της επιλογής γεγονότων. Αυτό το μειώσιμο υπόβαθρο αποτελείται από $Z + jets$, $t\bar{t}$ και fake ηλεκτρόνια κυριώς. Υπάρχουν επίσης κάποια μη μειώσιμα υπόβαθρα τα οποία προκύπτουν από την παραγωγή $ZZ^{(*)}$.

Για να αποφευχθούν οι αβεβαιότητες της θεωρίας και της προσομοίωσης το μειώσιμο υπόβαθρο υπολογίζεται από τα πραγματικά δεδομένα (Data Driven Estimation). Δύο διαφορετικές μέθοδοι χρησιμοποιούνται για τα $ll\mu\mu$ και $llee$ κανάλια, καθώς οι διαδικασίες υποβάθρου έχουν διαφορετική σχετική συνείσφορα σε αυτές τις καταστάσεις. Το $ll\mu\mu$ κανάλι απαρτίζεται κυρίως από Z + Heavy Flavor (HF) jets και $t\bar{t}$. Αντιθέτως το $llee$ απαρτίζεται κυρίως από Z + Light Flavor (LF) jets και fakes .

Για το $ll\mu\mu$ κανάλι η εκτίμηση βασίζεται σε 4 περιοχές ελέγχου. Οι περιόχες αυτές κατασκευάζονται αντιστρέφοντας κάποια από τα κριτήρια επιλογής γεγονότων, ώστε να εμπλουτιστούν σε υπόβαθρο. Οι 4 περιοχές ελέγχου είναι :

- Inverted d_0 : Απαιτείται ένα τουλάχιστον από τα λεπτόνια του δευτερευόντος ζεύγους να αποτυγχάνει να περάσει το κριτήριο παραμέτρου κρούσης. Η περιοχή η οποία δημιουργείται είναι εμπλουτισμένη σε HF jets παραγόμενα είτε από Z + jets είτε από $t\bar{t}$.
- Inverted Isolation : Απαιτείται ένα τουλάχιστον από τα λεπτόνια του δευτερευόντος ζεύγους να αποτυγχάνει να περάσει το κριτήριο απομόνωσης. Ένα επιπλέον κριτήριο στην ανισορροπία ορμής (σχετική διαφορά της ορμής όπως αυτή μετριέται από τον ID και το MS) ευνοεί τα LF jets.
- $e\mu + \mu\mu$: Απαιτείται το πρωτεύον ζεύγος να είναι διαφορετικής γεύσης. Συνεπώς απορρίπονται τα Z + jets και η περιοχή είναι εμπλουτισμένη σε $t\bar{t}$.
- Same Sign : Απαιτείται το δευτερεύον ζεύγος να είναι ομόσημο. Σε αυτήν την περιοχή όλες οι διαδικασίες έχουν σημαντική συνεισφορά, αλλά χρησιμοποιείται και πάλι το κριτήριο ανισορροπίας ορμής για να ευνοηθεί το LF jets.

Οι περιοχές ελέγχου συνδέονται μεταξύ τους μέσω μιας πέμπτης περιοχής. Η περιοχη αυτή είναι

- Relaxed Isolation and d_0 : Δεν εφάρμόζονται τα κριτήρια απομόνωσης και παραμέτρου κρούσης στα λεπτόνια του δευτερεύοντος ζεύγους, όπως και το κριτήριο κορυφής για το γεγονός συνολικά.

Ο τρόπος σύνδεσης βασίζεται στον λόγο των γεγονότων μεταξύ των περιοχών ελέγχου και της Relaxed. Οι λόγοι αυτοί δεσμέυονται απο το MC. Τα αποτελέσματα εκφράζονται αρχικά στην Relaxed και από εκεί χρησιμοποιούνται κατάλληλοι παράγοντες (Transfer Factors) ώστε να μεταφερθούν στην περιοχή σήματος (Signal Region), όπου τα πλήρη κριτήρια εφαρμόζονται.

Σε κάθε μία από τις παραπάνω περιοχές, χρεησιμοποιείται η κατανομή της αναλλοίωτης μάζας του πρωτεύοντος ζεύγους για να κατασκευάστει ένα μοντέλο το οποίο θα προσαρμοστεί στα πραγματικά δεδομένα. Για κάθε μία απο τις διαδικασίες Z + HF jets, Z + LF jets και $t\bar{t}$ ένα διαφορετικό μοντέλο χρησιμοποιείται. Το άθροισμα των μοντέλων είναι αυτό το οποίο προσαρμόζεται, μεγιστοποιώντας την συνάρτηση πιθανοφάνειας. Η προσαρμογή γίνεται ταυτόχρονα και στις 4 περιοχές. Η συνέπεια του μοντέλου, κάθως και της διαδικάσιας ελέγχεται προγενέστερα με ψευδοδεδομένα δημιουργημένα από το MC. Εκτός από την κύρια μέθοδο προσαρμογής υπάρχουν ακόμα δυο με μικρές παραλλαγές. Στην πρώτη από αυτές, το Z LF και HF jets συγχωνεύονται, ενώ στην δεύτερη η προσαρμογή γίνεται σε δύο στάδια, με 2 + 1 περιοχές ελέγχου. Οι 3 μέθοδοι δίνουν συγκρίσιμα αποτελέσματα ενισχύοντας την εμπιστοσύνη μας στην διαδικασία εκτίμησης.

Οι παράγοντες μεταφοράς ελέγχονται επίσης από τα πραγματικά δεδομένα χρησιμοποιώντας ένα MC δείγμα το οποίο περιέχει γεγονότα με ένα Z και ένα επιπλέον μιόνιο. Οι παράγοντες είναι απλοϊκά η απόδοση των δύο κριτηρίων (απομόνωσης και παραμέτρου κρούσης) για το επιπλέον μιόνιο στο τετράγωνο. Δεδομένου ότι χρειάζονται 2 TFs, ένας για LF και ένας για HF jets δύο υπο-δείγματα εμπλουτισμένα σε LF και HF jets αντίστοιχα χρησιμοποιούνται. Το LF δείγμα κατασκευάζεται θέτοντας ένα κριτήριο στην ανισορροπία ορμής. Το HF δείγμα κατασκευάζεται αντιστρέφοντας το κριτήριο παραμέτρου κρούσης. Η απόδοση των κριτηρίων απομόνωσης και παραμέτρου κρούσης υπόλογιζεται από αυτά τα υπο-δείγματα είτε κατευθείαν από το MC, είτε από τα δεδομένα. Για το LF υπάρχει μια σημαντική διαφορά στην απόδοση της απομόνωσης μεταξύ των δύο τρόπων υπολογισμού. Οπότε χρησιμοποιείται η τιμή η οποία προκύπτει από τα πραγματικά δεδομένα, ενώ η σχετική αβεβαιότητα λογίζεται σαν συστηματική αβεβαιότητα στον τελικό αριθμό γεγονότων στην περιοχη σήματος.

Πολλές μέλετες δεν χρειάζονται μόνο τον συνολικό αριθμό γεγονότων του μειωσίμου υποβάθρου, αλλά και κάποια διαφορική κατανομή του. Σε αυτήν την περίπτωση, τα γεγονότα της κάθε διαφορικής κατηγορίας προσαρμόζονται ξεχωριστά. Επειδή το Z + LF jets έχει μικρή στατιστική γενικά, χρησιμοποιείται η μέθοδος στην οποία τα LF και HF είναι συγχωνευμένα. Ωστόσο, το άθροισμα των κατηγοριών κανονικοποιείται στο αποτέλεσμα της συνδυασμένης προσαρμογής όπως προέκυψε από την κύρια μέθοδο. Για κάθε μία από τις κατηγορίες υπολογίζεται ένας ξεχωριστός Transfer Factor, ο οποίος διορθώνεται στην περίπτωση μικρής στατιστικής. Οι διαφορικές κατανομές οι οποίες προκύπτουν από τον υπολογισμό από τα δεδομένα συγκρίνονται με τις αναμενόμενες από το MC . Δεν παρατηρήθηκαν σημαντικές διαφορές.

Αναζήτηση για βαρείς ZZ συντονισμούς

Πολλές ΠΚΠ θεωρίες προβλέπουν την ύπαρξη επιπλέον βαρύτερων μποζονίων Higgs. Στην περίπτωση αναζήτησης νέων σωματίδιων η υπόθεση H_0, η οποία περιλαμβάνει μόνο υπόβαθρο, πρέπει να ελεγχθεί κόντρα στην υπόθεση H_1, η οποία περιλαμβάνει σήμα και υπόβαθρο. Η ύπαρξη σήματος στην H_1 παραμετροποιείται μέσω της ισχύος σήματος μ. Αρχικά πραγματοποιείται μία προσαρμογή μέγιστης πιθανοφάνειας. Ωστόσο χρησιμοποιείται μια παράλλαγη της συνάρτησης πιθανοφάνειας, η οποία ορίζεται έτσι ώστε να είναι συνάρτηση μόνο του μ και όχι και των παραμέτρων όχλησης ($\lambda(\mu)$). Η προσαρμογή με αυτή τη συνάρτηση αποδίδει την τιμή του μ η οποία περιγράφει καλύτερα τα πραγματικά δεδομένα. Καθώς όμως τα πραγματικά δεδομένα έχουν διακυμάνσεις η προσαρμογή δεν θα αποδώσει την τιμή του μ την οποία προβλέπει το ΚΠ. Οπότε απαιτείται ένας τρόπος για να διαπυστωθεί αν η ασυμφωνία προέρχεται όντως από διακυμάνσεις των δεδομένων ή από κάποιο νέο φαινόμενο φυσικής. Από την συνάρτηση λ προκύπτει επίσης η test statistic μεταβλητή q_0. Αυτή η μεταβλήτη έχει την δυνατότητα να διακρίνει τις δύο υποθέσεις H_1 και H_0. Από την κατάνομη της για τις 2 υποθεσεις H_1 και H_0 προκύπτει η πιθανότητα ένα συγκεκριμένο q_0 να έχει προέλεθει είτε από την H_1 είτε H_0. Από αυτές τις πιθανότητες, μέσω της μεθόδου CLs, υπολογίζεται το ανώτερο όριο στο μ σε επιπέδο εμπιστοσύνης 95%. Εκτός από τα όρια που παρατηρούνται από τα πραγματικά δεδομένα, ενδιαφερόμαστε και για τα αναμενόμενα όρια (διαμέσο τιμή.) Αυτά μπορούν να υπολογιστούν πολύ αποδοτικά μέσω ενός ειδικού σετ δεδομένων, του Assimov Dataset. Οι συστημάτικες αβεβαιότητες περιλαμβάνονται στην προσαρμόγη σαν γκαουσιανοί όροι και μελετώνται ξεχωριστά.

Στην παρούσα μελέτη η διακρίνουσα μεταβλήτη που χρησιμοποιείται στην προσαρμογή είναι η αναλλοίωτη μάζα των τεσσάρων λεπτονίων, καθώς αναζητείται ένας συντονισμός. Η κατανομή της αναλλοίωτης μάζας για το σήμα και το μη μειώσιμο υποβάθρο παραμετροποιείται με αναλυτικές συναρτήσεις προσαρμόζοντας τις MC κατανομές, ενώ για το μειώσιμο υπόβαθρο κατασκευάζεται λειαίνοντας τις MC κατανομές. Ο αριθμός γεγονότων για το μειώσιμο υπόβαθρο αποκτάταται από την εκτίμηση από τα πραγματικά δεδομένα, όπως περιγράφτηκε στο προηγούμενο κεφάλαιο. Επίσης υπολογίζεται και η γεωμετρική αποδοχή σήματος σαν συνάρτηση της μάζας του υποθετικού νέου σωματιδίου.

Στην τελική προσαρμογή οι παράμετροι ενδιαφέροντος είναι οι ενεργοί διατομές για ggF και VBF παραγωγή. Έτσι χρησιμοποιούνται 4 κανάλια, 3 ευαίσθητα σε παραγωγή μέσω ggF και ένα μέσω VBF. Επίσης υπάρχουν δύο ελεύθεροι παράμετροι, οι οποίες περιγράφουν την κανονικοποίηση του μη μειώσιμου υποβάθρου στα ggF και VBF κανάλια. Όλες οι συστηματικές αβεβαιότητες προερχόμενες από την θεωρία, το πείραμα, την εκτίμηση από τα πραγματικά δεδομένα και την παραμετροποίηση, καθώς και κάποιες συνολικές αβεβαιότητες περιλαμβάνονται στην προσαρμογή. Η διαδικάσια προσαρμογής ελέγχεται με Assimov Data , τα οποία χρησιμοποιούνται και για την εξαγωγή των αναμενόμενων ορίων.

Γενικά, δεν παρατηρήθηκε καποιά σημαντική ασυμφωνία μεταξύ των αναμενόμενων και παρατηρηθέντων κατανομών. Τα τελικά όρια στην παραγωγή είτε μέσω ggF είτε μέσω VBF σε επίπεδο εμπιστοσύνης 95% υπολογισμένα από τα δεδομένα ξεπερνούν ελάχιστα τα 2σ των αναμενόμενων σε 2-3 σημεία. Νέα αποτέλεσματα με βελτιωμένες τεχνικές ανάλυσης κάθως και με συνδυασμό με την ανάλυση τελικής κατάστασης $2l2\nu$ αναμένονται σύντομα.

Μέτρηση της off-shell ισχύος σήματος

Το τελευταίο κεφάλαιο πραγματεύεται την μέτρηση του πλάτους διάσπασης του μποζονίου Higgs. Για να πραγματοποιηθεί η μέτρηση αυτή απαιτείται μέτρηση της off-shell ενεργού διατομής ή της αντίστοιχης ισχύος σήματος ($\mu_{off-shell}$). Ένα φαινόμενο το οποίο πρέπει να ληφθεί υπ όψιν σε αυτή τη μελέτη είναι η συμβολή σήματος-υποβάθρου. Το σήμα προερχόμενο από ggF ($gg \to H^* \to ZZ$) συμβάλει με το αντίστοιχο υπόβαθρο ($gg \to ZZ$), καθώς έχουν ίδια αρχική και τελική κατάσταση. Η μελέτη της συμβολής είναι αρκέτα σημαντική, αφού χρησιμοποιείται για να παραμετροποιηθεί η ενεργός διατομή σαν συνάρτηση της ισχύος σήματος. Η παραμετροποίηση συγκρίνεται με MC το οποίο δημιουργείται απευθείας με διαφορετική ισχύ σήματος.

Στην μελέτη αυτή η αναλλοίωτη μάζα των 4 λεπτονίων δεν προσφέρει αρκετά καλή διακριτική ικανότητα. Για αυτό χρησιμοποιείται η μέθοδος του στοιχείου πίνακα. Αυτή η μέθοδος εκμεταλλεύεται 8 κινηματικές μεταβλητές, οι οποίες ορίζονται στο σύστημα ηρεμίας των 4 λεπτονίων, επιστρέφοντας μία διακρίνουσα. Αυτή η διακρίνουσα εμπεριέχει τις πιθανότητες ένα συγκεκριμένο γεγονός να έχει προέλθει από off-shell Higgs ή από υπόβαθρο. Με την χρήση της βελτιώνεται σημαντικά η ευαισθησία. Επιπλέον εκπαιδεύτηκε ένα BDT με την προσδοκία περαιτέρω βελτίωσης. 3 κινηματικές μεταβλητές του συστήματος των 4 λεπτονίων και η διακρίνουσα της μεθόδου στοιχείου πίνακα χρησιμοποιήθηκαν για την εκπαίδευση του. Ωστόσο, δεν υπήρξε αξιοσημείωτη διαφορά χρησιμοποιώντας την διακρίνουσα από το BDT, οπότε επελέγη αυτή του στοιχείου πίνακα για την τελική προσαρμογή.

Οι MC κατανομές σήματος και υποβάθρου διορθώνονται με την βοήθεια των k-factors οι οποίοι λαμβάνουν υπ΄ όψιν τις διορθώσεις ανώτερης τάξης που είναι διαθέσιμες. Το μειώσιμο υπόβαθρο και σε αυτήν την μελέτη υπολογίζεται με παρόμοιο τρόπο, παίρνοντας την κανονικοποιήση από τα πράγματικά δεδομένα και λειαίνοντας τις κατανομές της διακρίνουσας του στοιχείου πίνακα.

Για την εξαγωγή των τελικών αποτελεσμάτων, η προσαρμογή από τα κανάλια $4l$ συνδυάζέται με αυτή από τα κανάλια $2l2\nu$. Με τα δεδομένα, τα οποία συλλέχθηκαν το 2015-2016 και αντιστοιχούν σε ολοκληρωμένη φωτεινότητα 36 fb^{-1}, κατέστη δυνατόν να μπεί μόνο ένα ανώτερο όριο στο πλάτος του μποζονίου Higgs. Συγκεκριμένα, το όριο αυτό ήταν 4.2 φορές η τιμή η οποία προβλέπεται από το ΚΠ. Η ανάλυση και των υπόλοιπων δεδομένων της 2ης περιόδου, καθώς και η βελτίωση των τεχνικών ανάλυσης ανάμενεται να μειώσουν σημάντικα το όριο.

Acknowledgements

First of all, I would like to thank my grandfather Panagiotis, who has passed away, for his support in various ways during my studies.

I am also really grateful to my supervisor, professor Dimitris Fassouliotis. We worked together for more than 8 years and under his guidance I completed my undergraduate, M.Sc. and Ph.D. theses. Our teamwork were excellent and he taught me too many aspects of physics. Also thanks to professor Christine Kourkoumelis who was also co-supervising me since my undergraduate studies. At last thanks to professor Konstantinos Nikolopoulos who co-supervised me and provide guidance during my qualification work.

I would like to thank all the colleagues of the ”Higgs to 4 leptons” group, in which I was working for 4 years. Special thanks to Dr. Lailin Xu and Dr. Will Leight for their guidance and help during my work in the group. Also thanks to all the colleagues of the ”New Small Wheel” group, in which I worked for 2 semesters. At last thanks to Dr. Stelios Angelidakis who helped me a lot at the beginning of my Ph.D. .

I would like also to thank my family and my friends and colleagues from Greece for all the good memories we shared during my studies.

At last, I have to thank the Greek State Scholarships Foundation as,
“This research was co-financed by Greece and the European Union (European Social Fund- ESF) through the Operational Programme ≪Human Resources Development, Education and Lifelong Learning≫ in the context of the project “Strengthening Human Resources Research Potential via Doctorate Research” (MIS-5000432), implemented by the State Scholarships Foundation (IKY)”

Ευρωπαϊκή Ένωση
European Social Fund

Operational Programme
Human Resources Development,
Education and Lifelong Learning
Co-financed by Greece and the European Union

ΕΣΠΑ
2014-2020
ανάπτυξη - εργασία - αλληλεγγύη

Abstract

The discovery of Higgs boson in 2012 by the ATLAS and CMS experiments marked a key milestone in the history of particle physics. It confirmed a long-standing prediction of the Standard Model (SM), the theory that describes our present understanding of elementary particles and their interactions. The Higgs boson was the last particle of the SM which was observed. After its observation the research in in the ATLAS experiment focused on the measurement of its properties and also on the effort to observe particles beyond the SM. During Run II (2015-2018) it collected data corresponding to about 140 fb^{-1}, having a key role in these studies. This thesis presents a study for search of new high mass Higgs-like bosons as well a study for the measurement of Higgs boson decay width. It presents also the data driven estimation of the reducible background for these studies.

The first chapter (1) is a short theoretical introduction to the SM. The particles and the way that their interactions emerge are described. The Higgs mechanism is introduced as a way to retain the invariance of a Lagrangian with massive bosons. The mechanism can be extended to give mass to the fermions too. Afterwards the Higgs boson production and decay modes are described. Except the SM Higgs boson, additional Higgs-like bosons are predicted by beyond the SM models. Lastly an innovative way to measure Higgs boson decay width is presented.

In the second chapter (2) the ATLAS experiment is described, after a short introduction about about CERN and LHC. The ATLAS experiment consists of 3 main sub-detector systems, the Inner Detector (ID), the Calorimeters and the Muon Spectrometer (MS). The ID goal is to reconstruct charge particle tracks close to the interaction point. The Calorimeters measure the energy which is deposit in them by electrons/photons and hadrons. Lastly the MS reconstructs muon tracks. A trigger and a data acquisition system are used in order to choose and store the interesting event collisions. The ATLAS detector will be undergone two major upgrades. Soon the inner wheel of the end-cap MS will be replaced by the New Small Wheel. Also during Upgrade phase II the inner detector will be replaced by the New Inner Tracker (ITk).

In the third chapter (3) a study for electron identification in the forward region is described. The new ITk will extend pseudorapidity coverage up to $|\eta| = 4$. An identification method for the electrons in the region $2.5 < |\eta| < 4.0$ was developed. It uses track-cluster matching criteria and a Artificial Neural Network to separate the true electrons from the fakes, which come either from pile-up or jets. Lastly the potential of improving identification by using an Isolation variable is studied.

In the forth chapter (4) the event selection and the background estimation in the 4-lepton channel are described. The description focuses on the Data Driven Estimation of the $ll\mu\mu$ reducible background. The estimation is performed in 4 Control Regions (CRs). Each of them is enriched in a specific background component. The 4 CRs are linked via a fifth region, called Relaxed Region (RR). A simultaneous likelihood fit is performed in the 4 CRs and the results are extrapolated to the RR via Fractions. The results from the RR are subsequently extrapolated to the Signal Region via Transfer Factors (TFs). The TFs are estimated and controlled using a sample containing Z+μ events.

In the fifth chapter (5) the search for a high mass ZZ resonance is described. In this analysis a cut based or a Neural Network based selection is used to categorized the events. The signal and the ZZ backgrounds are modeled with analytic functions, while the reducible background is data Driven estimated. The methodology of the Likelihood fit and the extraction of 95% Confidence Level limits is described in detail. Lastly the final limits for the cut-based selection are presented.

In the sixth chapter (6) the measurement of the Higgs boson decay width is described. For this

measurement, a measurement of the Higgs boson off-shell cross section is required. For this study the MC samples are corrected with the latest k-factors. Then in additional to the nominal event selection a Matrix Element based discriminant is used to suppress the ZZ background. The reducible background is estimated in a Data Driven way. Finally the results are combined with these of the $ll\nu\nu$ channel to set limits on the decay width.

Contents

1 The Standard Model

At the beginning of the twentieth century the only known particle was the electron. A few years later, the photon, the quantum of the electromagnetic field, was proposed in order to explain the photoelectric effect. In 1919 and 1932 proton and neutron were discovered respectively. In 1932 also the positron was discovered, the first particle of antimatter. The development of the detectors and accelerators the following decades enabled the discovery of many more particles. Some of these particles are elementary, hence they are not made up from other particles. They interact through four fundamental forces. The theory which describes the elementary particles and their interactions is called Standard Model (SM) [1]. The last particle of the SM was discovered in 2012, the famous Higgs boson.

1.1 Standard Model Particles

The Standard Model includes 12 elementary particles of spin 1/2 known as fermions. Each fermion has a corresponding antiparticle. The SM also includes 12 bosons of spin 1, which mediate the three forces that the SM describes, electromagnetic, weak, and strong (SM does not describe gravity). The electromagnetic interaction acts on electrically charged particles. The charge of weak interaction is called weak isospin and the charge of strong interaction is called color. The last part of the SM is the Higgs boson (spin 0) which is necessary to give mass to the massive particles.

1.1.1 Fermions

The fermions are the particles which compose the matter and they have spin 1/2. They are classified in two type , quarks and leptons. The quarks carry colour charge, and hence, they interact via the strong interaction. They also carry electric charge and weak isospin and so they interact with other fermions both electromagnetically and via the weak interaction. On the contrary leptons do not have colour. So the electron, muon, and tau interact electromagnetically and weakly and neutrinos which do not have either color or electric charge interact only weakly. The leptons are also classified in three generations. Each member of a generation has greater mass than the corresponding particles of lower generations. The first generation particles on the contrary to two others are stable and do not decay; hence all ordinary matter is made up of such particles.

1.1.2 Bosons

The three fundamental forces, which are described by the SM, are carried by the gauge bosons. The bosons are the quanta of the corresponding fields. The photon is the quantum of electromagnetic field and it mediates the electromagnetic interaction. The three bosons Z, W^+ and W^- mediate the weak interaction. Finally there are 8 gluons which carry the strong interaction.

1.1.3 Higgs Boson

The Higgs boson (Brout–Englert–Higgs mechanism) was proposed in 1960s to solve the problem with the masses of Z, W^+ and W^- bosons. The internal symmetries of the SM do not allow these bosons to have mass. The Higgs mechanism is a way for these particles to obtain mass without violation of the symmetries. The same mechanism can be generalized to give mass to every particle.

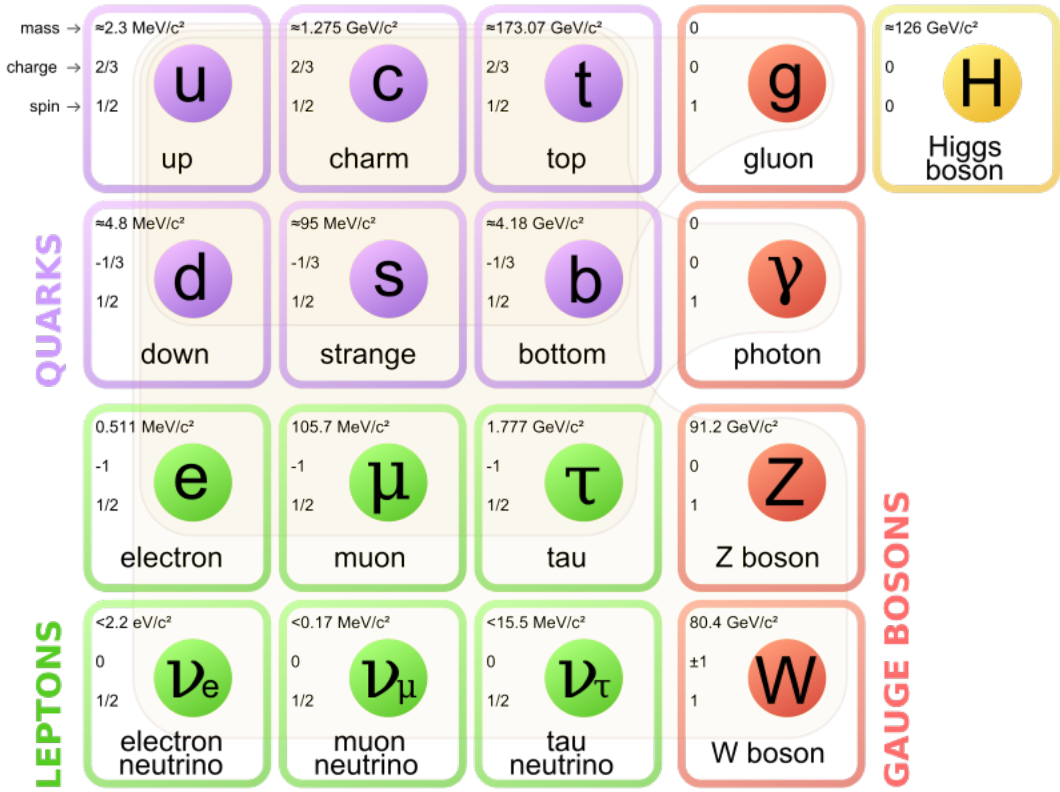

Figure 1.1: Standard Model particles

1.2 Mathematical Formulation of the SM

The Standard Model of particle physics [2, 3, 4] is a gauge quantum field theory. In a quantum field theory the particles are described as excitations of 3 types of fields according their spin. The SM also contains the internal gauge symmetries of the unitary product group $SU(3) \times SU(2) \times U(1)$. The demand for a Lagrangian which is invariant under these internal symmetries is enough to produce all the dynamics of the three interactions which the SM describes. Invariance under $U(1)$ hypercharge combined with $SU(2)$ weak isospin produces the unified electroweak interaction and invariance under $SU(3)$ color transformations produces quantum chromodynamics (QCD).

1.2.1 Noether's Theorem

As it is known from classical mechanics the Lagrangian formalism is based on the demand of action extremization, $\delta S = 0$. In quantum field theory the Lagrangian density $\mathcal{L}$ is a function of fields and their time-space derivatives $\mathcal{L} = \mathcal{L}(\psi_i, \partial_\mu \psi_i)$. The action is defined as

$$S = \int \mathcal{L} d^4 x \tag{1.1}$$

and the demand for its extremization leads to Euler-Langange equation for the fields ψ_i

$$\frac{\partial \mathcal{L}}{\partial \psi_i} = \partial_\mu \left(\frac{\partial \mathcal{L}}{\partial(\partial_\mu \psi_i)} \right) \tag{1.2}$$

The great advantage of this formalism is that every symmetry in the Lagrangian leads to a conservation law. Noether offered this theorem in her 1918 work [5, 6]

If the action S is invariant under a finite dimensional continuous group of transformations depending smoothly on ρ independent parameters ω_α then the current

$$j^\mu_\alpha = -\sum_i \frac{\partial \mathcal{L}}{\partial(\partial_\mu \psi_i)} \frac{\partial \delta \psi_i}{\partial(\Delta \omega_\alpha)} \tag{1.3}$$

is conserved

$$\partial_\mu j^\mu_\alpha = 0 \tag{1.4}$$

1.2.2 Free Fields

The free particles in SM are described by 3 different equations according their spin.
Spinless particles are described by the Lagrangian density (or Lagrangian for short)

$$\mathcal{L} = \frac{1}{2}(\partial^\mu \phi \partial_\mu \phi) - \frac{1}{2} m^2 \phi^2 \tag{1.5}$$

and the Euler-Lagrange equation leads to

$$(\partial^\mu \partial_\mu + m^2)\varphi = 0 \tag{1.6}$$

which is known as Klein-Gordon equation. Its solution is the wavefunction

$$\phi \sim e^{i p_\mu x^\mu} \tag{1.7}$$

So spinless particle, like Higgs Boson, are described as scalar fields.

Fermions are described by the Lagrangian

$$\mathcal{L} = i\bar{\psi}\gamma^\mu \partial_\mu \psi - m\bar{\psi}\psi \tag{1.8}$$

from which the Dirac equation is derived

$$(i\gamma^\mu \partial_\mu - m)\psi = 0 \tag{1.9}$$

where γ^μ are the Dirac matrices. The solution of this equation is

$$\psi \sim e^{-ix^\mu p_\mu} u^i \tag{1.10}$$

So fermions are described as spinors. The four different Dirac spinors u^i describe the four combinations of particles or antiparticles with spin 1/2 in up or down direction.

Bosons lastly are described by

$$\mathcal{L} = -\frac{1}{4} F^{\mu\nu} F_{\mu\nu} + \frac{1}{2} m^2 A_\mu A^\mu \tag{1.11}$$

where the field strength tensor $F^{\mu\nu}$ is a shorthand for, $F^{\mu\nu} \equiv \partial^\mu A^\nu - \partial^\nu A^\mu$. It leads to

$$\partial_\mu F^{\mu\nu} + m^2 A^\nu = 0 \tag{1.12}$$

for which the solution is

$$A^\mu \sim \epsilon^\mu e^{p_\nu x^\nu} \tag{1.13}$$

where ϵ^μ stands for the 3 possible field polarizations.

1.2.3 Interactions

The above three equations describe only free particles. In order to describe interactions some additional terms have to be added in the Lagrangian. For a charged particle inside a electromagnetic field, for example, the momentum has an extra term coming from the interaction with the field

$$p_\mu \to p_\mu - qA_\mu \tag{1.14}$$

Substituting with the equivalent quantum operator for the momentum in equation 1.8

$$\partial_\mu \to \partial_\mu + iqA_\mu \tag{1.15}$$

an extra term, which can be identified as the interaction term, emerges

$$\mathcal{L}_{int} = q\bar{\psi}\gamma^\mu A_\mu \psi \tag{1.16}$$

describing the interaction shown in Figure 1.2

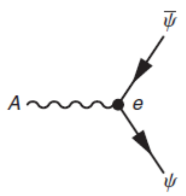

Figure 1.2: Interaction term as Feynman diagram

This extra interaction term can be obtained purely by constructing a Lagrangian which is invariant under local gauge transformations, invariance under inserting a different phase in the wavefunction for every time-space point namely. Dirac Lagrangian 1.8 is obviously invariant under a global gauge transformation (inserting the same phase for all the time-space points) of the field ψ, so if

$$\psi \rightarrow \psi' = \psi \cdot e^{i\theta} \tag{1.17}$$

then

$$\mathcal{L} \rightarrow \mathcal{L}' = \mathcal{L} \tag{1.18}$$

This symmetry, according Noether's theorem 1.3, leads to the conservation of the probability current

$$j^\mu = \bar{\psi}\gamma^\mu\psi \tag{1.19}$$

But under a local gauge transformation

$$\psi \rightarrow \psi' = \psi \cdot e^{iq\theta(x)} \tag{1.20}$$

the Lagrangian 1.8 [1] is not invariant as

$$\mathcal{L} \rightarrow \mathcal{L}' = \mathcal{L} - q\bar{\psi}\gamma^\mu\psi\partial_\mu\theta(x) \tag{1.21}$$

In order to make an invariant Lagrangian a new term has to be added to cancel the contribution of $q\bar{\psi}\gamma^\mu\psi\partial_\mu\theta(x)$. An appropriate choice is

$$q\bar{\psi}\gamma^\mu\psi A_\mu \tag{1.22}$$

with the additional demand for the field A_μ to be transformable as

$$A_\mu \rightarrow A_\mu + \partial_\mu\theta \tag{1.23}$$

So the new Lagrangian

$$\mathcal{L} = i\bar{\psi}\gamma^\mu\partial_\mu\psi - m\bar{\psi}\psi - q\bar{\psi}\gamma^\mu\psi A_\mu \tag{1.24}$$

is invariant under the local phase transformations. The field A_μ can be identified as the electromagnetic vector potential (or photon) which, as it is known from the classical electrodynamics, it can be transformed as 1.23 without changing the physically observable fields E and B. This way the interaction term 1.16 arises naturally. Also an additional terms has to be added for representing the free field A_μ. As the photon is a massless vector field the term has to be the first term (which is locally invariant) of the Lagrangian 1.11. The complete Lagrangian is

$$\mathcal{L} = i\bar{\psi}\gamma^\mu\partial_\mu\psi - m\bar{\psi}\psi - q\bar{\psi}\gamma^\mu\psi A_\mu - \frac{1}{4}F^{\mu\nu}F_{\mu\nu} \tag{1.25}$$

and describes one massive spinor field interacting with a massless vector field. The Euler-Lagrange equation for the above Lagrangian yields

[1] as the function $\theta(x)$ is arbitrary a constant q can be added

$$\partial_\mu F^{\mu\nu} = j^\nu \tag{1.26}$$

with $j^\nu = q\bar{\psi}\gamma^\mu\psi A_\mu$ being the four-vector electromagnetic current, which is conserved

$$\partial_\mu j^\mu = 0 \tag{1.27}$$

Hence the whole of electromagnetism can be derived by requiring a local gauge symmetry of the Lagrangian for a particle satisfying the Dirac equation.

The phase transformation factor can be seen as an unitary 1×1 matrix

$$U = e^{i\theta} \tag{1.28}$$

This is a U(1) transformation depending on the real parameter θ. In the Standard Model all the fundamental interactions are generated by constructing a locally invariant Lagrangian to the corresponding phase transformation of each interaction. The term which is added, in order to make it invariant, is the interaction term between a fermion and the interaction bosons. For the strong interaction the QCD can be produced from a SU(3) color invariant Lagrangian. In this case the transformation matrix is

$$U = e^{i\boldsymbol{\lambda}\cdot\boldsymbol{\theta}} \tag{1.29}$$

acting on a wavefuction which has three components, one for each color

$$\psi = \begin{pmatrix} \psi_r \\ \psi_g \\ \psi_b \end{pmatrix}, \qquad \bar{\psi} = (\bar{\psi}_r, \bar{\psi}_g, \bar{\psi}_b) \tag{1.30}$$

and hence the interaction derivative is also a 3×3 matrix

$$\partial_\mu \rightarrow \partial_\mu + i\alpha_s \boldsymbol{\lambda} \boldsymbol{G_\mu} \tag{1.31}$$

where α_s is the coupling strength between the field and the particle, $\boldsymbol{\lambda}$ are the 8 3×3 Gell-Mann matrices, which are the generators of the SU(3) group, G are the 8 gluon fields and $G_{\mu\nu}$ the color field tensors. According Noether's theorem 8 color currents are conserved. The complete QCD Lagrangian, which is invariant under $SU(3)$ color transformations, is

$$\mathcal{L} = i\bar{\psi}\gamma^\mu\partial_\mu\psi - m\bar{\psi}\psi - g\bar{\psi}\gamma^\mu\boldsymbol{\lambda}\psi\boldsymbol{G_\mu} - \frac{1}{4}\boldsymbol{G_{\mu\nu}}\boldsymbol{G^{\mu\nu}} \tag{1.32}$$

This method works perfectly as long as the boson fields are massless. For the electrodynamics and chromodynamics this is the case as both photons and gluons are massless. However the fields of the weak interaction, the Z and W bosons namely, are massive. Adding a mass term in the Lagrangian makes it no-invariant under the local gauge transformations and this leads the theory to be unrenormalizable. The problem solved by the Higgs mechanism, proposed by Robert Brout, François Englert [7] and Peter Higgs [8] in 1964.

1.2.4 The Higgs Mechanism

Assuming a complex scalar field

$$\phi = \frac{1}{\sqrt{2}}(\phi_1 + i\phi_2) \qquad with \qquad V(\phi) = \mu^2(\phi^*\phi) + \lambda(\phi^*\phi)^2 \tag{1.33}$$

the corresponding Lagrangian is

$$\mathcal{L} = (\partial_\mu \phi)^*(\partial^\mu \phi) - \mu^2 \phi^* \phi - \lambda(\phi^*\phi)^2 \tag{1.34}$$

For the case that $\lambda > 0$ and $\mu^2 < 0$ the term proportional to $\phi\phi^*$ can not be identified as mass term as it leads to a negative mass.
The potential $V(\phi)$ has a circle of minima in the ϕ_1, ϕ_2 plane such as

$$\phi_1^2 + \phi_2^2 = \upsilon^2 \qquad with \qquad \upsilon^2 = -\frac{\mu^2}{\lambda} \tag{1.35}$$

Choosing one of these points $\phi_1 = \upsilon, \phi_2 = 0$ and expanding the field $\phi(x)$ about it in terms of $\eta(x) = \phi_1(x) - \upsilon$ and $\xi(x) = \phi_2(x)$, so

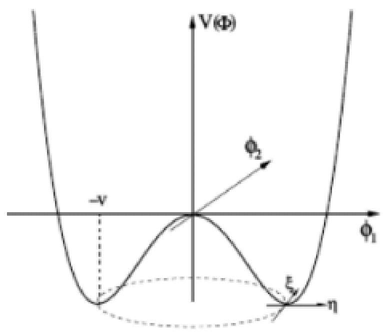

Figure 1.3: The potential $V(\phi)$ for a complex scalar field for the case $\mu^2 < 0$ and $\lambda > 0$ [4].

$$\phi(x) = \frac{1}{\sqrt{(2)}}\left[\upsilon + \eta(x) + i\xi(x)\right] \tag{1.36}$$

the initial Lagrangian can be rewritten in terms of excitation about this minimum

$$\mathcal{L} = \left[\frac{1}{2}(\partial_\mu \eta)(\partial^\mu \eta) - m_\eta^2 \eta^2\right] + \left[\frac{1}{2}(\partial_\mu \xi)(\partial^\mu \xi)\right] + \mathcal{L}_{int}(\eta, \xi) \tag{1.37}$$

The arbitrary choice of the point $(\upsilon, 0)$ as minimum is an example of a spontaneously broken symmetry. In the new Lagrangian the field η has mass $m_\eta = \sqrt{2\lambda\upsilon^2}$. The massless scalar field ξ that emerged is known as Goldstone boson. The term $\mathcal{L}_{int}$ includes all the interaction terms between the fields η and ξ as shown in figure

$$\mathcal{L}_{int} = \lambda\upsilon\eta^3 + \frac{1}{4}\lambda\eta^4 + \frac{1}{4}\lambda\xi^4 + \lambda\upsilon\eta\xi^2 + \frac{1}{2}\lambda\eta^2\xi^2 \tag{1.38}$$

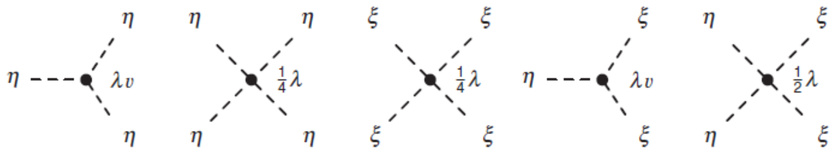

Figure 1.4: η - ξ interaction vertices representing Lagrangian 1.38 terms.

Including an interaction term with a vector field in the initial Lagrangian 1.34, using the usual substitution $\partial_\mu \to \partial_\mu + iqA_\mu$, it becomes

$$\mathcal{L} = (\partial_\mu - iqA_\mu\phi)^*(\partial^\mu + iqA^\mu\phi) - \mu^2\phi^*\phi - \lambda(\phi^*\phi)^2 - \frac{1}{4}F^a_{\mu\nu}F^{\mu\nu}_a \tag{1.39}$$

Rewriting again the ϕ in terms of η and ξ the Lagrangian becomes

$$\mathcal{L} = \left[\frac{1}{2}(\partial_\mu\eta)(\partial^\mu\eta) - \mu^2\eta^2\right] + \left[\frac{1}{2}(\partial_\mu\xi)(\partial^\mu\xi)\right] + \left[\frac{1}{4}F_{\mu\nu}F^{\mu\nu} + \frac{1}{2}g^2v^2A_\mu A^\mu\right] + [guB_\mu(\partial^\mu\xi)] - L_{int} \tag{1.40}$$

The Goldstone boson can be eliminated by choosing an appropriate gauge for the field A_μ

$$A_\mu \to A_\mu + \frac{1}{gv}\partial_\mu\xi(x) \tag{1.41}$$

This gauge is equivalent to writing ϕ in the Unitary gauge, namely

$$\phi(x) = \frac{1}{\sqrt{2}}(v + \eta(x)) \tag{1.42}$$

This choice yields

$$\begin{aligned}\mathcal{L} = &\left[\frac{1}{2}(\partial_\mu\eta)(\partial^\mu\eta) - \mu^2\eta^2\right] + \left[\frac{1}{4}F_{\mu\nu}F^{\mu\nu} + \frac{1}{2}g^2v^2A_\mu A^\mu\right] \\ &+ \left[g^2vA_\mu A^\mu\eta + \frac{1}{2}g^2A_\mu A^\mu\eta^2\right] - \lambda v\eta^3 - \frac{1}{4}\lambda\eta^4\end{aligned} \tag{1.43}$$

Finally the above Lagrangian can be embedded in the Dirac Lagrangian

$$\begin{aligned}\mathcal{L} = &[i\bar{\psi}\gamma^\mu\partial_\mu\psi - m\bar{\psi}\psi] - [q\bar{\psi}\gamma^\mu\psi A_\mu] + \left[\frac{1}{4}F_{\mu\nu}F^{\mu\nu} + \frac{1}{2}g^2v^2A_\mu A^\mu\right] \\ &+ \left[\frac{1}{2}(\partial_\mu\eta)(\partial^\mu\eta) - \mu^2\eta^2\right] + \left[g^2vA_\mu A^\mu h + \frac{1}{2}g^2A_\mu A^\mu\eta^2\right] - \lambda v\eta^3 - \frac{1}{4}\lambda\eta^4\end{aligned} \tag{1.44}$$

This Lagrangian in now invariant under local U(1) transformations. Hence, in order to retain the invariance of a Lagrangian, which includes a massive interaction field, a new scalar field has to be introduced.

1.2.5 The SM Higgs Boson

In the SM the Higgs mechanism is used to create massive vector bosons for the unified electroweak interaction, which was proposed in 1960s by Sheldon Glashow, Abdus Salam and Steven Weinberg [9, 10]. For this purpose a doublet of Higgs fields is required

$$\phi = \begin{pmatrix} \phi^{\dagger} \\ \phi^{0} \end{pmatrix} = \frac{1}{\sqrt{2}} \begin{pmatrix} \phi_1 + i\phi_2 \\ \phi_3 + i\phi_4 \end{pmatrix} \tag{1.45}$$

The corresponding potential is

$$V(\phi) = \mu^2 \phi^{\dagger}\phi + \lambda(\phi^{\dagger}\phi)^2 \tag{1.46}$$

Firstly, the field has to be written again in the Unitary gauge to eliminate the Goldstone bosons

$$\phi(x) = \frac{1}{\sqrt{2}} \begin{pmatrix} 0 \\ \upsilon + h(x) \end{pmatrix} \tag{1.47}$$

Then it is embedded in a Lagrangian with a $SU(2) \times SU(1)$ interaction term which includes both the electromagnetic and weak interactions. The interaction with the Higgs field is

$$\left[\partial_\mu + ig_w \boldsymbol{T} \cdot \boldsymbol{W_\mu} + ig\frac{Y}{2}B_\mu\right] \begin{pmatrix} 0 \\ \upsilon + h(x) \end{pmatrix} \tag{1.48}$$

where $\boldsymbol{T} = \boldsymbol{\sigma}/2$ and σ are the three generators of the SU(2) symmetry, known as Pauli matrices. Y is the weak hypercharge defined form the electromagnetic charge and the 3rd component of weak isospin, $Y = 2(q - I_w^3)$. The partial derivative of the interaction is now a 2×2 matrix which mixes the fields W^1, W^1, W^2, B producing the physically observable fields W^+, W^-, Z^0, γ

$$\begin{aligned} W^+ &= \frac{1}{\sqrt{2}}(W^1 - iW^2) \\ W^- &= \frac{1}{\sqrt{2}}(W^1 + iW^2) \\ Z^0 &= -\sin\theta_W B + \cos\theta_W W^3 \\ \gamma &= \cos\theta_W B + \sin\theta_W W^3 \end{aligned} \tag{1.49}$$

where $cos\theta_W$ is defined from the ratio of weak and electromagnetic coupling strengths

$$tan\theta_W = \frac{g'}{g_W} \tag{1.50}$$

The masses of the particles that arise are

$$\begin{aligned} m_W &= \frac{1}{2}g_w\upsilon \\ m_Z &= \frac{1}{2}\upsilon\sqrt{g^2 + g'^2} \\ m_\gamma &= 0 \end{aligned} \tag{1.51}$$

and lead to a crucial evidence for Higgs boson existence

$$\frac{m_W}{m_Z} = cos\theta_W \tag{1.52}$$

as the ratio of the coupling strengths g_W and g' as long the masses of W and Z are experimentally measurable and they had been found in agreement with the prediction of the above equation.

1.2.6 Fermion Masses

The observed form of the weak charged-current interaction couples only to left-handed chiral particle states and right-handed chiral antiparticle states, so the gauge transformation has to affect only left-handed (LH) particles and right-handed (RH) antiparticles. To achieve this, LH particle and RH antiparticle chiral states are placed in weak isospin SU(2) doublets with $I_W^3 = -1/2$ for the upper component and $I_W^3 = 1/2$ for the lower, while RH particle and LH antiparticle chiral states are placed in singlets with $I_w = 0$ and they are therefore unaffected by the SU(2) local gauge transformation. For the first generation of particles (e, ν_e, u, d) the doublets and singlets are

$$\begin{aligned} L &= \begin{pmatrix} \nu_e \\ e^- \end{pmatrix}_L \quad \text{and} \quad R = e_R^- \\ L &= \begin{pmatrix} u \\ d \end{pmatrix}_L \quad \text{and} \quad R = u_R \quad , \quad R = d_R \end{aligned} \tag{1.53}$$

As the two complex scalar fields of the Higgs mechanism are also placed in an SU(2) doublet a SU(2) local gauge transformation has the same effect on them. Consequently, the combination $\bar{L}\phi$ is invariant under the SU(2) gauge transformations. When it is combined with a right-handed singlet, $\bar{L}\phi R$ is invariant under SU(2) and U(1) gauge transformations. Hence, a term in the Lagrangian of the form $(\bar{L}\phi R + \bar{R}\phi L)$ satisfies the SU(2)×U(1) gauge symmetry of the Standard Model. For the leptons after spontaneously symmetry breaking the corresponding Lagrangian terms are

$$\mathcal{L} = -\frac{g}{\sqrt{2}}\upsilon(\bar{e_L}e_R + \bar{e_R}e_L) - -\frac{g}{\sqrt{2}}h(\bar{e_L}e_R + \bar{e_R}e_L) \tag{1.54}$$

The first term is the mass of the leptons while the second one is the interaction with the Higgs boson. This way only the upper component of the weak isospin doublet acquire mass. For the quarks the same terms, but including the hermitian conjugate Higgs field have to be added, in order to give mass to the lower doublet component. So all the fermions can acquire mass by including in the Lagrangian the terms

$$\mathcal{L} = -g_f \left[\bar{L}\phi R + (\bar{L}\phi R)^\dagger\right] \quad \text{and} \quad \mathcal{L} = g_f \left[\bar{L}\phi_c R + (\bar{L}\phi_c R)^\dagger\right] \tag{1.55}$$

Nowadays it is known that the neutrinos have mass. As they are neutral they may be their own antiparticles (Majorana particles) or not (Dirac particles). Hence one term needed to admit the possibility that neutrino masses arise from the spontaneous symmetry breaking of the Higgs mechanism as the rest of the fermions. Additionally, the gauge-invariant Majorana mass term is added by hand, so the general Lagrangian term including both the Dirac and Majorana mass is

$$\mathcal{L}_{DM} = -\frac{1}{2}\left[m_D\bar{\nu_L}\nu_R + m_D\bar{\nu_R^c}\nu_L^c + M\bar{\nu_R^c}\nu_R\right] \tag{1.56}$$

1.2.7 Unification

The complete Lagrangian of the Standard Model can be written shortly as [11]

$$\mathcal{L} = -\frac{1}{4}F_{\mu\nu}F^{\mu\nu} + i\bar{\psi}\gamma^{\mu}D_{\mu}\psi + \psi_i y_{ij}\psi_j\phi + h.c. + |\gamma^{\mu}D_{\mu}\phi|^2 - V(\phi) \tag{1.57}$$

where $F_{\mu\nu}$ is the sum of all field strength tensors, D_{μ} stands for the interaction derivative and the Yukawa matrix y_{ij} represent the coupling parameters of the fermions to the Higgs field. This Lagrangian is invariant under the $SU(3)_c \times SU(2)_{I^3} \times U(1)_Y$ symmetry. These three seemingly unrelated symmetries may be contained in a Grand Unified Group G such as

$$G \supset SU(3)_c \times SU(2)_{I^3(L)} \times U(1)_Y \tag{1.58}$$

In this case all the interactions would be described by a Grand Unified Theory (GUT) with a single coupling to which all the couplings are related in a specific way. A unification scheme is shown in figure 1.5 The coupling of the three interactions depend on the characteristic momentum. The couplings of QCD and Weak interaction are asymptotically free, whereas the coupling of QED increases with increasing momentum Q, suggesting that for large-momentum (or short distance) scale the three coupling are merged into a single grand unified coupling

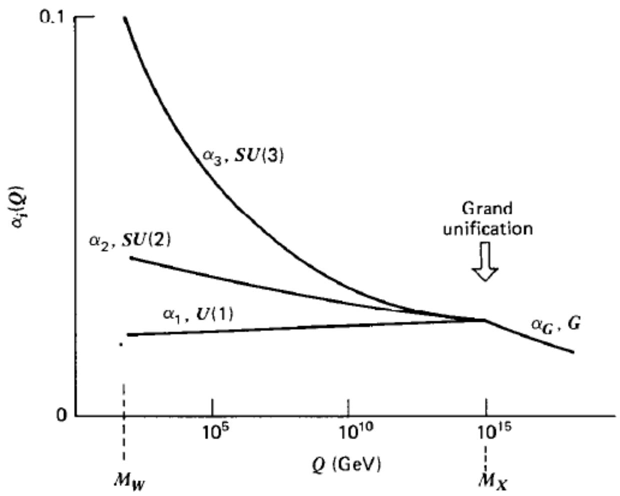

Figure 1.5: The variation of coupling strengths α_i with Q, showing the speculative grand unification of strong [$SU(3)_c$] and electroweak [$SU(2)_{I^3(L)} \times U(1)_Y$] interactions at very short distances, or high energies [4].

1.2.8 Beyond the SM Higgs Bosons

The possibility that the Higgs Boson is part of an extended Higgs sector or other extension of the SM cannot be ruled out. Many of these models, motivated by hierarchy and naturalness arguments [12, 13, 14], predict the existence of new heavy resonances decaying into dibosons. In models with an extended Higgs sector, such as the two-Higgs-doublet models (2HDM) [15] and the electroweak-singlet model [16], a heavy spin-0 neutral Higgs boson is predicted.

The Two-Higgs-Doublet model

The Two-Higgs-Doublet models is the simplest extension of the electroweak Higgs sector carried by the addition of another scalar doublet. Their phenomenology is extremely rich, since it contains a charged Higgs, a pseudoscalar and two neutral scalars, flavour-changing neutral currents, and more

possibilities for CP violation and baryogenesis. There are many motivations for 2HDMs, the best known motivation is supersymmetry [12]. In supersymmetric theories the scalars belong to chiral multiplets and their complex conjugates belong to multiplets of the opposite chirality; since multiplets of different chiralities cannot couple together in the Lagrangian, a single Higgs doublet is unable to give mass simultaneously to the charge 2/3 and charge -1/3 quarks. Moreover, since scalars sit in chiral multiplets together with chiral spin-1/2 fields, the cancellation of anomalies also requires that an additional doublet be added. Thus, the Minimal Supersymmetric Standard Model (MSSM) contains two Higgs doublets.Another motivation for 2HDMs comes from axion models [17] used in order to cancel a possible CP-violating term in the QCD Lagrangian [18]. Still another motivation for 2HDMs is the fact that the SM is unable to generate a baryon asymmetry of the Universe of sufficient size whereas Two-Higgs-doublet models can do so [19].
The most general 2HDM scalar potential contains 14 parameters and can have CP conserving, CP violating, and charge violating minima. In writing that potential one must be careful in defining the various bases and in distinguishing parameters which can be rotated away from those which have physical implications. However, most phenomenological studies of 2HDMs make several simplifying assumptions. It is usually assumed that CP is conserved in the Higgs sector (only then can one distinguish between scalars and pseudoscalars), that CP is not spontaneously broken, and that discrete symmetries eliminate from the potential all quartic terms odd in either of the doublets; however, usually one considers all possible real quadratic coefficients, including a term which softly breaks these symmetries. Under those assumptions, the most general scalar potential for two doublets Φ_1 and Φ_2 with hypercharge +1 is

$$\begin{aligned} V =& m_{11}^2\Phi_1^\dagger\Phi_1 + m_{22}^2\Phi_2^\dagger\Phi_2 - m_{12}^2(\Phi_1^\dagger\Phi_2 + \Phi_2^\dagger\Phi_1) + \frac{\lambda_1}{2}(\Phi_1^\dagger\Phi_1)^2 + \frac{\lambda_2}{2}(\Phi_2^\dagger\Phi_2)^2 \\ &+ \lambda_3\Phi_1^\dagger\Phi_1\Phi_2^\dagger\Phi_2 + \lambda_4\Phi_1^\dagger\Phi_1\Phi_2^\dagger\Phi_2 + \frac{\lambda_5}{2}\left[(\Phi_1^\dagger\Phi_2)^2 + (\Phi_2^\dagger\Phi_1)^2\right] \end{aligned} \tag{1.59}$$

With two complex scalar SU(2) doublets there are eight fields

$$\Phi_\alpha = \begin{pmatrix} \phi_\alpha^\dagger \\ (\upsilon_\alpha + \rho_\alpha + i\eta_\alpha/\sqrt{2}) \end{pmatrix}, \qquad \alpha = 1, 2 \tag{1.60}$$

Three of those get eaten to give mass to the $W^\pm$ and Z^0 gauge bosons; the remaining five are physical scalar (Higgs) fields. There are two charged scalar, two neutral scalars, and one pseudoscalar.

1.3 Higgs Boson

Evidence of the discovery of a new particle compatible with the Standard Model Higgs boson was published by the ATLAS and CMS experiments in the Summer of 2012 [20, 21]. Both of these experiments are installed on the Large Hadron Collider at CERN and they discovered Higgs boson from the debris of proton-proton collisions. The new particle mass was found to be about 125 GeV.

1.3.1 Production

In hadron colliders Higgs bosons are mainly produced by four processes. The total cross section for the Higgs (m=125GeV) boson production at LHC Run II operating center of mass energy of 13 TeV is about 55 pb. The most significant production process is the gluon-gluon fusion (ggF) with cross section of about 48.6 pb. The vector boson fusion (VBF) is the second one with about 3.78 pb. Smaller contributions from the associated production with W/Z bosons (ZH / WH) and Higgs production with heavy top or bottom quarks (ttH).

There are also several mechanisms for the pair production of the Higgs particles Higgs pair production : $pp \to HH + X$ and the relevant sub–processes are the $gg \to HH$ mechanism, which proceeds

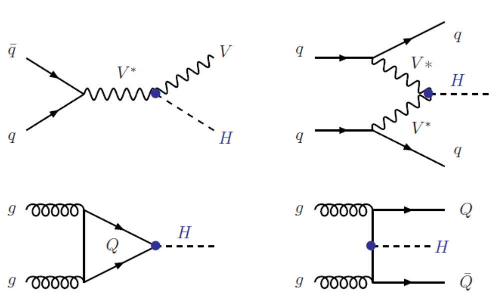

(a) Main Feynman diagrams; ZH/WH, VBF, ggF, ttH

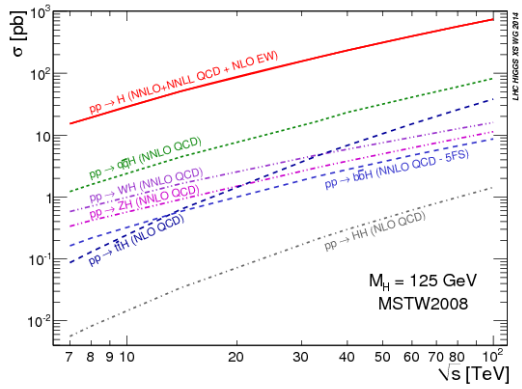

(b) Production cross sections as a function of the center of mass energy for pp collisions

Figure 1.6: Main Feynman diagrams (a) and cross section (b) of the main Higgs boson production processes

through heavy top and bottom quark loops, the associated double production with massive gauge bosons, $qq \to HHV$, and the vector boson fusion mechanisms $qq \to VV \to HHqq$. However, because of the suppression by the additional electroweak couplings, they have much smaller production cross sections than the single Higgs production mechanisms listed above.

A mixture of perturbative and non perturbative aspects of QCD is needed to evaluate the cross sections, leading to uncertainties in the predictions. Detailed information about the SM Higgs boson properties and phenomenology, including uncertainties in the theoretical calculations due to missing higher-order effects and experimental uncertainties on the determination of SM parameters involved in the calculations, can be found in [22, 23, 24, 25]. The latest studies for the impact of PDF uncertainties, QCD scale uncertainties and uncertainties due to different procedures for including higher-order corrections matched to parton shower simulations, as well as uncertainties due to hadronisation and parton-shower events are used. The State-of-the-art of the theoretical calculations in the main Higgs boson production channels in the SM, and the major MC tools used in the simulations are shown in Tables 1.1. The cross sections for the production of a SM Higgs boson as a function of the center of mass energy, for pp collisions, including bands indicating the theoretical uncertainties, as well the main Feynman diagrams of Higgs boson production are summarized in Figure 1.6.

1.3.2 Decay Modes

In the SM, once the Higgs boson mass is fixed, its profile is uniquely determined. The couplings to gauge bosons and fermions are directly proportional to the masses of the particles and the Higgs boson will have the tendency to decay into the heaviest ones allowed by phase space. Since the masses of the gauge bosons and fermions are known all the Branching Ratios (BRs) for the Higgs decays into these particles can be predicted. The main Feynman diagrams and BRs are shown in Figure 1.7(a). The uncertainties in the branching ratios include the missing higher-order corrections in the theoretical calculations as well as the errors in the SM input parameters, in particular fermion masses and the QCD gauge coupling, involved in the decay. The state-of-the-art of the theoretical calculations are shown in Figure 1.7(b) and Table 1.3. The branching ratios of the Higgs boson in the SM have been determined using the programs *HDECAY* [26] and *PROPHECY4F* [27, 28]. In a first step, all partial widths have been calculated as accurately as possible and then the branching ratios have been derived from this full set of partial widths.

ggF	VBF	VH	$t\bar{t}H$
Fixed Order: N3LO QCD + NLO EW ***HIGLU, 1H1XS*** ***, FeH1Pro, HNNLO***	Fixed Order: NNLO QCD ***VBF@NNLO***	Fixed Order: NLO QCD + EW ***V2HV, HAWK***	Fixed Order: NLO QCD + EW ***Powheg*** ***MG5_aMC@NLO***
Resummed: NNLO + NLLL QCD ***HRes***	Fixed Order: NLO QCD + EW ***HAWK***	Fixed Order: NLLO QCD ***VH@NNLO***	
Higgs p_T: NNLO+NNLL ***HqT, HRes***			
Jet Veto: N3LO+NNLL			

Table 1.1: Major MC tools used in the simulations for Higgs boson production.

XS (pb)	ggF	VBF	WH	ZH	$t\bar{t}H$	Total
$\sqrt{s} = 13TeV$	$48.6^{+4.6\%}_{-6.7\%}$	$3.78^{+2.2\%}_{-2.2\%}$	$1.37^{+2.6\%}_{-2.6\%}$	$0.88^{+4.1\%}_{-3.5\%}$	$0.50^{+6.8\%}_{-9.9\%}$	55.1

Table 1.2: State-of-the-art of the theoretical cross section calculations in the main Higgs production channels for m_H = 125 GeV in pp collisions at $\sqrt{s} = 13TeV$

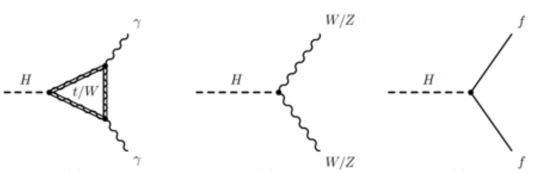

(a) Feynman diagrams of the main decay channels; $\gamma\gamma$, VV, $f\bar{f}$

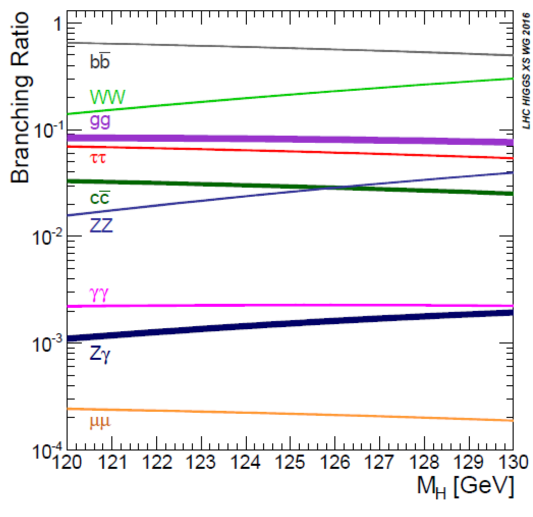

(b) The branching ratios for the main decays of the SM Higgs boson near m_H = 125GeV. The theoretical uncertainties are indicated as bands.

Figure 1.7: Feynman diagrams and branching ration for main Higgs boson decays

1.3.3 Decay Width

The total width of a 125 GeV SM Higgs boson has been calculated to be Γ_H=4.07 MeV, with a relative uncertainty of +4.0% -3.9% using *HDECAY* and *PROPHECY4F*. *HDECAY* calculates the decay

Decay Channel	Branching Ratio	Relative Uncertainty
$H \to b\bar{b}$	$5.82 \cdot 10^{-1}$	$^{+1.2\%}_{-1.3\%}$
$H \to W^+W-$	$2.14 \cdot 10^{-1}$	$\pm 1.5\%$
$H \to \tau^+\tau^-$	$6.27 \cdot 10^{-2}$	$\pm 1.6\%$
$H \to c\bar{c}$	$2.89 \cdot 10^{-2}$	$^{+5.5\%}_{-2.0\%}$
$H \to ZZ$	$2.62 \cdot 10^{-2}$	$\pm 1.5\%$
$H \to \gamma\gamma$	$2.27 \cdot 10^{-3}$	$\pm 2.1\%$
$H \to Z\gamma$	$1.53 \cdot 10^{-3}$	$\pm 5.8\%$
$H \to \mu^+\mu_-$	$2.18 \cdot 10^{-4}$	$\pm 1.7\%$

Table 1.3: The branching ratios and the relative uncertainty for a SM Higgs boson with $m_H = 125GeV$.

widths and branching ratios of the Higgs boson(s) in the SM and the MSSM, while *PROPHECY4F* is a Monte Carlo event generator for $H \to WW/ZZ \to 4f$ (leptonic, semi-leptonic,and hadronic) final states. The Higgs total width is obtained by

$$\Gamma_H = \Gamma^{HD} - \Gamma^{HD}_{ZZ} - \Gamma^{HD}_{WW} + \Gamma^{Proph}_{4f}. \tag{1.61}$$

where Γ_H is the total Higgs width, Γ^{HD} the Higgs width obtained from *HDECAY*, Γ^{HD}_{ZZ} and Γ^{HD}_{WW} stand for the partial widths to ZZ and WW calculated with *HDECAY*, while $\Gamma^{Proph.}_{4f}$ represents the partial width of $H \to 4f$ calculated with *PROPHECY4F*.

1.4 Higgs boson Experimental Profile

For a given m_H, the sensitivity of a channel depends on the production cross section of the Higgs boson, its decay branching fraction, the reconstructed mass resolution, the selection efficiency and the level of background in the final state [29]. For the SM Higgs boson for which the width is only a few MeV, five decay channels play an important role at the LHC. In the $H \to \gamma\gamma$ and $H \to ZZ^* \to 4\ell$ channels, all final state particles can be very precisely measured and the reconstructed mH resolution is excellent (typically 1-2%). While the $H \to W^+W^- \to ll\nu\nu$ channel has relatively large branching fraction, however, due to the presence of neutrinos which are not reconstructed in the final state, the m_H resolution, obtained through observables sensitive to the Higgs boson mass such as the transverse mass, is poor (approximately 20%). The $H \to b\bar{b}$ and the $H \to \tau^+\tau^-$ channels suffer from large backgrounds and lead to an intermediate mass resolution of about 10% and 15% respectively. With the increase in the size of datasets, measurements in the most sensitive channels are now carried out differentially or in exclusive modes depending on specific production characteristics. The candidate events in each Higgs boson decay channel are split into several mutually exclusive categories based on the specific topological, kinematic or other features present in the event. The categorization of events increases the sensitivity of the overall analysis and allows a separation of different Higgs boson production processes. Most categories are dominated by signal from one Higgs boson decay mode but contain an admixture of various Higgs boson production processes. Simulations are used to determine the relative contributions of the various Higgs boson production modes in each specific categories.

During Run I The ATLAS and CMS Collaborations have independently measured the mass of Higgs boson using the samples of proton-proton collision data collected in 2011 and 2012, during LHC Run I. The analyzed samples correspond to approximately 5 fb^{-1} of integrated luminosity at $\sqrt{s} = 7$ and 20 fb^{-1} at $\sqrt{s} = 8$ for each experiment. The mass of the Higgs boson was measured to be 125.09 ± 0.24 GeV [30] based on the combined Run 1 data samples of the ATLAS and CMS Collaborations, who also reported individual mass measurements in Refs. [31, 32]. ATLAS latest measurement based on $H \to \gamma\gamma$ and $H \to ZZ^* \to 4\ell$ decay channels with 36.1 fb^{-1} at a centre-of-mass energy of 13 TeV recorded by the ATLAS detector in 2015 and 2016. The measured value in the

$H \to ZZ^* \to 4\ell$ channel is $m_{ZZ^*H} = 124.79 \pm 0.37$ GeV, while the measured value in the $H \to \gamma\gamma$ channel is $m_{\gamma\gamma H} = 124.93 \pm 0.40$ GeV. Combining these results with the ATLAS measurement based on 7 TeV and 8 TeV proton-proton collision data yields a Higgs boson mass of $m_H = 124.97 \pm 0.24$ GeV as shown in Figure 1.8(a).

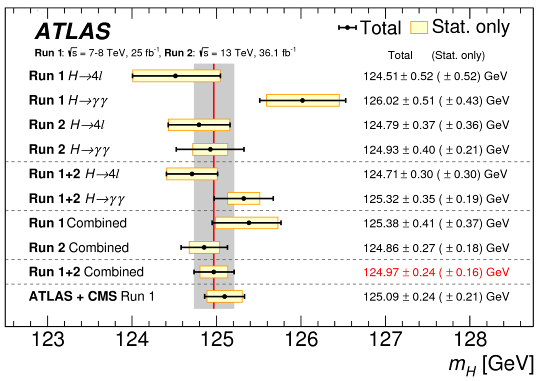

(a) Summary of the Higgs boson mass measurements from the individual and combined analyses performed here, compared with the combined Run 1 measurement by ATLAS and CMS. The statistical-only (horizontal yellow-shaded bands) and total (black error bars) uncertainties are indicated. The (red) vertical line and corresponding (grey) shaded column indicate the central value and the total uncertainty of the combined ATLAS Run 1 + 2 measurement, respectively [33].

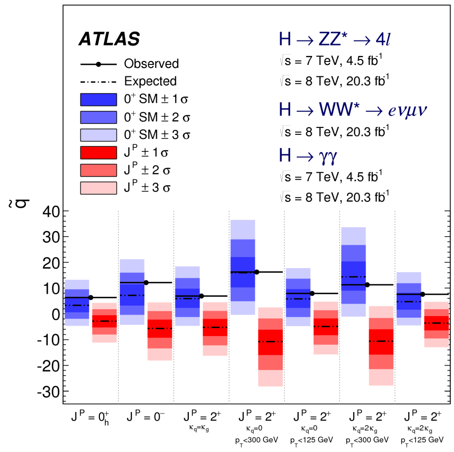

(b) Distributions of the test statistic q for the SM Higgs boson and for the JP alternative hypotheses. They are obtained by combining the $H \to ZZ^* \to 4\ell$, $H \to WW^* \to e\nu\mu\nu$ and $H \to \gamma\gamma$ decay channels. The expected median (black dashed line) and the ±1, ±2 and ±3 σ regions for the SM Higgs boson (blue) and for the alternative JP hypotheses (red) are shown for the signal strength fitted to data. The observed q values are indicated by the black points[34].

Figure 1.8: Results of Higgs boson mass and spin-parity measurements

Studies of the spin, parity and tensor couplings of the Higgs boson [34] in the $H \to ZZ^* \to 4\ell$, $H \to WW^* \to e\nu\mu\nu$ and $H \to \gamma\gamma$ decay processes at the LHC were also carried out. The investigations are based on 25 fb^{-1} of pp collision data collected by the ATLAS experiment at $\sqrt{s}$=7 and 8 TeV. The Standard Model (SM) Higgs boson hypothesis, corresponding to the quantum numbers $J^p = 0$, was tested against several alternative spin scenarios, including non-SM spin-0 and spin-2 models with universal and non-universal couplings to fermions and vector bosons. All tested alternative models are excluded in favour of the SM Higgs boson hypothesis at more than 99.9% confidence level 1.8(b). Using the $H \to ZZ^* \to 4\ell$ and $H \to WW^* \to e\nu\mu\nu$ decays, the tensor structure of the interaction between the spin-0 boson and the SM vector bosons is also investigated. The observed distributions of variables sensitive to the non-SM tensor couplings are compatible with the SM predictions and constraints on the non-SM couplings are derived.

Combined measurements of Higgs boson production cross sections and branching fractions 1.9(a), 1.9(b) have been also carried out [35]. The combination is based on the analyses of the Higgs boson decay modes $H \to \gamma\gamma, ZZ^*, WW^*, \tau\tau, b\bar{b}, \mu\mu$, searches for decays into invisible final states and on measurements of off-shell Higgs boson production. Up to 79.8 fb^{-1} of proton-proton collision data collected at $\sqrt{s} = 13$ TeV with the ATLAS detector were used. The global signal strength was determined to be $\mu = 1.11^{+0.09}_{-0.08}$. The results are interpreted in terms of modifiers applied to the Standard Model couplings 1.9(c), 1.9(d) of the Higgs boson to other particles, and are used to set exclusion limits on parameters in two-Higgs-doublet models and in the simplified Minimal Supersymmetric Standard Model. No significant deviations from Standard Model predictions are observed.

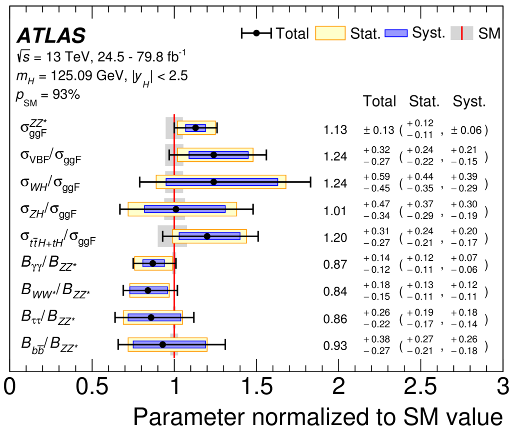

(a) Results of a simultaneous fit for σ^{ZZ}_{ggF}, $\sigma_{VBF}/\sigma_{ggF}$, σ_{WH}/σ_{ggF}, σ_{ZH}/σ_{ggF}, $\sigma_{t\bar{t}H}/\sigma_{ggF}$, $B_{\gamma\gamma}/B_{ZZ}$, B_{WW}/B_{ZZ}, $B_{\tau\tau}/B_{ZZ}$, and B_{bb}/B_{ZZ}. The fit results are normalized to the SM predictions. The black error bars, blue boxes and yellow boxes show the total, systematic, and statistical uncertainties in the measurements, respectively. The grey bands show the theory uncertainties in the predictions

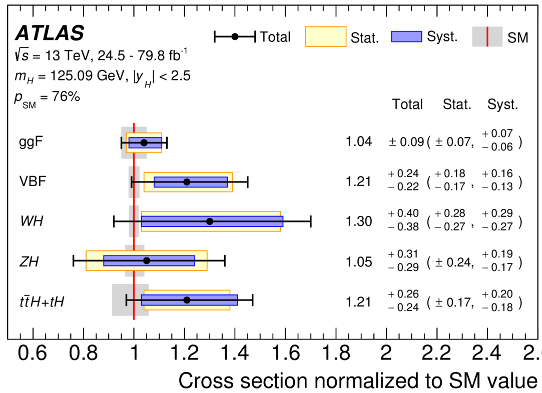

(b) Cross-sections for ggF, VBF, WH, ZH and $t\bar{t}H+tH$ normalized to their SM predictions, measured with the assumption of SM branching fractions. The black error bars, blue boxes and yellow boxes show the total, systematic, and statistical uncertainties in the measurements, respectively. The grey bands indicate the theory uncertainties in the cross-section predictions.

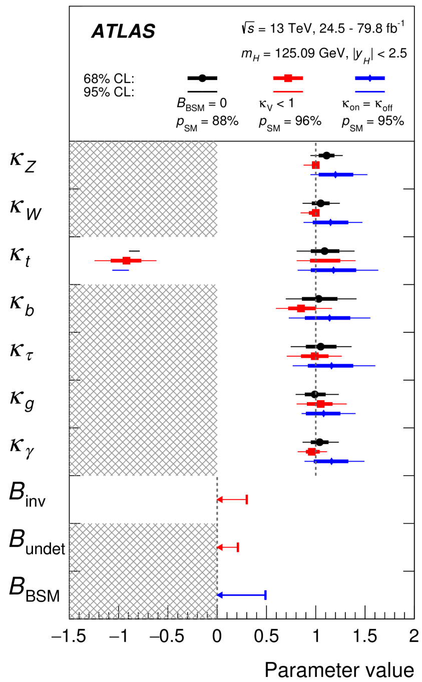

(c) Best-fit values and uncertainties for Higgs boson coupling modifiers per particle type with effective photon and gluon couplings and either $B_{inv} = B_{undet} = 0$ (black); B_{inv} and B_{undet} included as free parameters, the conditions $\kappa_{W,Z} \leq 1$ applied and the measurement of the Higgs boson decay rate into invisible final states included in the combination (red); or $B_{BSM} = B_{inv} = B_{undet}$ included as a free parameter, the measurement of off-shell Higgs boson production included in the combination, and the assumptions described in the text applied to the off-shell coupling-strength scale factors (blue). The SM corresponds to $B_{inv} = B_{undet} = 0$ and all κ parameters set to unity. All parameters except κ_t are assumed to be positive

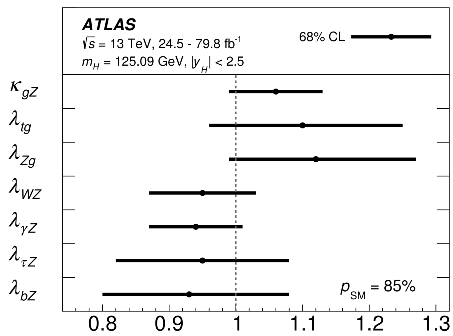

(d) Measured ratios of coupling modifiers. The dashed line indicates the SM value of unity for each parameter.

Figure 1.9: Results of Higgs boson Cross Sections and Couplings measurements [35].

Decay Width Measuremnt

Currently particle experiments do not have the needed resolution to measure the Higgs boson decay width directly. However recent studies [36, 37, 38, 39] have shown that the high-mass off-peak regions beyond $2m_V$ $(V = Z, W)$, well above the measured resonance mass of 125 GeV, in the $H \to ZZ$ and $H \to WW$ channels are sensitive to Higgs boson production through off-shell and interference effects with the continuum background. This presents a novel way of characterising the properties of the Higgs boson in terms of the off-shell event yields, normalised to the SM prediction (referred to as signal strength μ), and the associated off-shell Higgs boson couplings. Such studies provide sensitivity to new physics that alters the interactions between the Higgs boson and other fundamental particles in the high-mass region [40, 41, 42, 43]. This approach was used by the ATLAS and CMS collaborations [44, 45] to set an indirect limit on the total width with the data collected in pp collisions at the centre-of-mass energy $\sqrt{s} = 7$ and 8 TeV.

The representative diagrams for $pp \to ZZ$ production are shown in Figure 1.10, involving resonant Higgs boson production and non-resonant ZZ continuum originating from $q\bar{q}$ and gg initial states. In the dominant gluon fusion production mode for the Higgs boson at the LHC, the off-shell production cross section, away from the resonance peak, is known to be sizable, contributing O(15%) to the total cross section. This is due to two threshold effects, one near $2M_Z$ from the enhancement of the Higgs boson decay amplitude as the two Zs go on-shell and the other at $2m_t$ from the $gg \to H$ production [46]. The production cross-section for $gg \to H^* \to ZZ$ can be written as:

$$\frac{\mathrm{d}\sigma_{pp\to H\to ZZ}}{\mathrm{d}M_{ZZ}^2} \sim \frac{g_{Hgg}^2 g_{HZZ}^2}{(M_{ZZ}^2 - m_H^2)^2 + m_H^2\Gamma_H^2}, \tag{1.62}$$

where g_{Hgg}, g_{HZZ} are coupling constants for Higgs production and decay. For on-shell Higgs, we can write:

$$\frac{\mathrm{d}\sigma_{\text{on-shell}}^{pp\to H\to ZZ}}{\mathrm{d}M_{ZZ}^2} \sim \frac{g_{Hgg}^2 g_{HZZ}^2}{m_H^2\Gamma_H^2}, \tag{1.63}$$

while for off-shell Higgs,

$$\frac{\mathrm{d}\sigma_{\text{off-shell}}^{pp\to H\to ZZ}}{\mathrm{d}M_{ZZ}^2} \sim \frac{g_{Hgg}^2 g_{HZZ}^2}{(M_{ZZ}^2 - m_H^2)^2}, \tag{1.64}$$

The total cross-section $\sigma_{\text{off-shell}}^{gg\to H^*\to ZZ}$ for the off-shell Higgs boson production through gluon fusion with subsequent decay into vector-boson pairs,[2] as illustrated by the Feynman diagram in Figure 1.10(a), is proportional to the product of the Higgs boson couplings squared for production and decay. However, unlike the on-shell Higgs boson production, $\sigma_{\text{off-shell}}^{gg\to H^*\to ZZ}$ is independent of the total Higgs boson decay width Γ_H [36, 37]. The off-shell signal strength in the high-mass region at an energy scale $\hat{s}$, $\mu_{\text{off-shell}}(\hat{s})$, can be expressed as:

$$\mu_{\text{off-shell}}(\hat{s}) \equiv \frac{\sigma_{\text{off-shell}}^{gg\to H^*\to ZZ}(\hat{s})}{\sigma_{\text{off-shell, SM}}^{gg\to H^*\to ZZ}(\hat{s})} = \kappa_{g,\text{off-shell}}^2(\hat{s}) \cdot \kappa_{V,\text{off-shell}}^2(\hat{s}) \quad , \tag{1.65}$$

where $\kappa_{g,\text{off-shell}}(\hat{s})$ and $\kappa_{V,\text{off-shell}}(\hat{s})$ are the off-shell coupling scale factors associated with the $gg \to H^*$ production and the $H^* \to ZZ$ decay. Due to the statistically limited sensitivity, the off-shell signal strength and coupling scale factors are assumed in the following to be independent of $\hat{s}$ in the high-mass region. The off-shell Higgs boson signal cannot be treated independently from the $gg \to ZZ$ background (Figure 1.10(b)), as sizable negative interference effects appear [36] for the gg initiated

[2] In the following the notation $gg \to (H^* \to)ZZ$ is used for the full signal+background process for ZZ production, including the Higgs boson signal (S) $gg \to H^* \to ZZ$ process, the continuum background (B) $gg \to ZZ$ process and their interference. For vector-boson fusion (VBF) production, the analogous notation VBF $(H^* \to)ZZ$ is used for the full signal plus background process, with VBF $H^* \to ZZ$ representing the Higgs boson signal and VBF ZZ denoting the background.

processes as shown in Figure 1.10(a) and Figure 1.10(b). The interference term is proportional to $\sqrt{\mu_{\text{off-shell}}} = \kappa_{g,\text{off-shell}} \cdot \kappa_{V,\text{off-shell}}$.

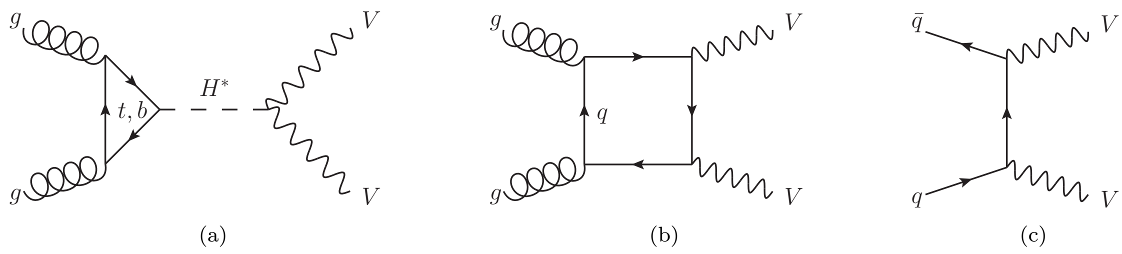

Figure 1.10: The leading-order Feynman diagrams for (a) the $gg \to H^* \to ZZ$ signal, (b) the continuum $gg \to ZZ$ background and (c) the $q\bar{q} \to ZZ$ background.

In contrast, the cross-section for on-shell Higgs production allows a measurement of the signal strength:

$$\mu_{\text{on-shell}} \equiv \frac{\sigma^{gg\to H\to ZZ}_{\text{on-shell}}}{\sigma^{gg\to H\to ZZ}_{\text{on-shell, SM}}} = \frac{\kappa^2_{g,\text{on-shell}} \cdot \kappa^2_{V,\text{on-shell}}}{\Gamma_H/\Gamma_H^{\text{SM}}}, \tag{1.66}$$

which depends on the total width Γ_H through the Higgs boson propagator. Assuming identical on-shell and off-shell Higgs couplings, the ratio of $\mu_{\text{off-shell}}$ to $\mu_{\text{on-shell}}$ provides a measurement of the total width of the Higgs boson. This assumption is particularly relevant to the running of the effective coupling $\kappa_g(\hat{s})$ for the loop-induced $gg \to H$ production process, as it is sensitive to new physics that enters at higher mass scales and could be probed in the high-mass m_{ZZ} signal region of this analysis. More details are given in Refs. [40, 41, 42, 43].

2 The ATLAS Experiment

The ATLAS (A Toroidal LHC ApparatuS) experiment is currently the biggest experiment in the world, employing over 3000 scientists. ATLAS is a particle detector installed on the Large Hadron Collider (LHC) in Conseil Européen pour la Recherche Nucléaire (CERN) near Geneva. The LHC is also the biggest particle accelerator capable of accelerating protons at 14 TeV center of mass energy. ATLAS design began in 1994 [47, 48] when a general purpose detector was proposed t o be installed on the upcoming LHC [49, 50]. Construction was completed in 2008 and the experiment detected the first high energy collisions in Spring 2010.

ATLAS is capable to investigate a wide range of physics, from the search for the Higgs boson to extra dimensions and particles that could make up dark matter. Beams of particles from the LHC collide at the centre of the ATLAS detector making collision debris in the form of new particles, which fly out from the collision point in all directions. The different detecting subsystems, arranged in layers around the collision point, record the paths, momentum, and energy of the particles, allowing them to be individually identified. The interactions in the ATLAS detectors create an enormous flow of data. To digest the data, ATLAS uses an advanced trigger system to choose which events to record and which to ignore. Complex data-acquisition and computing systems are then used to analyse the collision events recorded.

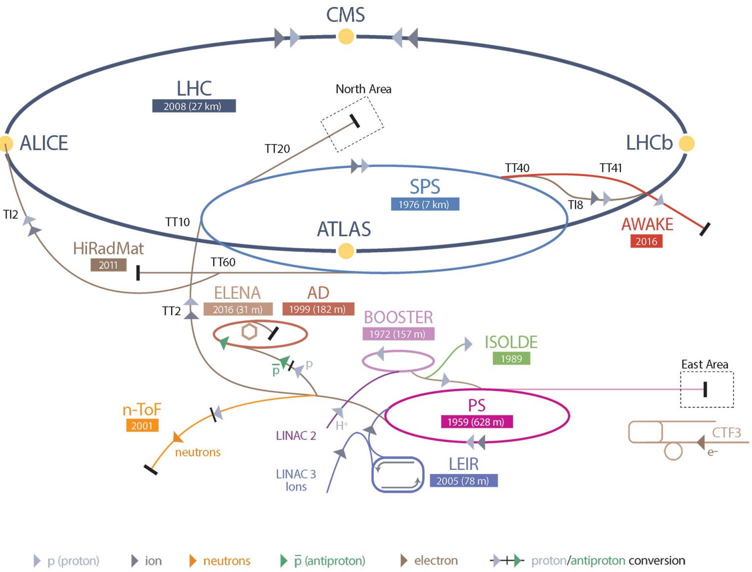

Figure 2.1: CERN's accelerator complex.

2.1 The Large Hadron Collider

In 1994 a new proton accelerator was proposed to replace the existing Large Electron Positron Collider (LEP) in CERN. The new accelerator, the LHC [51, 52, 53], was built between 1998 and 2008 in collaboration with over 10,000 scientists and engineers from over 100 countries, as well as hundreds of universities and laboratories. Now it is the biggest and most powerful particle accelerator in the world, capable to accelerate protons up to 14TeV center of mass energy.

The LHC has circular shape (Figure 2.1), about 27 km perimeter, lied in a tunnel about 100 m under the surface. The collider tunnel contains two adjacent parallel beam pipes, kept at ultra-high vacuum, in which the particles travel in opposite directions around the ring. A cross section of the pipes is shown in Figure 2.2. They intersect at four points where ATLAS and the other three major detectors are installed. The particles are being accelerated due radio frequency cavities alongside the pipes and 1232 dipole superconducting magnets producing magnetic field up to 7.7 T keeping the beams on their circular path. In additional 392 quadrupole magnets are used to keep the beams focused, in order to maximize the chances of interaction between the particles. Approximately 96 tonnes of superfluid helium-4 is needed to keep the magnets, made of copper-clad niobium-titanium, at their operating temperature of 1.9 K.

The beam is accelerated gradually as injected in multiple smaller accelerators, until it reaches to LHC. The first accelerator is the Radio Frequency Quadrupole (QRF) which speeds up the beam to 750 keV. From the quadrupole, the particles are sent to the linear accelerator LINAC2 which accelerates them to 50 MeV. The next is the circular accelerator Proton Synchrotron Booster (PSB) with energy 1.4 GeV. The Proton Sychrotron (PS) is following with energy 25 GeV. The Super Proton Synchrotron (SPS) is the last step before the LHC with an energy of 450 GeV.

The beams in the LHC are not continuous but separated in bunches.About 2808 bunches fit at the total LHC perimeter, with about $1.5 \cdot 10^{11}$ protons each, colliding every 25 ns. This corresponds to an instantaneous Luminosity $L = 10^{34}\mathrm{cm}^{-2}\mathrm{s}^{-1}$. The number of interaction per second is proportional to this luminosity and to the total cross section for proton-proton interaction, yielding about 600 million proton interactions per second.

Seven detectors have been constructed at the LHC's intersection points. Two of them, the ATLAS experiment and the Compact Muon Solenoid (CMS), are large, general purpose particle detectors. On the contrary ALICE and LHCb have more specific roles and the last three, TOTEM, MoEDAL and LHCf, are much smaller and for specialized research. The LHC physics program is mainly based on proton–proton collisions. However, shorter running periods, typically one month per year, with heavy-ion collisions are included in the program. The main goals of these programs are

- Search and study of Higgs boson
- Search for Supersymmetric particles
- Search for other beyond the SM particles, heavy gauge bosons, exotic particles etc
- Investigation of various models based on string theory, implying extra dimensions
- Search for the nature of dark matter
- Investigation of Grand Unification Theories
- Study of Gravity and Hierarchy problem
- Study of sources of quark flavour mixing
- Study of violations of the symmetry between matter and antimatter (CP violation)
- Study of the nature and properties of quark–gluon plasma

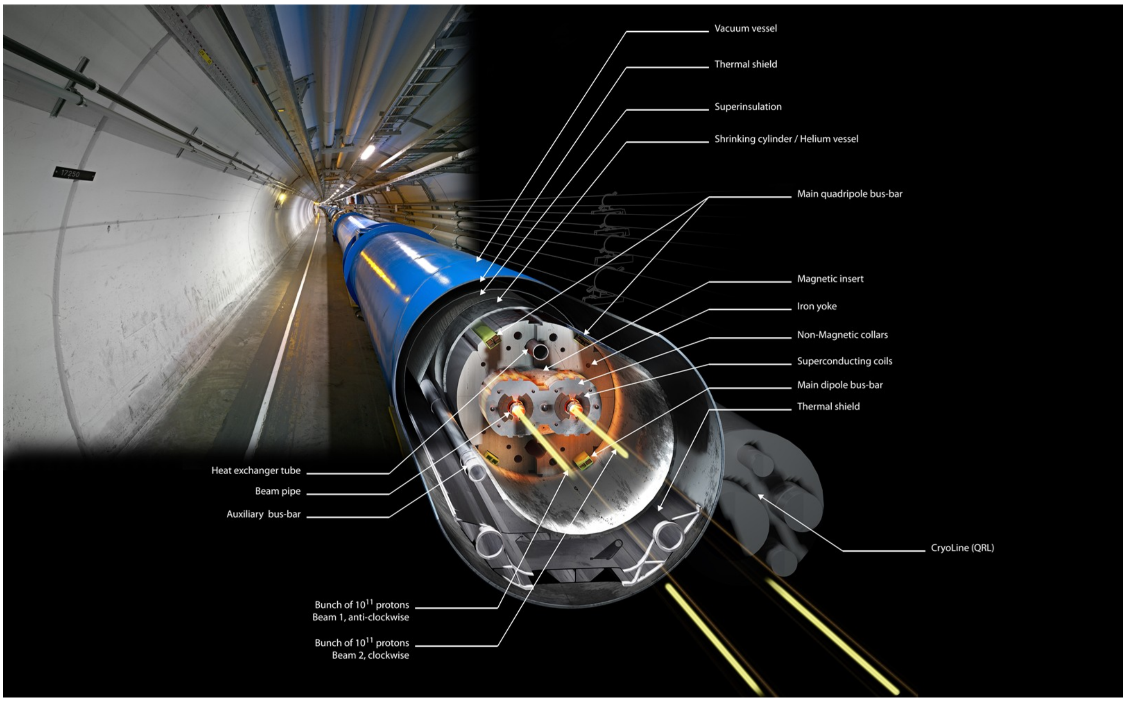

Figure 2.2: LHC cross section

2.2 The ATLAS Detector

ATLAS (Figure 2.3) is a cylindrical detector consisting of three different main detecting subsystems, wrapped concentrically in layers around the collision point. Its dimension are 46 m long, 25 m in diameter, and weights 7,000 tonnes. It is capable to record the trajectory, momentum, and energy of particles, allowing them to be individually identified and measured. A huge magnet system bends the paths of the charged particles so that their momenta can be measured as precisely as possible. The four major components of the ATLAS detector are the Inner Detector, the Calorimeter, the Muon Spectrometer and the Magnet System. Components also integrated with the detector are the Trigger and Data Acquisition System, a specialized multi-level computing system, which selects physics events with distinguishing characteristics, and the Computing System, which develops and improves computing software used to store, process and analyse vast amounts of collision data at 130 computing centres worldwide.

2.2.1 Goals and Physics Requirements

A broad spectrum of detailed physics studies led to the overall detector concept presented in the ATLAS Technical Proposal [54]. The basic design criteria of the detector include the following.

- Very good electromagnetic calorimetry for electron and photon identification and measurements, complemented by full-coverage hadronic calorimetry for accurate jet and missing transverse energy (ET miss) measurements
- High-precision muon momentum measurements, with the capability to guarantee accurate measurements at the highest luminosity using the external muon spectrometer alone
- Efficient tracking at high luminosity for high-p_T lepton-momentum measurements, electron and photon identification, tau lepton and heavy-flavour identification, and full event reconstruction capability at lower luminosity

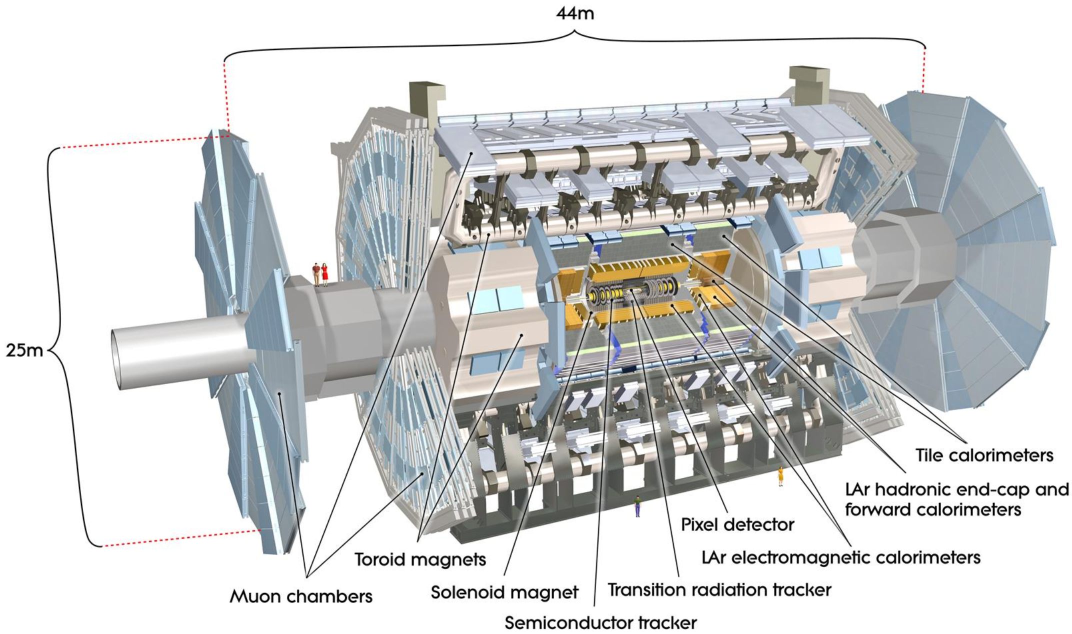

Figure 2.3: ATLAS Detector

- Large acceptance in pseudorapidity with almost full azimuthal angle coverage everywhere.
- Triggering and measurements of particles at low-p_T thresholds, providing high efficiencies for most physics processes of interest at LHC.

The main performance goals of ATLAS detector [55, 56] are listed in table 2.1. The Layout of the ATLAS detector as well as the traces of the particles go through it are shown in Figure 2.4. A visualization of a typical event recorded by ATLAS is shown in Figure 2.5.

Detector component	**Required resolution**	**η coverage**	
		Measurement	Trigger
Tracking	$\sigma_{p_T}/p_T = 0.05\% p_T \oplus 1\%$	± 2.5	
EM calorimetry	$\sigma_E/E = 10\%/\sqrt{E} \oplus 0.7\%$	± 3.2	$\pm$ 2.5
Hadronic calorimetry (jets)			
barrel and end-cap	$\sigma_E/E = 50\%/\sqrt{E} \oplus 3\%$	± 3.2	± 3.2
forward	$\sigma_E/E = 100\%/\sqrt{E} \oplus 10\%$	$3.1 - 4.9$	$3.1 - 4.9$
Muon spectrometer	$\sigma_{p_T}/p_T = 10\% \quad at \quad p_T = 1TeV$	± 2.7	± 2.4

Table 2.1: General performance goals of the ATLAS detector.

2.2.2 The Coordinate System

The centre of ATLAS coordinate system is defined at the interaction point at the centre of the detector. X-axis is defined towards LHC centre, Y upwards and Z tangentially to the beams. So the X-Y plane is transverse to the beams. Angle coordinates also used (ϕ, η) where ϕ is the azimuthal angle around

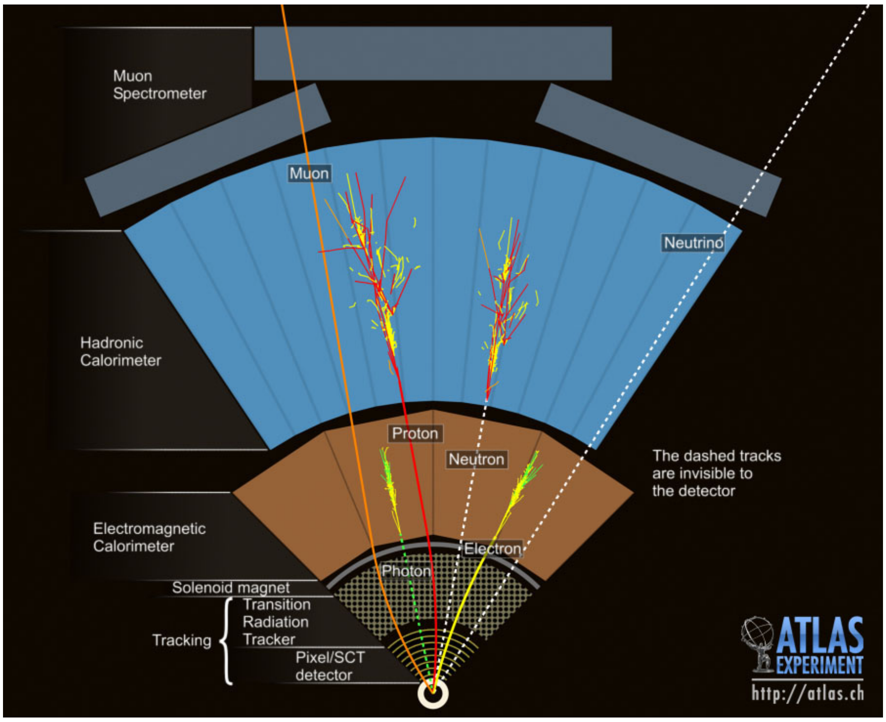

Figure 2.4: Particle signatures through ATLAS detector.

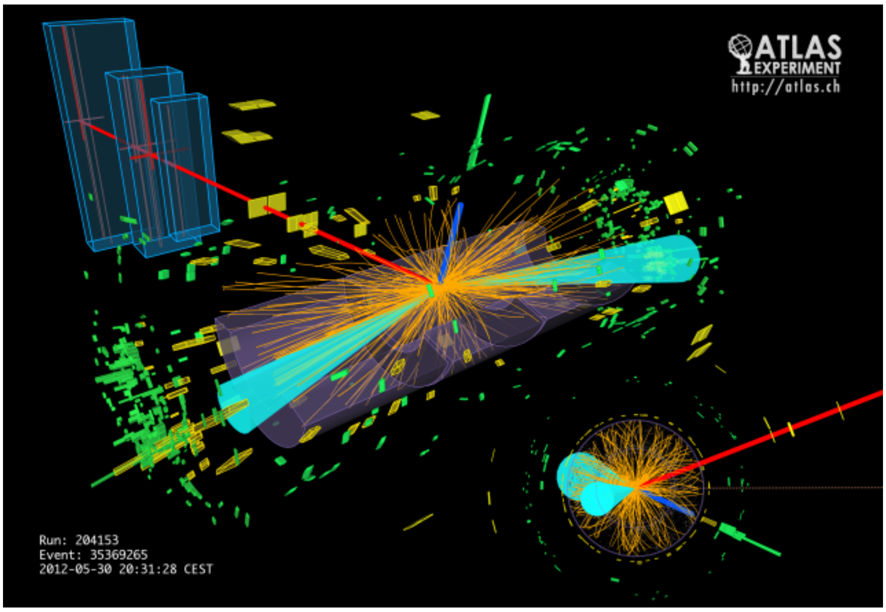

Figure 2.5: Graphical representation of one of a collision event, showing traces and energy deposits left by the particles flying through the ATLAS detector.

the Z axis and η is the pseudorapidity which is defined as:

$$\eta = ln(tan\frac{\theta}{2}) \tag{2.1}$$

where θ is the angle with the Z axis. The angles of tracks originating from the interaction point are then described as coordinate pairs (ϕ, η) and the angular separation for higly relativistic particles, expressed as $(\Delta\phi, \Delta\eta)$ is a Lorentz invariant under boosts along the beam axis. The (dimensionless) distance ΔR in the (ϕ, η) plane is defined as:

$$\Delta R = \sqrt{(\Delta\eta)^2 + (\Delta\phi)^2} \tag{2.2}$$

2.2.3 The Inner Detector

The ATLAS Inner Detector (ID) [57, 58] (Figure 2.6) is designed to provide hermetic and robust pattern recognition, excellent momentum resolution and both primary and secondary vertex measurements for charged tracks above a given p_T threshold and within the pseudorapidity range $|\eta| < 2.5$. It also provides information for electron pion separation over $|\eta| < 2.0$ and a wide range of energies requirements. The ID is contained within a solenoidal magnetic field of 2 T. It consists of three independent but complementary sub-detectors, the pixel detector, the semiconductor tracker and the transition radiation tracker.

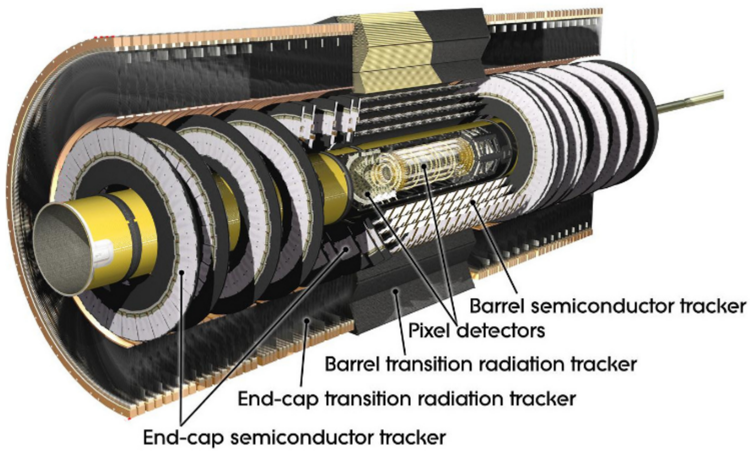

Figure 2.6: The Inner Detector.

The Pixel Detector

The Pixel Detector [59] is designed to provide a very high-granularity, high-precision set of measurements as close to the interaction point as possible. The system provides three of the precision measurements over the full acceptance, and determines the impact parameter resolution and the ability of the Inner Detector to find short-lived particles such as b-quarks and tau leptons.

The system consists of three barrels at average radii of about 4 cm, 11 cm, and 14 cm, and four disks on each side, between radii of 11 and 20 cm, which complete the angular coverage. It is designed to be highly modular, containing approximately 1500 identical barrel modules and 1000 identical disk modules, and uses only one type of support structure in the barrel and one type in the disks. The pixel modules are very similar in design for the disks and barrels. Each barrel module is 62.4 mm long and 22.4 mm wide, with 61440 pixel elements, read out by 16 chips each serving an array of 24 by 160 pixels. The output signals are routed on the sensor surface to a hybrid on top of the chips, and from there to a separate clock and control integrated circuit. The modules are overlapped on the support structure in order to give hermetic coverage.

The Semiconductor Tracker

The Semiconductor Tracker (SCT) system is designed to provide four precision measurements per track in the intermediate radial range, contributing to the measurement of momentum, impact parameter and vertex position, as well as providing good pattern recognition by the use of high granularity. The barrel SCT uses four layers of silicon microstrip detectors to provide precision points in the R, ϕ, and z coordinates, using small angle stereo to obtain the z measurement.

Each silicon detector is$6.36 \times 6.40 cm^2$ with 768 readout strips each with 80 μm pitch. Each module consists of four detectors. On each side of the module, two detectors are wire-bonded together to form 12.8 cm long strips. Two such detector pairs are then glued together back-to-back at a 40 $mrad$ angle, separated by a heat transport plate, and the electronics is mounted above the detectors on a hybrid. The readout chain consists of a front-end amplifier and discriminator, followed by a binary pipeline which stores the hits above threshold until the first level trigger decision.

The Transition Radiation Tracker

The Transition Radiation Tracker (TRT) is based on the use of straw detectors, which can operate at the very high rates needed by virtue of their small diameter and the isolation of the sense wires within individual gas envelopes. The TRT contributes to the accuracy of the momentum measurement in the Inner Detector by providing a set of typically 36 measurements roughly equivalent to a single point of 50 μm precision. It aids the pattern recognition by the addition of around 36 hits per track, and allows a simple and fast level-2 track trigger to be implemented. It allows the Inner Detector to reconstruct vertices which are especially interesting in CP-violating β decays. In addition it provides additional discrimination between electrons and hadrons, with a pion rejection varying with η between a factor of 15 and 200 at 90% electron efficiency. Each straw is 4 mm in diameter, giving a fast response and good mechanical properties for a maximum straw length of 150 cm. The barrel contains about 50000 straws, each divided in two at the centre in order to reduce the occupancy and read out at each end. The end-caps contain 320000 radial straws, with the readout at the outer radius. The total number of electronic channels is 420000. Each channel provides a drift-time measurement, giving a spatial resolution of 170 μm per straw, and two independent thresholds. These allow the detector to discriminate between tracking hits, which pass the lower threshold, and transition-radiation hits, which pass the higher.

Insertable B-Layer

The ATLAS Insertable B-Layer (IBL) [60] was installed in May 2014 at a radius of 3.3 cm from the beam axis, between the existing Pixel detector and a new smaller radius beam-pipe. It is the additional innermost pixel layer that has been built around the new beryllium beam pipe and then inserted inside the Pixel detector in the core of the ATLAS detector. It consists of 14 carbon fibre staves each 2 cm wide and 64 cm long, and tilted by 14^o in ϕ surrounding the beam-pipe at a mean radius of 33 mm and covering a pseudo-rapidity of $\pm$ 3. Each stave has an integrated CO_2 cooling pipe, and is equipped with 32 FE-I4 front-end chip bump bonded to silicon sensors. The FE-I4 chip is fabricated with 130 nm CMOS technology and consists of 26880 pixel cells organized in a matrix of 80 columns (50 μm pitch) by 336 rows (250 μm pitch).

2.2.4 The Calorimeters

The main tasks of calorimetry at hadron colliders is an accurate measurement of the energy and position of electrons and photons, a measurement of the energy and direction of jets and of the missing transverse momentum. ATLAS calorimetry [61] (Figure 2.7) consists of electromagnetic and hadronic calorimeters covering rapidity region up to $|\eta| < 4.9$. The electromagnetic (EM) calorimetry is only based on liquid argon technology, while hadronic calorimetry also uses scintillating tiles technology The calorimeters closest to the beam-line are housed in three cryostats, one barrel and two end-caps.

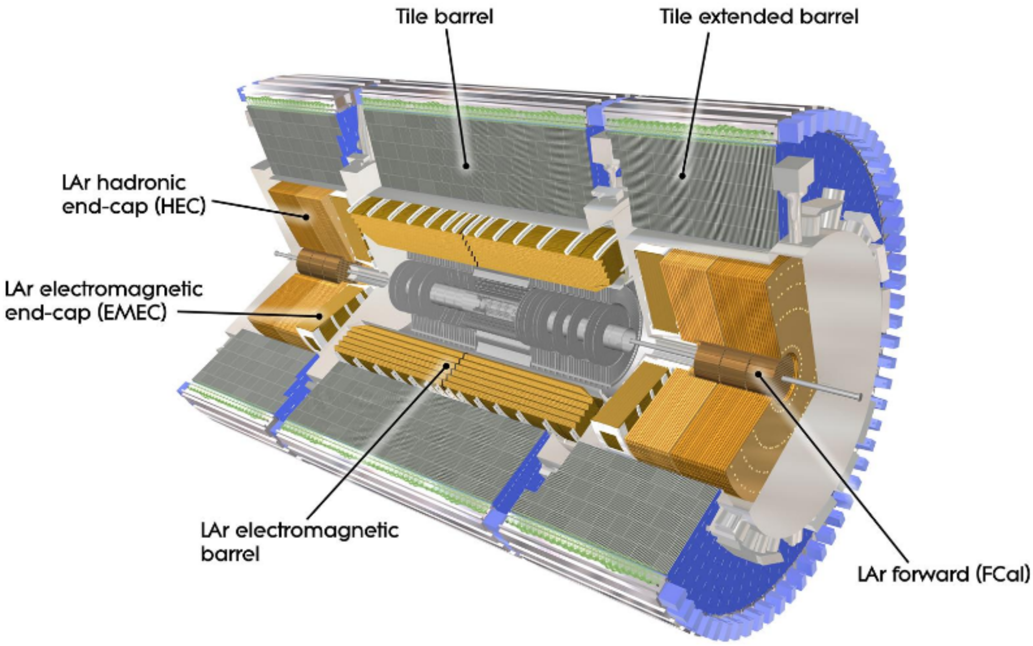

Figure 2.7: ATLAS calorimeters.

The Electromagnetic Calorimeter

The Electromagnetic (EM) calorimeter is lead-liquid argon (LAr) detectors [62] with accordion shape absorbers and electrodes. This geometry allows the calorimeters to have several active layers in depth, three in the precision-measurement region ($0 < |\eta| < 2.5$) and two in the higherη region ($2.5 < |\eta| < 3.2$) and in the overlap region between the barrel and the EMEC. The total thickness of the EM calorimeter is > 22 radiation lengths (X_0) in the barrel and > 24 X_0 in the end-caps In the precision measurement region, an accurate position measurement is obtained by finely segmenting the first layer in η. The η direction of photons is determined by the position of the photon cluster in the first and the second layers. The calorimeter system also has electromagnetic coverage at higher $\eta(3.1 < \eta < 4.9)$ provided by the Forward Calorimeter. Furthermore in the region ($0 < \eta < 1.8$) the electromagnetic calorimeters are complemented by presamplers, an instrumented argon layer, which provides a measurement of the energy lost in front of the electromagnetic calorimeters.

The Hadronic Calorimeter

The Hadronic barrel Calorimeter is a tile calorimeter (TileCal) [63] placed directly outside the EM calorimeter envelope. It is a sampling calorimeter using steel as absorber and scintillating tiles as active material. Its barrel covers the region $|\eta| < 1.0$, and its two extended barrels the range $0.8 < |\eta| < 1.7$. The barrel and extended barrels are divided azimuthally into 64 modules. It is segmented in depth in three layers, approximately 1.5, 4.1 and 1.8 interaction lengths (λ) thick for the barrel and 1.5, 2.6, and 3.3 λ for the extended barrel. The total detector thickness at the outer edge of the tile-instrumented region is 9.7 λ at $\eta = 0$. Two sides of the scintillating tiles are read out by wavelength shifting fibres into two separate photomultiplier tubes.

The Hadronic End-cap Calorimeter (LArHEC) is a liquid argon calorimeter consisting of two independent wheels per end-cap, located directly behind the end-cap electromagnetic calorimeter and sharing the same LAr cryostats. To reduce the drop in material density at the transition between the end-cap and the forward calorimeter (around $|\eta| = 3.1$), the HEC extends out to $|\eta| = 3.2$, thereby overlapping with the forward calorimeter. Similarly, the HEC η range also slightly overlaps that of the tile calorimeter ($|\eta| = 1.7$) by extending to $|\eta| = 1.5$. Each wheel is built from 32 identical wedge-shaped modules, assembled with fixtures at the periphery and at the central bore. Each wheel is divided into two segments in depth, for a total of four layers per end-cap. The wheels closest to the interaction point are built from 25 mm parallel copper plates, while those further away use 50 mm copper plates (for all wheels the first plate is half-thickness). The End-Cap Hadronic Calorimeter is supplemented with two more modules of the forward calorimeter, made of tungsten.

2.2.5 The Muon Spectrometer

The Muon Spectrometer (MS) [64] (Figure 2.8) forms the outer part of the ATLAS detector. It is designed to detect charged particles exiting the calorimeters by measuring their momentum in the pseudorapidity range $|\eta| < 2.7$ and provide trigger on these particles in the region $|\eta| < 2.4$. The MS also associates the particles with the bunch that they come from and lastly it matches them with their tracks from the ID. It consists from four different technologies, Monitored Drift Tubes, Cathode Strip Chambers, Resistive Plate Chambers and Thin Gap Chambers.

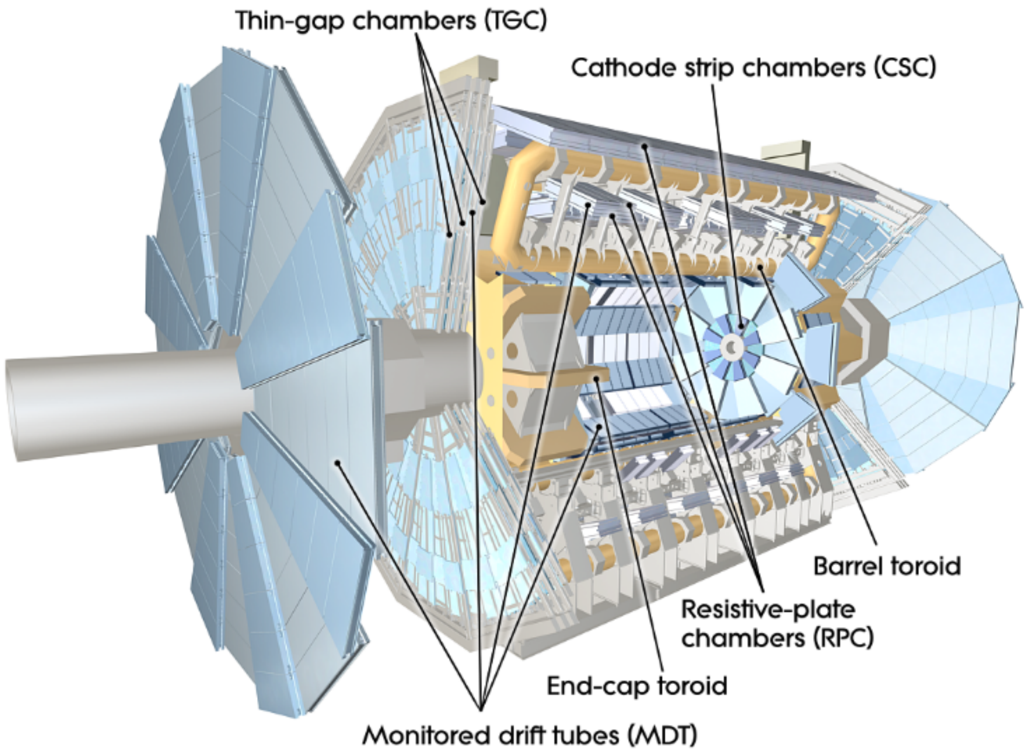

Figure 2.8: ATLAS Muon Spectrometer.

The Monitored Drift Tubes

The Monitored Drift Tubes (MDT) are gas detectors, their basic element is a pressurised drift tube with a diameter of 29.970 mm, operating with Ar/CO_2 gas (93/7) at 3 bar. The chambers are rectangular in the barrel and trapezoidal in the end-cap. Their shapes and dimensions were chosen to optimise solid angle coverage, while respecting the envelopes of the magnet coils, support structures and access ducts. The direction of the tubes in the barrel and end-caps is along ϕ, i.e. the center points of the tubes are tangential to circles around the beam axis. While all tubes of a barrel chamber are of identical length (with the exception of some chambers with cut-outs), the tube lengths in the end-cap chambers vary along R in steps of 24 tubes. All regular MDT chambers consist of two groups of tube layers, called multi-layers, separated by a mechanical spacer. In the innermost layer of the muon detector, each multi-layer consists of four tube layers to enhance the pattern-recognition performance; in the middle and outer layer of the muon detector, each multi-layer consists of three tube layers only. In ATLAS there are totally 380,000 MDTs grouped in 1194 chambers.

The Cathode Strip Chambers

The limit for safe operation of the MDT's is at counting rates of about 150 Hz/cm^2, which will be exceeded in the region $|\eta| > 2$ in the first layer of the end-cap. In this η region of the first layer, the MDT's are replaced by Cathode Strip Chambers (CSC), which combine high spatial, time and double track resolution with high-rate capability and low neutron sensitivity. Operation is considered safe up to counting rates of about 1000 Hz/cm^2, which is sufficient up to the forward boundary of the muon system at $|\eta| = 2.7$. The CSC's are multiwire proportional chambers with the wires oriented in the radial direction.They are segmented into large and small chambers in ϕ. The whole CSC system consists of two disks with eight chambers each (eight small and eight large). Each chamber contains four CSC planes resulting in four independent measurements in η and ϕ along each track.

The Resistive Plate Chambers

The Resistive Plate Chambers (RPC) is a gaseous parallel electrode-plate detector. Two resistive plates, made of phenolic-melaminic plastic laminate, are kept parallel to each other at a distance of 2 mm by insulating spacers. The signal is read out via capacitive coupling to metallic strips, which are mounted on the outer faces of the resistive plates. They are used mainly for triggering. The large lever arm between inner and outer RPC's permits the trigger to select high momentum tracks in the range 9–35 GeV (high p_T trigger), while the two inner chambers provide the low-p_T trigger in the range 6–9 GeV. Each station consists of two independent detector layers, each measuring η and ϕ. A track going through all three stations thus delivers six measurements in η and ϕ. A RPC trigger chamber is made of two rectangular detectors, contiguous to each other, called units. Each unit consists of two independent detector layers, called gas volumes, which are each read out by two orthogonal sets of pick-up strips.

The Thin Gap Chambers

The Thin Gap Chambers (TGC) are multi-wire proportional chambers with the characteristic that the wire-to cathode distance of 1.4 mm is smaller than the wire-to-wire distance of 1.8 mm. Thin Gap Chambers (TGC's) provide two functions in the end-cap muon spectrometer: the muon trigger capability and the determination of the second, azimuthal coordinate to complement the measurement of the MDT's in the bending (radial) direction. The middle layer of the MDT's in the end-cap (EM-wheel) is complemented by seven layers of TGC's, while the inner (I) layer is complemented by only two layers. The inner layer is segmented radially into two non-overlapping regions: end-cap (EI) and forward (FI, also known as the small wheel). EI TGC's are mounted on support structures of the barrel toroid coils. The seven detector layers in the middle layers are arranged in one triplet and two doublets. The triplet is to cope with false coincidences from background hits, which are more likely in the end-cap region than in the barrel.

2.2.6 The Magnet System

ATLAS features a unique hybrid system of four large superconducting magnets (Figure 2.9). This magnetic system is 22 m in diameter and 26 m in length, with a stored energy of 1.6 GJ. The ATLAS magnet system [65] consists of a central solenoid, which is aligned on the beam axis and provides a 2

T axial magnetic field for the inner detector, while minimising the radiative thickness in front of the barrel electromagnetic calorimeter, and a barrel and two end-cap toroids which produce a toroidal magnetic field of approximately 0.5 T and 1 T for the muon detectors in the central and end-cap regions, respectively.

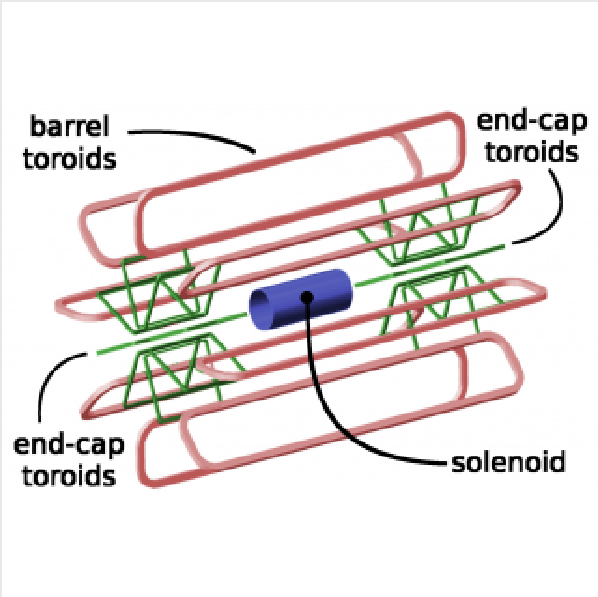

Figure 2.9: ATLAS magnet system.

The central solenoid

The central solenoid [66] is designed to provide a 2 T axial field. To achieve the desired calorimeter performance, the layout was carefully optimised to keep the material thickness in front of the calorimeter as low as possible, resulting in the solenoid assembly contributing a total of ∼0.66 radiation lengths at normal incidence. The single-layer coil is wound with a high-strength Al-stabilised NbTi conductor, specially developed to achieve a high field while optimising thickness. The coil mass is 5.4 tonnes and the stored energy is 40 MJ. The stored-energy-to-mass ratio of only 7.4 kJ/kg at nominal field clearly demonstrates successful compliance with the design requirement of an extremely light-weight structure.

The Toroids

The cylindrical volume surrounding the calorimeters and both end-cap toroids [67] is filled by the magnetic field of the barrel toroid, which consists of eight coils encased in individual racetrack-shaped, stainless-steel vacuum vessels. The coil assembly is supported by eight inner and eight outer rings of struts. The conductor and coil-winding technology is essentially the same in the barrel and end-cap toroids; it is based on winding a pure Al-stabilised Nb/Ti/Cu conductor into pancake-shaped coils, followed by vacuum impregnation. These toroids generate the magnetic field required for optimising the bending power in the end-cap regions of the muon spectrometer system. They are supported off and can slide along the central rails, which facilitates the opening of the detector for access and maintenance. Each end-cap toroid consists of a single cold mass built up from eight flat, square coil units and eight keystone wedges, bolted and glued together into a rigid structure to withstand the Lorentz forces.

2.2.7 The Trigger and Data Acquisition System

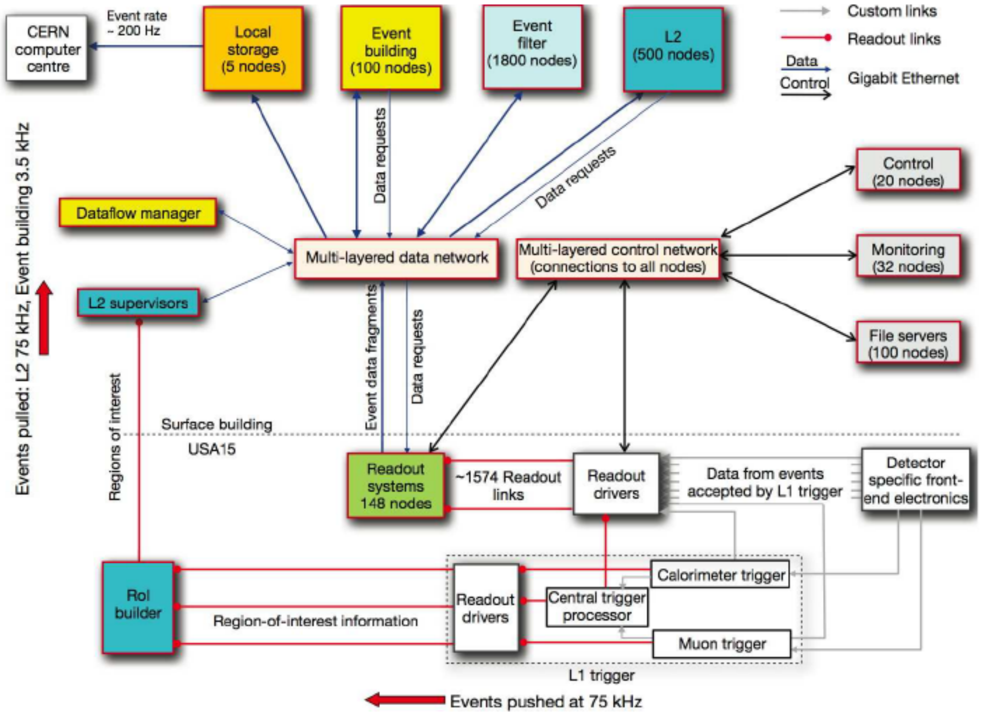

Figure 2.10: Block scheme of the Trigger and DAQ system [68].

The trigger

The trigger consists of three levels of event selection: Level-1 (L1), Level-2 (L2), and event filter. The L2 and event filter together form the High-Level Trigger (HLT). The L1 trigger is implemented using custom-made electronics, while the HLT is almost entirely based on commercially available computers and networking hardware. The L1 trigger searches for signatures from high-pT muons, electrons/photons, jets, and t-leptons decaying into hadrons. It also selects events with large missing transverse energy (Emiss T) and large total transverse energy.

The L1 trigger [69] uses reduced-granularity information from a subset of detectors: the Resistive Plate Chambers (RPC) and Thin-Gap Chambers (TGC) for high-p_T muons, and all the calorimeter sub-systems for electromagnetic clusters, jets, t-leptons, E_{Tmiss}, and large total transverse energy. The maximum L1 accept rate which the detector readout systems can handle is 75 kHz (upgradeable to 100 kHz), and the L1 decision must reach the front-end electronics within 2.5 ms after the bunch-crossing with which it is associated.

The L2 trigger is seeded by Regions-of-Interest (RoI's). These are regions of the detector where the L1 trigger has identified possible trigger objects within the event. The L2 trigger uses RoI information on coordinates, energy, and type of signatures to limit the amount of data which must be transferred from the detector readout. The L2 trigger reduces the event rate to below 3.5 kHz, with an average event processing time of approximately 40 ms.

The event filter uses offline analysis procedures on fully-built events to further select events down to a rate which can be recorded for subsequent offline analysis. It reduces the event rate to approximately 200 Hz, with an average event processing time of order of four seconds.

The HLT [70] algorithms use the full granularity and precision of calorimeter and muon chamber data, as well as the data from the inner detector, to refine the trigger selections. Better information on energy deposition improves the threshold cuts, while track reconstruction in the inner detector significantly enhances the particle identification (for example distinguishing between electrons and photons). The event selection at both L1 and L2 primarily uses inclusive criteria, for example high-ET objects above defined thresholds. One exception is the L2 selection of events containing the decay of a b-hadron, which requires the reconstruction of exclusive decays into particles with low momentum.

The data acquisition system

The data acquisition system (DAQ) (Figure 2.10) receives and buffers the event data from the detector specific readout electronics at the L1 trigger rate. The data transmission is performed over point-to-point Readout Links (ROL's). It transmits to the L2 trigger any data requested by the trigger (typically the data corresponding to RoI's) and, for those events fulfilling the L2 selection criteria, event-building is performed. The assembled events are then moved by the data acquisition system to the event filter, and the selected events are moved to permanent event storage.

In addition to controlling movement of data down the trigger selection chain, the data acquisition system also provides for the configuration, control and monitoring of the ATLAS detector during data-taking. Supervision of the detector hardware (gas systems, power-supply voltages, etc.) is provided by the Detector Control System (DCS).

2.2.8 The Computing System

The Software and Computing Project [71] is responsible for the provision of the software framework and services, the data management system, user-support services, and the worldwide data access and job-submission system. The development of detector-specific algorithmic code for simulation, calibration, alignment, trigger and reconstruction is under the responsibility of the detector projects, but the Software and Computing Project plans and coordinates these activities across detector boundaries. In particular, a significant effort has been made to ensure that relevant parts of the "offline" framework and event-reconstruction code can be used in the High Level Trigger. Similarly, close cooperation with Physics Coordination and the Combined Performance groups ensures the smooth development of global event-reconstruction code and of software tools for physics analysis.

The primary event processing occurs at CERN in a Tier-0 Facility. The RAW data (output from the online software) is archived at CERN and copied (along with the primary processed data) to the Tier-1 facilities. These facilities archive the raw data, provide the reprocessing capacity, provide access to the various processed versions, and allow scheduled analysis of the processed data by physics analysis groups. Derived datasets produced by the physics groups are copied to the Tier-2 facilities for further analysis. The Tier-2 facilities also provide the simulation capacity for the experiment, with the simulated data housed at Tier-1s. In addition, Tier-2 centres will provide analysis facilities, and some will provide the capacity to produce calibrations based on processing raw data. Additional computing resources will be available for data processing and analysis at Tier-3.

A complex set of tools and distributed services, enabling the automatic distribution and processing of the large amounts of data, has been developed and deployed by ATLAS in cooperation with the LHC Computing Grid (LCG) Project.

Athena

Athena is ATLAS software framework that manages almost all production workflows and it is a concrete implementation of an underlying architecture called Gaudi which was originally developed by LHCb. All levels of processing of ATLAS data, from high-level trigger to event simulation, reconstruction and analysis, take place within the Athena framework. Major design principles are the clear separation of data and algorithms, and between transient (in-memory) and persistent (in-file) data. This way it is easier for code developers and users to test and run algorithmic code, with the assurance that all geometry and conditions data will be the same for all types of applications (simulation, reconstruction, analysis, visualization).

2.3 ATLAS upgrades

The scientific programme of the LHC spans over the next 20 years and includes an ambitious series of upgrades that will ultimately result in an accumulated integrated luminosity for proton-proton collisions of 3000 fb^{-1}. This represents an order of magnitude more data than what would be collected prior to the HL-LHC run. The improvements necessary to achieve this accelerator performance will be mostly realised during two long shutdowns [72], each of two to three years duration:

- in 2015, Long Shutdown 1 (LS1) was completed to prepare the accelerator for operation at 13 TeV and its design luminosity
- in 2019/2020 Long Shutdown 2 (LS2) further improvements of the LHC are foreseen, accompanied by significant detector upgrades (Phase-I)
- long Shutdown 3 (LS3) starting at the end of 2023 will include major performance upgrades of the accelerator for the high-luminosity phase (HL-LHC) which requires replacement of several major detector components (Phase-II)

During LS1 ATLAS Phase-0 upgrade was the installation of a new, 4th barrel layer in the Pixel detector (Insertable B-Layer). The second shutdown (LS2) is currently ongoing. The LCH is being upgraded by integrating the Linac4 into the injector complex, to increase the energy of the PS Booster to reduce the beam emittance, and upgrade the collider collimation system. When data taking resumes in 2021, the peak luminosity is expected to reach $2-3{\cdot}10^{34}$cm^{2}s^{-1} corresponding to 55 - 80 interactions per crossing (pile-up) with 25 ns bunch spacing, well beyond the initial design goals. ATLAS Phase-I upgrades will enable the experiment to exploit the physics opportunities afforded by the upgrades to the accelerator complex. At the end of Run III it will have collected an integrated luminosity of 300-400 fb^{-1}, extending the reach for discovery of new physics and the ability to study new phenomena and states. Furthermore, these upgrades are designed to be fully compatible with the physics program of the high luminosity HL LHC, where the instantaneous luminosity should reach $5-7\cdot10^{34}$cm^{2}s^{-1}. With a nominal (ultimate) luminosity of and an average = 140 (200) inelastic proton-proton collisions per beam-crossing (pileup), the HL-LHC will present an extremely challenging environment to the ATLAS experiment, well beyond that for which it was designed.

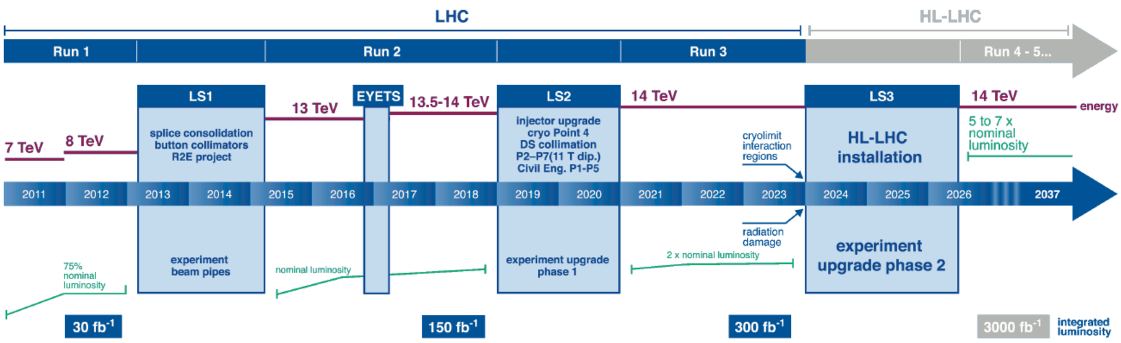

Figure 2.11: LHC long term schedule

2.3.1 Phase I

The main focus of the Phase-I ATLAS upgrade is on the Level-1 trigger. ATLAS capability to maintain an optimal trigger system as the luminosity increases beyond its nominal design value requires a strong reduction of the main source of backgrounds: jets mimicking electrons in the calorimeters and fake muons in the forward spectrometer. Otherwise, increased threshold cuts would have to be deployed to control rates that would reduce significantly the signal efficiency. The success of the overall ATLAS physics program during Phase-I data taking is therefore depended on the implementation of several upgrades [73]. In the case of the muon spectrometer a new tracking and trigger device in the inner layer of the forward spectrometer will be introduced. It will not only provide a sharper trigger threshold, but also greatly improve the tracking performance under the higher backgrounds expected with the LHC upgrades. Similarly, for the case of electrons, new trigger read-out boards will be implemented in the electromagnetic and forward calorimeters to exploit the longitudinal sampling of the calorimeter as well as including a higher trigger granularity comparable to that presently available in the full calorimeter read-out, which will lead to an improvement in rejecting fake electron triggers. A new topological processor will add significant flexibility to the Level-1 trigger system. Fast accurate tracking at Level-2 trigger will permit the isolation of t and b events and therefore improve the quality of the selected events without any substantial increase in rates. Finally, a new set of forward detectors will permit ATLAS to retain its capabilities for forward physics at the highest possible LHC luminosities. These upgrades are designed to be fully compatible with the physics program of the high luminosity HL-LHC.

The New Small Wheels

The New Small Wheels (NSW) [74] is the most extended upgrade project during LS1. The Phase-I upgrade of the ATLAS muon spectrometer focuses on the end-cap region where the inner wheels will be replaced. The end-cap system covers the $1.0 < |\eta| < 2.7$ for muon tracking and $1.0 < |\eta| < 2.4$ for Level-1 trigger. Currently, it consists of three stations each, measuring the muon momentum based on the curvature in the ATLAS toroid magnets. At high luminosity the following two points are of particular importance.

The performance of the muon tracking chambers (in particular in the end-cap region) degrades with the expected increase of cavern background rate. The degradation will be substantial for tracking performance, both in terms of efficiency and resolution in the inner end-cap station. Given that the high resolution muon momentum measurement crucially depends on the presence of measured points at the Small Wheel level, this degradation is detrimental for the performance of the ATLAS detector.

The Level-1 muon trigger in the end-cap region is based on track segments in the TGC chambers of the middle muon station (End-cap Muon detector, EM) located after the end-cap toroid magnet1. The transverse momentum, of the muon is determined by the angle of the segment with respect to the direction pointing to the interaction point. A significant part of the muon trigger rate in the end-caps is background. Low energy particles, mainly protons, generated in the material located between the Small Wheel and the EM station, produce fake triggers by hitting the end-cap trigger chambers at an angle similar to that of real high p_T muons. An analysis of 2012 data demonstrates that approximately 90% of the muon triggers in the end-caps are fake. As a consequence the rate of the Level-1 muon trigger in the end-cap is eight to nine times higher than that in the barrel region.

Both of these two issues represent a serious limitation on the ATLAS performance beyond design luminosity, reduced acceptance of good muon tracking and an unacceptable rate of fake high p_T Level-1 muon triggers coming from the forward direction. In order to solve the two problems together, ATLAS proposes to replace the present muon Small Wheels with the New Small Wheels. The NSW is a set of precision tracking and trigger detectors able to work at high rates with excellent real-time spatial and time resolution. These detectors can provide the muon Level-1 trigger system with online track segments of good angular resolution to confirm that muon tracks originate from the IP. In this way the end-cap fake triggers will be considerably reduced. With the proposed NSW the ATLAS muon system will maintain the full acceptance of its excellent muon tracking at the highest LHC luminosities expected. At the same time the Level-1 low p_T (typically $p_T > 20$ GeV) single muon trigger rate will be kept at an acceptable level.

The NSW consists of 16 detector planes in two multilayers (Figure 2.12). Each multilayer comprises four small-strip TGC (sTGC) and four Micromegas (MM) detector planes. The sTGC are primarily deployed for triggering given their single bunch crossing identification capability. The detectors are arranged in such a way (sTGC – MM – MM – sTGC) as to maximize the distance between the

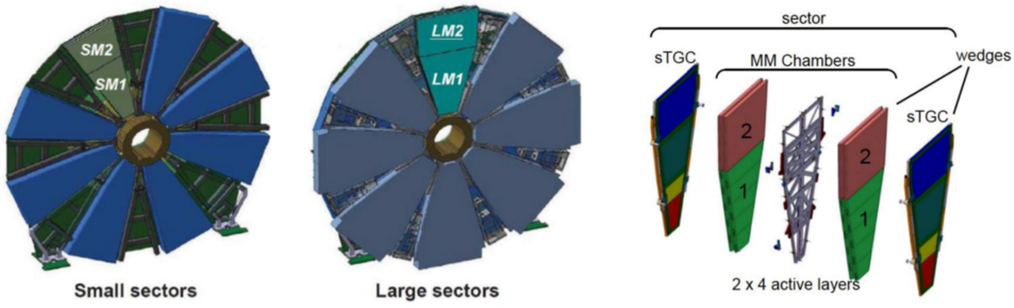

Figure 2.12: Components and layout of the New Small Wheel

sTGCs of the two multilayers. As online track hits are reconstructed with limited accuracy, increased distance between detector multilayers leads to an improved online track segment angle reconstruction resolution. Hence this detector configuration is optimal for the online track resolution. The MM detectors have exceptional precision tracking capabilities due to their small gap (5 mm) and strip pitch (0.45 mm), that exceed the needed requirements.

2.3.2 Phase II

In most cases, the design and techniques used for the Phase-II upgrades [75, 76] represent an evolution from the new designs and technologies already introduced during the LS1 improvement program, which included the installation of the IBL pixel detector, and the Phase-I upgrades now being prepared for installation during LS2. Full performance and physics capability, at $\mu = 200$, has been considered as the design goal for the Phase-II ATLAS upgrade.

At the end of the current LHC programme the silicon tracking systems will be approaching the end of their lifetimes. Moreover, the higher luminosity will increase significantly the occupancies in both the silicon detectors, and the occupancy in the straw tube transition radiation tracker severely compromising the tracking performance. Therefore the need for good performance in vertex and track reconstruction, lepton identification and heavy flavour tagging, even in the high occupancy and radiation fluence environment of the HL-LHC, require a complete replacement of the current tracking system. Based on the experience gained with the current tracker, a new all-silicon tracker design is being developed.

The very high luminosities also present significant challenges to the operation and performance of the rest of the detector systems as well as the trigger; the consequent high number of collisions per crossing will degrade the performance of ATLAS unless the LAr and Tile calorimeters and the Muon Spectrometer readout systems are upgraded. A new trigger architecture will be implemented exploiting the upgrades of the detector readout systems that will maintain and improve the event selection. The increased luminosity may also degrade the performance of the forward calorimetry. Options for upgrading the hadronic endcap calorimeter readout electronics and the forward calorimeter detector design have been suggested to address the performance degradation. Finally, the computing and software must be upgraded to meet the challenges of the increased luminosity and changes in computer architectures.

The New Inner Tracker

The new Inner Tracker (ITK) (Figure 2.13) is designed for 10 years of operation at instantaneous luminosities of $7.5 \cdot 10^{34}$ cm^{-2}s^{-1}, 25 ns between bunch crossings and an total integrated luminosity

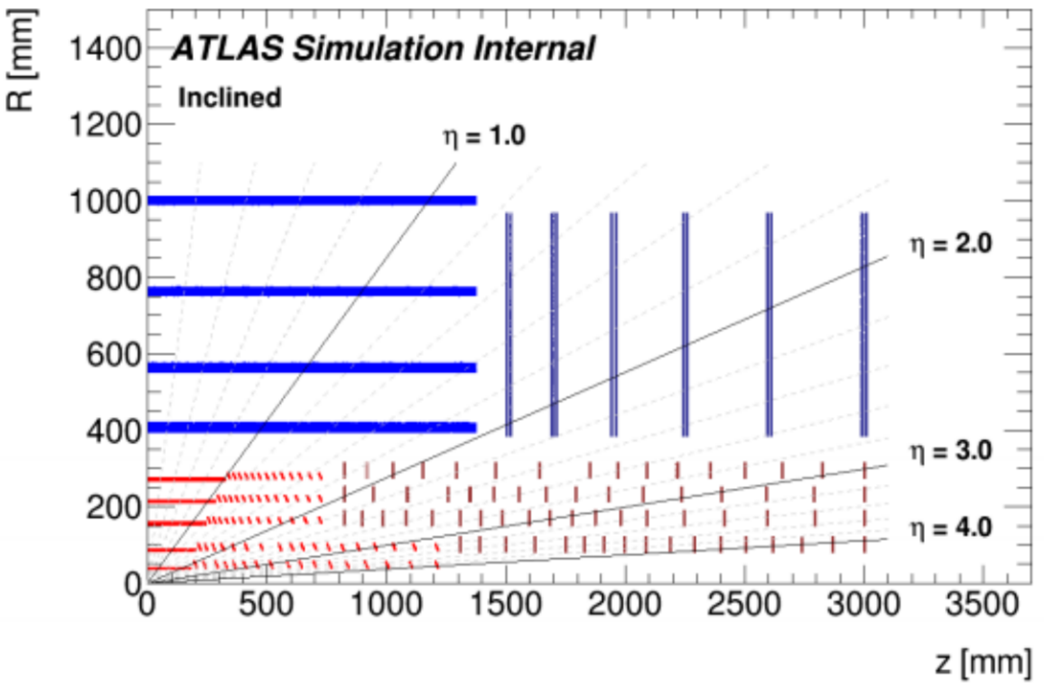

Figure 2.13: The new Inner Tracker layout

of 3000 fb^{-1}. It will combine precision central tracking with the ability to extend the coverage to a pseudorapidity up to 4, with excellent tracking efficiency and performance. All performance requirements must be met for average pile-up scenarios up to $< \mu >= 200$.

The ITk comprises two subsystems, a Strip Detector [77] surrounding a Pixel Detector [78] . The Strip Detector has four barrel layers and six end-cap petal design disks, both having double modules each with a small stereo angle to add z/R resolution in the barrel/endcaps, respectively. The Strip Detector, covering $|\eta| < 2.7$, is complemented by a 5 layer Pixel Detector extending the coverage to $|\eta| < 4$. The Pixel and Strip Detector volumes are separated by a Pixel Support Tube (PST). In addition, and because of the harsh radiation environment expected for the HL-LHC, the inner two layers of the Pixel Detector are replaceable.

The inner two and outer three pixel layers are separated by an Inner Support Tube or IST. The combined Strip plus Pixel Detectors provide a total of 13 hits for $|\eta|$ <2.6, with the exception of the barrel/end-cap transition of the Strip Detector, where the hit count is 11 hits. The pixel end-cap system is designed to supply a minimum of at least 9 hits from the end of the strip coverage in pseudorapidity close to 4.

The ITK is designed to measure the transverse momentum and direction of isolated particles (in particular muons and electrons), to reconstruct the vertices of pile-up events and associate the vertex with the hard interaction. It is also able to identify secondary vertices in b-jets with high efficiency and purity, measure the tracks in the cores of high energy jets with high efficiency, provide good two track resolution and ensure a low rate for reconstruction of fake tracks. It can identify the decay of tau leptons, including impact parameter information, and is also able to reconstruct the tracks associated with converted photons.

The current solenoid magnet will remain providing a magnetic field intensity of 2 T. However, in the region $|\eta| > 2.5$ the strength of magnetic field is decreased and so does the ability of the ITk to measure particle momenta.

3 Forward Electron Identification

In the ATLAS Experiment the detection of the electrons and photons takes place in the Electromagnetic(EM) calorimeter. They deposit their energy in several cells forming clusters. The hadrons also deposit a part of their energy in the EM Calorimeter, forming generally clusters with different shapes. The identification of electrons is based on these cluster shapes and also on tracking variables from the associated tracks from the Inner Detector. However the Inner Detector does not cover fully the acceptance of the calorimeter, it covers pseudorapidity (η) up to 2.5, while the calorimeter covers up to 4.9. So in the forward region $|\eta| > 2.5$ the clusters are not associated with tracks and the identification is based only on cluster shapes. In addition there is no way to distinguish the electrons from photons without tracking information. In the LS3 period during the years 2024–2026 a new Inner Detector will be placed in ATLAS. The new Inner Tracker (ITk), will cover up to $|\eta| = 4.0$ expanding the region in which the clusters can be matched with tracks and giving the opportunity to improve identification and separate electrons from photons.

In this study an identification method for electrons in the η region 2.5–4.0 is suggested. The method uses at first level some matching criteria for the angular distances ($\Delta\eta$ and $\Delta\phi$) between the clusters and the associated tracks. Next a multivariate analysis for cluster shapes and angular distances is used. The validation of the method was done with a sample including events with a Z boson decaying to 2 electrons ($Z \to e^+e^-$). Also the capability to improve identification with some additional tracking variables is checked. The additional tracking variables and the usage of Multivariate methods finally improve the identification significantly.

3.1 Simulation

For this study 4 types of Monte Carlo samples were used; single electron without pile-up, single electron with pile-up, dijet with pile-up and $Z- > e^+e^-$ also with pile-up. The samples are listed in table (3.1).

The simulated ITk geometry is the HGTD+PS_I1.6 and the pile up scenario is $< \mu >= 200$ for all the samples including pile-up. The beamspot is the nominal (50 mm). For the Single electron samples the electrons are uniformly distributed in the region ($2.5 < \eta < 4.0$) and three different transverse momentum values are simulated (20 GeV, 45 GeV and 100 GeV).

3.2 Matching and association

In order to use the tracking information from the ITk, every cluster in the forward region $2.5 < |\eta| < 4.0$ is matched with the closest track (minimum ΔR). Loose preselection criteria are applied to the clusters and the tracks, to reduce the number of possible matching combinations, in order to save computation time. Only tracks with $p_T > 5$ GeV and clusters with $E_T > 10$ GeV are taken into

Type	Name	Tags
Single e	ParticleGun_single_ele_Pt20_etaFlatp23_43 ParticleGun_single_ele_Pt45_etaFlatp23_43 ParticleGun_single_ele_Pt100_etaFlatp23	e5604_s3069_s3058_r8955
Single e & pile-up	ParticleGun_single_ele_Pt20_etaFlatp23_43 ParticleGun_single_ele_Pt45_etaFlatp23_43 ParticleGun_single_ele_Pt100_etaFlatp23_43	e5604_s3069_s3058_r9072
di-jet	Pythia8EvtGen_A14NNPDF23LO_jetjet_pt20_200GeV_minEta22	e5800_s3069_s3058_r9072
$Z \to e^+e^-$	PowhegPythia8_AU2CT10_Zee	e1564_s3069_s3058_r9072

Table 3.1: Simulated samples used for the forward electron identification study.

account. At first, the performance of the ITk was studied. Using the single electron sample, the total number of electrons, the number of clusters and the number of clusters matched with a track are counted. The efficiency of the ITk and the calorimeter as a function of η and p_T can arise from Figure (3.1). The calorimeter efficiency is near 100% in all η regions except the transition region between the end-cap and the Forward Calorimeter, especially for low p_T electrons. The ITk efficiency is more than 90%, increasing as a function of the electron p_T.

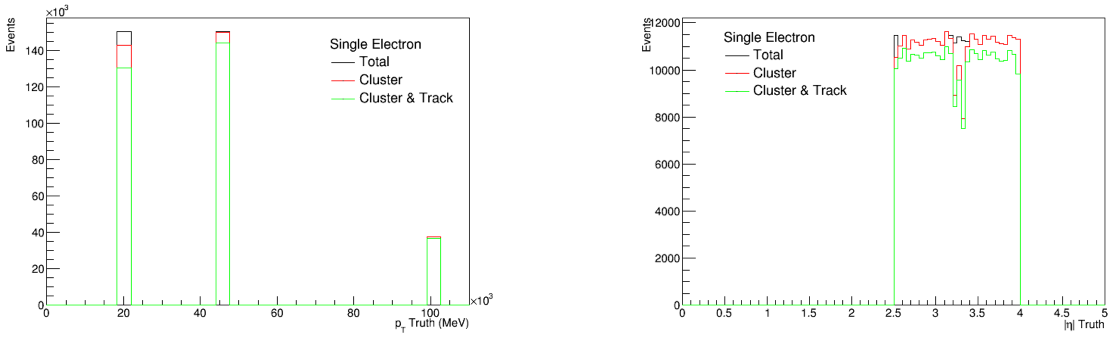

(a) ITk and Calorimeter Efficiency as fuction of p_T

(b) ITk and Calorimeter Efficiency as fuction of $|\eta|$

Figure 3.1: With black color the total number of electrons, with red the electrons reconstructed in the calorimeter and with green the electrons reconstructed both in the calorimeter and ITk.

For high p_T electrons exists a small possibility ($\sim 1\%$) two tracks to have been reconstructed. In a later approach this effect should be taken into account. So if two tracks are very close to a cluster the better (in terms of track quality, p_T, etc) has to be matched with it. This could also reduce the possibility of a pile-up track to have been matched with an electron cluster.

In the single electron sample the only one[1] cluster has come from the truth electron, so it is associated with it. In the single electron with pile-up sample the cluster which is closer (minimum ΔR) to the truth electron is associated with it. The rest of the clusters are considered to be from pile-up. If ΔR between the cluster and the truth electron is more than 0.1, the truth electron probably has not been reconstructed in the calorimeter, or reconstructed out of region of interest, so this event is not taken into account. Figure (3.2) presents the angular distance between every cluster and the truth electron. In the di-jet sample the clusters are split in two categories. Clusters from truth jets and clusters from pile-up. As a cluster is associated with a truth jet with $p_T > 20GeV$ if it is close enough ($\Delta R < 0.4$) to it. Figure (3.2) presents the angular distance between every cluster and the closest truth jet. The accuracy of the association method is presented in Fig. (3.3). The truth clusters

[1]A small probability for two reconstructed clusters exists. In this case the same procedure with single electron with pile-up is followed.

from the single e with pile-up sample behave very similarly to these of single e sample. The pile-up clusters from the single electron with pile-up sample are very similar to the pile-up clusters from di-jet sample.

The purpose of this study is the identification of the clusters which have come from electrons (under pile-up) while rejecting these which have come from jets or pile-up.

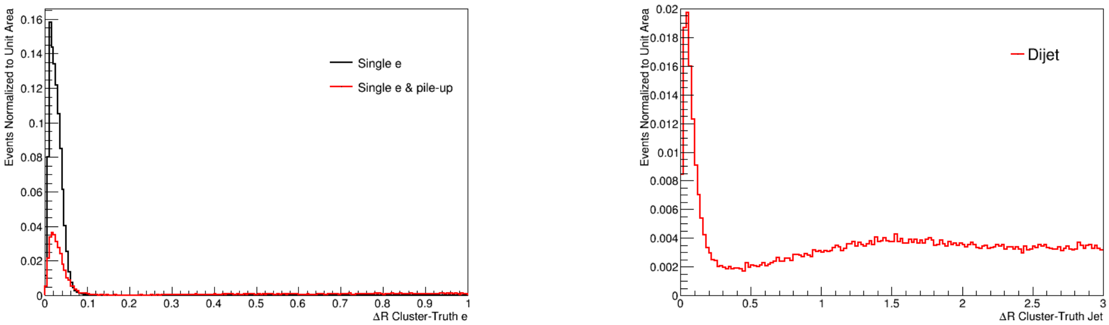

(a) ΔR beteween every cluster and the truth e

(b) ΔR beteween every cluster and the closest truth jet

Figure 3.2: An upper limit of 0.1 & 0.4 is applied for cluster truth e & truth jet association.

As it is shown in Fig. (3.3) the truth electron associated clusters (with or without pile-up) are matched with a track with an angular accuracy better than 0.1. The majority of clusters from Jets or pile-up are not so close to the tracks.

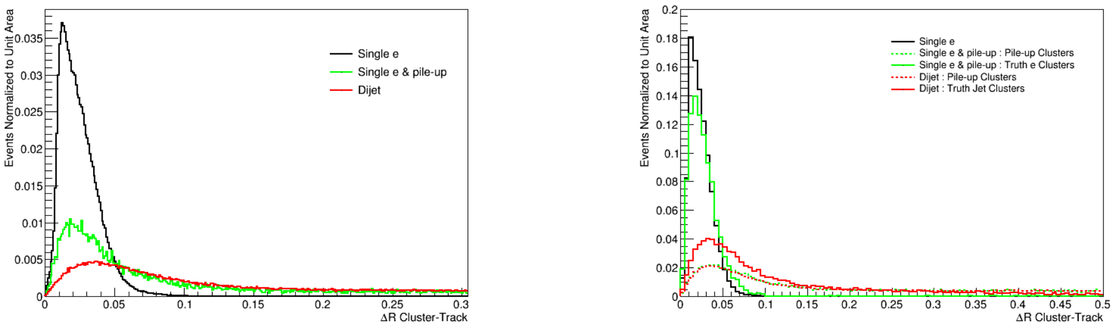

(a) ΔR between cluster and its matched track

(b) ΔR between cluster and its matched track

Figure 3.3: Cluster-Track matching with and without truth association.

3.3 Track-Cluster Matching Criteria

The fact that, the angular distance between the clusters and the tracks is much less for the truth electron associated clusters, can be used to separate electrons from background applying track-cluster matching criteria. To improve the efficiency the criteria are not applied to ΔR but to $\Delta\eta$ and $\Delta\phi$ independently. The End Cap and the Forward calorimeter have very different design [79]. This fact indicates that the two regions have to be treated independently. Also as shown in Fig. (3.1(b)) the

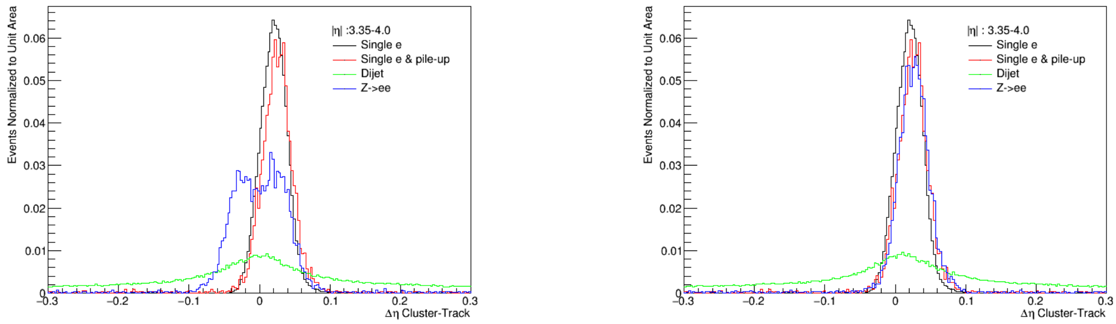

(a) Raw $\Delta\eta$ distribution (b) Corrected $\Delta\eta$ distribution

Figure 3.4: $\Delta\eta$ offset correction. It effects $Z \rightarrow e^+e^-$ electrons which are generated equally to positive and negative η.

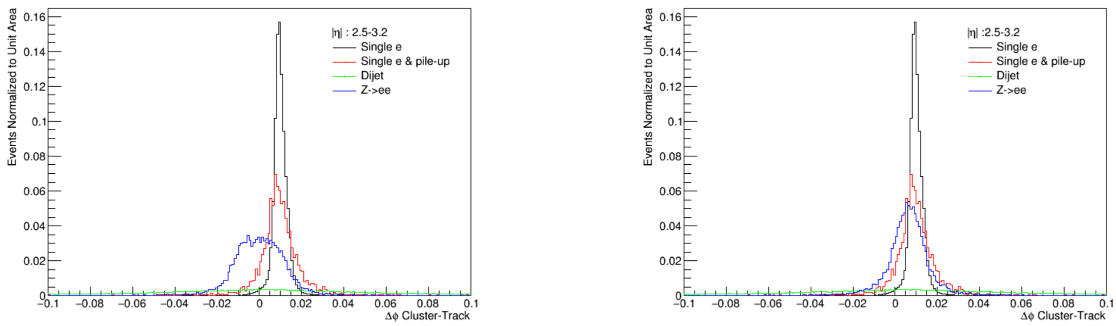

(a) Raw $\Delta\phi$ distribution (b) Corrected $\Delta\phi$ distribution

Figure 3.5: $\Delta\phi$ offset correction. It effects only $Z \rightarrow e^+e^-$ electrons which are generated equally to positive and negative η.

intermediate region seems to have different behaviour[2], so it will also be examined independently. Therefore the values of the criteria are different for the three η regions; the region 2.5–3.2 which is covered by the EC Calorimeter, the transition region 3.2–3.35 and the region 3.35–4.0 which is covered by the Forward calorimeter.

Observing the $\Delta\eta$ and $\Delta\phi$ distributions an offset is observed between the η and ϕ of the cluster and track respectively. The peak of the distributions is not on 0. In the single electron samples all the electrons are generated in positive η. For the $Z \rightarrow e^+e^-$ sample two peaks are observed. This indicates that the offset is opposite in negative η. The case that this effect is due to the charge has been checked and rejected. To correct this offset the parity of $\Delta\eta$ and $\Delta\phi$ distributions has been inverted for negative η clusters. Examples of the raw and corrected distributions are shown in Fig. (3.4) and (3.5) respectively.

After the correction of the distributions the criteria can be applied. They are chosen to be relatively loose as the matching variables ($\Delta\eta$ and $\Delta\phi$) will be used in a Multivariate method on a later stage. However they reject a large amount of clusters from jets and pile-up, loosing only a small percentage of truth electron clusters, mainly these without reconstructed tracks. Figures (3.6) and (3.7) presents the distribution of $\Delta\eta$ and $\Delta\phi$ variables for the different η regions. Table (3.2) summarizes the cut

[2] Can be also confirmed by the clusters shapes (Appendix A.1.2)

values.

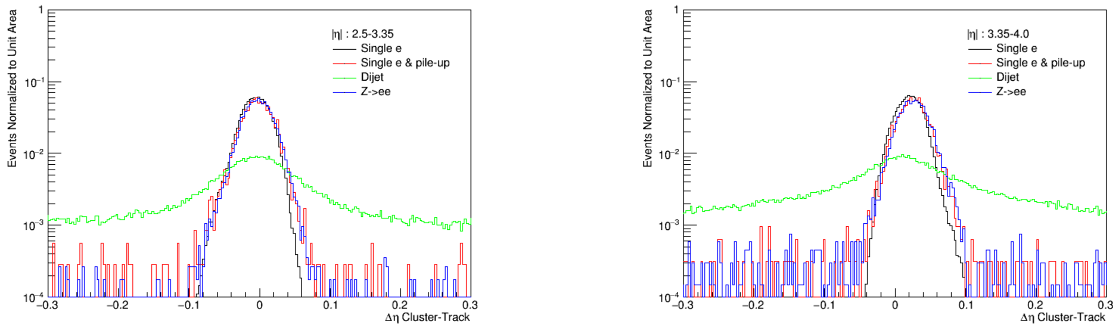

(a) $\Delta\eta$ distribution in $|\eta| : 2.5 - 3.2$ region (b) $\Delta\eta$ distribution in $|\eta| : 3.35 - 4.0$ region

Figure 3.6: $\Delta\eta$ criteria are applied to cut only the tails, coming mainly from clusters without reconstructed tracks.

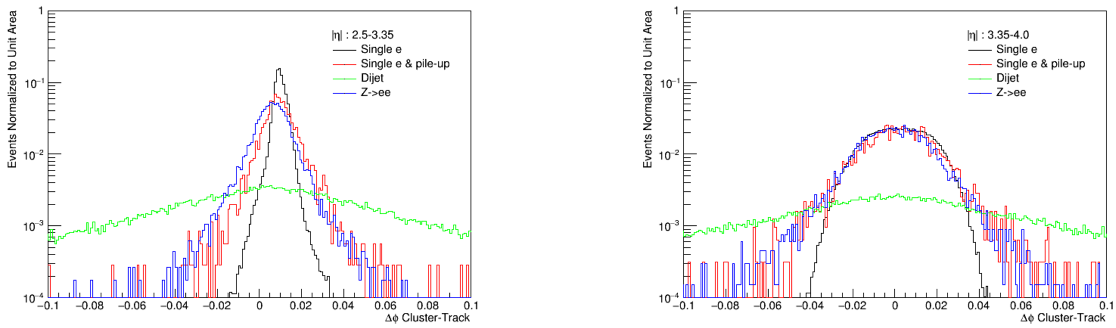

(a) $\Delta\phi$ distribution in $|\eta| : 2.5 - 3.2$ region (b) $\Delta\phi$ distribution in $|\eta| : 3.35 - 4.0$ region

Figure 3.7: $\Delta\phi$ criteria are applied to cut only the tails, coming mainly from clusters without reconstructed tracks.

$\|\eta\|$	$2.5 - 3.2$	$3.2 - 3.35$	$3.35 - 4.0$
$\Delta\eta$	$-0.10, 0.08$	$-0.04, 0.08$	$-0.06, 0.11$
$\Delta\phi$	$-0.03, 0.05$	$-0.03, 0.05$	$-0.08, 0.08$

Table 3.2: Matching Criteria Values.

The efficiency of the matching criteria is very high as it was expected. More than 90% in all three η regions. Especially if taken into account that the ITk has an inefficiency of about 5% so not all clusters have their track reconstructed. Also the efficiency of single e (with or without pile-up) and $Z \to e^+e^-$ is similar. The fake rate is quite high but it is obvious that with a very small loss in efficiency more than the half of the fakes can be rejected.

The efficiency has a weak dependency on p_T, in the 100 GeV electrons is about 6% higher than in 20 GeV. The exact dependency can be found in Appendix A.1.1.

$\|\eta\|$	2.5-3.2	3.2-3.35	3.35-4.0
Single e	94.81±0.05	94.0±0.2	94.59±0.06
Single e with pile-up	93.8±0.4	91±1	93.2±0.4
di-jet – Truth Jets	33.4±0.5	43±1	43.0±0.6
di-jet – pile-up	17.1±0.1	27.4±0.41	8.5±0.1
$Z \to e^+e^-$	94.1±0.2	91.7±0.8	92.7±0.03

Table 3.3: Matching criteria efficiency-fake rate(%). Only statistical errors included.

3.4 Electromagnetic Cluster Shape Criteria

Currently the Identification in the forward region is based only on the cluster shape variables [80] as the Inner Detector covers up to $|\eta| = 2.5$. Electromagnetic showers generally start earlier, are more compact and exhibit a larger energy density than hadronic showers. The photon and electron clusters are similar and they can not be distinguished without tracking information. The 6 variables which are used to define the shape of a cluster are listed below :

- λ_{center}: the distance of the shower center from the calorimeter front face measured along the shower axis
- $< \lambda^2 >$: mean square of longitudinal extension
- $< r^2 >$: mean square of lateral extension
- $longitudinal$: normalized second longitudinal moment
- $lateral$: normalized second lateral moment
- f_{max} : energy fraction in the most energetic cell

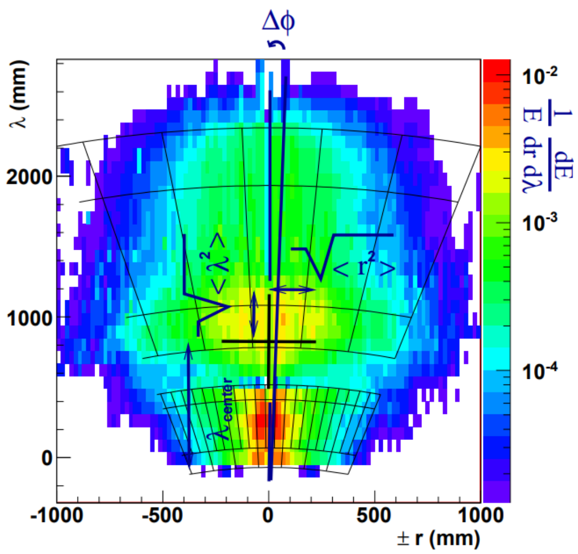

Figure 3.8: A cluster and some of the shape variables [4].

An example of a cluster and some of the shape variables are shown in Fig. (3.8). Currently the identification is carried out with some criteria at the above variables. The criteria are split in 8 categories according the η of the cluster (2.5–2.3 and 3.2–4.0) and the total reconstructed vertices of the event (1–3, 4–6, 7–10, and >10). These criteria, shown in table (3.4), are applied to the Monte Carlo samples to be checked and compared with the matching criteria. Of course they are optimized for the current pile-up conditions ($<\mu>= 60$) and they are not expected to have very good efficiency. The two η categories were used for the corresponding regions. Only the last category of the number of vertices was used, assuming that all the events have more than 10 vertices. The criteria in this category are looser and more compatible with the $<\mu>= 200$ pile-up expected in Run4.

Working point	loose		medium		tight	
$\|\eta\|$	2.5-3.2	3.2-4.0	2.5-3.2	3.2-4.0	2.5-3.2	3.2-4.0
λ_{center} (mm)	255	252	255	250	250	250
$<\lambda^2>$ (mm^2)	4500	10000	4500	9700	2800	7500
$<r^2>$ (mm^2)	3900	1900	3300	1200	3000	1100
longitudinal	0.55	0.73	0.29	0.52	0.24	0.41
lateral	0.69	0.63	0.64	0.45	0.64	0.42
f_{max}	0.22	0.23	0.23	0.26	0.39	0.28

Table 3.4: Cluster shape cut values for more than 10 vertices.

The results are shown in the table (3.5). An interesting remark is that the efficiency and the fake rate of the cluster shape criteria exhibits asymmetry between the two η regions. This probably indicates that in the 3.35-4.0 region the pile-up is much more than the 10 reconstructed vertices which are assumed so far.

wp	loose		medium		tight	
$\|\eta\|$	2.5-3.2	3.2-4.0	2.5-3.2	3.2-4.0	2.5-3.2	3.2-4.0
Single e	93	88	88	83	80	78
Single e with pile-up	90	77	85	71	77	63
di-jet – Truth Jets	17	15	11	6.4	6.4	4
di-jet – Pile-up Jets	14	13	9.4	3.9	4.9	2.5
$Z \to e^+e^-$	89	72	83	65	75	57

Table 3.5: Cluster shape criteria efficiency-fake rate(%).

wp	loose		medium		tight	
$\|\eta\|$	2.5-3.2	3.2-4.0	2.5-3.2	3.2-4.0	2.5-3.2	3.2-4.0
Single e	88	82	84	78	76	73
Single e with pile-up	84	73	79	66	73	59
di-jet – Truth Jets	5.2	5.4	3.4	2.4	2.1	1.6
di-jet – Pile-up Jets	2.7	2.2	1.8	0.9	1.0	0.5
$Z \to e^+e^-$	84	68	79	60	71	53

Table 3.6: Matching & cluster shape criteria efficiency-fake rate(%).

At the next step the matching criteria were combined with the cluster shape criteria. The results are shown in table (3.6). The efficiency drops about 5% but the fake rate drops about 3 times. An interesting point is that after the application of the cluster shape criteria the rejection of matching criteria improves, indicating that they are not correlated and that a multivariate approach will improve the identification significantly.

3.5 Multivariate Analysis

As it was concluded in the previous section the addition of simple track-cluster matching criteria can improve the identification significantly. However a better approach is to use a multivariate method [81] using both the cluster shapes and the track-cluster matching variables. A good idea is to apply the matching criteria before the multivariate analysis as they are very efficient. As input variables for the training, the 6 cluster shapes and the 2 cluster-track matching variables are used. As signal, the truth electron associated clusters from the single e with pile-up sample are used as they are more realistic than clusters from single e sample. And as background, the truth jets associated clusters from the dijet sample. The input variables have not strong dependency on cluster p_T (Appendix A.1.3), so all the clusters will be treated together. Two different trainings are done for the two different calorimeters. For the End Cap calorimeter the training includes the clusters in region $2.5 < |\eta| < 3.2$ and for the Forward the clusters in region $3.35 < |\eta| < 4.0$. The intermediate region 3.2–3.35 is excluded, due to the different behaviour of cluster shapes.

The shapes of the input variables for the two η regions are shown in Fig. (3.9). Also the correlation matrices are shown in Fig. (3.10). As it is expected $< \lambda^2 >$ and $< r^2 >$ variables are strongly correlated with *longitudinal* and *lateral* respectively. Also the matching variables are not correlated with the cluster shape variables.

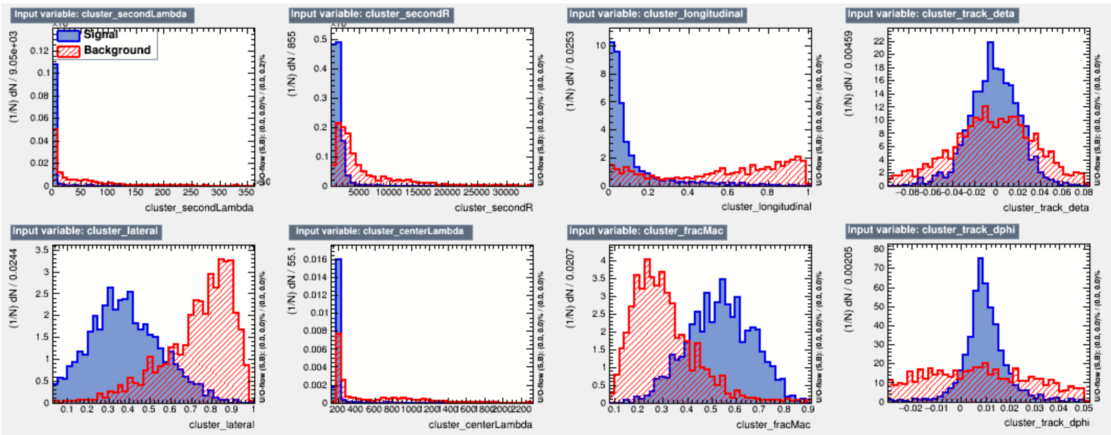

(a) Input variables distributions in $|\eta| : 2.5 - 3.2$ region

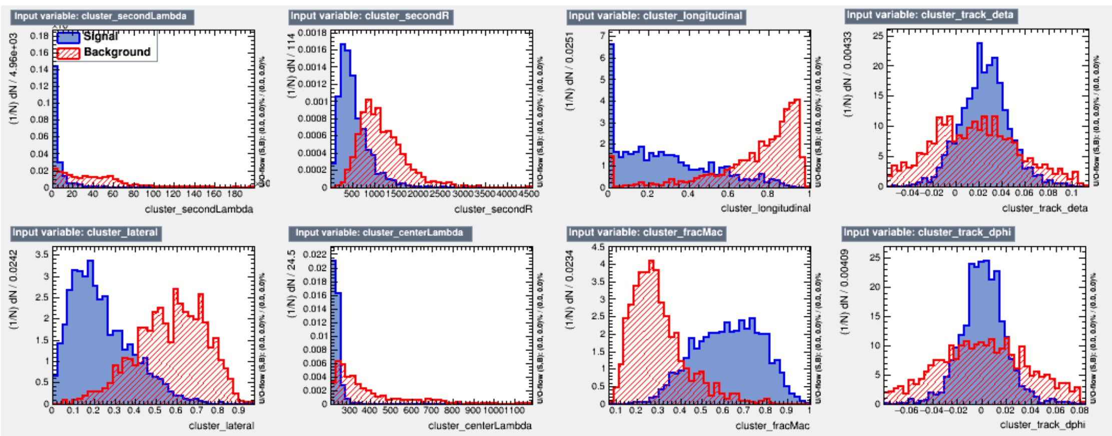

(b) Input variables distributions $|\eta| : 3.35 - 4.0$ region

Figure 3.9: Input variables distributions; cluster shapes & track-cluster angular distances.

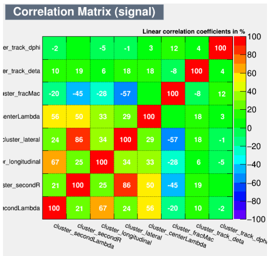

(a) Signal correlation matrix in $|\eta| : 2.5 - 3.2$ region

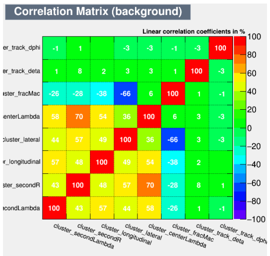

(b) Background correlation matrix in $|\eta| : 3.35 - 4.0$ region

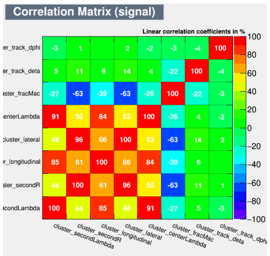

(c) Signal correlation matrix in $|\eta| : 2.5 - 3.2$ region

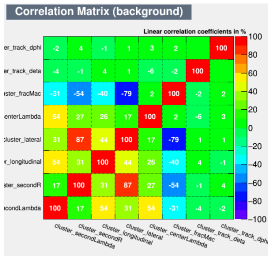

(d) Background correlation matrix in $|\eta| : 3.35 - 4.0$ region

Figure 3.10: Input variables correlation matrices

Three different methods were trained, Fisher, Boosted Decision Tree (BDT) and Artificial Neural Network (ANN). The settings of the methods are shown in table (3.7).The available events after the application of matching requirements are about 3000 for both signal and background. Therefore about 1500 events have been used for the training and the rest 1500 for the testing of the methods. The classifier discriminants for the three methods in the two η regions are shown in Fig. (3.11), (3.12) and (3.13) respectively. Although the small number of events used the training and testing distributions are in reasonable agreement.

Fisher	*TMVA::Types::kFisher, "Fisher", "H:!V:Fisher:VarTransform=None:CreateMVAPdfs: PDFInterpolMVAPdf=Spline2:NbinsMVAPdf=50:NsmoothMVAPdf=10"*
Boosted Decision Tree	*TMVA::Types::kBDT, "BDT", "!H:!V:NTrees=850:MinNodeSize=2.5%:MaxDepth=3:BoostType=AdaBoost:* AdaBoostBeta=0.5:UseBaggedBoost:BaggedSampleFraction=0.5: SeparationType=GiniIndex:nC=20"
Artificial Neural Network	*TMVA::Types::kMLP, "MLPBNN", "H:!V:NeuronType=tanh:VarTransform=N:NCycles=1000: HiddenLayers=N+10:TestRate=5:TrainingMethod=BFGS:UseRegulator"*

Table 3.7: Multivariate methods settings.

As it is expected the BDT and the ANN which are machine learning algorithms have better performance than the Fisher which is a simple linear discriminant. The comparison of the methods performance is shown in Fig. (3.14).

After the application of the methods a cut is applied at the discriminants in order to achieve the loose (90%), medium (80%) and tight (70%) working points. The signle e under pile up efficiency is taken as reference for these working points. This way the tighter working points are subsets of looser. The complete results from the BDT and the ANN are shown in the tables (3.8) and (3.9) respectively. The Fisher method has much lower performance so it has not been included in the results.

The ANN has slightly better performance. The intermediate region (3.2-3.35) has been excluded from the final results as the multivariate methods have not been trained to identify clusters in this region. However, if the ANN weights from the 3.35-4.0 region are applied, it will lead to a truth jet fake rate of about 15%, 5% and 3% for the loose, medium and tight working points respectively. The weights from 2.5-3.2 region give worse results. So, if there is not capability of further study for the intermediate region, is suggested to be merged with the 3.35-4.0 region.

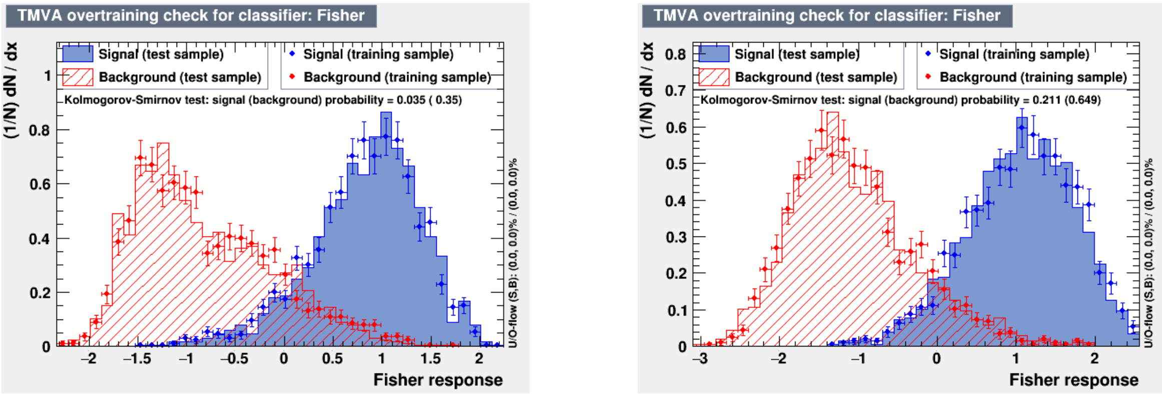

(a) $|\eta|$: $2.5 - 3.2$ (b) $|\eta|$: $3.35 - 4.0$

Figure 3.11: Fisher discriminant

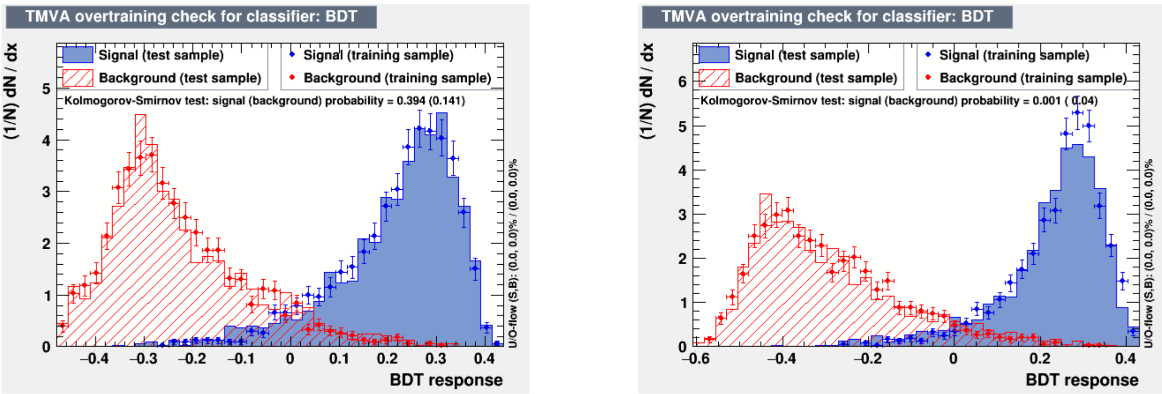

(a) $|\eta|$: $2.5 - 3.2$ (b) $|\eta|$: $3.35 - 4.0$

Figure 3.12: Boosted Decision Tree discriminant

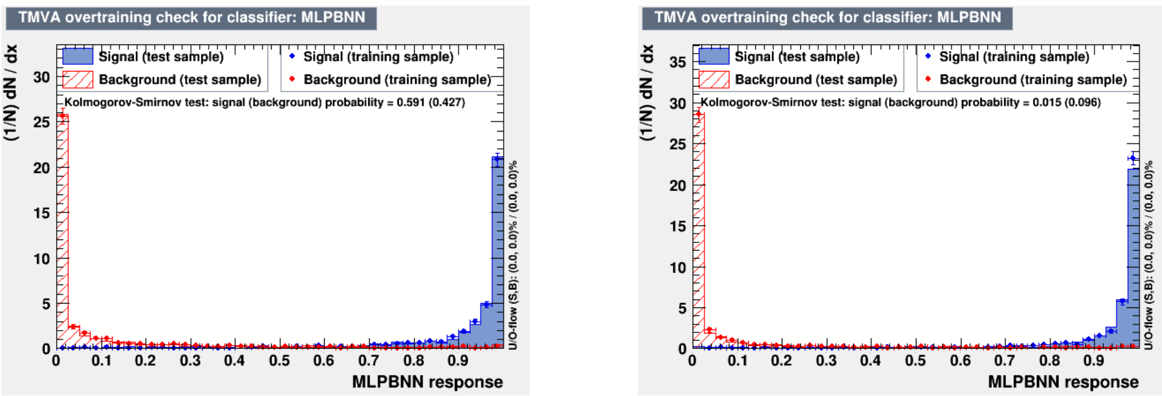

(a) $|\eta|$: $2.5 - 3.2$ (b) $|\eta|$: $3.35 - 4.0$

Figure 3.13: Artificial Neural Network discriminant

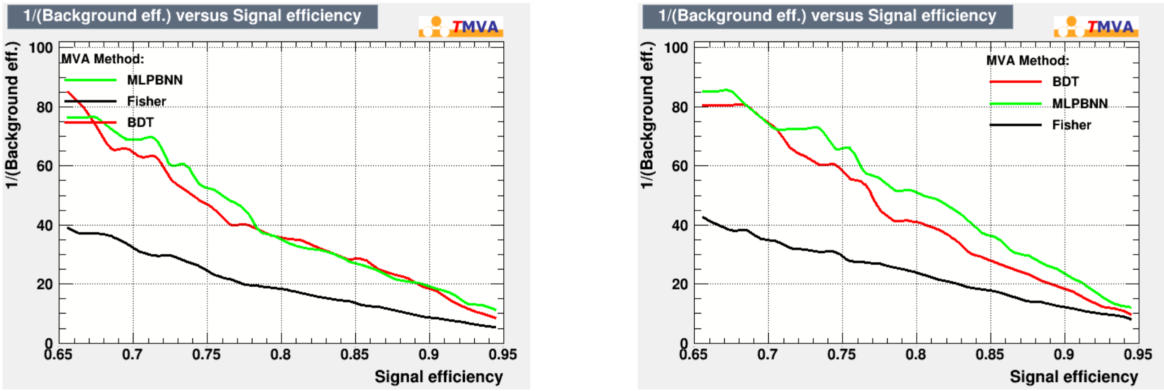

(a) $|\eta|:2.5-3.2$ (b) $|\eta|:3.35-4.0$

Figure 3.14: Classifiers comparison

wp	loose		medium		tight	
$\lvert\eta\rvert$	2.5-3.2	3.35-4.0	2.5-3.2	3.35-4.0	2.5-3.2	3.35-4.0
cut value	-0.045	-0.365	0.095	0.125	0.165	0.195
Single e	92.26±0.06	92.80±0.06	84.97±0.09	87.80±0.08	72.3±0.1	79.5±0.1
Single e pile-up	89.6±0.5	90.0±0.5	79.7±0.7	79.7±0.7	69.6±0.7	68.9±0.8
di-jet – Truth Jets	3.8±0.2	4.5±0.2	1.1±0.1	1.1±0.1	0.58±0.07	0.50±0.08
di-jet – pile-up	2.09±0.04	1.56±0.04	0.76±0.02	0.40±0.02	0.35±0.01	0.17±0.01
$Z \to e^+e^-$	87.7±0.3	88.2±0.4	77.0±0.4	77.1±0.5	64.6±0.4	66.5±0.6

Table 3.8: Matching criteria & Decision Tree efficiency-fake rate(%). Only statistical errors included.

wp	loose		medium		tight	
$\lvert\eta\rvert$	2.5-3.2	3.35-4.0	2.5-3.2	3.35-4.0	2.5-3.2	3.35-4.0
cut value	0.375	0.365	0.795	0.855	0.915	0.932
Single e	93.65±0.05	92.75±0.06	88.45±0.08	88.17±0.08	78.7±0.1	79.2±0.1
Single e pile-up	90.0±0.5	89.9±0.5	79.7±0.7	79.2±0.7	69.5±0.8	68.9±0.8
di-jet – Truth Jets	3.6±0.2	3.9±0.2	1.1±0.1	1.0±0.1	0.53±0.07	0.59±0.09
di-jet – pile-up	2.01±0.04	1.28±0.03	0.72±0.02	0.33±0.02	0.38±0.02	0.16±0.01
$Z \to e^+e^-$	88.5±0.3	88.2±0.4	77.0±0.4	77.1±0.5	64.6±0.4	66.5±0.6

Table 3.9: Matching criteria & Neural Network efficiency-fake rate(%). Only statistical errors included.

3.6 Additional tracking variables

The separation of electrons and clusters can be further increased if additional tracking variables are used. Two suitable variables are the d0 and the track isolation. As the isolation variables are not stored for forward electrons, 4 such variables were made for this study. For the cone two options were studied, either $\Delta R < 0.2$ or $\Delta R < 0.3$. Only tracks with $p_T > 1$ GeV are included in the cone. Also only tracks coming from the same direction with the reference track are included. To achieve this a cut to z_0 difference of the tracks with the reference track is applied. For the Δz_0 two options are studied to, 5mm and 10mm. Combining the two cone options and the two Δz_0 options four isolation variables are formed. The isolation variables are constructed by summing the transverse momenta of the tracks found within the cone of radius ΔR aligned with the electron track (excluding the candidate's own contribution) divided by the candidate's transverse momentum. The distributions of all four isolation variables are similar.The distribution of d0 and one of isolation variables are shown in Fig. (3.15).

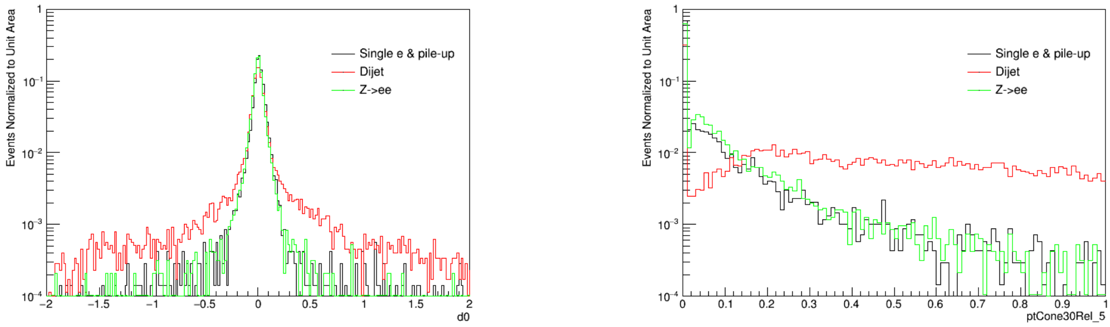

(a) d_0 (b) Isolation

Figure 3.15: Additional tracking variables distributions.

It is obvious that the isolation can be used in order to achieve better background rejection. Of course it has to be studied in detail in order to be optimized. The d0 variable appears not to improve the rejection. The separation ability of the variables is shown in Fig. (3.16) via the background rejection vs signal efficiency plots. On these plots both signal and background consist of clusters which have passed the ANN selection as it was described in previous section.

The isolation with the 0.3 cone and the maximum Δz_0 of 5 mm is the best option. The d0 variable cannot contribute to better rejection. As shown in table (3.10) if an isolation cut on 0.25 is applied the efficiency drops about 5% but the fake-rate drops at least 40%.

wp	loose		medium		tight	
$\lvert\eta\rvert$	2.5-3.2	3.35-4.0	2.5-3.2	3.35-4.0	2.5-3.2	3.35-4.0
$Z \rightarrow e^+e^-$	88.5±0.3	88.2±0.4	77.0±0.4	77.1±0.5	64.6±0.4	66.5±0.6
$+iso < 0.25$	82.9±0.3	82.0±0.5	72.4±0.4	71.9±0.5	60.1±0.4	62.2±0.6
di-jet − Truth Jets	3.6±0.2	3.9±0.2	1.1±0.1	1.0±0.1	0.53±0.07	0.59±0.09
$+iso < 0.25$	2.01±0.04	1.28±0.04	0.71±0.02	0.33±0.02	0.06±0.01	0.17±0.01

Table 3.10: Isolation potential contribution on efficiency-fake rate(%). Only statistical errors included.

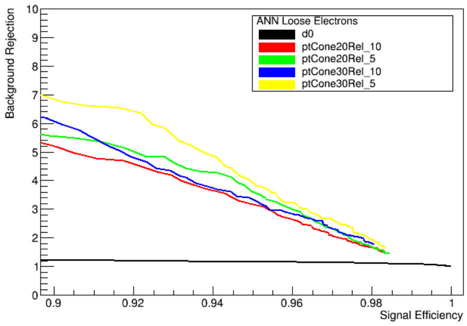

(a) Neural Network loose electrons

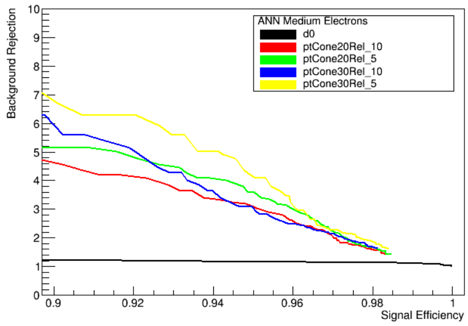

(b) Neural Network medium electrons

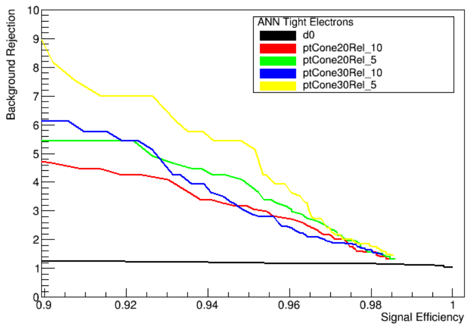

(c) Neural Network tight electrons

Figure 3.16: Background rejection vs signal efficiency for the four isolation and d0 variables.

3.7 Results-Summary

After the confirmation of the potential of the multivariate methods in identification, it is important to examine their performance as a function of some interesting quantities. The ANN results have been used for the next set of figures. The efficiency and fake rate are drawn as a function of ρ, number of reconstructed vertices, p_T and η, Fig. 3.17, 3.18, 3.19 and 3.20 respectively. The ρ quantity is the average pile-up density and is defined as:

$$\rho = \frac{1}{\sqrt{2\pi}}\sigma_b \cdot < \mu > \cdot e^{-\frac{z_{pv}^2}{2\sigma_b^2}} \tag{3.1}$$

where b is the nominal beamspot (50mm) and z_{pv} is the z of the primary vertex.

The dependency of the performance as a function of p_T is very important for the studies which are carried out with smearing functions, so it has been parametrized. The parametrizing functions and the parameter values are shown in table (3.11).

The average pile-up seems that does not effect the efficiency and the fake rate. On the contrary as the number of vertices increases both the efficiency and the fake rate decrease. The efficiency increases as a function of p_T until 40-50 GeV and remains steady for bigger values. The fake rate also increases as a function of p_T. Lastly the efficiency and fake rate seem not to depend strongly on the η. The same set of plots for using the BDT can be found in Appendix A.1.4. Also the in Appendix A.1.5 the same plots can be found with a isolation requirement <0.25.

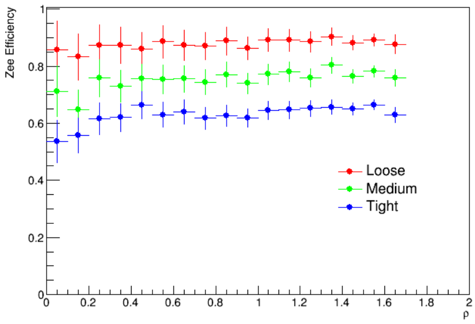

(a) $Z \to e^+e^-$ efficiency

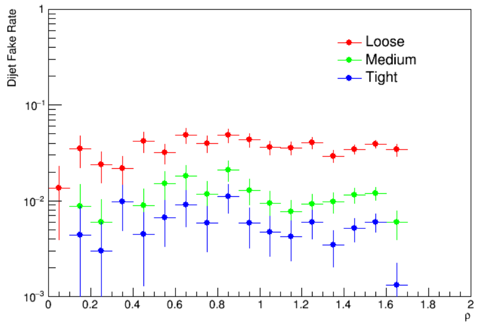

(b) Truth jets fake rate

Figure 3.17: Neural Network performance as a function of average pile-up density.

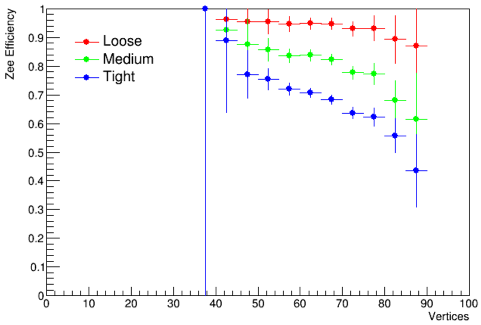

(a) $Z \to e^+e^-$ efficiency

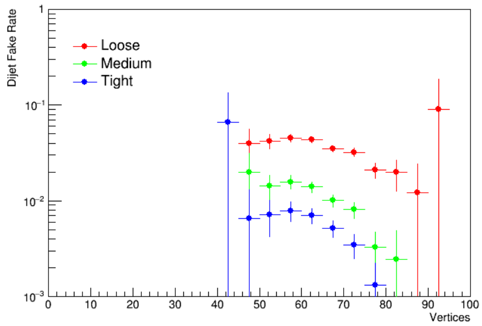

(b) Truth jets fake rate

Figure 3.18: Neural Network performance as a function of reconstructed vertices.

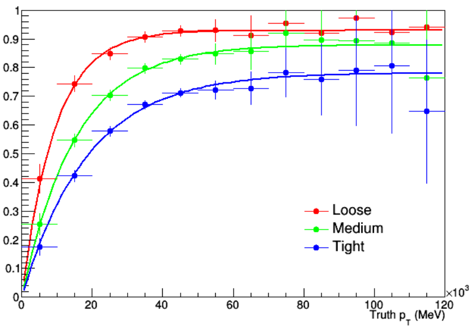

(a) $Z \to e^+e^-$ efficiency

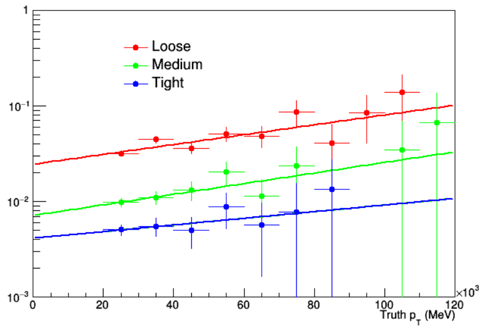

(b) Truth jets fake rate

Figure 3.19: Neural Network performance as a function of truth p_T.

This study showed that the electron identification in forward region can be improved significantly using tracking information from the new Inner Tracker. The ability of cluster-track matching with the ITk is very high and it can be exploited for the identification of electrons and the rejection of jets and pile-up. the matching criteria reject more than 60% of fakes loosing less than 7% of electrons.

	Efficiency			**Fake rate**		
Function	$ef(p_T) = a \cdot (1 - e^{b \cdot p_T})$			$fr(p_T) = a \cdot e^{b \cdot p_T}$		
wp	loose	medium	tight	loose	medium	tight
a	0.93	0.87	0.78	0.025	0.007	0.004
b	$-1.1 \cdot 10^{-4}$	$-6.5 \cdot 10^{-5}$	$-5.3 \cdot 10^{-5}$	$1.2 \cdot 10^{-5}$	$1.3 \cdot 10^{-5}$	$8 \cdot 10^{-6}$

Table 3.11: Efficiency-fake rate parametrization details.

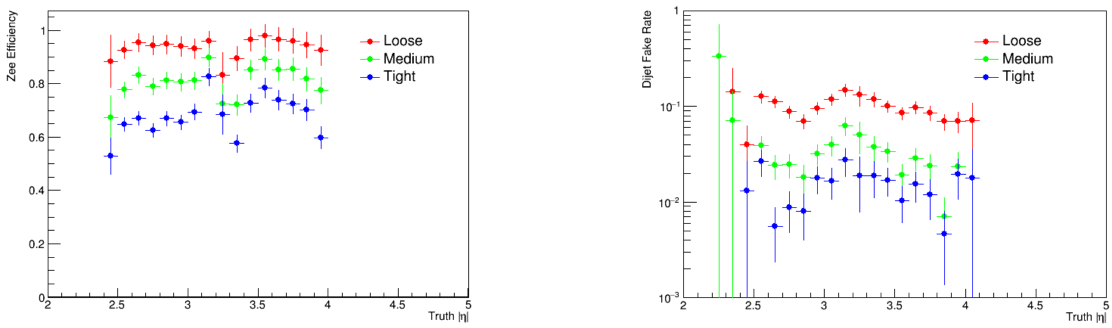

(a) $Z \to e^+e^-$ efficiency (b) Truth jets fake rate

Figure 3.20: Neural Network performance as a function of truth η.

In addition the matching variables are not correlated with the cluster shapes variables so if they are combined in a multivariate method the identification improves further. From these methods the Artificial Neural Network seems to be the best one. For the loose, medium, tight working point the fake rate from jets is about 4%, 1%, 0.6% respectively. The fake rate from pile-up is on average half of the corresponding one from jets. The addition of a track isolation requirement leads to further 40% rejection, decreasing the efficiency about 5%. Finally, the identification using multivariate methods has a dependency on the transverse momentum and the number of vertices, but it seems independent of pseudorapidity and pile-up density.

4 $H \to 4l$ Event Selection and Background Estimation

4.1 Introduction

This chapter presents the event selection and background estimation used in the different analyses done in the $H \to ZZ \to \ell^+\ell^-\ell^+\ell^-$ channel. They include the measurements of the mass, off-shell signal strength, fiducial and differential cross-sections, couplings and EFT measurements of the Higgs boson, as well as the differential m_{4l} analysis, and the search for additional heavy Higgs-like bosons. The analyses were performed using pp collision data corresponding to an integrated luminosity of about 139 fb^{-1} collected at $\sqrt{s} = 13$ TeV from 2015–2018. Measurement and search for Higgs bosons through the decay $H \to ZZ^* \to 4\ell$, where $\ell, \ell^{'} = e$ or μ, provides good sensitivity over a wide mass range. Events are split into four final states:$e^+e^-e^+e^-$ ($4e$), $\mu^+\mu^-\mu^+\mu^-$ (4μ), $e^+e^-\mu^+\mu^-$ ($2e2\mu$), and $\mu^+\mu^-e^+e^-$ ($2\mu 2e$); the difference between the last two channels is that the first two leptons quoted are the ones with a di-lepton invariant mass closest to the Z boson mass. The main background contribution to this decay channel comes from continuum $(Z^{(*)}/\gamma^*)(Z^{(*)}/\gamma^*)$ production, referred to as $ZZ^{(*)}$ hereafter. For $m_H < 180$ Gev, there is also non-negligible background contribution from $Z+$jets, $t\bar{t}$ and WZ production, where the leptons can mostly arise either from decays of hadrons with b- or c-quark content or from misidentification of jets. Finally, there is a small contribution from triboson events.

4.2 Data and simulation samples.

4.2.1 Data samples

For this analysis, the full Run-2 dataset, consisting of all proton-proton collision data collected from 2015-2018 at $\sqrt{s} = 13$ TeV with a 25 ns bunch spacing configuration, is used[1].

For 2015, 3.86 fb^{-1} of luminosity with a peak instantaneous luminosity of 5.0×10^{33} cm^{-2}s^{-1}, an average pile-up of $\langle\mu\rangle = 13.6$ and a peak pile-up of 40.5 was recorded. For 2016, the recorded integrated luminosity is 35.6 fb^{-1}, with a peak instantaneous luminosity of 13.7×10^{33} cm^{-2}s^{-1}, an average pile-up of $\langle\mu\rangle = 24.9$ and a peak pile-up of 51.1. For 2017, the recorded integrated luminosity is 46.9 fb^{-1}, with a peak instantaneous luminosity of 20.9×10^{33} cm^{-2}s^{-1}, an average pile-up of $\langle\mu\rangle = 37.8$ and a peak pile-up of 80. For 2018, the recorded integrated luminosity is 62.2 fb^{-1}, with a peak instantaneous luminosity of 21.4×10^{33} cm^{-2}s^{-1}, an average pile-up of $\langle\mu\rangle = 37.0$, and a peak pile-up of 90. The data taking efficiency is 92.0% in 2015, 92.4% in 2016, 93.6% in 2017, and 95.7% in 2018. The pile-up distributions for these datasets are shown in Fig. 4.1.

The data are subjected to quality requirements. Events recorded during periods when the relevant detector components were not operating normally are rejected. This analysis uses the standard "All

[1]This excludes 0.13 fb^{-1} of data collected in 2015 using the 50 ns bunch spacing configuration.

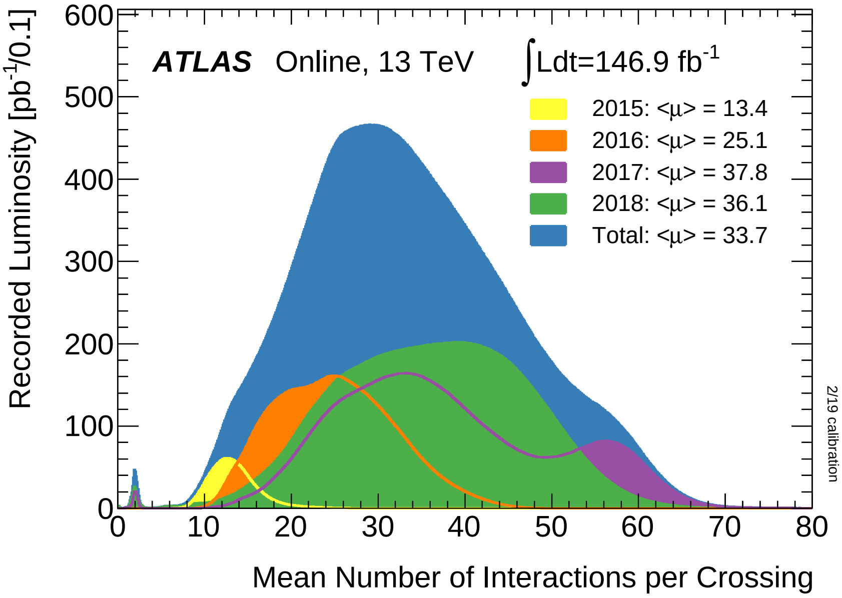

Figure 4.1: The luminosity-weighted distribution of the mean number of interactions per crossing is shown for Run-2 pp collision data.

Good" Good Run List. The resulting integrated luminosity is 139 fb^{-1} and data quality efficiency is 91.5%.

Over the course of Run-2, data taking conditions evolved. Specifically, the pile-up profile, as shown in Figure 4.1, is different and the gas mixture in the TRT has been changed. Section 4.2.2 describes how this is simulated.

This analysis uses di-lepton filter samples (`DAOD_HIGG2D1`). This filter requires at least two leptons (electrons and muons) with the di-lepton mass of > 5 GeV with at least one fired `HLT_e`, `HLT_mu`, `HLT_2e`, `HLT_2mu`, `HLT_3e`, or `HLT_3mu` trigger. This analysis uses samples reconstructed using release 21.0. Derivations of MC samples were produced with the tags `p3872` and `p3972` which use `AthDerivation 21.2.64` and `AthDerivation 21.2.75` respectively. Derivations of data samples were made the tag `p3917` using `AthDerivation 21.2.69`. Final processing and minitree production is performed using `AnalysisBase 21.2.91`.

4.2.2 Monte Carlo samples

Generated events are fully simulated using the ATLAS detector simulation [82] within the GEANT4 framework [83]. The simulation of the additional *pp* interactions (pile-up) is done in a separate step in the simulation chain, during digitization. Here minimum bias events, which were previously simulated, are superimposed on the simulated signal events. The distribution of the number of pile-up events reproduces the bunch structure and the average number of interactions of the run periods. The complete list of the MC samples and their configuration can be found in Appendix A.3.

For simulating both the 2015 and 2016 data-taking conditions, only one MC set, mc16a, is used. The pile-up profile is reweighed to a luminosity weighted combination of the 2015 and 2016 data. Separate MC campaigns are used to simulate the 2017 (mc16d) and 2018 (mc16e) data-taking conditions.

Higgs signal samples

The primary Monte Carlo (MC) event generators that are used to simulate gluon fusion (ggF), vector boson fusion (VBF), associated Higgs boson production (VH, $V = W, Z$), as well as Higgs boson production in association with a heavy quark pair ($t\bar{t}H$, bbH) are listed in Table 4.1. The accuracy of the calculations and the used PDF sets are also given. NLO is the abbreviation for next-to-leading order, NNLO for next-to-next-to-leading order, and NNLL for next-to-next-to-leading logarithm. For ggF and $t\bar{t}H$ production, samples are also produced using *Madgraph5_aMC@NLO* for cross-checks. Production cross-sections per production mode are summarized in appendix A.2.

For ggF, VBF, VH, $t\bar{t}H$ and bbH, *Pythia8* [84, 85] is used for decay, parton shower, hadronisation and multiple parton interactions. This in turn is interfaced to *EvtGen* v1.2.0 program [86] for the simulation of B-hadron decays. The *Madgraph5_aMC@NLO* signal samples are showered with *Herwig++* [87, 88].

Process	Generator	Accuracy in QCD	PDF set
ggF	*Powheg-Box* v2 (NNLOPS) [89, 90, 91, 92]	NNLO in y^H [93], p_T^H consistent with HqT (NNLO+NNLL) [95, 96]	PDF4LHC [94]
VBF	*Powheg-Box* v2 [89, 90, 91, 97]	NLO	PDF4LHC [94]
VH	*Powheg-Box* v2 (*MiNLO*) [89, 90, 91, 98]	NLO	PDF4LHC [94]
tH	*Powheg-Pythia8*	NLO	PDF4LHC [94]
$t\bar{t}H$	*Powheg-Box* v2 [89, 90, 91, 97]	NLO	PDF4LHC [94]
bbH	*Madgraph5_aMC@NLO* (v.2.3.3) [99, 100]	NLO	NNPDF23 [101]

Table 4.1: Description of MC samples used to simulate Higgs boson production, including the generators, accuracy of calculations in QCD, and PDF sets.

The Higgs boson decay branching ratio to the four-lepton final state ($\ell = e, \mu$) for m_H =125 Gev is predicted to be 0.0124% [102] in the SM using PROPHECY4 [103, 104], which includes the complete NLO QCD and EW corrections, and the interference effects between identical final-state fermions. Due to the latter, the expected branching ratios of the $4e$ and 4μ final states are about 10% higher than the branching ratios to $2e2\mu$ and $2\mu 2e$ final states.

Table A.2 gives the production cross sections and branching ratios for $H \to ZZ^* \to 4\ell$ which are used to normalize the signal MC samples. These production cross sections and branching ratios were calculated by LHC Higgs Cross Section Working Group for Yellow Report 4 [105].

m_H [GeV]	$\sigma\,(gg \to H)$ [pb]	$\sigma\,(qq' \to Hqq')$ [pb]	$\sigma\,(q\bar{q} \to WH)$ [pb]	$\sigma\,(pp \to ZH)$ [pb]
125.0	$48.58\ ^{+4.6\%}_{-6.7\%}\ ^{+3.2\%}_{-3.2\%}$	$3.782\ ^{+0.4\%}_{-0.3\%}\ ^{+2.1\%}_{-2.1\%}$	$1.373\ ^{+0.5\%}_{-0.7\%}\ ^{+1.9\%}_{-1.9\%}$	$0.8839\ ^{+3.8\%}_{-3.1\%}\ ^{+1.6\%}_{-1.6\%}$
m_H [GeV]	$\sigma\,(gg \to ZH)$ [pb]	$\sigma\left(q\bar{q}/gg \to t\bar{t}H\right)$ [pb]	$\sigma\left(q\bar{q}/gg \to b\bar{b}H\right)$ [pb]	$B\ (H \to ZZ^* \to 4\ell)$ [10^{-3}]
125.0	$0.1227\ ^{+25.1\%}_{-18.9\%}\ ^{+2.4\%}_{-2.4\%}$	$0.5071\ ^{+5.8\%}_{-9.2\%}\ ^{+3.6\%}_{-3.6\%}$	$0.4880\ ^{+20.2\%}_{-23.9\%}$	$0.1240 \pm 2.18\%$

Table 4.2: Calculated SM Higgs boson production cross sections (σ) for gluon fusion, vector-boson fusion and associated production with a W or Z boson or with a $b\bar{b}$ or $t\bar{t}$ pair in pp collisions at $\sqrt{s} = 13$ TeV. The first and second quoted uncertainties correspond to the theoretical systematic uncertainties calculated by adding in quadrature the QCD scale and PDF+α_s uncertainties, respectively. The decay branching ratio (B) for $H \to 4\ell$ with $\ell = e, \mu$, is reported in the last column.

Background samples

The $ZZ^{(*)}$ continuum background from quark-antiquark annihilation is simulated with *Sherpa* 2.2.2 [106, 107, 108], using the NNPDF3.0 NNLO PDF set. NLO accuracy is achieved in the matrix element calculation for zero- and one-jet final states and LO accuracy for two- and three-jet final states. The merging is performed with the *Sherpa* parton shower [109] using the *MePs*@NLO prescription [110]. NLO EW corrections are applied as a function of the invariant mass of the ZZ^* system $m_{ZZ^{(*)}}$ [111, 112]. The $gg \to ZZ^{(*)}$ process is modeled similarly (PDF, matrix element accuracy, and merging) by *Sherpa* 2.2.2.

The $q\bar{q} \to ZZ^{(*)}$ continuum background is also simulated with *POWHEG-BOX v2* interfaced to *PYTHIA 8* for parton shower and hadronization, and to *EvtGen* for the simulation of B- and C-hadron decays. The `CT10nlo` PDF set is used for the hard process and the `CTEQL1` PDF set for the parton shower, while non-perturbative effects are modeled using the `AZNLO` tune [113]. NNLO QCD and NLO EW corrections are considered for the quark-initiated $ZZ^{(*)}$ as a function of m_{ZZ^*} [114, 115, 111, 112]. The mass-dependent PDF and α_s scale uncertainties are parametrised as recommended in Ref. [116]. Cross-sections for all background samples are given in the tables in appendix A.3

The $Z+\text{jets}$ background is modelled using *Sherpa* at NLO for 0 to 2 jets and at LO for 3 and 4 jets using *Comix* [107] and *OpenLoop* [108] for matrix elements, and merged using the *Sherpa* ME+PS@NLO prescription. $Z+\text{jets}$ events are filtered into three categories, $Z+b$-jets (by B-hadron filter), $Z+c$-jets (by B-hadron veto and C-hadron filter) and Z+light jets (by B-hadron veto and C-hadron veto). Also, 4ℓ- and 3ℓ-filtered $Z+\text{jets}$ *Sherpa* samples are made. Alternative samples of the $Z+\text{jets}$ background are made with *POWHEG-BOX v2* and *MadGraph* [117]. Both of them are interfaced to *Pythia8* for parton shower and hadronization and to *EvtGen* for the simulation of B-hadron decays. The *POWHEG* samples also use *Photos++* [118] for the QED emissions from electroweak vertices and charged leptons.

The $t\bar{t}$ background is modelled using *POWHEG-BOX v2* with the NNPDF30 NLO matrix element and the hdamp parameter set equal to 1.5 times the top mass, interfaced to *PYTHIA 8* [84] with the A14 NNPDF23LO tune for parton shower and hadronization, and to *EvtGen* for the simulation of B-hadron decays.

The WZ background is modelled using *POWHEG-BOX v2* interfaced to *Pythia8* for parton shower and hadronization and to *EvtGen* for the simulation of B-hadron decays. The tribosons backgrounds ZZZ, WZZ, WWZ are modelled using *Sherpa*. For all-leptonic $t\bar{t}+V$, *MadGraph_aMC@NLO* interfaced with *Pythia8* is used.

4.3 Event selection

4.3.1 Trigger configuration

The trigger signatures for the online selection for this analysis are single lepton, di-lepton and tri-lepton triggers. Dilepton and trilepton triggers include electron(s)-muon(s) triggers. Tri-lepton triggers were introduced in 2015 into the $H \to ZZ^* \to 4\ell$analysis in Run 2 [119].

4.3.2 Physics objects selection

Electron candidates are reconstructed using the supercluster algorithm [120] which has the main ability to recover low energy photons radiated due to bremsstrahlung interactions in the ID. It uses topological clusters from deposits in the EM calorimeter and subsequently matched to a well constructed ID track. A Gaussian-sum filter algorithm [121] is used to compensate for radiative energy losses in the ID. Electron identification is based on a likelihood discriminant combining the measured track properties, electromagnetic shower shapes and quality of the track–cluster matching. The "loose" likelihood criteria applied in combination with track hit requirements provide an electron reconstruction and identification efficiency of about 95% [122]. Electrons are required to have $E_T > 7$ GeV and $|\eta| < 2.47$, with their energy calibrated as described in Ref. [123].

Muon candidate reconstruction [124] is performed within $|\eta| < 2.7$. In the range of the ID coverage, muon reconstruction is primarily performed by a global fit of fully reconstructed tracks in the ID and the MS (combined muons). In the central region ($|\eta| < 0.1$) of the detector where the MS lacks in coverage, muons can also be identified by matching a fully reconstructed ID track to either an MS track segment (segment-tagged muons) or a calorimetric energy deposit consistent with that of a minimum-ionizing particle (calorimeter-tagged muons). For these two cases, the muon momentum is determined by the ID track alone. In the forward MS region ($2.5 < |\eta| < 2.7$) outside the ID coverage, MS tracks with hits in the three MS layers are accepted (stand-alone muons) and combined with forward ID tracklets, if they exist (silicon-associated forward muons). Calorimeter-tagged muons are required to have $p_T > 15$ GeV. For all other muon candidates, the minimum transverse momentum is 5 GeV instead of the 6 GeV threshold in the Run-1 publication [125], increasing the signal acceptance in the 4μ final state by about 7%. At most one calorimeter-tagged or stand-alone or silicon-associated forward muon is allowed per event.

Jets are reconstructed from the output of the particle-flow algorithm [126] using the anti-k_t algorithm with a radius parameter $R = 0.4$. The jet four-momentum is corrected for the calorimeter's non-compensating response, signal losses due to noise threshold effects, energy lost in non-instrumented regions, and contributions from pile-up [127]. Jets are required to have $p_T > 30$ GeV and $|\eta| < 4.5$.

Finally, the MV2c10 b-tagging algorithm [128, 129, 130] is used to assign a b-tagging weight to jets with $|\eta| < 2.5$, with a pseudo-continuous calibration applied.

Ambiguities are resolved if electron, muon or jet candidates are reconstructed from the same detector information. If a reconstructed electron and muon share the same ID track, the muon is rejected if it is calorimeter-tagged; otherwise the electron is rejected. Reconstructed jets geometrically overlapping in a cone of radius $R = 0.2$ with electrons or muons are also removed.

4.3.3 Vertex requirements

Collision vertices are reconstructed from ID tracks with transverse momentum $p_T > 500$ MeV. Events are required to have at least one collision vertex with at least two associated tracks. The primary vertex used in the analysis is selected to be the vertex with the largest p_T sum in the event after refitting with a beam-spot constraint. As the four leptons should emerge from the primary vertex, the lepton tracks must have distances $|z_0 \cdot \sin(\theta)| < 0.5$ mm from the primary vertex along the proton beam pipe. To reduce the cosmic background, an additional cut on the muon transverse impact parameter is applied ($|d_0| < 1$ mm).

4.3.4 Quadruplet formation and selection

Candidate quadruplets in each channel (4μ, $2e2\mu$, $2\mu2e$, $4e$) are formed by selecting two opposite sign, same flavour di-lepton pairs in an event. In each quadruplet, the p_T thresholds for the three leading leptons are 20, 15 and 10 GeV.

In each quadruplet, the di-lepton with mass m_{12} closest to the nominal Z boson mass is called the leading di-lepton, while the second di-lepton of the quadruplet with mass m_{34} is the sub-leading one. Based on the lepton flavour, each quadruplet is classified into one of the following decay channels: 4μ, $2e2\mu$, $2\mu2e$ and $4e$, with the first two leptons always representing the leading lepton pair.

The leading lepton pair must satisfy $50 \text{ GeV} < m_{12} < 106$ GeV and the subleading lepton pair is required to have a mass $m_{\text{threshold}} < m_{34} < 115$ GeV, where $m_{\text{threshold}}$ is 12 GeV for the four-lepton invariant mass $m_{4\ell}$ below 140 GeV, rising linearly to 50 GeV at $m_{4\ell} = 190$ GeV and then remaining at 50 GeV for all higher $m_{4\ell}$ values.In the $4e$ and 4μ channels, the two alternative opposite-charge lepton pairings within a quadruplet must have a dilepton mass above 5 GeV to eliminate contributions from $J/\psi \to \ell\ell$ decays. The two lepton pairs within the quadruplet must have an angular separation of $\Delta R = \sqrt{(\Delta y)^2 + (\Delta\phi)^2} > 0.1$. Each electron (muon) must have a transverse impact parameter significance $|d_0|/\sigma_{d_0}$ below 5 (3) to suppress the background from heavy-flavour hadrons.

Reducible background from the Z+jets and $t\bar{t}$ processes is further suppressed by imposing track-based and calorimeter-based isolation criteria on each lepton: this is discussed in more detail below. Finally, to further suppress the reducible background, mainly Z+jets and $t\bar{t}$, on top of the suppression achieved by the lepton d_0 and isolation cuts, an additional cut based on the vertexing of 4ℓ events is applied. Leptons of the quadruplet are required to originate from a common vertex - this is ensured by performing a vertex fit using the ID tracks of the leptons and placing a requirement to the χ^2 value that is expected to maintain a signal efficiency of 99.5% in all decay channels while rejecting 20%-30% of Z+jets and $t\bar{t}$ background events. The cut value is different for 4μ ($\chi^2/N_{\mathrm{dof}} < 6$) and the other decay channels ($\chi^2/N_{\mathrm{dof}} < 9$) to account for the worse resolution of the electron track reconstruction affecting the quality of the vertex fit.

Multiple quadruplets may pass these selections, but only one per event is selected as the candidate. The final choice of quadruplet is affected by the possibility that VH-Lep or $t\bar{t}H$ production may lead to the presence of prompt leptons in the event from the decay of the V or top quark in addition to those from the Higgs boson decay. A first choice is made based on the decay channel and the mass of the leading lepton pair. If there are multiple quadruplets found in a channel, the quadruplet with the mass of the leading pair closest to the Z boson mass is chosen: if there is more than one such, the one with the mass of the subleading lepton pair closest to the Z boson mass is selected. If there is more than one decay channel per event with a quadruplet satisfying the above selection criteria, the quadruplet from the channel with highest efficiency is chosen as the Higgs boson candidate. The signal selection efficiencies are 31%, 21%, 17% and 16%, in the 4μ, $2e2\mu$, $2\mu 2e$ and $4e$ channels, respectively. If, following this choice of quadruplet, the event is found to contain a fifth lepton with $p_T > 12$ GeV and which satisfies the same identification and isolation criteria as the four quadruplet leptons, then the quadruplet choice is repeated, this time employing a matrix-element based method. For all possible quadruplet combinations which pass the selections, regardless of decay channel and m_{Z1}, a matrix element for the Higgs boson decay (so independent of the production mode to first order) is computed at LO using the *MadGraph5_aMC@NLO* [99] generator. The quadruplet with the largest matrix element value is selected as the final Higgs boson candidate. Studies performed prior to the 2016 analysis [131] showed this method led to an improvement in the probability for finding the correct quadruplet.

In order to improve the four-lepton mass reconstruction, the reconstructed final-state radiation (FSR) photons in Z boson decays are accounted for. Collinear FSR photons are added to muons from the leading Z boson in the case that it has mass $m_{Z1} < 89$ GeV, and non-collinear (far) FSR photons to both electrons and muons from both Z bosons. The collinear FSR search includes electrons as well as photons: the non-collinear search uses only photons. Only one FSR photon can be added to the quad: preference is given to collinear FSR. After the FSR correction, the lepton four-momenta of the leading lepton pair are recomputed by means of a Z-mass-constrained kinematic fit. The fit uses a Breit–Wigner Z line shape, and a single Gaussian function per lepton to model the momentum response function for the expected resolution of each lepton. The Z boson mass constraint improves the resolution of the four-lepton invariant mass $m_{4\ell}$ by about 15%. The expected mass resolution for the Higgs boson with a mass $m_H = 125.09$ GeV is 1.6 GeV, 1.7 GeV, 2.1 GeV and 2.4 GeV in the 4μ, $2e2\mu$, $2\mu 2e$ and $4e$ channels, respectively.

Finally, Higgs boson candidates in the $m_{4\ell}$ range [115, 130] GeV are used for the analyses. A comprehensive summary of all the cuts and requirements used in the event selection is given in Table 4.3.

Physics Objects	
Electrons	
Loose Likelihood quality electrons with hit in innermost layer, $E_T > 7$ GeV and $\lvert\eta\rvert < 2.47$ Interaction point constraint: $\lvert z_0 \cdot \sin\theta\rvert < 0.5$ mm (if ID track is available)	
Muons	
Loose identification with $p_T > 5$ GeV and $\lvert\eta\rvert < 2.7$ Calo-tagged muons with $p_T > 15$ GeV and $\lvert\eta\rvert < 0.1$, segment-tagged muons with $\lvert\eta\rvert < 0.1$ Stand-alone and silicon-associated forward restricted to the $2.5 < \lvert\eta\rvert < 2.7$ region Combined, stand-alone (with ID hits if available) and segment-tagged muons with $p_T > 5$ GeV Interaction point constraint: $\lvert d_0\rvert < 1$ mm and $\lvert z_0 \cdot \sin\theta\rvert < 0.5$ mm (if ID track is available)	
Jets	
anti-k_T jets with *bad-loose* identification, $p_T > 30$ GeV and $\lvert\eta\rvert < 4.5$ Jets with $p_T < 60$ GeV and $\lvert\eta\rvert < 2.4$ are required to pass the pile-up jet rejection at the 92% working point (JVT score ¿ 0.59). Jets with $p_T < 50$ GeV and $\lvert\eta\rvert > 2.5$ are required to pass the forward pile-up jet rejection at the 90% working point.	
b-tagging	
Previously selected jets with $\lvert\eta\rvert < 2.5$ are assigned a b-tagging weight by the `MV2_c10` algorithm	
overlap removal	
Jets within $\Delta R < 0.2$ of an electron or $\Delta R < 0.1$ of a muon are removed	
Event Selection	
Quadruplet Selection	- Require at least one quadruplet of leptons consisting of two pairs of same-flavour opposite-charge leptons fulfilling the following requirements: - p_T thresholds for three leading leptons in the quadruplet: $20, 15$ and 10 GeV - At most 1 calo-tagged, stand-alone or silicon-associated muon per quadruplet - Leading di-lepton mass requirement: $50 < m_{12} < 106$ GeV - Sub-leading di-lepton mass requirement: $m_{\text{threshold}} < m_{34} < 115$ GeV - $\Delta R(\ell, \ell') > 0.10$ for all lepton pairs in the quadruplet - Remove quadruplet if alternative same-flavour opposite-charge di-lepton gives $m_{\ell\ell} < 5$ GeV - Keep all quadruplets passing the above selection
Isolation	- Contribution from the other leptons of the quadruplet is subtracted max(ptcone20_TightTTVA_pt500, ptvarcone30_TightTTVA_pt500) $+ 0.4 \cdot$ neflowisol20/$p_T < 0.16$ (Variables defined in the text below)
Impact Parameter Significance	- Apply impact parameter significance cut to all leptons of the quadruplet - For electrons: $d_0/\sigma_{d_0} < 5$ - For muons: $d_0/\sigma_{d_0} < 3$
Best Quadruplet	- If more than one quadruplet has been selected, choose the quadruplet with highest Higgs decay ME according to channel: 4μ, $2e2\mu$, $2\mu2e$ and $4e$
Vertex Selection	- Require a common vertex for the leptons: - χ^2/ndof < 6 for 4μ and < 9 for others decay channels

Table 4.3: Summary of the event selection requirements. The two lepton pairs are denoted as m_{12} and m_{34}. (The choice of the threshold value $m_{threshold}$ for m_{34} can be found in the text.)

4.3.5 Isolation

Past versions of the isolation selection relied on two variables, ptvarcone (or track isolation), the sum of the p_T of the tracks surrounding the lepton from the same vertex in a cone whose size depended on the p_T of the particles (if the cone size is not allowed to vary, then the quantity is called ptcone), and topoetcone (or calorimeter isolation), the sum of the E_T of the topoclusters within a cone surrounding the lepton, both of which are then scaled by the inverse of the lepton p_T [132]. (In both cases, the radius of the cone – or the underlying radius, in the case of ptvarcone – could be adjusted as desired.) However, both variables are vulnerable to pileup. In the case of ptvarcone (or ptcone), this is because of the additional tracks in the event. The definition of this variable used in previous analyses attempted to limit the tracks used in the calculation to those from the vertex via a loose requirement of $|z_0 \sin(\theta)| < 3$: in the new pileup regimes of 2017 and 2018 data-taking, this cut proved to be too loose. By adding a requirement that the track be used in determining the vertex, or that, if not, it both pass the cut on $|z_0 \sin(\theta)|$ and not be used in determining any other vertex, the track isolation can be made largely isolation-robust in the regime that we are dealing with here. The resulting variable is referred to as pt(var)cone[cone]_TightTTVA_pt[p_T cut], where cone is the conesize and p_T cut is the cutoff for including tracks in the calculation: here, we use a cutoff of 500 MeV.

Removing isolation dependence from calorimeter isolation is more difficult. In previous analyses, the calculation of the topoetcone associated to a given particle attempted to account for the effect of pileup by subtracting an average pileup contribution, calculated over the entire detector. But the increasing energy density of events with pileup leads to an increase in the RMS of the topoetcone, increasing the likelihood the pileup fluctuations will not be accounted for by the pileup correction and thus that leptons will be incorrectly rejected. One possible method of improving pileup-robustness in this case is to use the particle-flow method of reconstructing particles to calculate calorimeter isolation as well. The main advantage this brings is a more coherent method of assigning clusters to tracks, which occurs as part of the particle-flow reconstruction process. Improved track-cluster association allows for better determination of the raw value of the E_{T} in the cone, and using particle-flow jets to calculate the pileup correction provides a further improvement: the resulting variable is referred to neflowisol[cone], where cone is the cone sized used.

Note that the standard isolation calculation includes a correction to remove other leptons from consideration, so that if two otherwise isolated leptons are close together they do not cause each other to fail the selection. As the method of applying this correction is not available for selections during the tests described below, a requirement of $\Delta R > 0.3$ between leptons was imposed to ensure that no lepton fell within the cone of any other lepton. For the final results, of course, this is not necessary.

In an attempt to determine the best isolation working point for the analysis, balancing signal efficiency, background rejection, and pileup robustness, a number of possible selections were considered, as shown in Table 4.4. There are three general types of selections. The simplest ones are the TrackOnly versions: these are based on the fact that the track isolation is much more pileup-robust than the calorimeter isolation is. Two versions are included to allow the balance between efficiency and significance to be checked.

Next come the more familiar mixed working points. FixedCutLoose is the working point used in previous analyses; FixedCutHighMuLoose updates this working point to loose the more pileup-robust version of ptvarcone; FixedCutPflowLoose uses a triangular cut to combine the new ptvarcone and the pflow calorimeter isolation variable, neflowisol, into a single selection. One approach to optimizing these cuts is to do a scan for the highest significance (as isolation selections are not expected to help remove the irreducible ZZ^* background, it is not considered here.) The scan was performed only on track isolation, as it has a much stronger effect than calorimeter isolation, on simulated signal samples for each of the main signal types.

The final choice of isolation selection, however, can only be made after carrying out the full data-driven reducible background calculation (see Section 4.4 for details): optimizations based on simulation point us in the right direction, and scans using the full calculation would not be feasible, but the final impact of the selections can only be gauged by comparison to the real background calculation. For the

Name	Requirement
FixedCutLoose	electron: topoetcone20 < 0.2 && ptvarcone20 < 0.15 muon: topoetcone20 < 0.3 && ptvarcone30 < 0.15
FixedCutLoose0p1	FixedCutLoose with the ptvarcone cuts reduced to 0.1
FixedCutHighMuLoose	topoetcone20 < 0.30 && ptvarcone30_TightTTVA_pt1000 < 0.15
TrackOnly0p15	ptvarcone30_TightTTVA_pt1000 < 0.15
TrackOnly0p20	ptvarcone30_TightTTVA_pt1000 < 0.2
FixedCutPflowLoose	ptvarcone30_TightTTVA_pt500 + 0.4 · neflowisol20 < 0.16
FixedCutPflowLoose0p1	ptvarcone30_TightTTVA_pt500 + 0.4 · neflowisol20 < 0.1
FixedCutPflowLoose0p3	ptvarcone30_TightTTVA_pt500 + 0.4 · neflowisol20 < 0.3
Tri_HighMuLoose500	bump: topoetcone20 / 0.45 + ptvarcone30_TightTTVA_pt500 / 0.13 < 1 bar: topoetcone20 < 0.5
Tri_HighMuLoose	bump: topoetcone20 / 0.38 + ptvarcone30_TightTTVA_pt1000 / 0.15 < 1 bar: topoetcone20 < 0.5
Tri_PflowLoose	bump: newflowisol20 / 0.42 + ptvarcone30_TightTTVA_pt500 / 0.14 < 1 bar: newflowisol20 < 0.3
Tri_PflowLoose1000	bump: newflowisol20 / 0.45 + ptvarcone30_TightTTVA_pt1000 / 0.13 < 1 bar: newflowisol20 < 0.3

Table 4.4: Summary of the possible isolation cuts considered.

definition of background categories used in data-driven calculation see Section 4.4.5 and Section 4.4.2. Due to the fact that these are experimental working points, they do not have the overlap removal that ensures that one lepton in a quadruplet is not counted as part of the isolation of other members of the quadruplet implemented: therefore, a slightly larger ΔR cut of 0.3 is imposed here to avoid this possibility. This should result in an overall decrease in efficiency in these studies, but the goal is to compare potential working points, and they should all be effected to the same extent. Table 4.5 shows the yield of the reducible background and the associated significance, in the llee channels for the most promising isolation selections, and Table 4.6 the same for ll$\mu\mu$, both for $115 < m_{4l} < 130$ GeV. As a further check, Table 4.7 shows the significance obtained in each of the categories used in the previous couplings analysis in the llee final state over the full $m_{4\ell}$ mass range: as the isolation will have a different impact in categories that are more or less busy, it's important to confirm that isolation selections which work well in the dominant 0-jet category are also successful in other categories.

As a result of all these studies, the FixedCutPflowLoose working point was chosen, as having the best or close to the best performance in all the tests.

Isolation selection	Signal	Fakes	Gammas	Heavy Flavor
FixedCutLoose	20.43	1.10	0.26	0.27
FixedCutPflowLoose	21.13	0.76	0.17	0.17
FixedCutPflowLoose0p3	24.07	1.52	0.30	0.44
TrackOnly0p15	22.65	1.37	0.24	0.26
TrackOnly0p20	23.66	1.58	0.26	0.32
Tri_HighMuLoose	22.58	1.17	0.23	0.22
Tri_PflowLoose1000	20.98	0.77	0.19	0.22

Table 4.5: Yields and significances for various isolation selections using the $\ell\ell ee$ reducible background calculation (signal taken from MC simulation).

Isolation selection	Signal	$t\bar{t}$	Z+jets
FixedCutLoose	34.027	0.260	1.230
FixedCutPflowLoose	35.811	0.329	1.841
FixedCutPflowLoose0p3	40.499	0.890	3.328
Tri_PflowLoose1000	35.488	0.258	1.588
Tri_HighMuLoose	35.995	0.219	1.731
TrackOnly0p20	39.653	0.778	2.925

Table 4.6: Yields and significances for various isolation selections using the $\ell\ell\mu\mu$ reducible background calculation (signal taken from MC simulation).

Category	FixedCut Loose	FixedCut PflowLoose	FixedCut PflowLoosep3	TrackOnly 0p15	TrackOnly 0p20	Tri_High MuLoose	Tri_Pflow Loose1000
0-jet $p_T^{4l} < 100$ GeV	3.05	**3.87**	2.96	3.4	3.04	3.45	3.84
0-jet $p_T^{4l} > 100$ GeV	**0.06**	**0.06**	**0.06**	**0.06**	0.05	**0.06**	**0.06**
1-jet $p_T^{4l} < 60$ GeV	1.91	**2.38**	1.88	2.09	1.91	2.12	2.35
1-jet $60 < p_T^{4l} < 120$ GeV	1.52	**1.87**	1.54	1.67	1.57	1.7	1.83
1-jet $p_T^{4l} > 120$ GeV	0.74	**0.86**	0.77	0.79	0.74	0.8	0.85
2-jet VH-enriched	1.21	**1.47**	1.19	1.28	1.18	1.29	1.41
2-jet VBF-enriched $p_T^{j1} < 200$ GeV	1.56	**2**	1.57	1.71	1.58	1.73	1.96
2-jet VBF-enriched $p_T^{j1} > 200$ GeV	**0.09**	**0.09**	0.08	0.08	0.08	0.08	0.08
VH-leptonic	1.07	1.05	**1.15**	1.11	1.14	1.1	1.04
ttH-enriched hadronic	0.59	**0.7**	0.56	0.59	0.52	0.62	0.69
ttH-enriched leptonic	0	0	0	0	0	0	0

Table 4.7: Significances for various isolation selections using the llee reducible background calculation in each category from the 2017 couplings analysis. The best significance in each category is marked in bold (with the exception of the ttH-enriched leptonic category, where the reducible background is negligible).

4.4 Background estimation

The backgrounds to be considered in the $H \to ZZ^* \to 4\ell$ analysis are the $pp \to ZZ^*$ production (which has exactly the same topology as the signal and has been historically referred to as the "irreducible background"), the reducible ones from Z+jets (comprised of both heavy- and light-flavour jets) and top-quark pair and WZ production, and finally minor backgrounds with four or more correctly identified isolated leptons such as tribosons and all-leptonic $t\bar{t}$+Z. The methods by which these components are estimated are described below.

4.4.1 Background Processes

These processes, of which ZZ^* production via $q\bar{q}$ annihilation is the main one, constitute the largest background for this analysis. In past iterations of the analysis, their contribution to the background was estimated from MC simulation, taking advantage of the fact that the final state consists solely of isolated leptons of good quality. However, with increasing data comes the possibility of obtaining the normalization for some or all of these processes, in particular the dominant $q\bar{q} \to ZZ^*$ component, using a data-driven approach. The method involves adding a normalization factor for the $qqZZ$ estimation to the fit, using constraints from the mass sideband in the signal region. This has the advantage of removing the theoretical systematic uncertainties on the $qqZZ$ normalization, as well as the luminosity systematic uncertainty. The contribution to the ZZ^* background from gluon fusion can also be estimated using this method, or taken from simulation. The contribution of other four-lepton backgrounds can estimated in this fashion as well in the couplings analysis, as there are categories in which they are significant enough to make it worthwhile: this applies mainly to ttV in ttH categories. Otherwise, these backgrounds – in addition to those mentioned above, the other relevant ones are triboson processes (ZZZ, WZZ, and WWZ) – are taken directly from MC simulation.

For the reducible background processes which contain fake and non-isolated leptons, the simulation is not as robust in the determination of selection efficiencies and is also subject to sizable theoretical uncertainties (e.g. from fragmentation). Thus to estimate their contribution different approaches are followed using input from data where possible. The following sections describe the data-driven reducible background estimation techniques and checks performed in different final states. The general procedure is as follows:

- The background composition and shapes are studied in special control regions (CR) constructed by relaxing or inverting selections and/or lepton identification requirements. The higher statistics in the control regions permit several distributions to be compared between data and simulation.

- The expected background in the signal region (SR) is computed by extrapolating from the control region using transfer (also referred to as extrapolation) factors. These factors are normally determined based on the efficiency of the relaxed or inverted selection criteria in the given control regions, but they can also be calculated by the ratio of the expected yields between the control and signal regions.

Since the dominant background components vary according to the flavour of the leptons of the subleading pair, the background analysis is performed separately for the Z+$\mu\mu$ and Z+ee final states, estimating the "muon" and "electron" backgrounds, respectively. The muon background comes mostly from heavy-flavour jets produced in association with a Z boson or in $t\bar{t}$ decays. The electron background also has a large contribution from light-flavour jets produced in association with a Z boson that are misidentified as electrons.

In the following, the methods for background estimation in the $Z + \ell\ell$ channels are discussed in detail and the corresponding results are quoted. Additionally, after the normalization for the reducible background components is obtained for the inclusive selection, the methodology for splitting the estimates in each analysis category and extracting the shapes for various observables is discussed.

4.4.2 Data Driven estimation of Z+$\mu\mu$ background

In the Z+$\mu\mu$ final state, there are several sources of background. The dominant contribution is from Z production accompanied by leptons from semi-leptonic decays of heavy flavour hadrons. There is a smaller contribution from Z production accompanied by leptons from in-flight decays of π/K from light-flavour jets. The sum of these two components is denoted as Z+jets. Another contribution is coming from top quark pair production $t\bar{t}$ and diboson production WZ.

Methodology

To estimate the muon backgrounds, the baseline "global fit" method, in which multiple control regions enhanced in each of the different sources of background are built and fitted to estimate the contribution of each background component, is employed.

Below is a brief description of each control region used in the fits.

1. Inverted d_0 CR (enhanced in heavy-flavour jets)
   The standard four-lepton analysis selection is applied to the leading dilepton and the vertex cut is not applied on the quadruplet. The subleading dilepton pair has the d_0 significance selection inverted for at least one lepton in the pair and the isolation selection is not applied. This control region is enhanced in Z+HF and $t\bar{t}$ since leptons from heavy-flavour hadrons are characterised by large d_0 significance.

2. $e\mu$+$\mu\mu$ CR (enhanced in $t\bar{t}$)
   In this control region an opposite-charge different-flavour leading dilepton is required, and it must pass the standard four-lepton analysis selections. In this way the leading lepton pair cannot originate from a Z boson decay, guaranteeing a clean $t\bar{t}$ CR. The vertex cut is not applied on the quadruplet. The subleading dilepton has neither the impact parameter significance nor the isolation selection applied, while both same and opposite charge leptons are accepted. This control region is dominated by the $t\bar{t}$ component.

3. Inverted isolation CR (enhanced in light-flavour jets)
   The standard four-lepton analysis selection is applied to the leading dilepton. The subleading dilepton pair is required to pass the d_0 significance selection but have at least one lepton failing the standard isolation selection. The vertex cut is applied. This control region aims to enhance the Z+LF over the Z+HF component by imposing the d_0 significance selection.

4. Same-sign (SS) CR
   The standard four-lepton analysis selection is applied on the leading dilepton. The subleading dilepton has neither the d_0 significance nor the isolation selection applied while the leptons are required to have same charge. This same-sign control region is not dominated by a specific background; all the reducible backgrounds have a significant contribution.

Note that each CR is orthogonal to the SR. In each CR, the standard quadruplet selections (with the possible exception of the vertex cut, as noted) are then applied to the quadruplets that are formed, and a single quadruplet is chosen for each event if multiple ones are possible. However, in the control regions the ME selection is not used regardless of the presence of additional leptons.

Additionally, a further CR, the Relaxed CR, is used in the estimation, though not in the fits. This is a higher-statistics CR obtained by applying the standard four-lepton analysis selection to the quadruplet, except that d_0 and isolation selections are not applied to the subleading lepton pair: the vertexing cut is also not applied. This CR is not orthogonal to the others and to the SR, therefore it is not included in the fit. Instead, since it has high statistics of all types of the reducible background, it is used to validate the normalisation of the background components after the fit.

The main principle of the method is that by fitting data to shapes obtained from MC in the CRs, we can obtain the normalization of each background component in the data. By expressing the result of the fit in the relaxed CR, we validate not only the result of the fit but also that the systematics that are profiled in this fit are under control. The yields of the background components in the relaxed CR are then extrapolated to the signal region by the application of transfer factors to account for selection efficiencies and other selection effects. The derivation of the transfer factors is performed either directly from the signal to relaxed region ratio denoted as TF_{SR}, or by using a control sample including $Z + \mu$ events denoted as $\mathrm{TF}_{Z\mu}$.

A simultaneous unbinned maximum likelihood fit is performed in the CRs on the distribution of the leading dilepton mass m_{12}, which allows a good separation of the Z+jets and $t\bar{t}$ components as the m_{12} distribution of the first forms a Z peak while the latter is non-resonant. The CRs used for the fit are chosen to be orthogonal both to each other and to the SR with no or minimal contamination from ZZ^* (and practically none from the Higgs signal). The $e\mu$+$\mu\mu$ CR is quite pure in $t\bar{t}$, while the inverted-d_0 CR provides a good discrimination of Z+HF and $t\bar{t}$ components. By including the other two CRs in the fit, we get a handle on the Z+LF component and constrain further the statistical uncertainties of all components.

The m_{12} distribution of events in the CRs for data and MC simulation of the various backgrounds is shown in Figure 4.2. This figure demonstrates how the chosen CRs can be used to discriminate the various background components and also the need for a data-driven procedure to correct for the observed mismatches.

Each background type in each CR is described by an analytical function obtained from a fit to MC distributions. The $t\bar{t}$ background shape is modelled by a 2$^{\text{nd}}$ order Chebyshev polynomial (parameters c_0, c_1) and has the same shape in all CRs. In the inv-d_0, inv-Iso and same-sign CRs, a Breit-Wigner (BW) function convolved with a Crystal Ball (CB) [133, 134] function (parameters μ, α, η_{CB}, σ_{CB} and m_Z) is used to describe the Z+HF and Z+LF jets resonant shape. In the $e\mu$+$\mu\mu$ CR, the Z+jets component cannot share the same *pdf* as the leading dilepton cannot originate from a Z decay but is instead formed from random opposite-flavour leptons in the event, so the non-resonant m_{12} distribution for Z+jets in this CR is modelled with a first order polynomial. The analytic expressions of the functions used for the various models are shown in Table 4.8.

Function	Expression
1st Pol.	$f(x) = Ax$
2nd Cheb. Pol.	$f(x) = Ax^2 + B$
Gauss	$f(x) = \frac{1}{\sigma\sqrt{2\pi}} e^{-\frac{1}{2}\left(\frac{x-\mu}{\sigma}\right)^2}$
Breit-Wigner	$f(x) = \frac{k}{(x^2-M^2)^2+M^2\Gamma^2}$
Crystal Ball	$f(x) = N \cdot \begin{cases} \exp(-\frac{(x-\bar{x})^2}{2\sigma^2}), & \text{for } \frac{x-\bar{x}}{\sigma} > -\alpha \\ A \cdot (B - \frac{x-\bar{x}}{\sigma})^{-n}, & \text{for } \frac{x-\bar{x}}{\sigma} \leqslant -\alpha \end{cases}$

Table 4.8: Model functions analytic expression.

Contributions from WZ and ZZ^* events that fail the nominal selections and end up in the background control regions are small and are included in the Diboson component. It also incorporates signal from Higgs and the minor ttV and VVV contributions. Its shape is similar to the Z+jets shape in every CR (since it mainly originate from Z boson decay), but there is also a tail, one that is increasingly visible with the lower value of the m_{34} cut introduced for this analysis. To account for the tail, the diboson contribution is modeled as

$$f \cdot G(m_{12}) + (1 - f) \cdot CBBW(m_{12}) \tag{4.1}$$

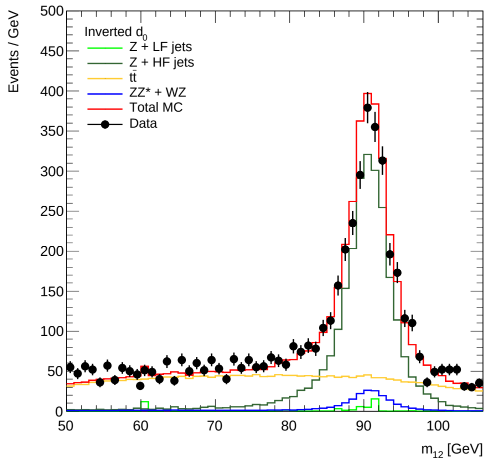

(a) inverted d_0 significance CR

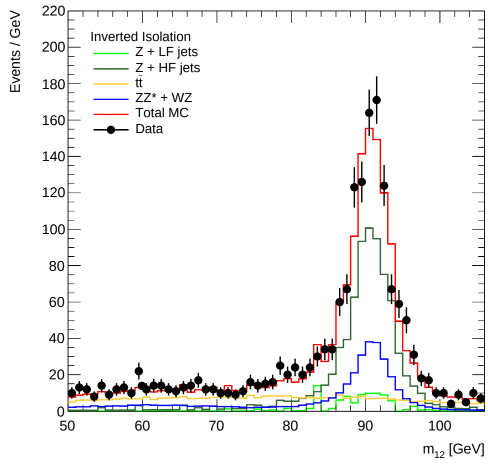

(b) inverted isolation CR

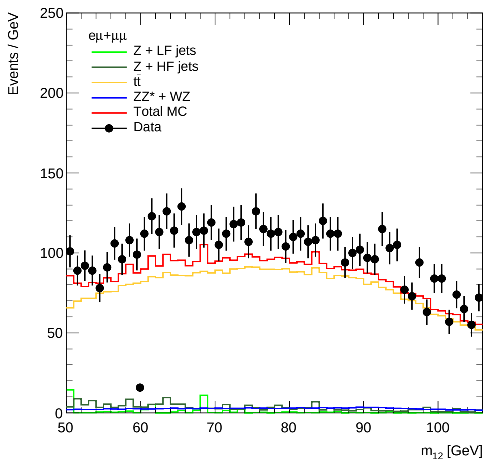

(c) $e\mu + \mu\mu$ CR

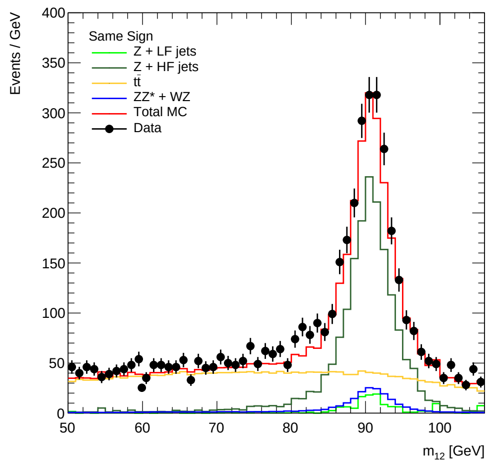

(d) same-sign CR

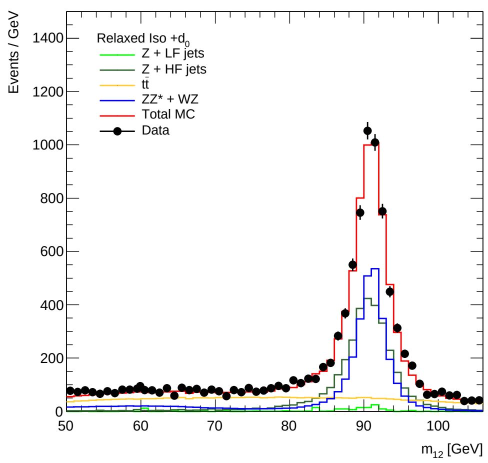

(e) Relaxed isolation & d_0 CR

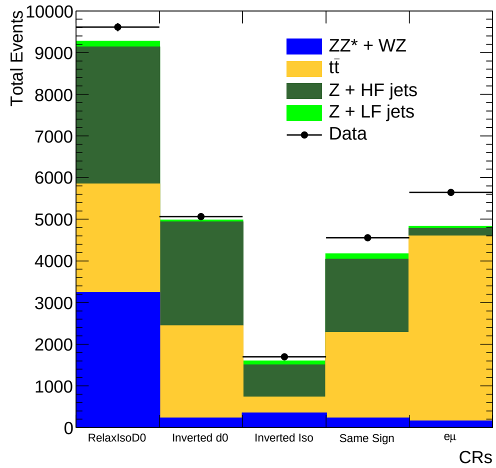

(f) Total observed and MC expected events in all CRs

Figure 4.2: Expected MC and data observed distributions of m_{12} in the (a) inverted-d0, (b) inverted isolation, (c) same-sign, (d) $e\mu$+$\mu\mu$ and (e) Relaxed isolation & d0 CR. The total number of MC expected and data observed events in each CR are shown in (f).

where G is a Gaussian and $CBBW$ is a CB-BW convolution and the fraction f is taken as the ratio of events with $m_{12} < 75$ GeV and $m_{12} > 75$ GeV (the tail and the peak, essentially). The Gaussian and CB-BW parameters are obtained by fitting the diboson component individually in the Relaxed CR and they are kept fixed during the main fit procedure. Table 4.9 shows the model of each component in each region and Table 4.10 shows the description of the shape and normalization parameters included in the the fit. The shape parameters may be free, fixed or constrained. Eventually, the yield (normalization) of the diboson events is taken from MC simulation. Minor contributions from ttV and VVV are also incorporated into what's referred to as the diboson sample, also using the MC prediction. The Higgs boson signal is also incorporated using its MC prediction: it has a marginal contribution in the CRs where the fit is done, but should be considered in the relaxed region validation plots.

	Relaxed Iso & d_0	Inverted Isolation	Inverted d_0	Same-sign	$e\mu$+$\mu\mu$
Z + LF jets	BW $*$ CB$_1$	BW $*$ CB$_1$	BW $*$ CB$_1$	BW $*$ CB$_1$	1st Poly
Z + HF jets	BW $*$ CB$_1$	BW $*$ CB$_1$	BW $*$ CB$_1$	BW $*$ CB$_1$	1st Poly
$t\bar{t}$	2nd Cheb	2nd Cheb	2nd Cheb	2nd Cheb	2nd Cheb
Diboson	BW $*$ CB$_2$ + G	BW $*$ CB$_2$ + G	BW $*$ CB$_2$	BW $*$ CB$_2$	1st Poly

Table 4.9: Models of each component in each Control Region.

Each *pdf* is a function of the shape parameters ($\boldsymbol{p}$). The total *pdf* in each Control Region is the sum of the individual components *pdf*s (M_{ij}). The Values of m_Z=91.1876 GeV and σ_{BW}=2.4952 GeV are given by theory and they are constant for all fits. The Z+HF, Z+LF and $t\bar{t}$ normalisation in each fitted CR is expressed in terms of the number of the total Relaxed CR events N_i for the i component using the fraction F_{ij} which bonds the Relaxed CR events with the events of the CR j. So for each fit CR the normalization of each component n_{ij} in each control region is given by

$$n_{ij} = N_j \cdot F_{ij} \tag{4.2}$$

N_j and F_{ij} are the parameters of interest in the fit, but note that the expression in the relaxed CR is used only as a cross-check of the fit result: the relaxed region is not actually used to constrain them. The fractions F_{ij} are initially obtained from the MC simulation and they are shown in Table 4.16. During the data fit they are constrained as they are not included as parameters but as gaussian functions with the MC expected value as mean and MC statistical error as sigma. This prevents large changes in their values. The 4 CR regions are simultaneously fitted by maximizing the likelihood of the product of the 4 CR models for the given datasets $\boldsymbol{x_i}$

$$\prod_i^{CR} \mathcal{L}\left(\sum_j^{comp} (N_j \cdot g_{ij}(F_{ij}, \sigma_{F_{ij}}) \cdot M_{ij}(\boldsymbol{p}) | \boldsymbol{x_i})\right) \to Max \tag{4.3}$$

The results of the relaxed region are extrapolated to the signal region using appropriate Transfer Factors. These are obtained from MC but due to lack of statistics in the Z+LF jets samples, and significant data-MC differences observed in the Z+μ control sample, the Transfer factor for Z+LF is taken from data using the $Z + \mu$ sample. Systematic uncertainties are assigned on the extrapolated yields in the SR due to the transfer factors. Apart from systematic uncertainties originating from the statistics of the MC samples (TF statistical error), additional (systematic) uncertainties are considered for the selection efficiencies. For Z+HF, uncertainties are assigned based on the differences observed in the Z+μ control sample between data and MC simulation. The same systematic is used for the ttbar TF. For Z+LF jets, uncertainties are assigned by varying the parameters used in the estimation of the TF. The way that the transfer factors are estimated is discussed in detail in Section 4.4.3.

Nuisance Parameter	Description	Fit status
c_0	First Chebyshev coefficient	free
c_1	Second Chebyshev coefficient	free
$\mu_{\rm CB}$	Crystal Ball mean for Z + jets	free
$\alpha_{\rm CB}$	Crystal Ball cutoff parameter for Z + jets	free
$\eta_{\rm CB}$	Crystal Ball exponent for Z + jets	free
$\sigma_{\rm CB}$	Crystal Ball width for Z + jets	free
b	Polynomial inclination	free
m_Z	Z mass used in the BW	constant
$\sigma_{\rm BW}$	Width of BW	constant
$\mu_{\rm CB}$	Crystal Ball mean for Diboson	fixed
$\alpha_{\rm CB}$	Crystal Ball cutoff parameter for Diboson	fixed
$\eta_{\rm CB}$	Crystal Ball exponent for Diboson	fixed
$\sigma_{\rm CB}$	Crystal Ball width for Diboson	fixed
μ_{DB}	Diboson gaussian mean	fixed
σ_{BD}	Diboson gaussian σ	fixed
f_i	Diboson fraction for $m_{12} < 75$ GeV in CR i	fixed (MC)

Parameter of Interest	Description	Fit status
F_{ij}	Fraction of i fitted component to j CR	constrained
N_i	Normalization of i fitted component	free

Table 4.10: Shape and normalization parameters for the various models and their status in the main fit procedure.

MC simulation of the Z+jets background requires huge statistics due to low probability for the jets to fake two leptons simultaneously, and such a statistics is simply not available due to limited computing resources. The problem was solved by applying 3- and 4-lepton filters at the generator level, which allow the rejection of a large fraction of the events which will not be selected even before passing them through the the whole simulation chain. This filter does not cut any interesting events from the heavy-flavour component (denoted Z+HF) since the heavy flavour hadron decay is treated inside the generator: thus all "fake" leptons are present already at the filter level. However, the light-flavour component (denoted Z+LF) is highly suppressed by the filter because π/K decay is treated within GEANT4 at the level of detector simulation, and so the "fake" leptons do not exist at the filter level. Due to this difficulty in simulating the Z+LF background, two additional, slightly different fit methods are used to validate the results. The first simply combines the Z+LF and Z+HF categories into a single Z+jets category, with the shape taken from Z+HF and a total Z+jets transfer factor used. This allows us to confirm that the results of estimating the individual Z+jets components are consistent with their total. This obtains a completely independent estimation of the Z+LF contribution and so provides a nice further confirmation of our main method. The description of the 3 methods is given below.

1. Standard Method
   In this method a 4 control region simultaneous fit is used. In order to improve the Z+LF estimation from the fit, the relative contribution of the Z+LF with respect to the dominant Z+HF jets background component is further enhanced in the inverted isolation and same-sign CRs, by exploiting the difference between HF and LF in the muon p_T balance, i.e. the balance between the p_T measurements in the inner detector and the muon spectrometer. Namely, at least one of the muons forming the secondary pair is required to satisfy $(p_T^{\rm ID} - p_T^{\rm MS})/p_T^{\rm ID} > 0.2$. For the Z+HF jets and $t\bar{t}$ the TF_{SR} are used. For the Z+LF jets component the transfer factor is $\mathrm{TF}_{SR[vtx]} \cdot \mathrm{TF}_{Z\mu[iso+d0]}$. The $\mathrm{TF}_{SR[vtx]}$ is just the vertex cut efficiency after applying

the isolation and d_0 cuts, it is to 86.39%. The statistical uncertainties for all the components come from the fit. The systematic uncertainty for Z+HF jets and $t\bar{t}$ is the squared sum of the MC statistical error and the transfer factor uncertainty $\delta\mathrm{TF}_{Z\mu[iso]}$. For the Z+LF jets the systematic uncertainty comes from varying the $\mathrm{TF}_{Z\mu[iso+d0]}$ estimation parameters.

2. Merged $Z + jets$
   In the second method the Z LF and HF jets components are merged. The merging enables to reduce the contribution of low statistics LF samples. The fit is performed again in all 4 control regions simultaneously, but without setting a p_T imbalance cut in Inverted Isolation and Same-Sign. For both Z jets and $t\bar{t}$ the TF_{SR} is used. The statistical uncertainties come from the fit and he systematic is the squared sum of the MC statistical error and the transfer factor uncertainty $\delta\mathrm{TF}_{Z\mu[iso]}$.

3. 2CR+1
   Lastly in this case the fit is performed in 2 stages. First the Inverted d_0 and the $e\mu + \mu\mu$ CRs are fitted and then the Inverted Isolation. In the Inverted Isolation the vertex cut is also applied to enable the direct extrapolation of Z + LF jets to signal region (without using the relaxed). The Same-Sign CR does not participate in the estimation. After the first stage of the fit, the $t\bar{t}$ component is normalized to the Data Driven estimation and it is kept fixed to this value for the second stage. The shape parameters of the models are also fixed, letting only the normalization parameters of Z jets to be fitted. In the first stage of the fit the Z + HF jets and $t\bar{t}$are estimated via the fit in the Inverted d_0 and $e\mu + \mu\mu$ correspondingly. The difference in Z + jets normalization in Inverted Isolation between the first and the second stage yields the Z + LF jets contribution. For the Z+HF jets and $t\bar{t}$ the TF_{SR} are used. For the Z+LF jets component the transfer factor is given by $TF_{Z\mu[InvIso]} = TF_{Z\mu[Iso]}/(1 - TF_{Z\mu[Iso]})$ accounting the extrapolation from Inverted Isolation to Relaxed CR and further from Relaxed to Signal Region. The statistical uncertainties for all the components come from the fit. The systematic uncertainty for Z+HF jets and $t\bar{t}$ is the squared sum of the MC statistical error and the transfer factor uncertainty $\delta\mathrm{TF}_{Z\mu[iso]}$. For the Z+LF jets the systematic uncertainty comes from varying the $\mathrm{TF}_{Z\mu[Iso]}$ estimation parameters.

Main Method

Prior to the main fit, the diboson shape is fitted individually in the Relaxed region 4.3 in order to obtain its shape parameters. Afterwards the values of the shape parameters 4.11 are kept fixed for all the fits in all 3 methods.

Shape Parameter	Description	Value
μ_{CB}	Crystal Ball mean for Diboson	0.432 GeV
α_{CB}	Crystal Ball cutoff parameter	0.958
η_{CB}	Crystal Ball exponent	18.9
σ_{CB}	Crystal Ball width	0.798 GeV
μ_{DB}	Diboson gaussian mean	58.1 GeV
σ_{BD}	Diboson gaussian σ	10.7 GeV
f_i	Diboson Fraction for $m_{12} < 75$ GeV in CR i	MC expectation

Table 4.11: Diboson shape parameters obtained by fitting the Relaxed CR.

In Table 4.16 and Table 4.13 the MC expected fractions F_{ij} and events n_{ij} for the main method are shown correspondingly.

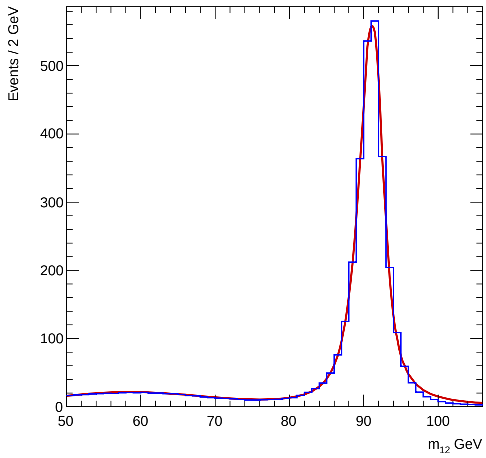

Figure 4.3: MC expected (red) and fitted (blue) Diboson distribution in Relaxed Isolation and d_0 CR.

	MC expectation		
F_i	Z+HF	Z+LF	$t\bar{t}$
inv.d_0/relaxed	0.760 ± 0.004	0.32 ± 0.55	0.851 ± 0.001
inv.iso/relaxed	0.040 ± 0.036	0.54 ± 0.18	0.023 ± 0.016
$e\mu$/relaxed	0.057 ± 0.053	0.34 ± 0.41	1.703 ± 0.003
ss/relaxed	0.095 ± 0.050	0.50 ± 0.23	0.098 ± 0.012

Table 4.12: Fractions F_i from each CR to the relaxed CR, expected from MC simulation, quoted with their statistical errors.

Events	Z+HF	Z+LF	$t\bar{t}$	Diboson	Data
Relaxed	3287 ± 24	140 ± 22	2605.3 ± 6.4	3235.3 ± 4.7	9612 ± 98
inv.d_0	2497 ± 19	45 ± 17	2218.3 ± 5.8	216.3 ± 1.3	5064 ± 71
inv.iso	132.0 ± 9.9	76 ± 13	59.6 ± 1.4	40.81 ± 0.72	333 ± 18
$e\mu$	312 ± 15	70 ± 11	255.7 ± 2.9	39.34 ± 0.71	832 ± 29
ss	186.9 ± 9.7	48 ± 18	4437.6 ± 8.5	150.9 ± 1.2	5642 ± 75

Table 4.13: MC expected and data observed events, quoted with their statistical errors.

MC closure test

The closure of each method is tested by applying the simultaneous fit procedure to MC produced (pseudo) data including all the relevant processes. The after-fit m_{12} distributions in each CR are shown in Figure 4.4 compared to the MC data in the four CRs, after the fit has been performed (top panels) along with the fit pulls (bottom panels). The number of events obtained from the fit for each fitted background component in each CR are shown in Table 4.14. Compared to the MC expected events from Table 4.13 they show good compatibility. Therefore the selected model describes efficiently the MC expected shapes. The MC Closure test parameter values are used as initial values for the data fit.

Events	Z+HF	Z+LF	$t\bar{t}$
Relaxed	3294 ± 97	132 ± 35	2607 ± 41
inv.d_0	2503 ± 74	42 ± 11	2220 ± 35
inv.iso	132.3 ± 3.9	72 ± 19	59.77 ± 0.94
ss	312.9 ± 9.3	66 ± 17	256.0 ± 4.0
$e\mu$	187.4 ± 5.5	45 ± 12	4442 ± 69

Table 4.14: MC Closure test events, quoted with their statistical errors.

Data fit result

Figure 4.5 shows the distribution of m_{12} for the contributing background components after fit on real Data. Figure 4.7(e) shows the comparison between the data and the background estimation of the fitting procedure expressed in the Relaxed region (reference region - validation plots). The comparison of the Data driven estimated events to the real observed data is also shown 4.7(f)
In Table 4.15 the values of the shape parameters obtained from fit on pseudo and real data are compared. Good compatibility is shown. In Table 4.16 the comparison of fraction F_{ij} obtained from fit on pseudo and real data is shown. There is also good compatibility among all three cases MC expectation, MC data, data as it is expected for the constrained parameters of the fit.

Nuisance Parameter	MC Closure test	Data Fit
c_0	-1.27e-01 ± 3.9e-02	-1.56e-01 ± 3.3e-02
c_1	-2.20e-01 ± 2.4e-02	-2.17e-01 ± 2.2e-02
μ_{CB}	-2.04e-01 ± 9.8e-02	-7e-02 ± 1.2e-01
α_{CB}	1.44e+00 ± 2.3e-01	1.20e+00 ± 2.3e-01
η_{CB}	2.5e+00 ± 1.1e+00	5.0e+00 ± 3.4e+00
σ_{CB}	1.92e+00 ± 1.2e-01	1.98e+00 ± 1.4e-01
b	-6.6e-03 ± 4.3e-03	-4.2e-03 ± 7.8e-03

Table 4.15: Shape parameters for various models: the Chebyshev (c_0, c_1) and Crystal Ball convoluted with a Breit-Wigner (μ_{CB}, α_{CB}, η_{CB}, σ_{CB}, m_Z and σ_{BW}) shapes. The values estimated from the fit to MC-simulated events are used as initial values for the data fit.

F_i	Z+HF		Z+LF		$t\bar{t}$	
	MC Closure	Data Fit	MC Closure	Data Fit	MC Closure	Data Fit
inv.d_0/relaxed	0.76	0.76	0.32	0.32	0.85	0.85
inv.iso/relaxed	0.040	0.040	0.54	0.45	0.023	0.023
ss/relaxed	0.095	0.097	0.50	0.64	0.098	0.098
$e\mu$/relaxed	0.057	0.057	0.34	0.34	1.7	1.7

Table 4.16: Comparison of fractions F_i from each fitted CR to the relaxed CR, estimated from the MC closure test and from data fit..

At last the number of events obtained from the fit on the real data is shown in Table 4.17.
The fit results together with the transfer factors and final SR estimates are summarized in Table 4.18.

In Table 4.18, the fit results are summarized. In the relaxed CR they are shown with their statistical uncertainty from the data. The transfer factors are shown with their statistical uncertainty, from the size of MC-simulated samples, and their systematic uncertainty (quadratically added), from the efficiency studies in the Z+μ control sample. In the Signal region both uncertainties are shown. The WZ contribution is taken from MC.

Events	Z+HF	Z+LF	$t\bar{t}$
Relaxed	2860 ± 110	277 ± 63	3074 ± 45
inv.d_0	2174 ± 84	86 ± 19	2617 ± 38
inv.iso	114.1 ± 4.4	116 ± 26	70.4 ± 1.0
ss	278 ± 11	172 ± 39	302.7 ± 4.4
$e\mu$	162.6 ± 6.3	93 ± 21	5236 ± 77

Table 4.17: Data fit events, quoted with their statistical errors.

Standard Method			
type	data fit	extrapolation factor [%]	SR yield
$t\bar{t}$	3074 ± 45	0.24 ± 0.02	$7.38 \pm 0.11 \pm 0.71$
Z+jets (HF)	2860 ± 110	0.43 ± 0.04	$12.39 \pm 0.48 \pm 1.11$
Z+jets (LF)	277 ± 63	1.08 ± 0.11	$2.98 \pm 0.68 \pm 0.30$
WZ	MC-based estimation		4.53 ± 0.52
Total			$27.28 \pm 0.84 \pm 1.44$

Table 4.18: Final $\ell\ell + \mu\mu$ background estimates in the relaxed region for each of the contributing background components, corresponding to the full m_{4l} range. The second column shows the extrapolation factors to the SR along with the corresponding uncertainties. The last column shows the estimates for the SR yields with both statistical and systematic uncertainties.

2e2μ - 4μ

The background yields are also derived in the 4μ and $2e2\mu$ channels by performing the fits and calculating the transfer factors separately for each channel. The separate estimation provides a good cross check of the method validity. Most of the analyses handle the 2e2μ - 4μ separately so the results for the individual channels are also provided. As their sum must be equal to the combined estimation the results are appropriately scaled. The fit is performed using the standard method again. All the m_{12} distributions are provided in Figure 4.6.

The fit results in the signal region before and after scaling, as well the individual sums are provided in Table 4.19. There is good agreement between the combined and the separate $2e2\mu$ and 4μ estimations.

	Z+HF	Z+LF	$t\bar{t}$	Total
4μ	$6.87 \pm 0.32 \pm 0.64$	$1.64 \pm 0.46 \pm 0.16$	$2.03 \pm 0.03 \pm 0.24$	$10.54 \pm 0.56 \pm 0.70$
$2e2\mu$	$5.48 \pm 0.26 \pm 0.52$	$1.15 \pm 0.30 \pm 0.11$	$5.40 \pm 0.08 \pm 0.54$	$12.02 \pm 0.40 \pm 0.76$
Sum	$12.35 \pm 0.41 \pm 1.01$	$2.79 \pm 0.54 \pm 0.28$	$7.42 \pm 0.09 \pm 0.71$	$22.56 \pm 0.69 \pm 1.34$
4μ Scaled	$6.90 \pm 0.32 \pm 0.64$	$1.76 \pm 0.49 \pm 0.18$	$2.01 \pm 0.03 \pm 0.24$	$10.67 \pm 0.58 \pm 0.70$
$2e2\mu$ Scaled	$5.50 \pm 0.26 \pm 0.52$	$1.23 \pm 0.32 \pm 0.12$	$5.37 \pm 0.08 \pm 0.54$	$12.09 \pm 0.42 \pm 0.76$
Sum Scaled	$12.39 \pm 0.41 \pm 1.06$	$2.98 \pm 0.58 \pm 0.30$	$7.38 \pm 0.09 \pm 0.71$	$22.76 \pm 0.72 \pm 1.35$
Combined	$12.39 \pm 0.48 \pm 1.11$	$2.98 \pm 0.68 \pm 0.30$	$7.38 \pm 0.11 \pm 0.71$	$22.76 \pm 0.84 \pm 1.35$

Table 4.19: Final estimates in the signal region $-$ corresponding to the full m_{4l} range $-$ for the $t\bar{t}$, Z+HF and Z+LF background components in each channel with both statistical and systematic uncertainties shown.

Merged Z + jets

The m_{12} distributions from the Merged Z + jets method are shown in Figure 4.7. The summary of the results from this method is in Table 4.20.

Merged Z + jets Method			
type	data fit	extrapolation factor [%]	SR yield
$t\bar{t}$	3077 ± 39	0.24 ± 0.02	$7.39 \pm 0.09 \pm 0.71$
Z+jets	3287 ± 72	0.43 ± 0.04	$14.23 \pm 0.31 \pm 1.27$

Table 4.20: Final $\ell\ell + \mu\mu$ background estimates in the relaxed region for each of the contributing background components, corresponding to the full m_{4l} range. The second column shows the extrapolation factors to the SR along with the corresponding statistical uncertainties. The last column shows the estimates for the SR yields with both statistical and systematic uncertainties.

2CR+1

Lastly the m_{12} distributions from the 2CR+1 method are provided shown in Figure 4.8. In this method the same-sign CR does not participate. Also the relaxed region cannot den used for validation as the LF component is extrapolated directly from the Inverted Isolation. The summary of the results from this method is in Table 4.21.

2CR+1 Method			
type	data fit	extrapolation factor [%]	SR yield
$t\bar{t}$	3111 ± 41	0.24 ± 0.02	$7.47 \pm 0.10 \pm 0.72$
Z+jets (HF)	2923 ± 87	0.43 ± 0.04	$12.66 \pm 0.38 \pm 1.13$
Z+jets (LF)	188 ± 42 (Δ_{InvIso})	0.0145 ± 0.0015	$2.71 \pm 0.59 \pm 0.27$

Table 4.21: Final $\ell\ell + \mu\mu$ background estimates in the relaxed region for each of the contributing background components, corresponding to the full m_{4l} range. The second column shows the extrapolation factors to the SR along with the corresponding statistical uncertainties. The last column shows the estimates for the SR yields with both statistical and systematic uncertainties.

Comparison & Conclusion

The different methods are compared in Table 4.22, all of them agree quite well. The Merged Z + jets method is expected to have a lower yield, as all the Z+jets events are extrapolated from the relaxed to the signal region using the HF Transfer factor, which is fairly smaller than this of LF. In any case the differences are within the errors which are provided. The standard method is preferred as it splits the LF and HF jets and uses more CRs to make the fit more accurate.

Method	Z+HF	Z+LF	$t\bar{t}$	Total
Standard	$12.39 \pm 0.48 \pm 1.11$	$2.98 \pm 0.68 \pm 0.30$	$7.38 \pm 0.11 \pm 0.71$	$22.76 \pm 0.84 \pm 1.35$
Std. $2e2\mu + 4\mu$	$12.35 \pm 0.41 \pm 1.01$	$2.79 \pm 0.54 \pm 0.28$	$7.42 \pm 0.09 \pm 0.71$	$22.56 \pm 0.69 \pm 1.34$
Merged Z+jets	$14.23 \pm 0.31 \pm 1.27$		$7.39 \pm 0.09 \pm 0.71$	$21.62 \pm 0.33 \pm 1.45$
2CR+1	$12.66 \pm 0.38 \pm 1.13$	$2.71 \pm 0.59 \pm 0.27$	$7.47 \pm 0.10 \pm 0.72$	$22.86 \pm 0.72 \pm 1.37$

Table 4.22: Comparison of the results in the signal region obtained from the various methods of estimating the background.

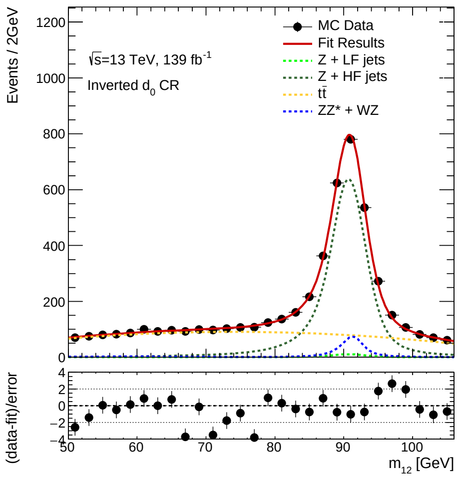

(a) inverted d_0 significance CR

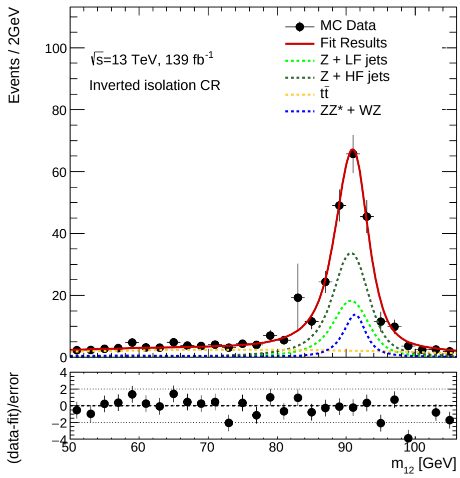

(b) inverted isolation CR

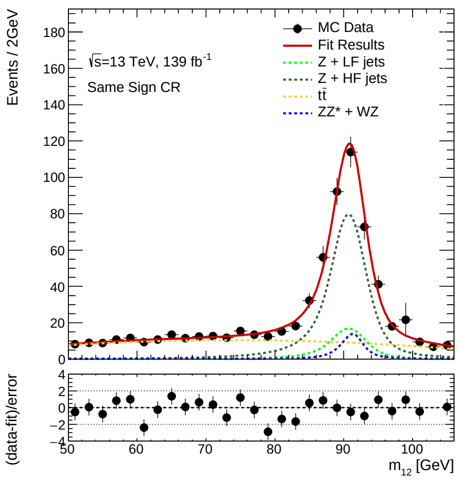

(c) same-sign CR

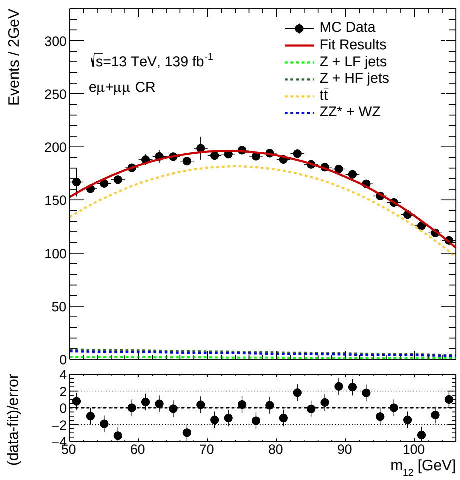

(d) $e\mu + \mu\mu$ CR

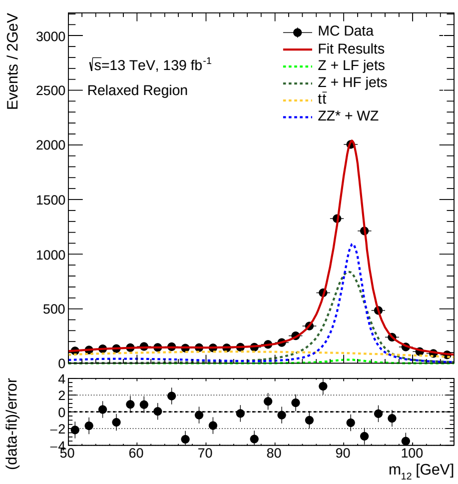

(e) Relaxed isolation & d_0 CR

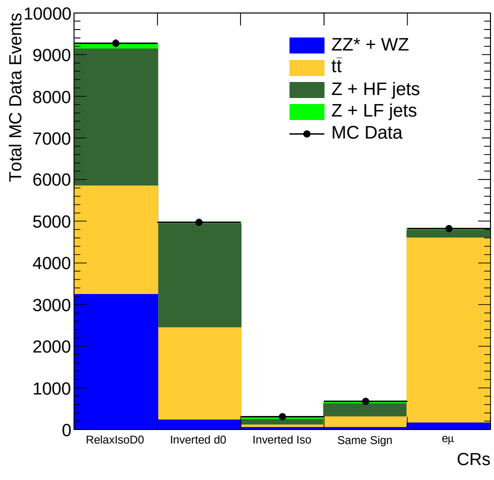

(f) Total observed and MC expected events in all CRs

Figure 4.4: Distributions of m_{12} from the MC Closure test in the (a) inverted-d0, (b) inverted isolation, (c) same-sign, (d) $e\mu$+$\mu\mu$ and (e) Relaxed isolation & d0 CR; the lower panels show the fit pulls. The total number of Data Driven estimated and MC pseudo events in each CR are shown in (f).

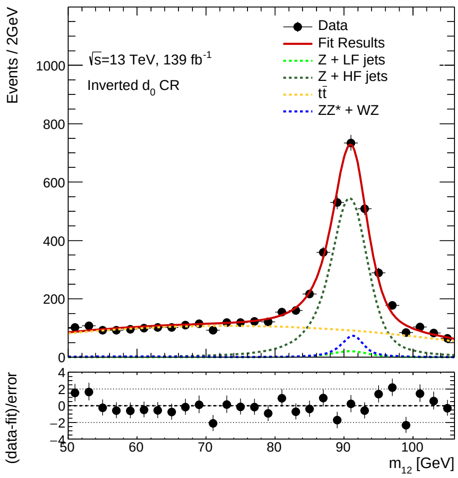

(a) inverted d_0 significance CR

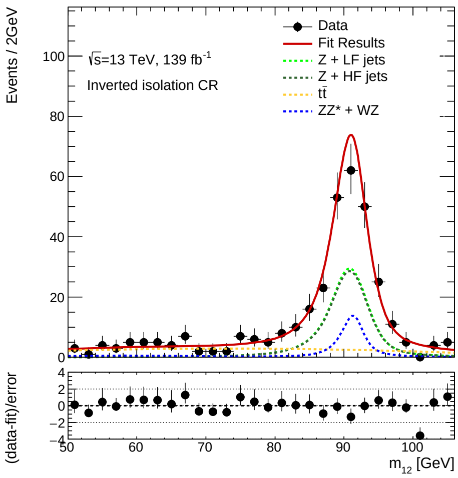

(b) inverted isolation CR

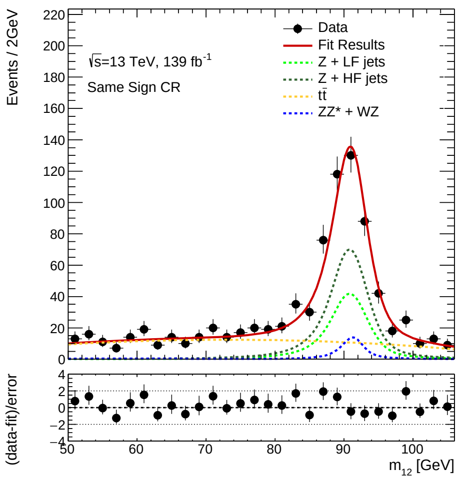

(c) $e\mu + \mu\mu$ CR

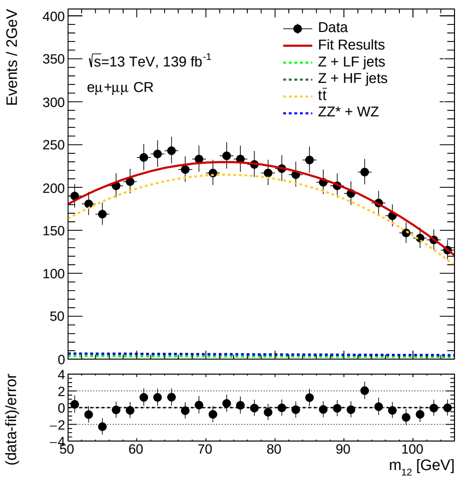

(d) same-sign CR

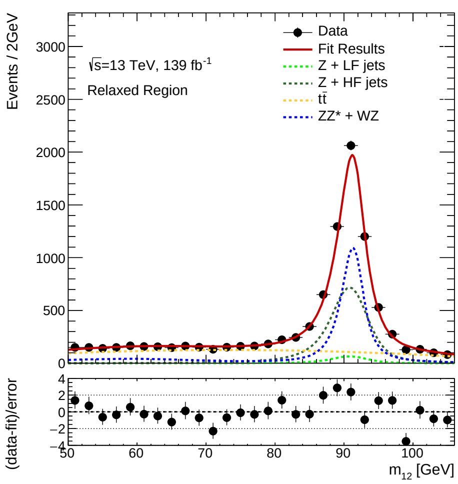

(e) Relaxed isolation & d_0 CR

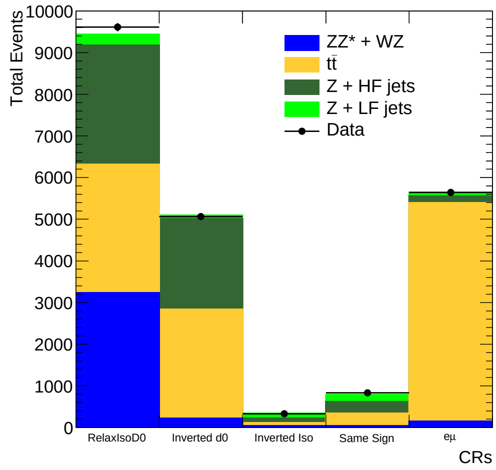

(f) Total observed and MC expected events in all CRs

Figure 4.5: Distributions of m_{12} in the (a) inverted-d0, (b) inverted isolation, (c) same-sign, (d) $e\mu$+$\mu\mu$ and (e) Relaxed isolation & d0 CR; the lower panels show the fit pulls. The total number of Data Driven estimated and data observed events in each CR are shown in (f).

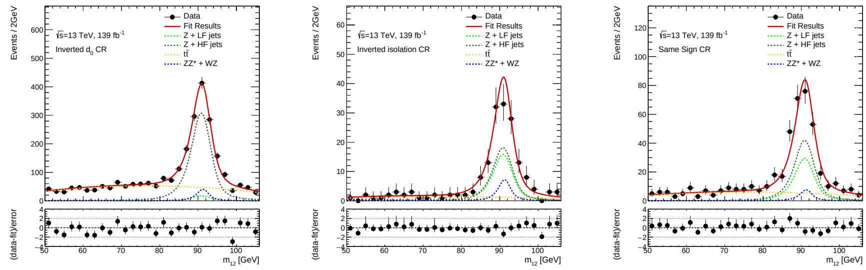

(a) inverted d_0 significance CR (b) inverted isolation CR (c) $e\mu + \mu\mu$ CR

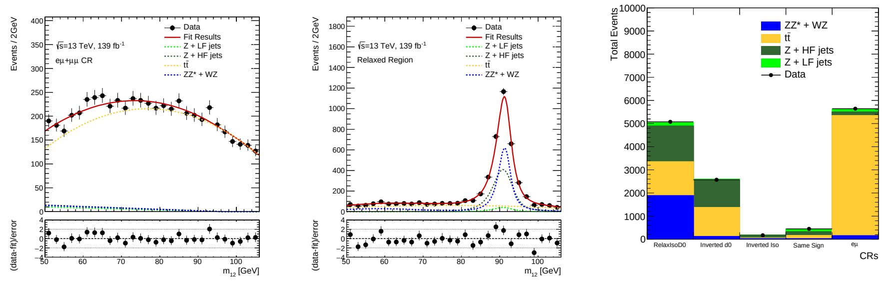

(d) same-sign CR (e) Relaxed isolation & d_0 CR (f) Total observed and MC expected events in all CRs

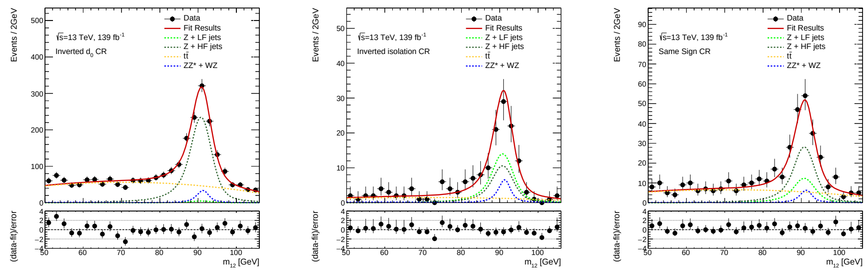

(g) inverted d_0 significance CR (h) inverted isolation CR (i) $e\mu + \mu\mu$ CR

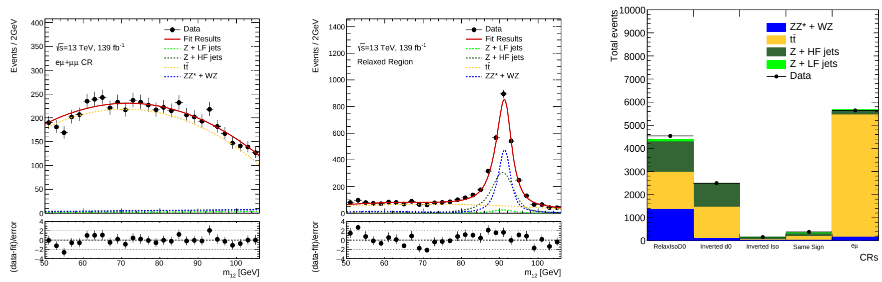

(j) same-sign CR (k) Relaxed isolation & d_0 CR (l) Total observed and MC expected events in all CRs

Figure 4.6: Distributions of m_{12} for 4μ and $2e2\mu$, channels in the (a , g) inverted-d0, (b, h) inverted isolation, (c, i) same-sign, (d, j) $e\mu$+$\mu\mu$ and (e, k) Relaxed & d0 CR isolation correspondingly; the lower panels show the fit pulls. The total number of Data Driven estimated and data observed events in each CR are shown in (f, l).

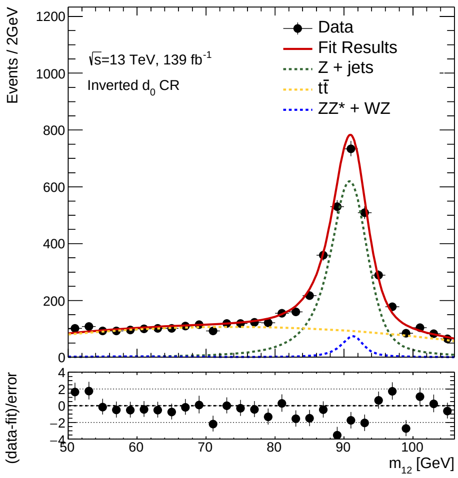

(a) inverted d_0 significance CR

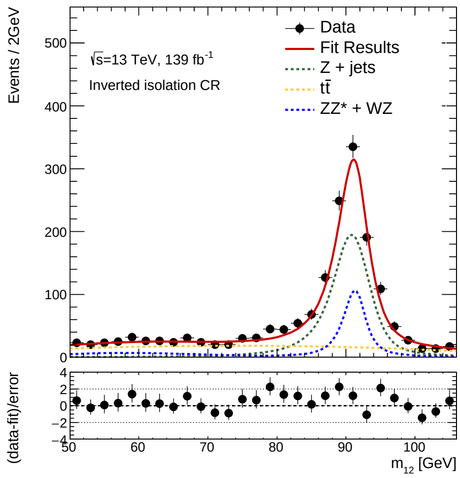

(b) inverted isolation CR

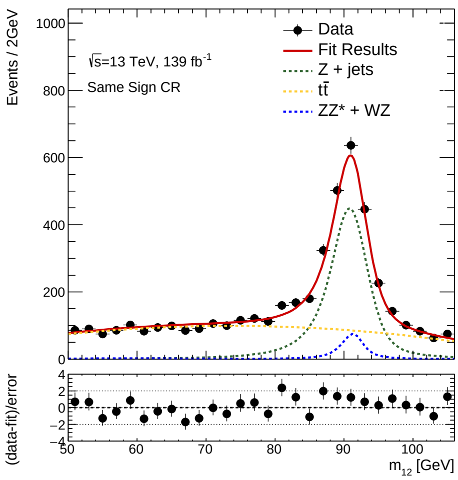

(c) $e\mu + \mu\mu$ CR

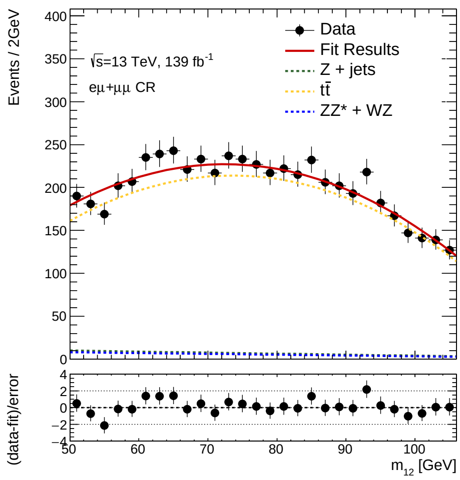

(d) same-sign CR

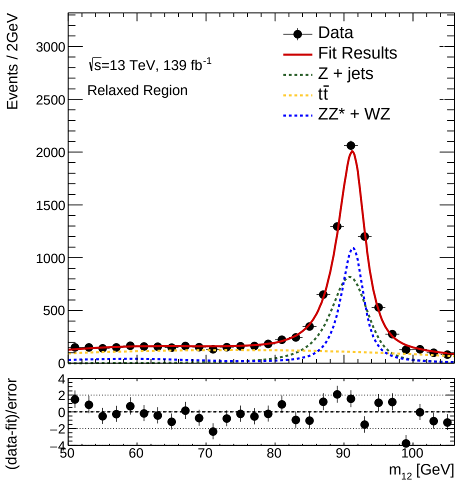

(e) Relaxed isolation & d_0 CR

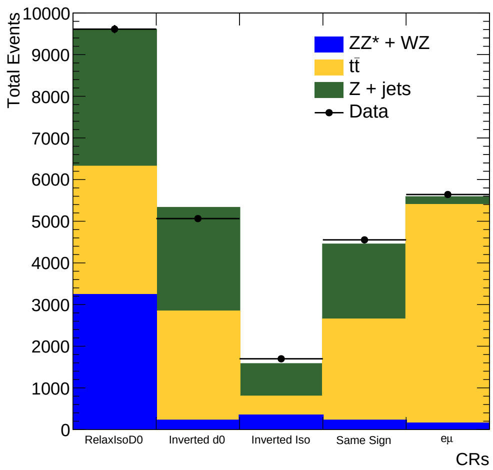

(f) Total observed and MC expected events in all CRs

Figure 4.7: Distributions of m_{12} of Merged Z + jets method in the (a) inverted-d0, (b) inverted isolation, (c) same-sign, (d) eμ+μμ and (e) Relaxed isolation & d0 CR; the lower panels show the fit pulls. The total number of Data Driven estimated and data observed events in each CR are shown in (f).

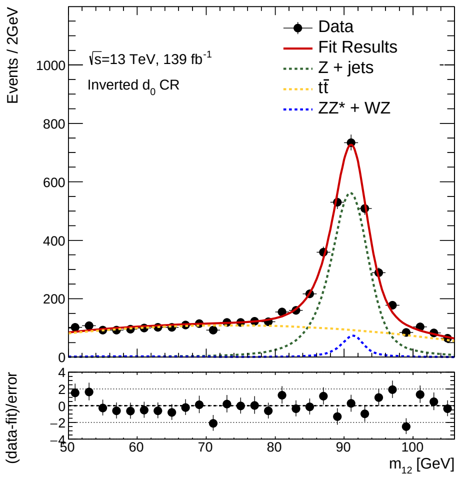

(a) inverted d_0 significance CR

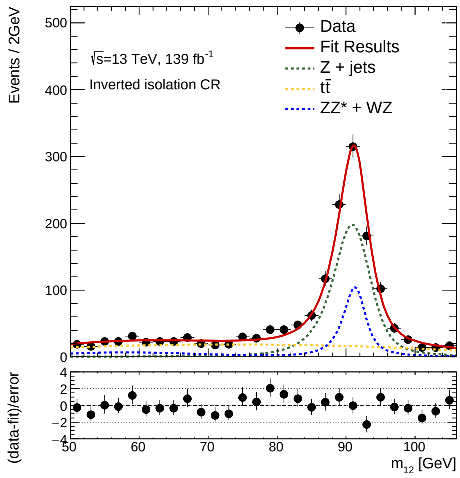

(b) inverted isolation CR (2nd fit)

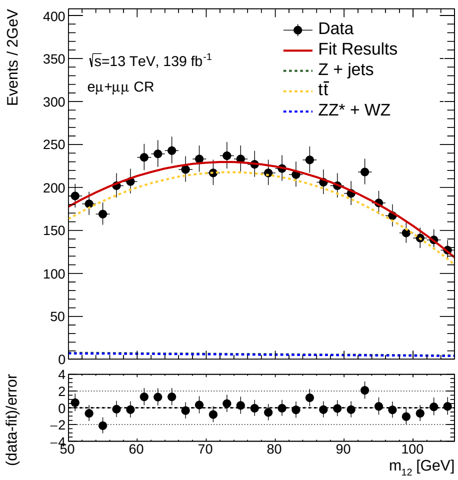

(c) $e\mu + \mu\mu$ CR

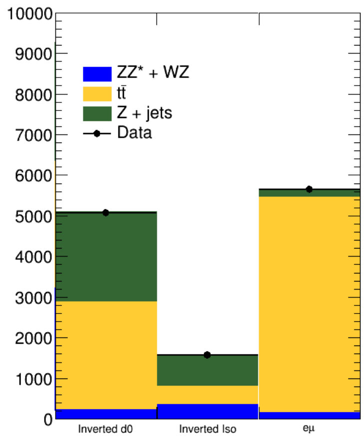

(d) Total observed and MC expected events in all CRs used for this method fit

Figure 4.8: Distributions of m_{12} of 2CR+1 method in the (a) inverted-d0, (b) inverted isolation (2nd fit) and (c) $e\mu$+$\mu\mu$; the lower panels show the fit pulls. The total number of Data Driven estimated and data observed events in each CR are shown in (d).

4.4.3 $Z+\mu$ control sample

The efficiency for muons initiated from background processes is studied with a sample of muons accompanying an on-shell Z decay to either electrons or muons. Events are collected with single- and dilepton triggers (Section 4.3.1); trilepton and e-μ triggers used in the nominal selection are dropped to avoid biasing the quality of the accompanying muon. The selection requires a reconstructed Z boson candidate formed based on the following steps (largely following the standard analysis selection). Pairs of oppositely-charged muons and electrons passing the nominal identification criteria are formed and required to have $p_T > 20$ GeV and 15 GeV for the leading and subleading lepton, respectively. If multiple pairs are found, the one with invariant mass closest to the Z pole is kept as the Z candidate. Z candidates in the invariant mass range $76 < m_{\ell\ell} < 106$ GeV are retained and standard isolation and impact parameter (d_0 significance) cuts on the Z leptons are imposed. Lastly, the Z leptons are required to be well separated, satisfying $\Delta R > 0.1$. Only events with exactly one additional muon with $p_T > 5$ GeV are retained. The additional muon is required to be well separated with respect to the Z leptons; a cut of $\Delta R > 0.1$ is applied, while the muon is excluded if it gives an invariant mass of less than 5 GeV when paired with another muon of the opposite sign. The invariant mass of the Z candidate for selected events in data and MC-simulated samples is shown in Figure 4.9(a). As expected, the sample is dominated by Z+jets production, with the accompanying muon originating from the decay of a heavy-flavour hadron in two thirds of the sample. Although diboson production, WZ in particular, contributes only 2.5% in total, it becomes more important the higher the p_T of the additional muon as shown in Figure 4.9(c). The muon type of the additional muon is also shown in Figure 4.9(b) After the nominal isolation and d_0 significance selections on the additional muon the contribution of WZ production goes up to 15%.

The fraction of events passing the isolation and impact parameter criteria over the total number of events provides an estimation of the efficiency of those selections for background muons (not coming from the decay of a W or Z boson). In this estimation the expected contamination of real isolated leptons from dibosons are subtracted using the MC simulation. The resulting efficiency is shown in Table 4.23. The efficiency of the d_0 significance cut is found to be in good agreement between data and simulation. For the isolation efficiency a difference of the order of 10% is observed and is studied separately for light- and heavy-flavour jets. For the purpose of calculating the systematic uncertainty on $t\bar{t}$ transfer factor, the HF-jets efficiency is used. The m_Z distributions after applying these selections on the additional muon are shown in Figure 4.10.

Selection applied	Data [%]	MC [%]	$\Delta/\epsilon^{\mu}_{MC}$
isolation	15.4 ± 0.03	14.7 ± 0.07	-5%
d_0 significance	64.40 ± 0.04	64.1 ± 0.10	-0.4%
iso+d_0 sig.	10.1 ± 0.03	9.1 ± 0.06	-11%

Table 4.23: Efficiency of isolation and impact parameter selections for background muons selected in $Z+\mu$ events. Data-MC efficiency differences divided by MC efficiency are also shown.

$Z+\mu$ light-flavour control sample

In order to study the behavior of the light-flavour component, a control sample is built using the momentum imbalance between the p_T measurements in the inner detector and the muon spectrometer ($\Delta p_T/p_T = (p_T^{\mathrm{ID}} - p_T^{\mathrm{MS}})/p_T^{\mathrm{ID}}$). Figure 4.11(a) shows this parameter for the muons accompanying the Z boson candidate in the $Z+\mu$ sample before the application of the isolation and impact parameter selection. The shoulder that appears at large values of the momentum balance variable is mainly coming from in-flight decays of light-flavour mesons (i.e. muons from π and K decays). Requiring $\Delta p_T/p_T > 0.1$, a control sample enriched in light-flavour is obtained: the resulting m_{12} distribution is shown in Figure 4.11(b). We also restrict this region to only combined muons, as other types are missing either ID or MS p_T values and so cannot be sorted using this method. A separate study of

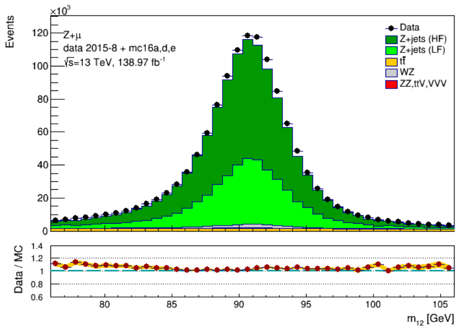

(a) Invariant mass of Z boson candidate

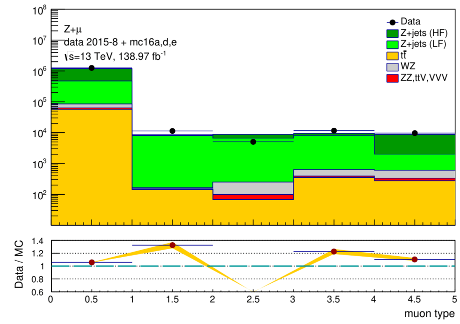

(b) Type of the additional muon

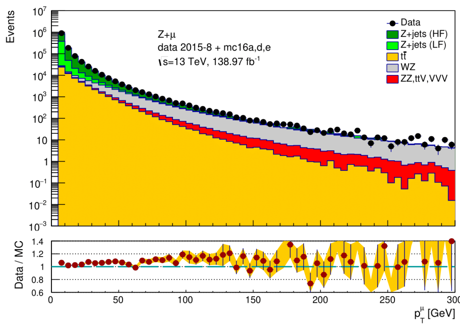

(c) Tranverse momentum of the addtional muon

Figure 4.9: Invariant mass of Z boson candidates (a), type (b) and p_T (c) of the additional muon in selected $Z+\mu$ events in data (points with errors) and MC-simulated background samples (stacked histograms) for the full Run2 dataset. In the lower panel, the Data/MC ratio appears, together with the ratio's statistical uncertainty.

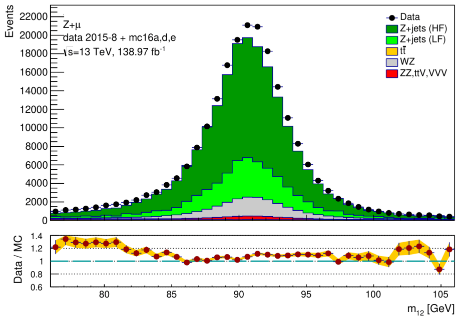

(a) Invariant mass of Z boson candidate after applying Isolation requirement

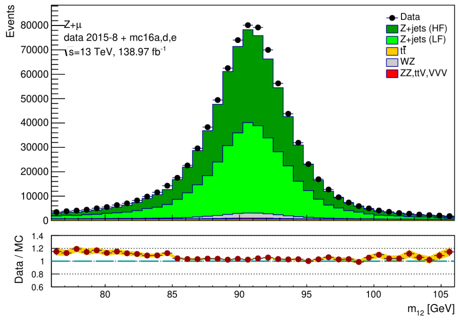

(b) Invariant mass of Z boson candidate after applying d_0 significance requirement

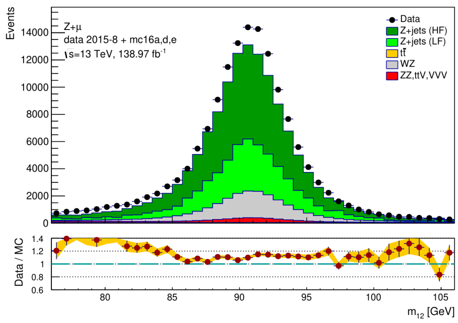

(c) Invariant mass of Z boson candidate after applying Isolation+d_0 significance requirements

Figure 4.10: Invariant mass of Z boson candidates after applying the (a) Isolation, (b) d_0 significance and (c) Isolation+d_0 significance cuts on the μ.

the efficiencies of these ”other” muons has been made, and their contribution has been taken into account, though minor.

According to simulation[2], 67% of the sample is made of light-flavour jets (Z+jets) and 32% of heavy-flavour jets (Z+jets and $t\bar{t}$). Contributions from WZ and ZZ^* are below 1% and are subtracted from the efficiency calculations using MC simulation. Owing to the relatively large heavy-flavour jet contamination in the light-flavour control sample, the expected contribution from Z+HF and $t\bar{t}$ is accounted for by simple subtraction of impurities as predicted by MC. To obtain the control region fraction systematic uncertainties described previously, the isolation efficiencies are calculated twice, once with respect to all muons in the light flavour enriched sample and once with respect to the muons passing the d_0-significance cut. The resulting isolation efficiencies, as well as the efficiency for a light-flavour jet to pass the nominal isolation and d_0-significance requirements are shown in Table 4.24. The m_Z distributions, for the LF enriched sample, after applying the selections on the additional muon are shown in Figure 4.12.

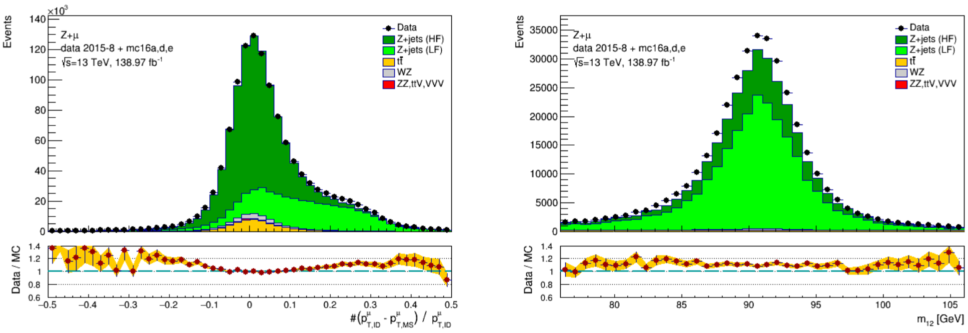

(a) Relative p_T imbalance between MS and ID for the additional μ

(b) m_Z for a light flavour enriched sample

Figure 4.11: Fractional p_T balance between the ID and MS measurements for additional muons in $Z+\mu$ events shown for data and MC simulation, and the m_{12} distribution in the light-flavor enriched CR. Requiring the fraction to be larger than 0.1, a sample enriched in light-flavour jets is obtained. The invariant mass of the Z boson candidates after this selection is also shown.

$Z+\mu$ heavy-flavour control sample

A heavy-flavour component can be crated by applying an inverted d_0-significance selection, cut on the additional muon, as it is shown in Figure 4.13(a). The invariant mass of Z boson candidates in the heavy-flavour control sample is shown in Figure 4.13(b). 93% of the sample is made of heavy-flavour jets and 6% of light-flavour jets. The expected contribution of leptons from dibosons is negligible and is subtracted with MC simulation from the efficiency calculations. In the scale factor calculation, the expected contribution from Z+LF jets and $t\bar{t}$ is also subtracted as predicted by the MC simulation. The m_Z distribution for the HF enriched sample, after applying the isolation cut is shown in Figure 4.14. The d_0 significance cut can not be applied in this case as it is orthogonal to the cut which is used to define this sample. The resulting isolation efficiency for a heavy flavour jet are shown in Table 4.24

Table 4.24 also shows the differences between efficiencies form data and MC simulation. For the HF sample an efficiency wrt d_0 significance cannot be defined as d_0 significance cut is orthogonal to the cut which is used to define this sample. The isolation efficiency of the LF enriched sample is quite different affecting also the Isolation + d_0 efficiency. On the contrary in the HF enriched sample, the

[2] Z+HF is defined as everything which passes the 3- and 4-lepton filtered samples and Z+LF anything which passes the BFilter, CFilterBVeto and CVetoBVeto samples after overlap removal with the filtered samples.

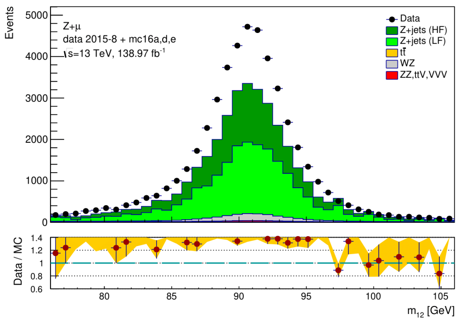

(a) Invariant mass of Z boson candidate after applying Isolation requirement

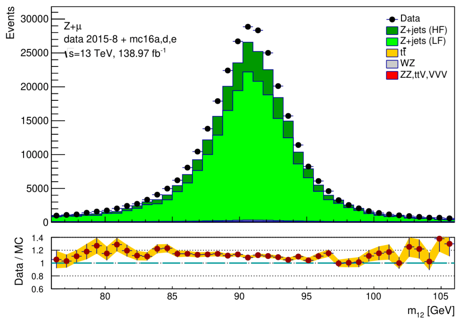

(b) Invariant mass of Z boson candidate after applying d_0 significance requirement

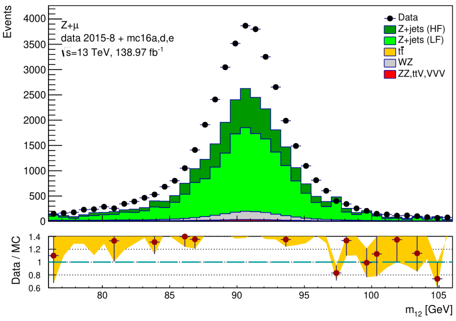

(c) Invariant mass of Z boson candidate after applying Isolation+d_0 significance requirements

Figure 4.12: Invariant mass of Z boson candidates for a LF enriched sample after applying the (a) Isolation, (b) d_0 significance and (c) Isolation+d_0 significance requirements on the μ.

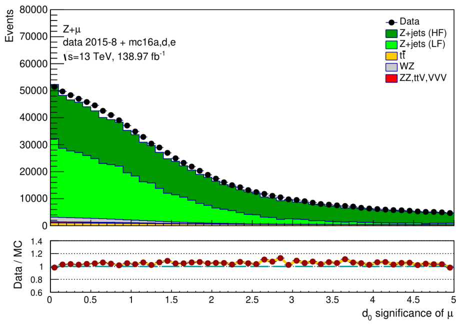

(a) d_0 significane of the additional μ

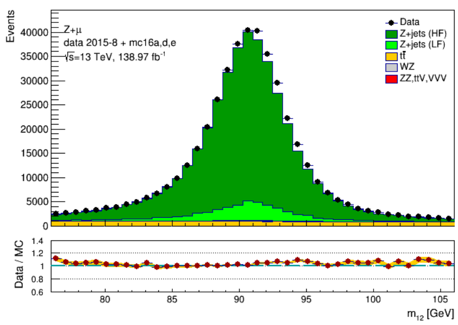

(b) m_Z for a heavy flavour enriched sample

Figure 4.13: Distribution of d_0 significance for additional muons in Z+μ events (left) for data and MC simulation. Requiring values of d_0 significance larger than 3 provides a sample enriched in heavy-flavour jets; the invariant mass of Z boson candidates after this selection is shown also.

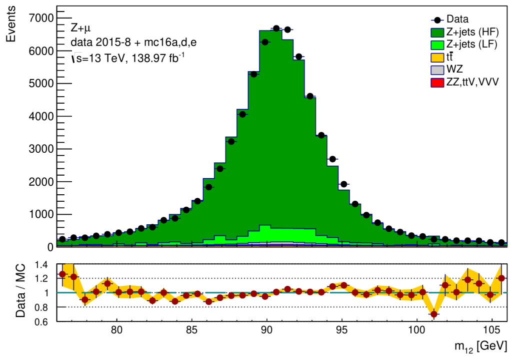

Figure 4.14: Invariant mass of Z boson candidates for a HF enriched sample after applying the Isolation requirement.

Selection (sample)	MC[%]	Data[%]	$\Delta/\epsilon^{\mu}_{MC}$
Isolation (LF)	8.0 ± 0.3	11.9 ± 0.09	-48%
d_0 significance (LF)	92.5 ± 0.3	91.6 ± 0.1	1.0%
Isolation + d_0 significance (LF)	7.5 ± 0.3	11.2 ± 0.09	-55%
Isolation after d_0 sig. (LF)	8.1 ± 0.3	12.2 ± 0.09	-51%
Isolation (HF)	17.1 ± 0.07	16.4 ± 0.09	4.3%

Table 4.24: Isolation and impact-parameter efficiencies for background muons in the light-flavour enriched and heavy-flavour enriched $Z+\mu$ sample, calculated using simple subtraction to account for impurities in the samples (for HF-enriched, only isolation efficiency is calculated, due to the way this sample is defined).

agreement between the isolation efficiencies calculated in data and MC simulation is quite good. The isolation variables for both LF and HF enriched samples are shown in Figure 4.15.

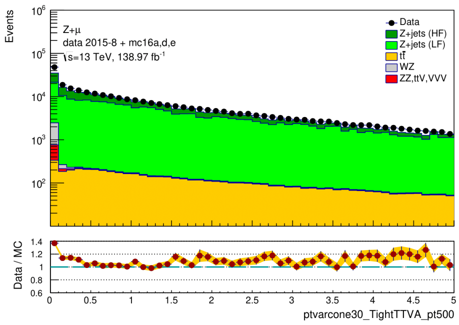

(a) $ptvarcone30\_TightTTVA\_pt500$

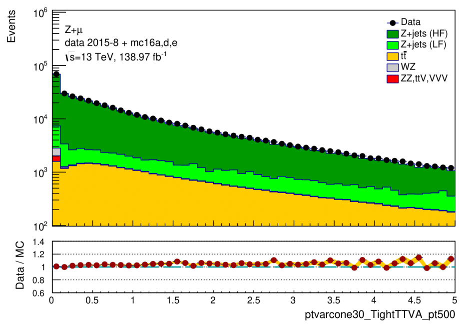

(b) $ptvarcone30\_TightTTVA\_pt500$

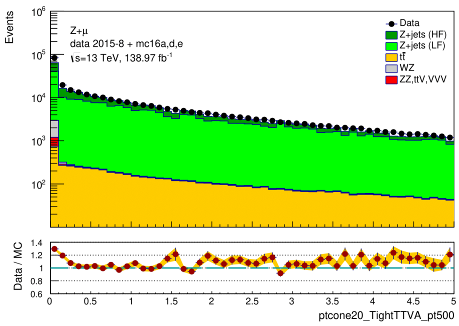

(c) $ptcone20\_TightTTVA\_pt500$

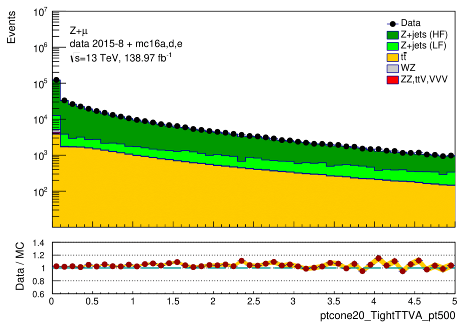

(d) $ptcone20\_TightTTVA\_pt500$

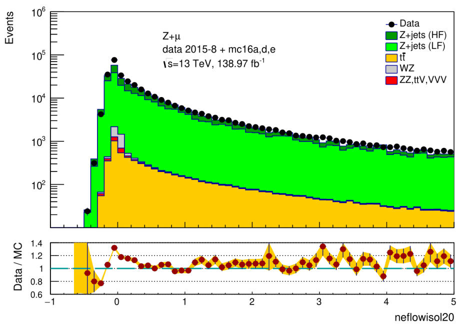

(e) $neflowisol20/p_T$

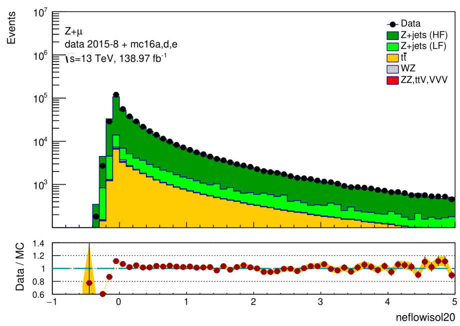

(f) $neflowisol20/p_T$

Figure 4.15: Isolation variables for light (a,c,e) and heavy (b,d,f) flavour enriched samples

The Transfer Factors which are used to extrapolate the LF component events from the Controls Region to the Signal Region are calculated by Data efficiencies. They are the efficiency squared as the are used to extrapolate 2 muons and their uncertainties are also used as systematic uncertainties for the signal region event yields. For the LF sample the TF coming from the Isolation+d_0 significance efficiency is used for the standard method. The inverted Isolation TF defined as $TF_{[InvIso]} = TF_{[Iso]}/(1-TF_{[Iso]})$ is used for the 2CR+1 method. The TF as well as their uncertainties coming from the relative difference between the data calculation and the MC expectation are shown in Figure 4.25. However for the LF an alternative way is used for calculating the TF uncertainty. For LF $TF_{[Iso+d0]}$ it is obtained by varying the parameters of the MC calculation. Contamination by Z+HF events is removed by subtracting MC from the Z+LF-enriched data sample, so the amount of this contamination is varied by a factor of 1.5. The p_T imbalance cut used to define the enriched region is also varied up and down by a factor of 2. Finally, WZ events also contribute to this region: an uncertainty based on this contribution is obtained by doubling their quantity. The variations and the results on the LF TF are shown in Table 4.26.Taking these results into account it was decided for both LF Transfer Factors ($TF_{[Iso+d0]}$, $TF_{[InvIso]}$) the uncertainty to be set equal to 10%.

Selection (sample)	TF	$\Delta/TF^{\mu\mu}_{MC}$
Inverted Isolation (LF)	0.0145	1.24
Isolation + d_0 significance (LF)	0.0124	1.22
Isolation (HF)	0.0268	-0.085

Table 4.25: Transfer Factors calculated from data efficiencies and their relative difference with the MC expected.

Variation	Relative Change in Transfer Factor
Imbalance cut value (0.05 and 0.2)	-5% and $+7\%$
Increase Z+HF, ttbar contributions (50%)	+4%
Increase WZ contribution (100%)	+3%

Table 4.26: Variables and their variance used for LF Transfer Factor uncertainty estimation. Relative change in the Transfer Factor is also shown.

4.4.4 Differential Estimation of Z+ $\mu\mu$ background

In several analyses differential distributions of the background are needed. Two such analyses are these which are performed in order to measure Higgs boson cross sections and couplings. For both analyses the estimation procedure is the following. The total reducible background normalization is determined by the standard method. Next the differential estimation decides the differential shape of each variable. Every differential category (bin) is fitted individually and the sum of the results is scaled to the combined estimation, using a similar method as in 2e2μ and 4μ estimation. As some categories have fairly poor statistics, the merged $Z + jets$ method which handles the LF and HF Z+jets together, is used for the individual estimations. However some fits still fail, especially in the $ee + e\mu$ CR. In order to avoid this, the shape parameters are fixed to the values of the combined estimation. The individual $TF_{[SR]}$ are used to extrapolate the results from the relaxed to the signal region. For some categories the statistics is low, so the $TF_{[SR]}$ is calculated from 1 or 0 MC entries. In this instance, the TF is calculated by extrapolation of the other categories. The method of the extrapolation depends on the specific variable.

Fit Methodology validation

The method was firstly tried for the estimation of the p_T differential distribution. Initially the fit was performed in each differential bin independently. Afterwards the shape parameters were fixed to the values obtained from the combined estimation and the fit was performed again. The comparison of the results are shown in Table 4.27. Good agreement is noticed [3].

	Free Shape Parameters		Fixed Shape Parameters	
p_T GeV	Z+jets	$t\bar{t}$	Z+jets	$t\bar{t}$
0-10	0.69 ± 0.12	0.01 ± 0	0.64 ± 0.1	0.01 ± 0
10-15	1.07 ± 0.15	0.04 ± 0	1.05 ± 0.13	0.04 ± 0
15-20	0.81 ± 0.1	0.08 ± 0.01	0.74 ± 0.09	0.09 ± 0.01
20-30	1.44 ± 0.13	0.16 ± 0.01	1.43 ± 0.11	0.16 ± 0.01
30-45	1.15 ± 0.08	0.5 ± 0.02	1.17 ± 0.07	0.5 ± 0.02
45-60	0.49 ± 0.04	0.48 ± 0.02	0.47 ± 0.03	0.49 ± 0.02
60-80	0.3 ± 0.03	0.95 ± 0.04	0.29 ± 0.02	0.96 ± 0.04
80-120	0.18 ± 0.02	0.51 ± 0.02	0.19 ± 0.01	0.5 ± 0.02
120-200	0.09 ± 0.01	0.13 ± 0.01	0.09 ± 0.01	0.13 ± 0.01
200-350	0 ± 0	0 ± 0	0 ± 0	0 ± 0
350-1000	0 ± 0	0 ± 0	0.02 ± 0.01	0 ± 0
Summary	6.22 ± 0.27	2.87 ± 0.06	6.08 ± 0.23	2.88 ± 0.05

Table 4.27

None event, or 100% error in the signal region indicate that the Transfer Factor has to be corrected as it comes from 0 or 1 MC entry. In Figure 4.16 the TFs after the correction are shown. The results after the correction are shown in Table 4.28.

Differential Cross sections

After the validation the method is used for all the variables used for the differential cross sections measurements. Three different types of variables are considered, Higgs Boson kinematic-related variables, variables related to the jets which are produced along with Higgs boson and lastly variables combining information from both Higgs boson and jets. The kinematics of the Higgs boson production and decay are of particular interest as deviations from the SM predictions could indicate non-SM properties of

[3] This check had been performed using 2017 data and the obsolete isolation wp

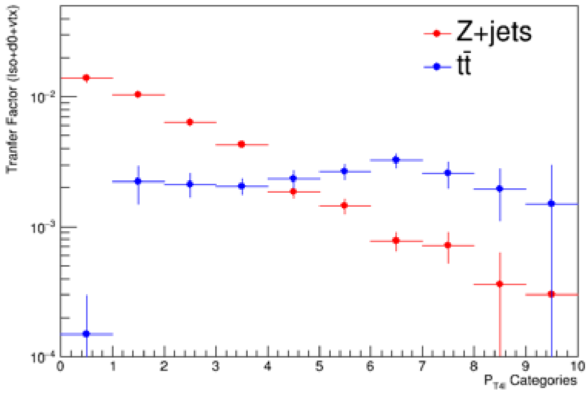

Figure 4.16: The TF of Z+jets and tt. The last 2 have been extrapolated from the previous bins

p_T GeV	Z+jets	$t\bar{t}$
0-10	0.64 ± 0.1	0.011 ± 0.002
10-15	1.07 ± 0.15	0.04 ± 0.005
15-20	0.81 ± 0.1	0.08 ± 0.01
20-30	1.44 ± 0.13	0.16 ± 0.01
30-45	1.15 ± 0.08	0.5 ± 0.02
45-60	0.49 ± 0.04	0.48 ± 0.02
60-80	0.3 ± 0.03	0.95 ± 0.04
80-120	0.18 ± 0.02	0.51 ± 0.02
120-200	0.09 ± 0.01	0.13 ± 0.01
200-350	0.02 ± 0.01	0.0085 ± 0.004
350-1000	0.003 ± 0.0015	0.0012 ± 0.0005
Summary	6.19 ± 0.26	2.87 ± 0.06
Combined	6.38 ± 0.22	2.9 ± 0.06

Table 4.28: Results after TF correction

the Higgs itself or the presence of other particles being produced in association with the Higgs boson. The $H \to 4l$ decay is particularly interesting because the full Higgs kinematic information is accessible through the reconstruction of all of the Higgs decay products. The measurement of the jet multiplicity and other jet properties probes both QCD radiation effects and contributions from the various production modes of the Higgs boson. The fraction of events coming from non-ggF production modes increases with jet multiplicity due to the presence of hadronic decays of the particles produced in association with the Higgs boson. Measurements of the following variables p_{T4lj}, m_{4lj}, p_{T4ljj}, m_{4ljj}, created from both Higgs boson and jets are also provided. The variables are summarized in Table 4.29. The m_{12} estimation is based only on MC as it is the fitting variable. The binning choice for each variable of interest has been defined using simulation only and it is chosen based on several criteria. The number of bins and their widths have been chosen to achieve an expected significance of at least 2 sigma and a statistical error of about 30% in each bin, and to keep as low as possible the event bin migration The binning of the variables considered is described in detail in [135]. Figures **??** show the MC expected (MCE) and the Data Driven estimated (DDE) distributions for both $Z + jets$ and $t\bar{t}$ background components for all the variables.

Higgs Boson kinematic-related variables	
p_{T4l}	p_T of the four-leptons system
m_{12}	invariant mass of the leading lepton pair
m_{34}	invariant mass of the sub-leading lepton pair
$\lvert y_{4l}\rvert$	rapidity of the four-leptons system
ϕ	azimuthal angle between the decay plane of Z_1 and the plane of Z_2
ϕ_1	azimuthal angle between the decay plane of the Z_1 and the plane formed between the Z_1 four momentum and the z-axis
$\lvert\cos\theta^*\rvert$	θ^* is the production angle of Z_1, defined in the four leptons rest frame
$\cos\theta_1$	θ_1 is the production angle of the anti-lepton from the Z_1 decay defined in the four leptons rest frame
$\cos\theta_2$	θ_2 is the production angle of the anti-lepton from the Z_2 decay defined in the four leptons rest frame
Jet-related variables	
N_{jets}	Number of jets
$p_T^{\text{lead. jet}}$	p_T of the leading jet
$p_T^{\text{sublead. jet}}$	p_T of the subleading jet
m_{jj}	invariant mass of the two jets
$\Delta\eta_{jj}$	difference in pseudorapidity of the two jets
$\Delta\phi_{jj}$	difference in the azimuthal angle of the two jets
$N_{b-\text{jets}}$	number of b-jets
Higs boson and jet-related variables	
p_{T4lj}	p_T of the 4 leptons - leading jet system
$m4lj$	invariant mass of the 4 leptons - leading jet system
p_{T4ljj}	p_T of the 4 leptons - two jets system
m_{4ljj}	invariant mass of the 4 leptons - two jets system

Table 4.29: Definitions of variables of interest.

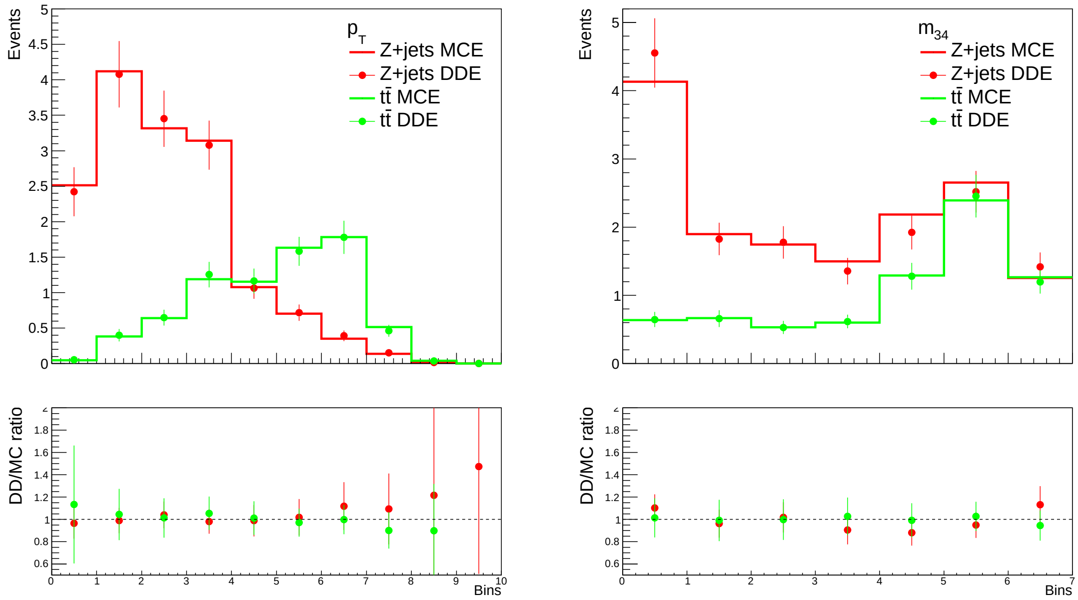

(a) p_{T4l} (b) m_{34}

Figure 4.17: Differential distributions expected from MC and estimated from data for $Z + jets$ and $t\bar{t}$ components.

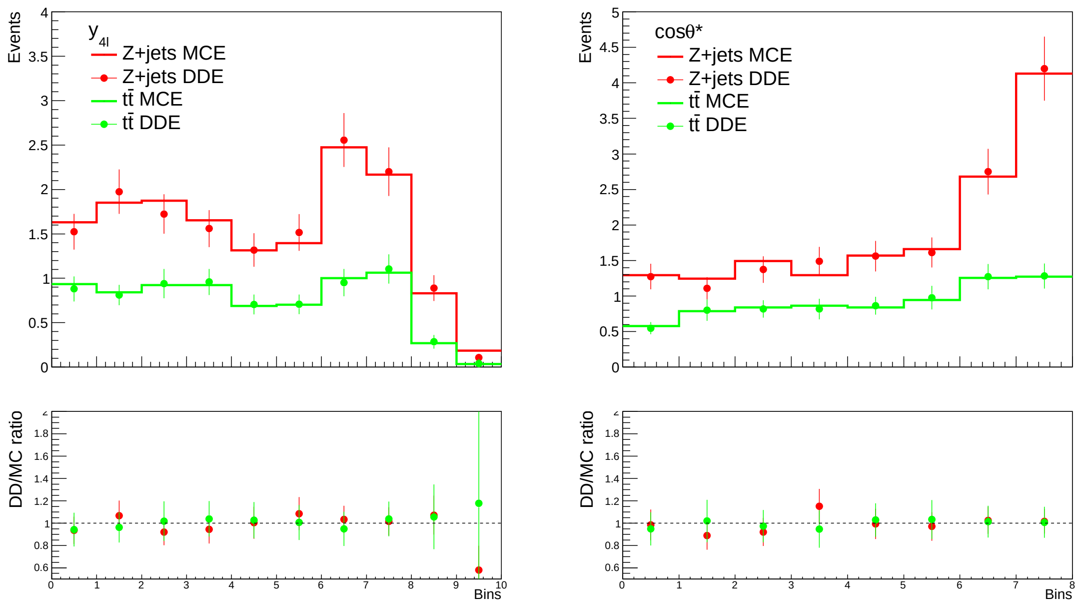

(a) $|y_{4l}|$ (b) $|\cos\theta^{*}|$

Figure 4.18: Differential distributions expected from MC and estimated from data for $Z + jets$ and $t\bar{t}$ components

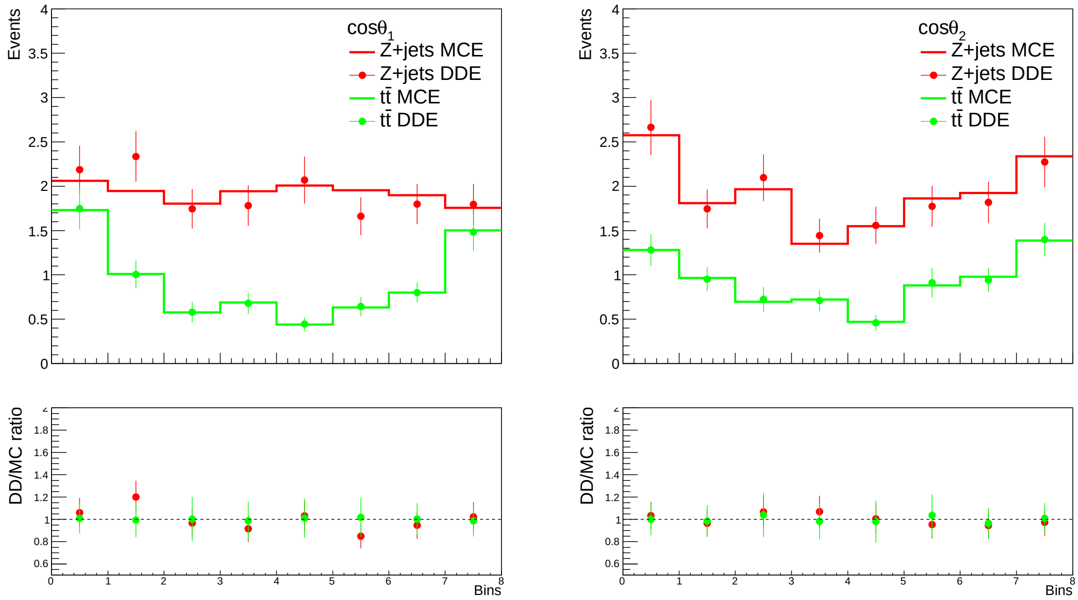

(a) $\cos\theta_1$ (b) $\cos\theta_2$

Figure 4.19: Differential distributions expected from MC and estimated from data for $Z + jets$ and $t\bar{t}$ components

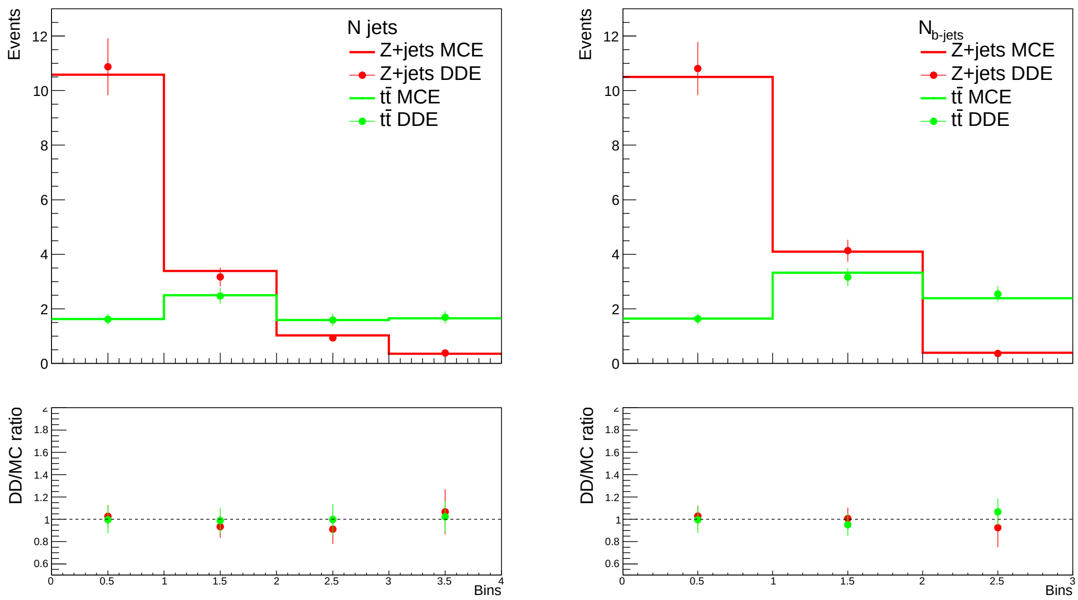

(a) Number of jets (b) Number of b-jets

Figure 4.20: Differential distributions expected from MC and estimated from data for $Z + jets$ and $t\bar{t}$ components

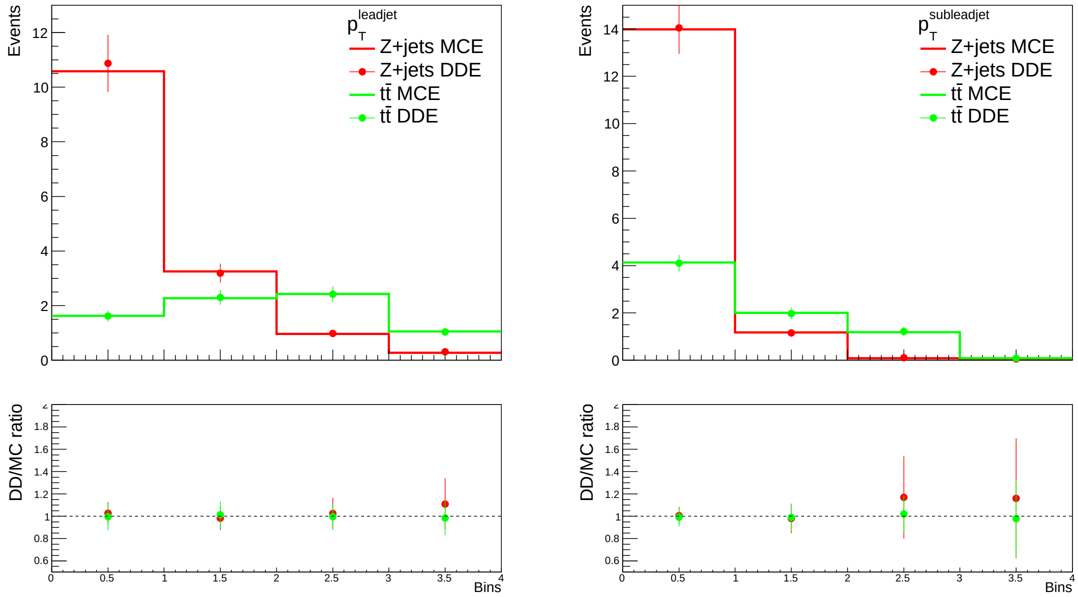

(a) $p_T^{\text{lead. jet}}$ (b) $p_T^{\text{sublead. jet}}$

Figure 4.21: Differential distributions expected from MC and estimated from data for $Z+jets$ and $t\bar{t}$ components

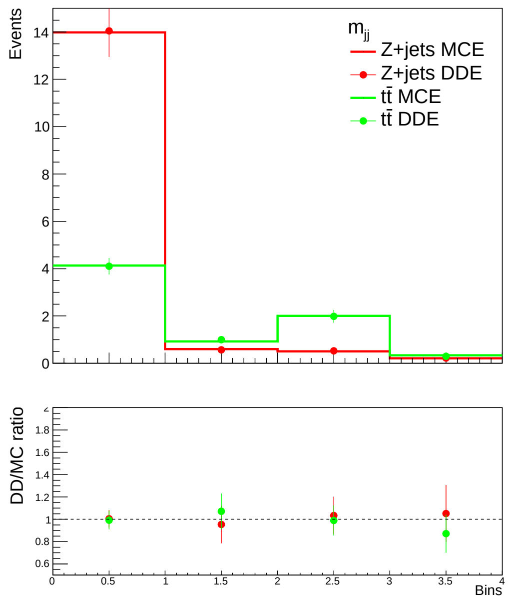

(a) m_{jj}

Figure 4.22: Differential distributions expected from MC and estimated from data for $Z+jets$ and $t\bar{t}$ components

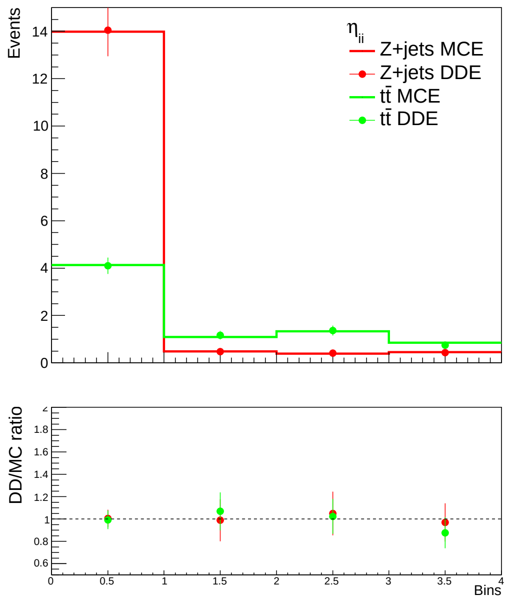

(a) $\Delta\eta_{jj}$

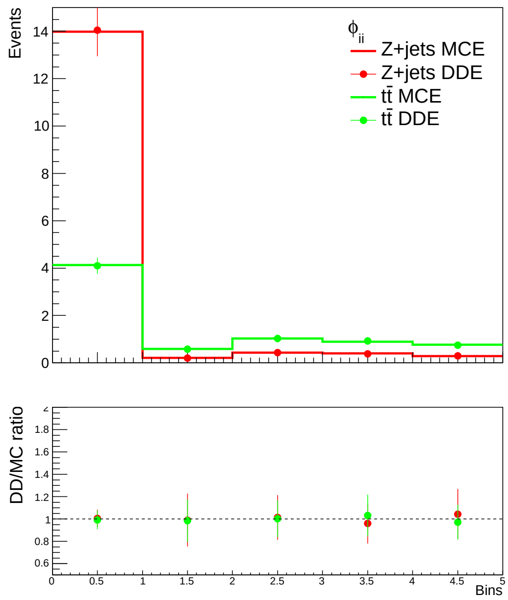

(b) $\Delta\phi_{jj}$

Figure 4.23: Differential distributions expected from MC and estimated from data for $Z + jets$ and $t\bar{t}$ components

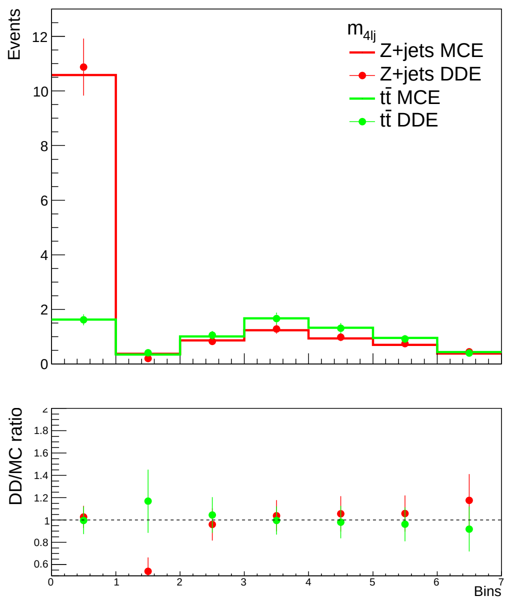

(a) $m4lj$

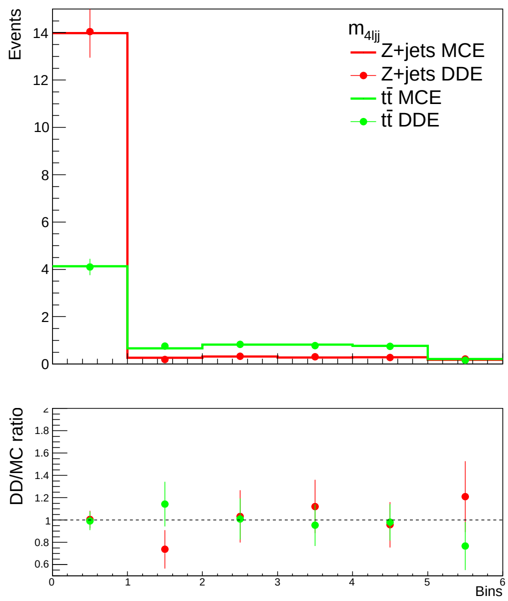

(b) $m4ljj$

Figure 4.24: Differential distributions expected from MC and estimated from data for $Z + jets$ and $t\bar{t}$ components

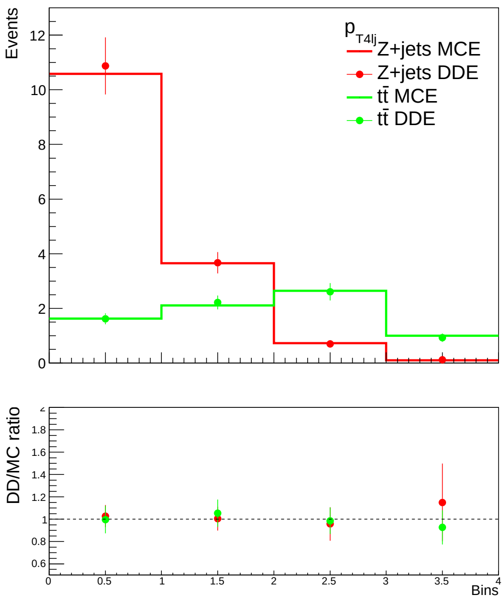

(a) p_{T4lj}

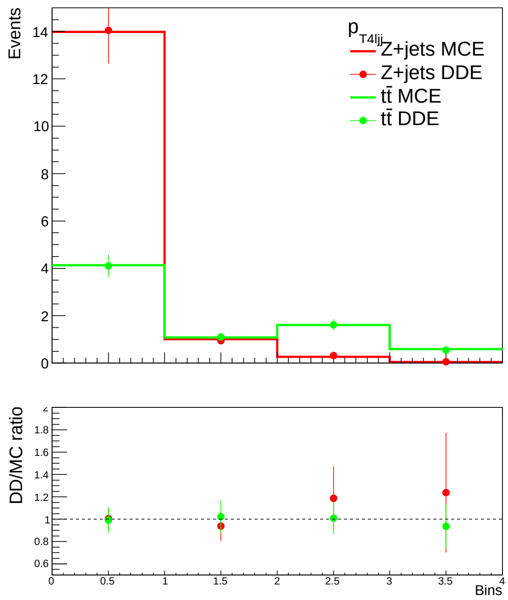

(b) p_{T4ljj}

Figure 4.25: Differential distributions expected from MC and estimated from data for $Z + jets$ and $t\bar{t}$ components

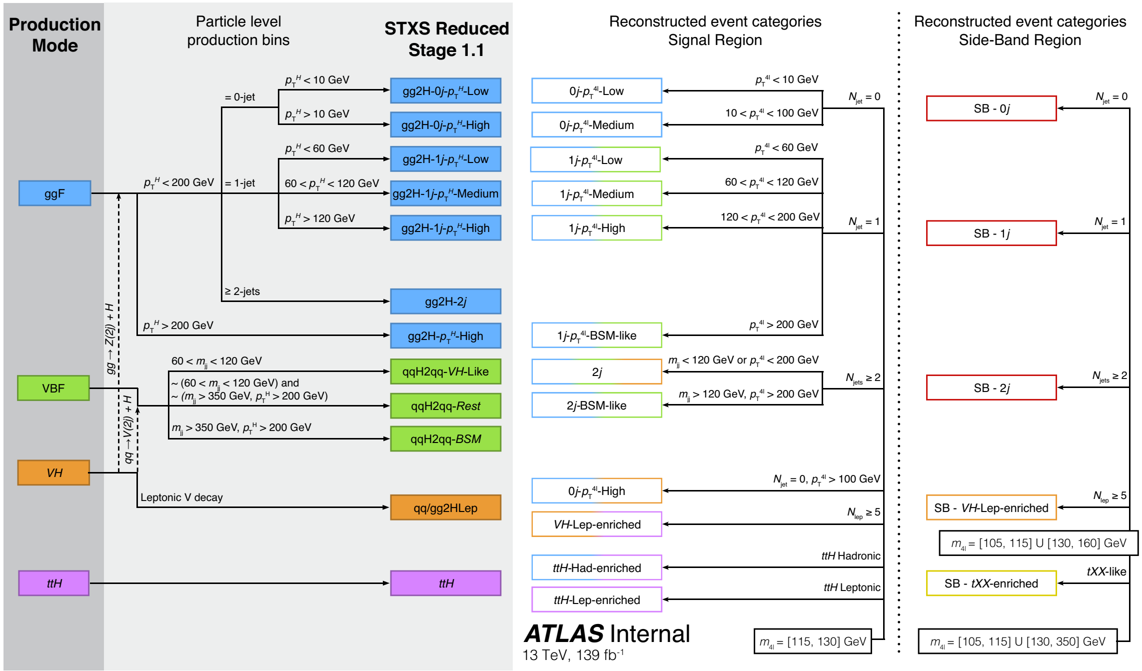

Figure 4.26: Event categorization scheme for STXS measurement with STXS: Reduced Stage 1.1 scheme. Unlike the previous scheme, gg2H includes bbH and hadronically decaying ggZH. qq2Hqq include VBF and hadronically decaying qqZH. All leptonically decaying VH is categorized under VH-lep. The colored outline for the reconstructed categories indicate the targeted signal process within that category [136].

Couplings

In the simplified template cross sections framework [46], the exclusive regions of phase space defined for measurements are specific to each production mechanism under study. These regions, referred to as bins, are motivated by:

- Minimizing the dependence on theoretical uncertainties which are directly folded into the measurements;
- Maximizing experimental sensitivity;
- Isolation of possible BSM effects; and
- Minimizing the number of bins without loss of experimental sensitivity.

With this design principle, several stages, each with an increasing number of bins, are defined. The categories which are used for this analysis are shown in scheme 4.26. They are described in detail in [136]. The MCE and DDE number of events for both background components in each of the 10 Reconstructed event categories in Signal Region is shown in Figure 4.27(a). In Figure 4.27(b) the corresponding events for the 5 Reconstructed event categories in Side-Band Region are shown.

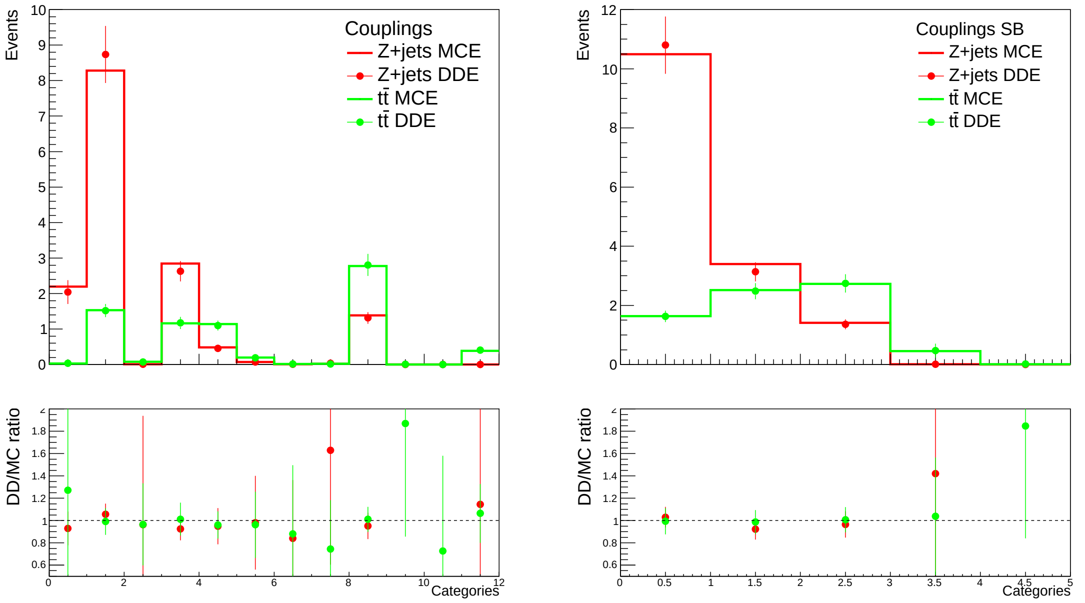

(a) Couplings Categories

(b) Couplings Side Band Categories

Figure 4.27: Number of events expected from MC and estimated from data for $Z+jets$ and $t\bar{t}$ components for the categories used in Higgs boson couplings measurement.

4.4.5 $Z + ee$ background

The estimate of the electron background, which is mainly composed of jets misidentified as electrons, is extracted from a control region denoted as $3\ell{+}X$, where the selection and identification criteria for the lower p_T electron in the subleading pair (denoted with "X") are relaxed while the remaining leptons in the quadruplet are required to pass the full analysis selection. Additionally, the subleading pair must have the same sign, thus ensuring orthogonality to the signal region. The standard quadruplet selections are then applied to the quadruplets that are formed. As for the $Z + \mu\mu$ background estimate, the ME quadruplet selection is not used, regardless of the presence of extra leptons. Unlike the $Z+\mu\mu$ background estimate, however, all possible $3\ell{+}X$ quadruplets sharing the same Z are kept. This approach simplifies significantly the decomposition of the different background contributions as it can be done by looking only at the X lepton.

The electron background is classified according to the process involved. The main contributions come from light jets with depositions in the calorimeter faking an electron (f) and electrons from semileptonic decays of heavy quarks (q). Also important are electrons coming from photon conversions or FSR (γ). Each background has different properties and efficiency, therefore the background estimation method is targeted to disentangle the various components using suitable discriminating variables. In MC simulation, the actual origin is known and is extracted using truth information (`MCTruthClassifier`). Electrons are sorted into the following categories:

1. Isolated electrons Electrons from W or Z bosons, or from bremsstrahlung originating from a W or Z boson.

2. Light flavour Electrons that are really misidentified hadrons, as well as those whose truth origin is unknown.

3. Heavy flavour Non-isolated electrons that do not come from conversions (unless from bremsstrahlung originating in a charm or bottom hadron).

4. Photons Electrons that are actually FSR photons, photons whose origin is another photon, photons from light meson decay, or photons from other conversions.

For data, the various components are unfolded directly using a template fit on the n_o^{InnerPix}bservable. This variable counts the number of IBL hits, unless no such hits are expected due to a dead area of the IBL: in such cases, the number of hits on the next-to-innermost pixel layer is counted instead. It provides discrimination for γ over f and q, as photons populate $n_=^{\mathrm{InnerPix}}0$ in the distribution.

A complementary control region denoted as $Z{+}X$ is used to estimate the efficiency needed to extrapolate from the relaxed electron requirements on the "X" for each of the background components to the full electron identification and isolation cuts used in the signal region. Table 4.30 shows the final results for the Z+ee background.

	Full Run-2	
type	$4e$	$2\mu 2e$
f	$7.06 \pm 0.38 \pm 1.10$	$7.73 \pm 0.40 \pm 1.23$
γ	$2.01 \pm 0.50 \pm 0.40$	$2.17 \pm 0.53 \pm 0.44$
h	4.33 ± 1.30	7.77 ± 2.33

Table 4.30: Electron reducible background estimates broken down by channel. Since these numbers are obtained by fitting each channel separately they do not add up exactly to the total result, but the difference is easily covered by the statistical uncertainties.

4.4.6 Background shape modelling

The m_{4l} shape of the reducible background in the signal region is obtained using the shapes of Z+HF and $t\bar{t}$ from MC simulation; Z+LF and WZ are not considered due to their small contribution ($<$ 10%) and the tiny number of MC events surviving the signal selection. The shape of Z+jets and $t\bar{t}$ is obtained after applying the full analysis selection and combining 4μ and $2e2\mu$ final states to obtain sufficient statistics (variation between the two channels is negligible): each component is then smoothed separately using kernel estimation (`RooKeysPDF`) [137]. Shape uncertainty arises from varying the fraction of each component by 20%. The electron $m_{4\ell}$ background shape is obtained by combining shapes for each of the HF, LF, and conversion components: the first is obtained from MC and the last two (which are assumed to be the same and so combined into a single shape for this purpose) from data in the 3L+X control region. As with the muon background shapes, each component is normalized to unit area, smoothed, and then added according to their fractions as measured in the data, with a systematic uncertainty obtained by varying that fraction. The total MC expected and the observed data m_{4l} distributions for the four individual channels ($4e, 4\mu, 2e2\mu, 2\mu2e$) as well as the combined are show in Figure 4.28 and Figure 4.29 correspondingly.

Summary tables

The numbers of expected and observed events for various background and signal processes are summarized in tables 4.31, 4.32, 4.33.

Final state	signal	qqZZ	ggZZ	redBkg	ttV	Total	Observed
4μ	78 ± 5	36.8 ± 2.0	1.2 ± 0.8	2.20 ± 0.16	0.58 ± 0.07	119 ± 5	115
$2e2\mu$	53.0 ± 3.1	25.3 ± 1.3	0.7 ± 0.5	2.50 ± 0.18	0.44 ± 0.04	82.0 ± 3.4	96
$2\mu2e$	40.1 ± 2.9	16.7 ± 1.2	0.56 ± 0.35	3.1 ± 0.5	0.33 ± 0.04	60.9 ± 3.2	57
$4e$	35.3 ± 2.6	14.5 ± 1.5	0.56 ± 0.35	2.37 ± 0.33	0.36 ± 0.04	53.0 ± 3.1	42
Total	206 ± 13	93 ± 5	3.1 ± 2.0	10.2 ± 0.9	1.72 ± 0.17	315 ± 14	310

Table 4.31: The number of events expected and observed for a $m_H = 125$ GeV hypothesis for the four-lepton final states in a window of $115 < m_{4\ell} < 130$ GeV, using the FSR-corrected $m_{4\ell}$. The columns show the number of expected signal events, the number of expected background events ($ZZ^{(*)}$ reducible background, and ttV) and the number of observed events, for 139 fb^{-1} at $\sqrt{s} = 13$ TeV.

Final state	signal	TotalIrred	TotalRed	Total	S/B	Observed
4μ	78 ± 5	38.0 ± 2.1	2.79 ± 0.18	119 ± 5	1.9	115
$2e2\mu$	53.0 ± 3.1	26.1 ± 1.4	2.94 ± 0.19	82.0 ± 3.4	1.8	96
$2\mu2e$	40.1 ± 2.9	17.3 ± 1.3	3.5 ± 0.5	60.9 ± 3.2	1.9	57
$4e$	35.3 ± 2.6	15.0 ± 1.5	2.73 ± 0.33	53.0 ± 3.1	2.0	42
Total	206 ± 13	96 ± 6	11.9 ± 0.9	315 ± 14	1.9	310

Table 4.32: The number of events expected and observed for a $m_H = 125$ GeV hypothesis for the four-lepton final states in a window of $115 < m_{4\ell} < 130$ GeV, using the FSR-corrected $m_{4\ell}$. The columns show the number of expected signal events, the number of expected irreducible and reducible background events, the expected S/B ratio for each final state, and the number of observed events, for 139 fb^{-1} at $\sqrt{s} = 13$ TeV.

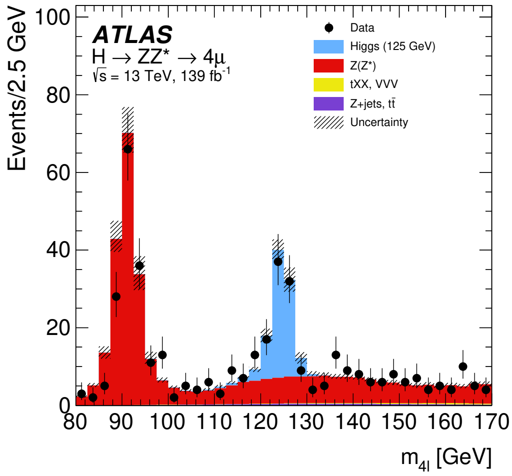

(a) 4μ

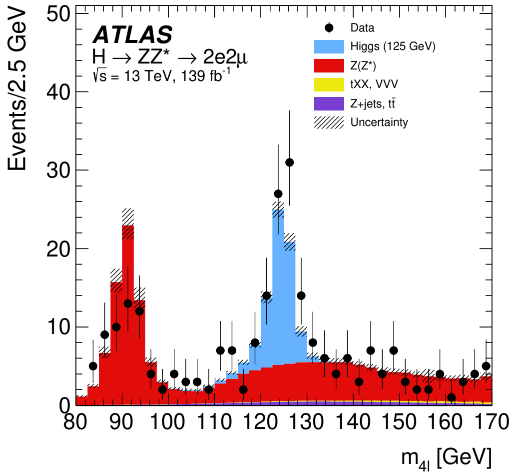

(b) $2e2\mu$

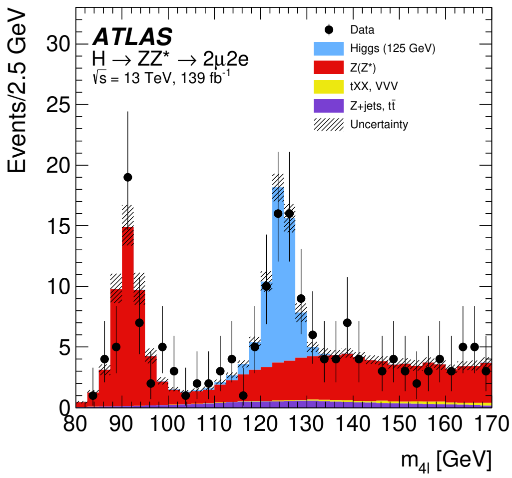

(c) $2\mu 2e$

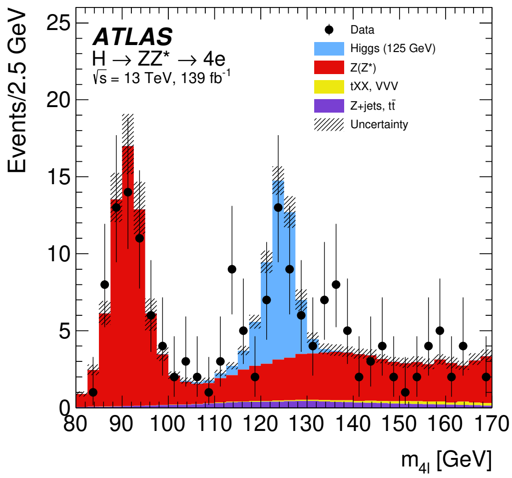

(d) $4e$

Figure 4.28: The 4 lepton invariant mass distribution for the 4 channels[138].

Final state	Signal	$ZZ^{(*)}$	$Z+$jets, $t\bar{t}$ WZ, ttV, VVV	Expected	Observed
4μ	81.1 ± 5.0	1454 ± 120	35.4 ± 2.8	1571 ± 120	1620
$2e2\mu$	55.9 ± 3.3	1027 ± 80	29.1 ± 2.0	1112 ± 80	1239
$2\mu 2e$	42.3 ± 3.0	1022 ± 100	35.3 ± 4.0	1099 ± 100	1266
$4e$	38.2 ± 2.8	803 ± 90	31.3 ± 2.9	873 ± 90	973
Total	219.0 ± 13.0	4306 ± 400	131.1 ± 9.0	4659 ± 400	5098

Table 4.33: The number of events expected and observed for a $m_H = 125$ GeV hypothesis for the four-lepton final states in the full $m_{4\ell}$ mass range. The columns show the number of expected signal events, the number of expected $ZZ^{(*)}$ and reducible background events, together with the number of observed events, for 139 fb^{-1} at $\sqrt{s} = 13$ TeV.

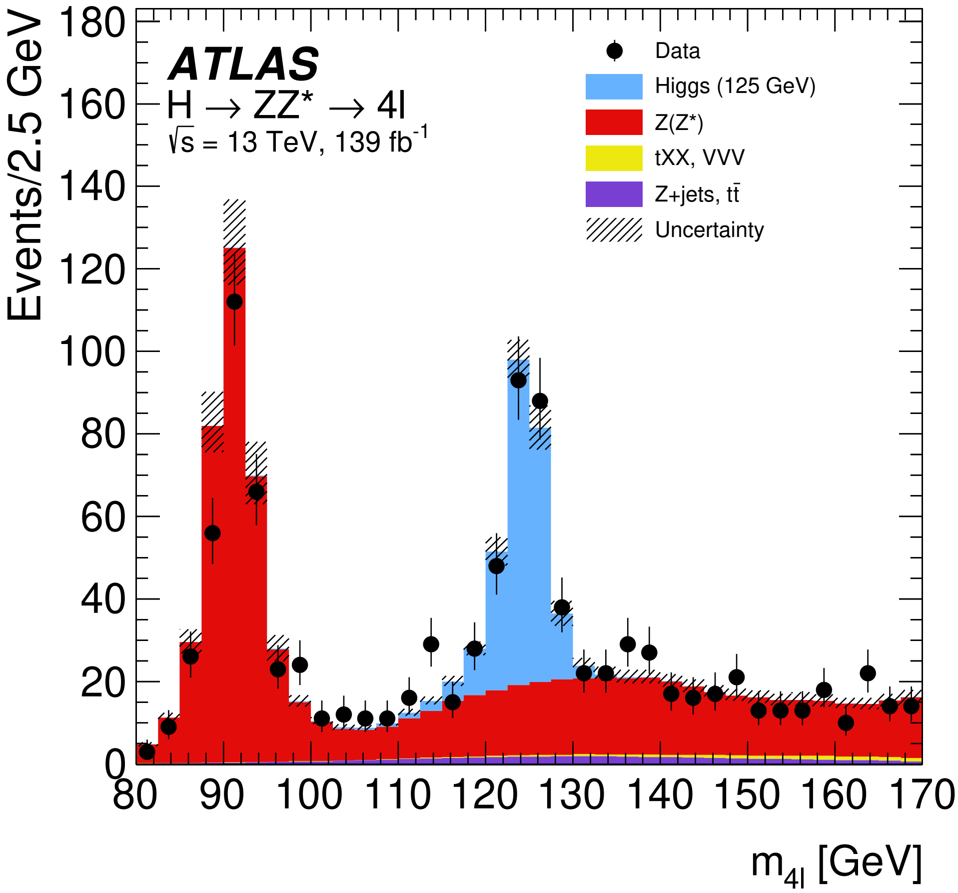

(a)

Figure 4.29: The 4 lepton invariant mass distribution, combining all 4 channels[138].

5 Search for heavy ZZ resonances

In 2012, the ATLAS and CMS Collaborations at the LHC discovered a new particle [139, 140], an important milestone in the understanding of the mechanism of electroweak (EW) symmetry breaking. Subsequent studies [141, 142, 143, 144] have shown that the properties of the new particle are consistent with those of the Standard Model (SM) Higgs boson. Nevertheless, the possibility that the particle is part of an extended Higgs sector or other extension of the SM cannot be ruled out. Many theoretical models predict heavy spin-0 neutral Higgs boson (H) decaying into a pair of Z bosons (Section 1.2.8). Also in models with warped extra dimensions [145, 146], spin-2 Kaluza–Klein (KK) excitations of the graviton (G_{KK}) are expected to decay into ZZ.

This chapter presents the search for heavy resonances decaying into a pair of Z bosons leading to the $\ell^+\ell^-\ell^+\ell^-$ final state, where ℓ stands for either an electron or a muon. The search uses proton-proton collision data at a centre-of-mass energy of 13 TeV collected with the ATLAS detector between 2015 and 2018 at the Large Hadron Collider. The study is based on a search for an excess in the distribution of the four-lepton invariant mass, $m_{4\ell}$, in the range $200 < m_{4\ell} < 2000$ GeV. In the absence of such an excess, limits on the production rate of the signal hypothesis is obtained from a fit to the mass distribution. The signal hypothesis tested here is the gluon-gluon fusion (ggF) and vector-boson fusion (VBF) production of a heavy Higgs boson (spin-0 resonance) under the narrow-width approximation (NWA).

5.1 Samples and Event Selection

Many models beyond the Standard Model of particle physics predict heavy particles that could decay into diboson final states. Below some models predicting a heavy ZZ resonance are described.

5.1.1 Heavy Higgs-like Scalar

One model considered here is that of a heavy Higgs decay, including both the Narrow Width Approximation (NWA) and the Large Width Approximation (LWA). The Higgs boson events are simulated using the *POWHEG* event generator [147, 97], which calculates separately the gluon fusion and vector-boson fusion production mechanisms with matrix elements up to next-to-leading order(NLO). *POWHEG* is interfaced to *PYTHIA* [84] for decaying the Higgs boson into the $ZZ \rightarrow \ell^+\ell^-\ell^+\ell^-$ final state, the showering and hadronization.

To have a better description of the jet multiplicity, *MGMC@NLO* is also used to generate events for the process of $pp \rightarrow H + \geq 2$jets at NLO QCD accuracy with the FxFx merging scheme [148] in the Effective Field Theory approach ($m_{\mathrm{t}} \rightarrow \infty$). The fraction of the ggF events that enter into the VBF-enriched category is estimated from the *MGMCatNLO* simulation.

Large width samples are produced only for ggF production. As seen in the samples with NWA the mass spectrum is the same between the ggF productions and VBF ones.

The Higgs effective field theory is modified to allow special handling of the width of the Higgs and implemented in the *AMC@NLO* framework [117, 149], which produces at next-to-leading-order the process of $pp \to ZZ$, where the Z decay is handled by *MADSPIN* [150], preserving all spin correlations. The generated particles at matrix-element level are showered by *PYTHIA8* with the A14 setting for the tunable parameters of the underlying event. The NNPDF23LO parton distribution function (PDF) set is used and the factorisation and renormalisation scale factors are set to $\mu_F = \mu_R = m_H$, where m_H is the invariant mass of the new scalar.

The NWA signal is simulated at mass points between 200 and 2000 GeV for both the ggF and VBF production modes. The mass points between 200 and 1000 GeV are simulated in steps of 100 GeV, and those between 1000 and 2000 GeV are simulated in steps of 200 GeV. The 2400 and 3000 GeV mass points are also simulated to validate the extrapolation of the signal model above 2000 GeV. These samples are mainly produced using the full detector simulation. Two of these samples were produced using a fast detector simulation [151] that uses a parameterisation of the response of electromagnetic and hadronic calorimeters [152], while the response of the ID and MS detectors is fully simulated. These two “FastSim” samples were for the VBF 300 and 700 GeV mass points in the mc16e campaign only.

5.1.2 Event Selection

First, a generic, model-independent, four-lepton event selection is applied following the common $4l$ selection (Chapter 4). After the common event selection, the events are split into different categories, in order to probe different production modes of BSM signals, such as VBF production and ggF production. To enhance the search sensitivity to NWA signals, multivariate classifiers are used for event categorization. Such multivariate classifiers are usually trained based on a specific signal model and thus would lead to some model dependence. For this consideration, a cut-based event categorization is also considered.

5.1.3 Event Categorization

As it is noted in the introduction, the VBF-enriched category is used to search for resonances produced via VBF production mode. Firstly a simple cut-based VBF categorization is used. Events that have two or more jets with $p_T$greater than 30 GeV, with the two leading jets being well separated in η, $\Delta\eta_{\mathrm{jj}} > 3.3$, and having an invariant mass $m_{\mathrm{jj}} > 400$ GeV, are classified in the VBF-enriched category. The choice of the cuts was revisited for this full Run-2 analysis, and it was found that these same cuts are satisfactory for the purposes of this analysis.

In order to improve the search sensitivity to heavy Higgs signals, multivariate (MVA) classifiers have been studied. To target heavy Higgs signals with different production modes, a VBF classifier and a ggF classifier are used produced by Deep Neural Networks (DNN). After the common event selection, a cut on the VBF classifier is applied and events passing the VBF classifier form the VBF category. Events failing the VBF classifier but passing the ggF classifier form the ggF category. All remaining events, failing both the VBF classifier and the ggF classifier, form the so-called “rest” category. The ggF category is further split into three regions of different lepton final states: $2e2\mu$, 4μ and $4e$. Given the relatively small fraction of events in the VBF and rest categories, inclusive lepton final states are used. Therefore, in total 5 regions are used in the analysis: VBF inclusive, ggF $2e2\mu$, ggF 4μ, ggF $4e$ and rest. Figure 5.1 show the classifier output for the SM background samples as well as the 700-GeV VBF and ggF signal samples. The classifiers have similar response for any Higgs mass.

The optimal classification cut is chosen on the basis of good overall performance across the entire mass range, while retaining a high signal selection efficiency and background rejection. For the VBF category, a cut on the VBF DNN score of 0.8 for events with at least two jets is found to produce the best overall performance improvement. For the ggF category, a combination of cuts (a VBF DNN score of less than 0.8 and a ggF DNN score of greater than 0.5 for events with at least two jets, and simply a ggF score greater than 0.5 for events with less than two jets), produces the best overall

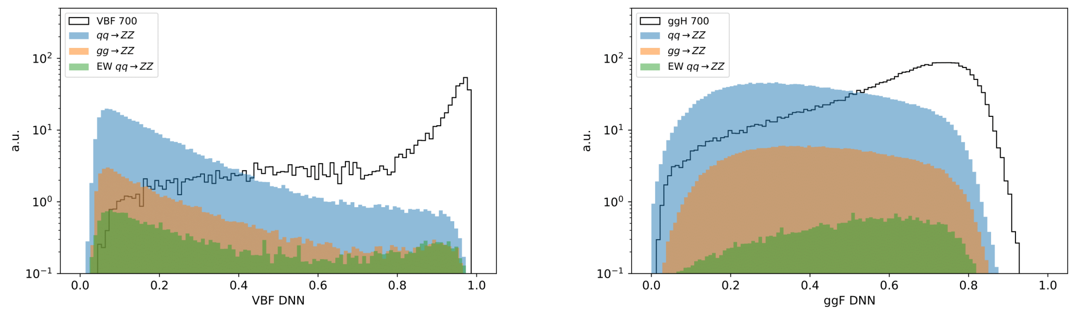

(a) VBF DNN classifier (b) ggF DNN classifier

Figure 5.1: VBF DNN and ggF DNN classifier response for the background samples (filled) and the 700 GeV VBF signal sample (black), for events with at least two jets.

improvement over the cut-based categorisation. The selection was tested for $m_{4\ell}$ sculpting and it was found that it sculpts neither signal nor background shape. Using the DNN-based VBF and ggF classifiers, the event categorization is the following:

- VBF-incl: $N_{\text{jets}} \geq 2$ && $DNN_{\text{VBF}} > 0.8$;
- ggF-($2e2\mu$, 4μ, $4e$): $(N_{\text{jets}} \geq 2\&\&DNN_{\text{VBF}} \leq 0.8\&\&DNN_{\text{ggF}} > 0.5)||(N_{\text{jets}} < 2\&\&DNN_{\text{ggF}} > 0.5)$;
- Rest: all remaining events.

The classifiers are tested also in the Control Region $m_{4l} : [80-170]$. Good agreement between data and MC is observed as shown in Figure 5.2. Only statistical uncertainties and experimental systematic uncertainties are included in these plots,since in general systematic uncertainties are subdominant given the data statistics in the control regions

5.1.4 Signal Acceptance

For the NWA case, in the cut-based analysis, four analysis regions are used: VBF incl, ggF $2e2\mu$, ggF 4μ, and ggF $4e$. For MVA-based analysis, five analysis regions are used: VBF incl, ggF $2e2\mu$, ggF 4μ, ggF $4e$ and rest. Figure 5.3 shows the acceptance plot as a function of signal mass of different ggF and VBF production mode samples by merging all three MC campaigns (mc16a, mc16d and mc16e) for the cut-based categorization. Given the excellent signal mass resolution in 4ℓ final states, it is possible to search for resonances with fine granularity of signal mass grids. In order to interpolate signal acceptance for any signal mass point, a third-order polynomial fit is applied from the mass point of 200 GeV to 2000 GeV. Signal acceptance decreases a bit in the high mass region, due to degraded lepton reconstruction and identification efficiencies for close-by leptons, which originate from boosted Z bosons. The acceptance plot for the DNN-based categorization is shown in Fig. 5.4. The acceptance is fitted with a polynomial function.

For the cut-based analysis a third degree polynomial is used to parametrize the acceptance, while for the MVA-based a fifth degree polynomial is used. The values of the parameters for both ggF and VBF are shown in tables 5.1,5.2,5.3,5.4 correspondingly.

Figure 5.5 shows the acceptance plot as a function of the signal mass for different channels for both the LWA and NWA case for comparison. For the LWA case, three categories can be used ($2e2\mu$, 4μ, $4e$), without splitting into ggF and VBF categories, as only ggF LW signal samples are available.

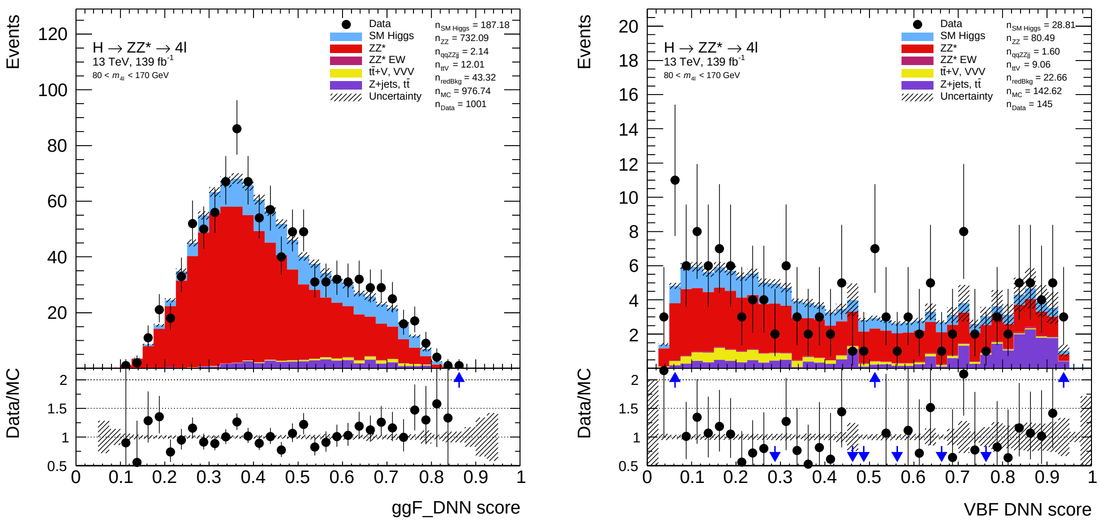

(a) ggf Classifier

(b) VBF Classifier

Figure 5.2: DNN ggF and VBF classifiers

	ggF $2e2\mu$	ggF $4e$	ggF 4μ	VBF incl
a0	1.71e-01	5.74e-02	1.05e-01	8.28e-05
a1	2.53e-04	1.42e-04	1.31e-04	7.27e-05
a2	-1.66e-07	-8.77e-08	-9.59e-08	-3.02e-08
a3	3.49e-11	1.78e-11	2.18e-11	4.71e-12

Table 5.1: Parameter values for the cut-based ggF acceptance.

	ggF $2e2\mu$	ggF $4e$	ggF 4μ	VBF incl
a0	1.33e-01	4.74e-02	8.60e-02	1.31e-01
a1	6.56e-05	5.30e-05	1.25e-05	3.55e-04
a2	-1.57e-08	-2.43e-08	4.50e-09	-2.58e-07
a3	-3.76e-13	4.87e-12	-2.75e-12	5.61e-11

Table 5.2: Parameter values for the cut-based VBF acceptance.

	ggF $2e2\mu$	ggF $4e$	ggF 4μ	rest	VBF incl
a0	-3.42e-03	3.40e-03	3.17e-03	3.77e-01	-4.30e-03
a1	8.93e-04	2.99e-04	5.15e-04	-1.40e-03	6.91e-05
a2	-1.39e-06	-3.40e-07	-8.82e-07	2.76e-06	-4.69e-08
a3	1.11e-09	1.91e-10	7.73e-10	-2.49e-09	-2.36e-11
a4	-4.52e-13	-5.78e-14	-3.44e-13	1.09e-12	2.89e-14
a5	7.16e-17	7.06e-18	5.95e-17	-1.82e-16	-6.67e-18

Table 5.3: Parameter values for the MVA-based ggF acceptance.

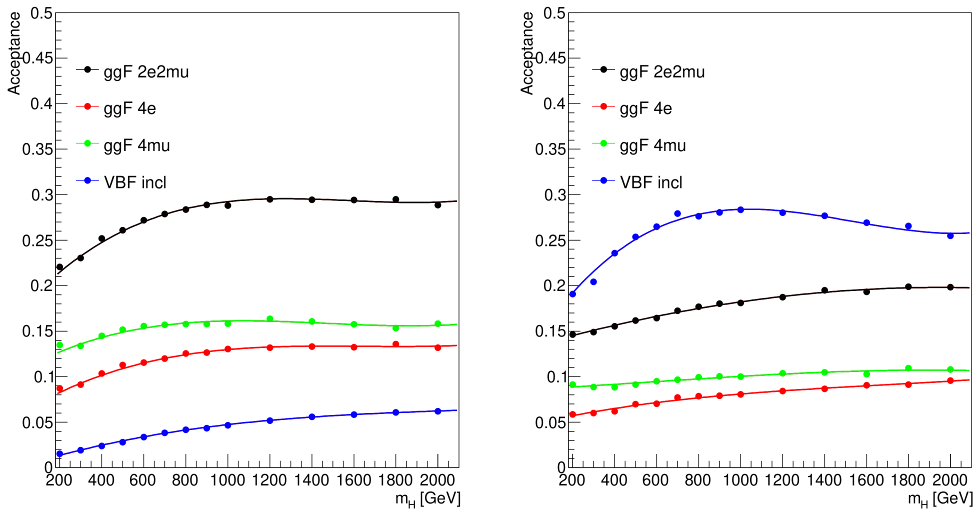

Figure 5.3: NWA acceptance as a function of m_H for the cut-based categorization, estimated by merging the three signal MC campaigns, mc16a, mc16d and mc16e, for the sample of (a) ggF production mode; (b) VBF production mode.

	ggF $2e2\mu$	ggF $4e$	ggF 4μ	rest	VBF incl
a0	1.61e-01	6.60e-02	1.15e-01	5.61e-02	3.60e-02
a1	-2.25e-04	-1.31e-04	-2.54e-04	1.92e-04	6.06e-04
a2	6.17e-07	4.28e-07	5.90e-07	-5.01e-07	-6.47e-07
a3	-6.00e-10	-4.76e-10	-5.60e-10	5.88e-10	2.35e-10
a4	2.47e-13	2.25e-13	2.34e-13	-2.72e-13	-1.32e-15
a5	-3.75e-17	-3.94e-17	-3.62e-17	4.59e-17	-1.15e-17

Table 5.4: Parameter values for the MVA-based VBF acceptance.

5.2 Signal and Background Modelling

The main background component in the $H \to ZZ \to \ell^+\ell^-\ell^+\ell^-$ final state, accounting for 97% of the total expected background events, is non-resonant ZZ production. This arises from quark-antiquark annihilation (86%), gluon-initiated production (10%) and a small contribution from EW vector-boson scattering (1%). The last is more important in the VBF-enriched category, where it accounts for 16% of the total expected background. The non-resonant ZZ background is modelled by fitting the MC expected $m_{4\ell}$ distributions. The normalization is profiled to data in the likelihood fit.

Additional background comes from the Z + jets, $t\bar{t}$ and WZ processes, denoted as reducible background, which contribute at the percent level and decrease more rapidly than the non-resonant ZZ production as a function of $m_{4\ell}$. The normalization of these backgrounds are estimated using data where possible and since the dominant background components vary according to the flavour of the leptons of the subleading pair. Their shapes are obtained by smoothing the MC distributions. Lastly there are some other minor backgrounds, like VVV and $t\bar{t}V$ whose normalization is obtained from MC and their shapes by smoothing the MC distributions.

The signal is modelled by the sum of a Crystal Ball ($\mathcal{C}$) function and a Gaussian ($\mathcal{G}$) function.

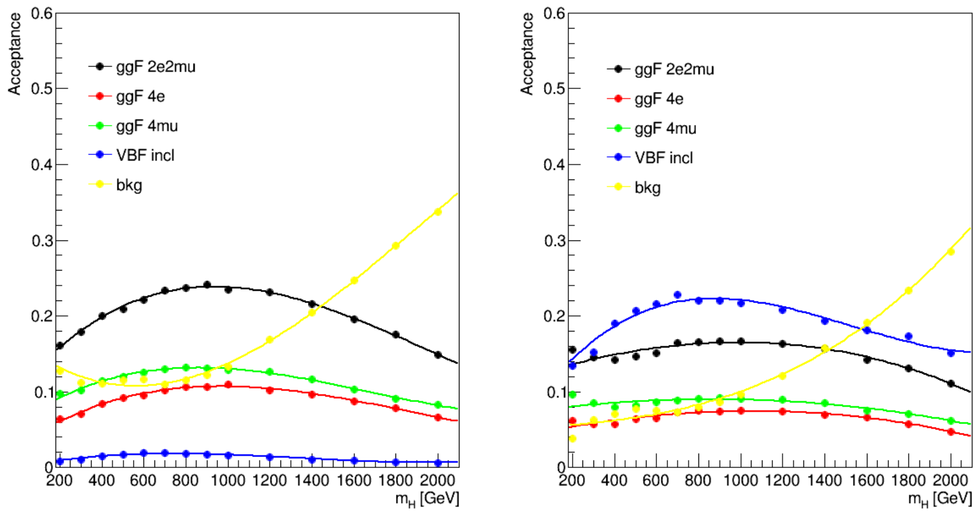

(a) (b)

Figure 5.4: NWA acceptance as a function of m_H for the double-DNN based categorization, estimated by merging the three signal MC campaigns, mc16a, mc16d and mc16e, for the sample of (a) ggF production mode; (b) VBF production mode. Here, "bkg" refers to the "rest" category.

5.2.1 Reducible background

The reducible background analysis is performed separately for the $\ell\ell + \mu\mu$ and $\ell\ell + ee$ final states, following slightly different approaches that estimate the "muon" and "electron" backgrounds, respectively (Section 4.4). The muon background comes mostly from heavy-flavour (HF) jets produced in association with a Z boson or in decays of top quarks. In the case of the electron background, the larger contribution comes from light-flavour (LF) jets produced in association with a Z boson that are misidentified as electrons. The corresponding fraction of yields for $m_{4\ell} > 200$ GeV are estimated using MC simulation. For the VVV and $t\bar{t}V$ backgrounds the event yields come purely from MC. The normalization factors are shown in Tables 5.5 and 5.6.

	ggF $2e2\mu$	ggF $4e$	ggF 4μ	VBF incl
$Z + jets$, WZ, $t\bar{t}$	6.59	3.04	2.08	0.28
VVV, $t\bar{t}V$	26.8	11.7	16.3	3.03

Table 5.5: Normalization values for "reducible" background components for the cut-based selection.

	ggF $2e2\mu$	ggF $4e$	ggF 4μ	rest	VBF incl
$Z + jets$, WZ, $t\bar{t}$	1.73	0.77	0.61	8.79	0.08
VVV, $t\bar{t}V$	17.5	7.74	9.8	21.9	0.96

Table 5.6: Normalization values for "reducible" background components for the MVA-based selection.

The reducible background $m_{4\ell}$ shapes for $Z + jets$ and VVV in the signal region is obtained using the shapes of $Z + jets$, WZ, $t\bar{t}$ and VVV, $t\bar{t}V$ correspondingly from the MC simulation. The

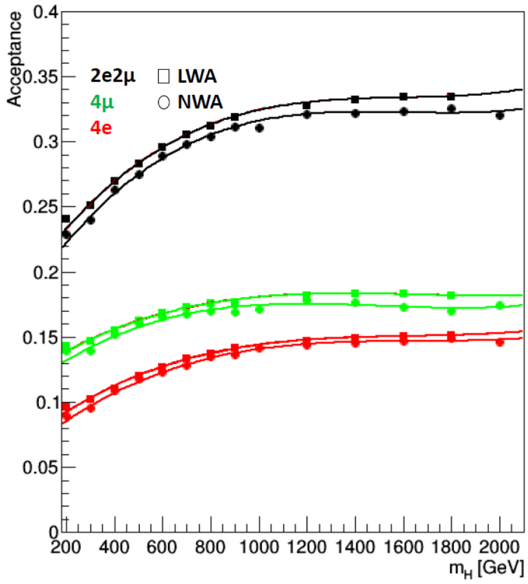

(a)

Figure 5.5: LWA acceptance as a function of m_H, estimated by merging the three signal MC campaigns, mc16a, mc16d and mc16e. The corresponding NWA acceptance is also provided for comparison.

total background $m_{4\ell}$ distributions are smoothed separately in each channel using kernel estimation (RooKeysPDF). It implements an one-dimensional kernel estimation p.d.f which model the distribution of an arbitrary input dataset as a superposition of Gaussian kernels, one for each histogram entry, each contributing 1/N to the total integral of the p.d.f. The value of smoothing strength (ρ) is chosen arbitrarily trying to compromise two effects, making the distribution smooth enough without changing the original shape too much. The smoothed distributions are normalized to the data driven estimated yields. By varying the value of ρ by 0.5 two more distribution are made. They are merged in one using the largest relative difference and symmetrizing it. The symmetrized distributions are taken into account as a shape systematic uncertainty. The raw MC, the smoothed distributions as well as the shape systematic uncertainties coming from the smoothing procedure are shown in Figures 5.6, 5.7, 5.8, 5.9.

5.2.2 Irreducible background

The $m_{4\ell}$ distribution for the ZZ continuum background is taken from MC simulation and parameterised by an empirical function for each of the quark-initiated processes, $q\bar{q} \to ZZ$, gluon-initiated processes, $gg \to ZZ$, and electroweak vector boson scattering, $q\bar{q} \to ZZ$ (EW):

$$f(m_{4\ell}) = C_0 H(m_0 - m_{4\ell}) f_1(m_{4\ell}) + H(m_{4\ell} - m_0) f_2(m_{4\ell}), \tag{5.1}$$

where,

$$\begin{aligned}
f_1(x) &= \left(\frac{x-a_4}{a_3}\right)^{a_1-1} \left(1+\frac{x-a_4}{a_3}\right)^{-a_1-a_2}, \\
f_2(x) &= \exp\left[b_0 \left(\frac{x-b_4}{b_3}\right)^{b_1-1} \left(1+\frac{x-b_4}{b_3}\right)^{-b_1-b_2}\right], \\
C_0 &= \frac{f_2(m_0)}{f_1(m_0)}.
\end{aligned}$$

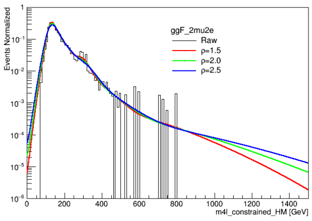

(a) $2e2mu$

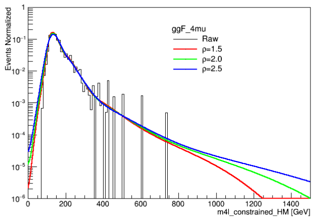

(b) $4mu$

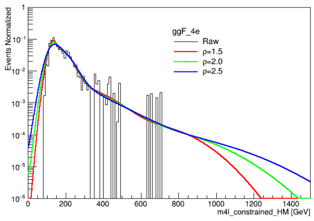

(c) $4e$

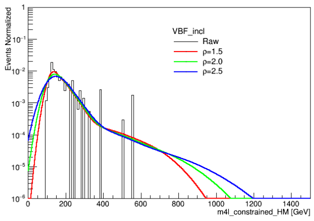

(d) VBF

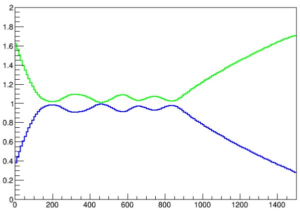

(e) $2e2mu$

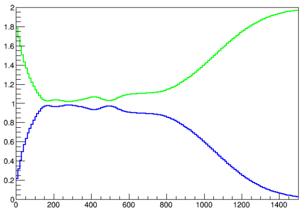

(f) $4mu$

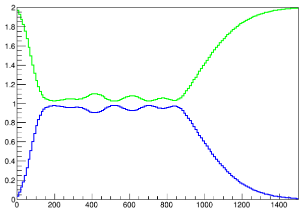

(g) $4e$

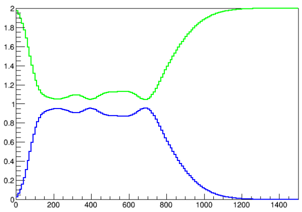

(h) VBF

Figure 5.6: Raw and smoothed and shape systematic uncertainties $m_{4\ell}$ distributions for the Zjets background component in each cut based analysis channel.

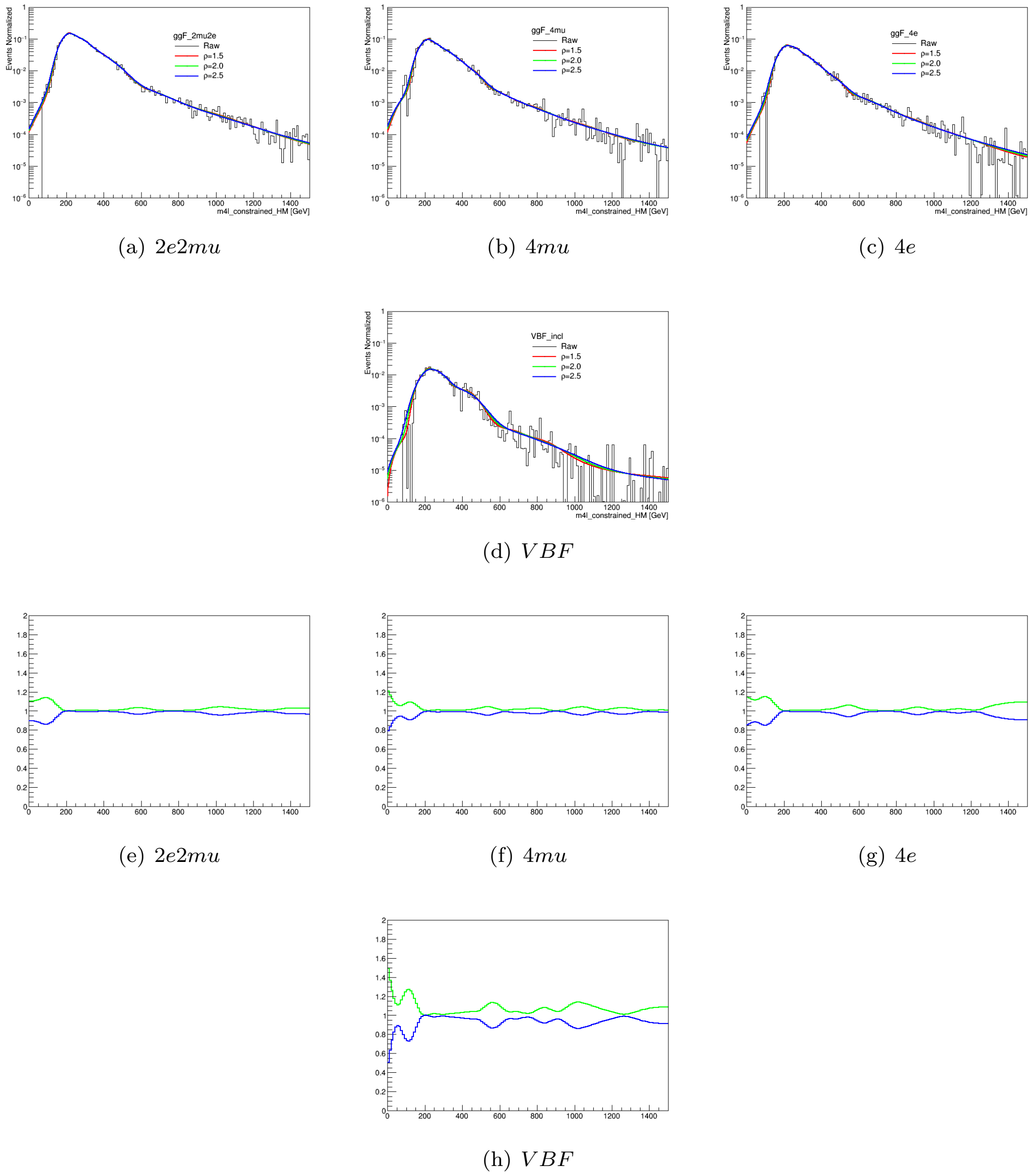

(a) $2e2mu$ (b) $4mu$ (c) $4e$

(d) VBF

(e) $2e2mu$ (f) $4mu$ (g) $4e$

(h) VBF

Figure 5.7: Raw and smoothed and shape systematic uncertainties $m_{4\ell}$ distributions for the VVV background component in each cut based analysis channel.

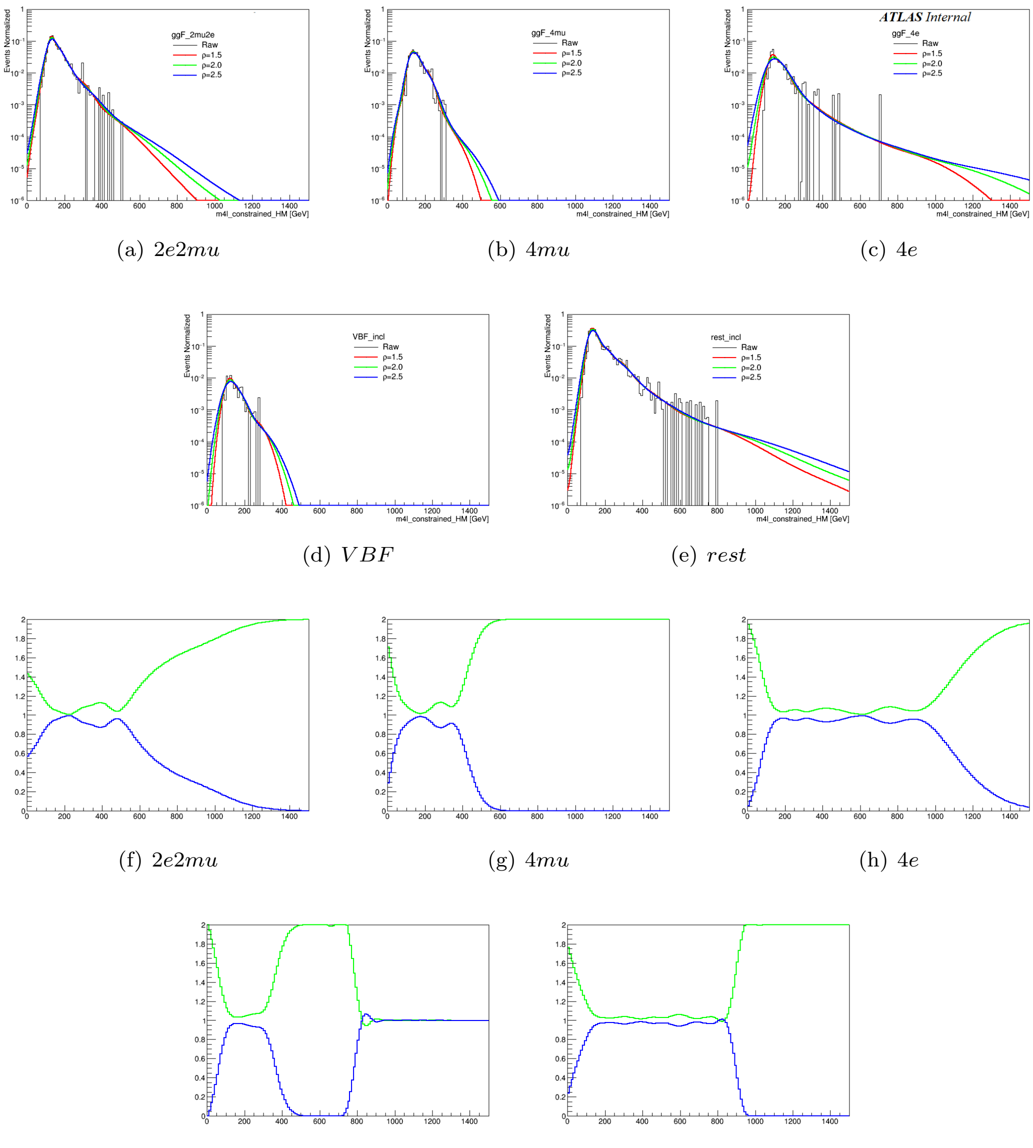

(a) $2e2mu$ (b) $4mu$ (c) $4e$

(d) VBF (e) $rest$

(f) $2e2mu$ (g) $4mu$ (h) $4e$

(i) VBF (j) $rest$

Figure 5.8: Raw and smoothed (a-e) and shape systematic uncertainties (f-j) $m_{4\ell}$ distributions for the Zjets background component in each NN based analysis channel.

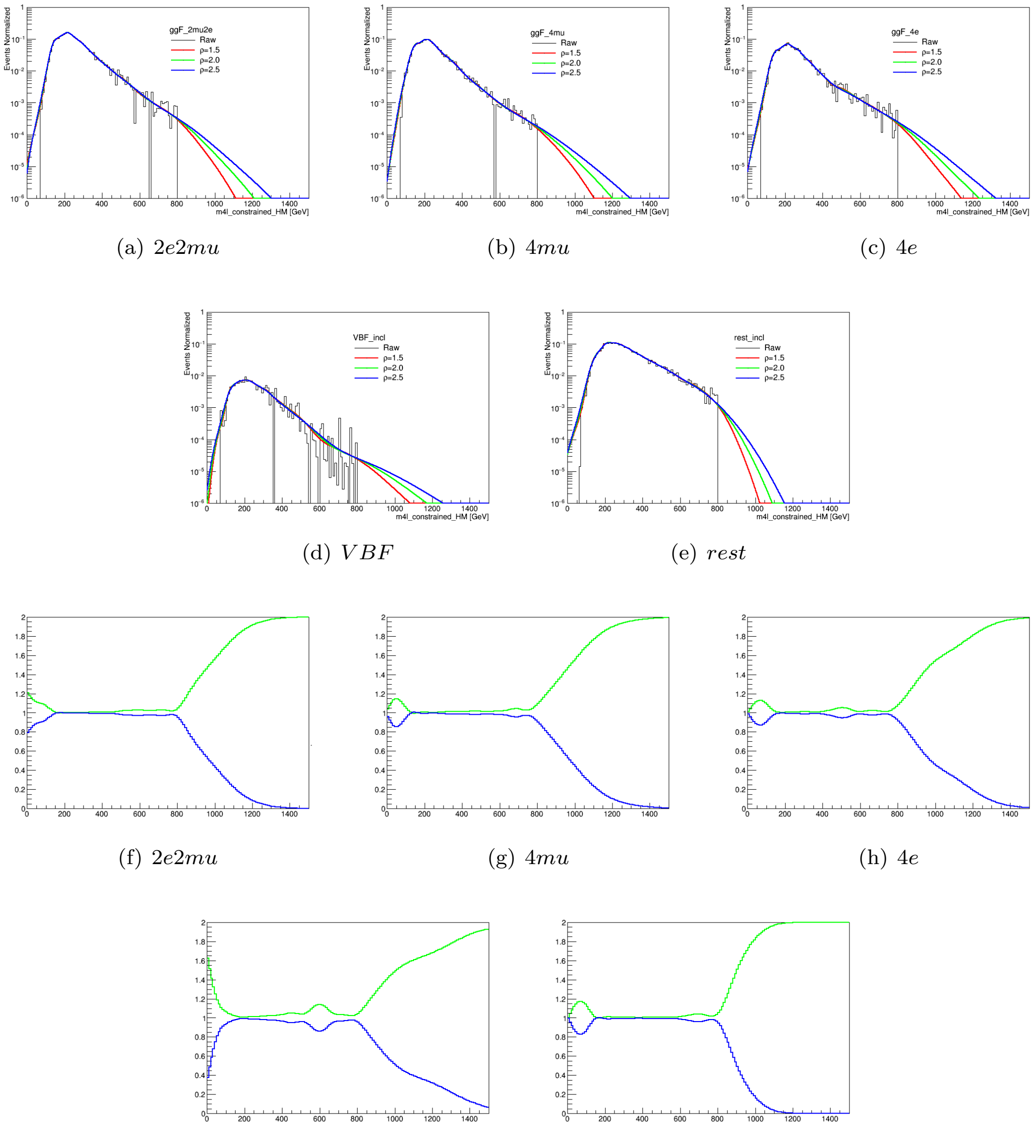

(a) $2e2mu$ (b) $4mu$ (c) $4e$

(d) VBF (e) $rest$

(f) $2e2mu$ (g) $4mu$ (h) $4e$

(i) VBF (j) $rest$

Figure 5.9: Raw and smoothed (a-e) and shape systematic uncertainties (f-j) $m_{4\ell}$ distributions for the VVV background component in each NN based analysis channel.

The function's first part, f_1, covers the low-mass part of the spectrum where one of the Z bosons is off-shell, while f_2 models the ZZ threshold around $2 \cdot m_Z$ and f_3 describes the high-mass tail. The transition between low- and high-mass parts is performed by the Heaviside step function $H(x)$ around $m_0 = 240$ GeV. The continuity of the function around m_0 is ensured by the normalisation factor C_0 that is applied to the low-mass part. Finally, a_i, b_i and c_i are shape parameters which are obtained by fitting the $m_{4\ell}$ distribution in simulation for each category. The uncertainties in the values of these parameters from the fit are found to be negligible. The MC statistical uncertainties in the high-mass tail are taken into account by assigning a 1% uncertainty to c_4.

5.2.3 Signal

In the case of a narrow resonance, the width in $m_{4\ell}$ is determined by the detector resolution, which is modelled by the sum of a Crystal Ball ($\mathcal{C}$) and a Gaussian ($\mathcal{G}$) function, hereafter referred to as the $\mathcal{C}+\mathcal{G}$ distribution:

$$P_s(m_{4\ell}) = f_{\mathcal{C}} \cdot \mathcal{C}(m_{4\ell}; \mu, \sigma_{\mathcal{C}}, \alpha_{\mathcal{C}}, n_{\mathcal{C}}) + (1 - f_{\mathcal{C}}) \cdot \mathcal{G}(m_{4\ell}; \mu, \sigma_{\mathcal{G}}). \tag{5.2}$$

The Crystal Ball and the Gaussian functions share the same peak value of $m_{4\ell}$ (μ), but have different resolution parameters, $\sigma_{\mathcal{C}}$ and $\sigma_{\mathcal{G}}$. The $\alpha_{\mathcal{C}}$ and $n_{\mathcal{C}}$ parameters control the shape and position of the non-Gaussian tail[1] and the parameter $f_{\mathcal{C}}$ ensures the relative normalisation of the two probability density functions. The ggF and VBF production modes are found to have similar $m_{4\ell}$ spectra, therefore only the distributions from ggF production are presented here. The $\mathcal{C}+\mathcal{G}$ function parameters are determined separately for each final state by fitting to signal simulation, and are then fitted with a polynomial in scalar mass m_H to interpolate between the generated mass points. The order of the polynomial is determined by first fitting a third-order polynomial and decreasing its order until the the magnitude of the highest-order term is greater than its associated error (to avoid over-fitting). The use of this parameterization for the function parameters introduces an additional bias in the signal yield and m_H.

5.3 Statistical Treatment and results

The goal of this analysis is the search for a new BSM Higgs-like particle in the 200–2000 GeV mass range. Fits are performed for several mass points in order to check for any excess in the data and exclusion limits for a new particle are set. The statistical treatment uses workspaces within RooFit [153] and RooStats [154] frameworks .

5.3.1 Search for new particles

A H_1 hypothesis, which includes both signal and background, has to be tested against the H_0 hypothesis including only background, for every possible mass. A likelihood fit is used to extract a test statistic variable to discriminate the 2 alternative hypotheses. Depending on the experiment discrimination ability (sensitivity) an upper limit on new particle production cross section can be set. The expected upper limit at 95% Confidence Level is calculated for every mass and compared to the observed values from data. Lastly the look elsewhere affect has to be taken into account, as when the search is performed in a wide mass range, a random background fluctuation in a random mass may be misinterpreted as signal.

[1] $\alpha_{\mathcal{C}}$ is a measure of how far from the peak the distribution becomes non-Gaussian, while $n_{\mathcal{C}}$ is related to the slope of the tail.

The Likelihhod Function

The likelihood function is the function that returns the value of a probability density function (*pdf*) evaluated at the observed data sample. Assuming a *pdf* $f(x)$, depending on the parameters $\theta_1, ..., \theta_m$, then for a given dataset $x_1, ..., x_n$ the $\mathcal{L}$ is

$$\mathcal{L}(x_1, ...x_n; \theta_1, ..., \theta_m) = \prod_i^n f(x_i; \theta_1, ..., \theta_m) \tag{5.3}$$

If the numbers of the events in the dataset is also a random variable an extended likelihood function can defined. In case that the number of these events is a Poisson distribution (like in most particle experiments) whose average μ may also depends on the m unknown parameters, then

$$\mathcal{L}(\boldsymbol{x}; \boldsymbol{\theta}) = \frac{e^{-\mu(\boldsymbol{\theta})}\mu(\boldsymbol{\theta})^n}{n!} \prod_i^n f(x_i; \boldsymbol{\theta}) \tag{5.4}$$

The total *pdf* f can be written as superposition of two components, one *pdf* for the signal f_s and another for the background f_b, weighted by the expected signal and background fractions, respectively. The signal normalization is usually written in terms of the signal strength μ

$$f(x; \boldsymbol{\theta}) = \frac{\mu s}{\mu s + b} f_s(x; \boldsymbol{\theta}) + \frac{b}{\mu s + b} f_b(x; \boldsymbol{\theta}) \tag{5.5}$$

Substituting in the likelihood function

$$\mathcal{L}_{s+b}(\boldsymbol{x}; \boldsymbol{\theta}, \mu) = \frac{e^{-\mu s(\boldsymbol{\theta}) + b(\boldsymbol{\theta})}}{n!} \prod_i^n (\mu s \cdot f_s(\boldsymbol{x}; \boldsymbol{\theta}) + b \cdot f_b(\boldsymbol{x}; \boldsymbol{\theta})) \tag{5.6}$$

where μ can be identified as the parameter of interest while $\boldsymbol{\theta}$ as nuisance parameters. The profile likelihood ratio is defined as

$$\lambda(\mu) = \frac{\mathcal{L}(\boldsymbol{x}; \mu, \hat{\hat{\boldsymbol{\theta}}}(\mu))}{\mathcal{L}(\boldsymbol{x}; \mu, \hat{\boldsymbol{\theta}})} \tag{5.7}$$

Here $\hat{\hat{\boldsymbol{\theta}}}$ in the numerator denotes the values of $\boldsymbol{\theta}$ that maximize L for the specified μ. So it is the conditional maximum-likelihood (ML) estimator of $\boldsymbol{\theta}$ (and thus is a function of μ). The denominator is the maximized (full) likelihood function as $\hat{\mu}$ and $\hat{\boldsymbol{\theta}}$ are the ML estimators. Technically the fit is performed by minimizing the logarithm of the profile likelihood ratio

$$-2 \cdot \ln(\lambda(\mu)) \rightarrow \text{Min} \tag{5.8}$$

By definition the minimum value is equal to 0, occurring for $\mu = \hat{\mu}$ which is the observed signal strength as shown in Figure 5.10.

The test statistic

When the search of a new signal is performed any upwards fluctuation of the data can lead to a positive signal strength. A test has to be defined to show if indeed this comes from a fluctuation of the background data or from a new signal. Two possibilities have to be taken into account. Firstly the possibility of the H_0 hypothesis giving a larger signal strength than the observed. Secondly the possibility of H_1 hypothesis giving a smaller signal strength than the observed. For this reason a test statistic t_μ, which reflects the level of agreement between the data and the hypothesized value of μ, is defined

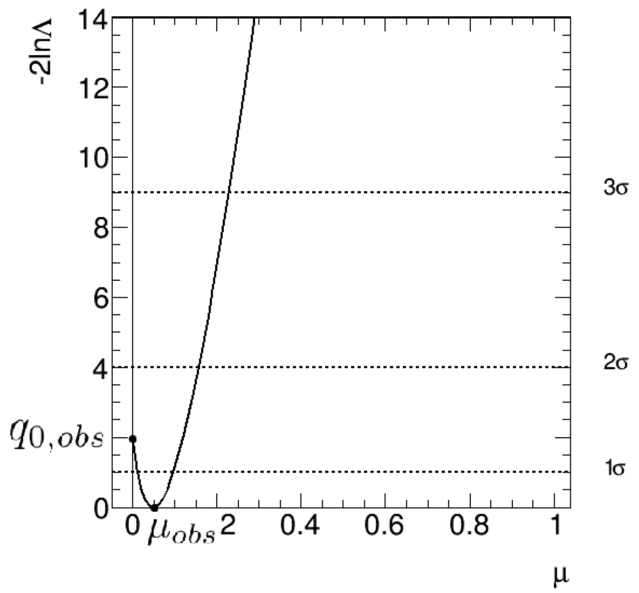

Figure 5.10: Example of likelihood function, -2lnλ as a function of μ. The minimum value is 0 occurring for $\mu = \hat{\mu} \equiv \mu_{obs}$. The error contour of the observed μ, corresponding to $N\sigma$, is defined by the $-2ln\lambda_{min} + N^2$ and it may lead to asymmetric errors.

$$t_\mu = \ln\lambda(\mu) \tag{5.9}$$

In order to assess the presence of a new signal, the hypothesis of a positive signal strength has to be tested against the background only hypothesis. This is done using the test statistic t_μ evaluated at 0, which is called q_0

$$q_0 = \begin{cases} -2 \cdot \log\left(\lambda(0)\right) & \hat{\mu} \geqslant 0 \\ 0 & \hat{\mu} < 0 \end{cases} \tag{5.10}$$

Actually, q_0 is the intersection point of the likelihood function and Y axis [2] as it is shown in Figure 5.10. The observed value of q_0, or any other q_μ depends on the specific dataset. Doing the same experiment multiple times, different values of q_μ will be observed. Its distribution depend also on the hypothetised signal strength μ' used for generating the multiple experiment datasets. So the statistic q_μ will have a sampling distribution $f(q_\mu|\mu')$. When a large number of measurements is available, Wilks' theorem allows finding an approximate asymptotic expression for a test statistic based on a likelihood ratio inspired by the Neyman–Pearson lemma [155]. According this theorem the distribution of q_μ can be approximated by a χ^2 distribution with one degree of freedom. In case that the μ that is used for generating the experiments is the same as the μ used for the test statistic the chi^2 distribution is centred on 0. Otherwise it is centered on larger q_μ as it is shown in Figure 5.11. As the difference beteween the μ and the μ' becomes larger the center of the distribution moves to larger values. The sampling distribution can also be estimated using a large number of pseudoexperiments. The degree of agreement between the two methods was studied in detail in [155] and it was found sufficiently good.

[2]Generally q_μ is the intersection point of the likelihood function and the line $x = \mu$

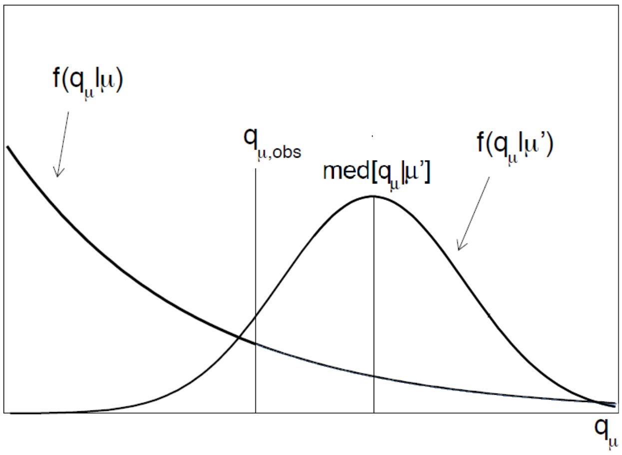

Figure 5.11: Illustration of q_μ distribution made under the assumptions of μ and μ'.

The expected and observed limits

For defining the CLs [156], using the q_0 as test statistic, the probability that a signal + background hypothesis gives a larger value of q_0 than the observed is divided by the probability that the background only hypothesis gives a smaller q_0 than the observed. Usually the value 95% is used for the CL. This condition is summarized in equation 5.11

$$CLs = \frac{p_{s+b}}{1-p_b} = 95\% \tag{5.11}$$

where

$$p_{s+b} = \int_{q_{0,obs}}^{\infty} f(q_0|\mu) dq_0 \tag{5.12}$$

and

$$p_b = \int_{q_{0,obs}}^{\infty} f(q_0|0) dq_0 \tag{5.13}$$

In order to find the μ which satisfies the equation 5.11 an iteration on different μ is performed. For larger values of μ the distribution $f(q_0|\mu)$ is shifted to larger q_0. The first μ for which the equation 5.11 is satisfied is the smallest μ that can be excluded at 95% CL and this is the upper limit for exclusion at this CL.

The sensitivity of an experiment to exclude a new particle is the median upper limit. So the expected sensitivity of an experiment is determined not from a random observed value of q_0 but from its median value. The median value of any distribution $f(q_\mu|\mu')$ can be obtained using the Asimov Dataset. This dataset is defined such as when one uses it to evaluate the estimators for all parameters, one obtains the true parameter values. Thus when the Likelihood fit is performed on a Asimov dataset the observed q_μ takes its median value, offering a pragmatic and CPU efficient solution to obtain the median experimental sensitivity of a search or measurement as well as fluctuations about this expectation. The procedure to find the expected smallest value of the μ that can be excluded at a CL 95% is the same as the observed but using the median value of q_0, instead the observed.

It is also useful to know by how much the sensitivity is expected to vary, given the expected fluctuations in the data. As the observed value of μ is Gaussian distributed around the μ', these error bands are simply the quantiles that map onto the variation of $\hat{\mu}$ of $\pm$Nσ about μ'. The standard deviation σ of $\hat{\mu}$ can be obtained from the Asimov value of the test statistic q_0. The profile ratio likelihood function can be approximated by a 2nd order polynomial

$$-2log\lambda(\mu) \approx \frac{(\mu-\hat{\mu})^2}{\sigma^2} + \mathcal{O}(1/\sqrt{N}) \tag{5.14}$$

As the Asimov data set corresponding to a strength μ' gives $\mu' = \hat{\mu}$

$$-2log\lambda_A(\mu) \approx \frac{(\mu-\hat{\mu})^2}{\sigma^2} \tag{5.15}$$

subtituing for $q_{0,A} = -2log\lambda_A(0)$ it yields

$$\sigma_A^2 = \frac{\mu'^2}{q_{0,A}} \tag{5.16}$$

The expected and observed limits from the SM Higgs boson discovery are shown as an example in Figure 5.12.

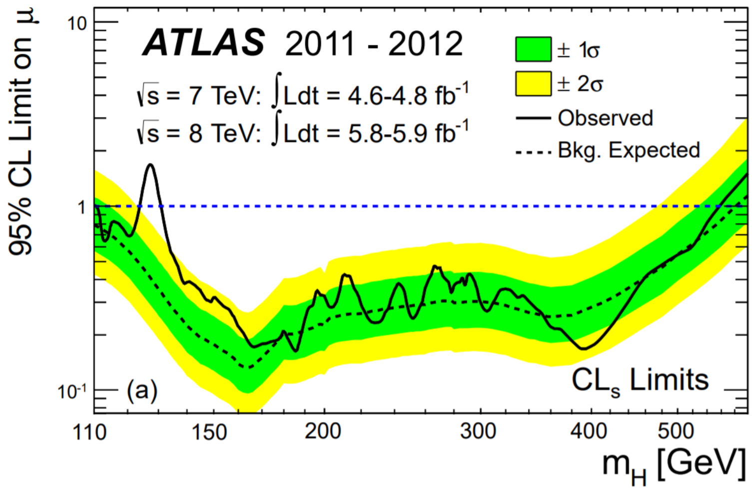

Figure 5.12: The upper limit on the Standard Model Higgs boson production cross section divided by the Standard Model expectation as a function of m_H is indicated by the solid line. This is a 95% CL limit using the CLs method. The dotted line shows the median expected limit and the green and yellow bands reflect the corresponding 1 and 2 σ error bands [20].

The systematic uncertainties

The dependence of the expected number of signal and background events and the shape of the PDFs on the systematic uncertainties is described by a set of nuisance parameters (NP). Gaussian constraints are used to constrain the NPs to their nominal values within their estimated uncertainties. The constraints are implemented via additional 'penalty' terms added to the likelihood which will increase the negative log likelihood when any nuisance parameter is shifted from its nominal value. The terms are constructed with template morphing techniques on the expected and $\pm 1\sigma$ distributions. The best fit values for the gaussian mean and sigma of each parameter may be different than these which were initially inserted in the model. The presence of the nuisance parameters $\boldsymbol{\theta}$ broadens the profile likelihood ratio as a function of μ relative to what one would have if their values were fixed. This reflects a decrease of the expected sensitivity. In order to check the effect of each systematic uncertainty on the parameter of interested the fit is redone fixing the specific nuisance parameter at

± 1 pre-fit and post-fit sigmas ($\Delta\theta$ and $\Delta\hat{\theta}$ = uncertainty on $\hat{\theta}$). Impact is extracted as difference in central value of μ.

The effect on the parameter of interest before and after the fit for both $\pm 1\sigma$, as well the value of the parameter after the fit and its error are typically plotted in the "ranking plot" (Figure 5.13) which sorts the systematic uncertainties according to their effect. The pull of the mean value, as well the the after fit sigma is shown. The decreased impact on μ after the fit reflects the possibility that this nuisance parameter is correlated to others. Also a smaller error bar on the pull shows that the uncertainty of the specific parameter is further constrained from the data.

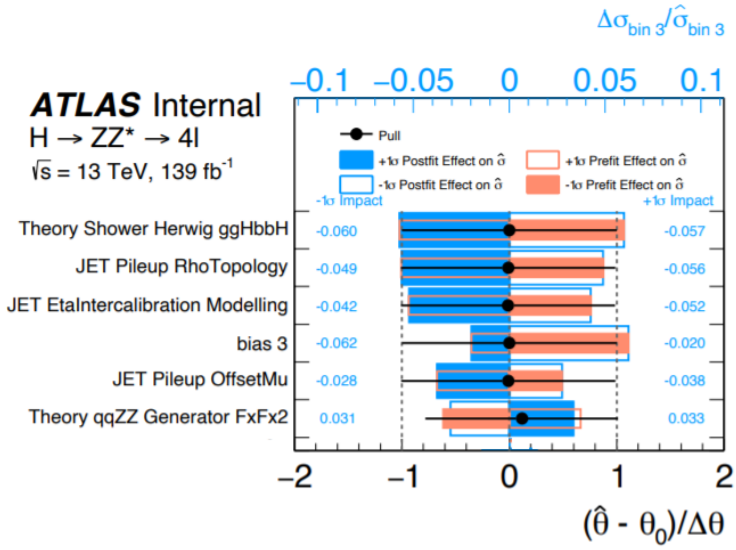

Figure 5.13: Example of nuisance parameters ranking plot [157]

The look elsewhere effect

In a search for a new particle, whose mass is not predicted by theory a wide ranges of masses has to be checked. If an excess in data, compared with the background expectation, is found at any mass value, the excess could be interpreted as a possible signal of a new resonance at the observed mass. The peak could be produced either by the presence of a real new signal or by a background fluctuation. The significance of an observation of an excess in the specific mass is called local significance. The significance of an observation of an excess in any mass is called global significance. One way to compute the local significance of the new signal is to use the p-value corresponding to the measured test statistic q assuming a fixed value m_0 of the resonance mass m. In this case

$$p^{m_0} = \int_{q_{0,obs}^{m_0}}^{\infty} f(q^{m_0}|0)dq \tag{5.17}$$

so $p(m_0)$ gives the probability that a background fluctuation at a fixed value of the mass m_0 results in a value of q greater or equal to the observed value $q_{0obs}(m_0)$.

The probability of a background fluctuation at any mass value in the range of interest is called global p-value and is in general larger than the local p-value. So, the local significance is an underestimate, if interpreted as global significance. In general, the effect of the reduction of significance, when evaluated from local to global, in case one or more parameters of interest are determined from data, is called look elsewhere effect [158]. The global significance can be calculated using the test statistic q_0 which comes from he largest value of the estimator over the entire parameter range

$$p^{glob} = \int_{q_{0,obs}^{glob}}^{\infty} f(q^{glob}|0) dq^{glob} \tag{5.18}$$

In this case the distribution of $f(q_0^{glob}|0)$ cannot be approximated by a χ^2 as Wilks' theorem cannot be applied. An approximate way to determine the global significance taking into account the look elsewhere effect is described in Ref. [159].

5.3.2 Systematic uncertainties

The uncertainties are divided into three categories: experimental uncertainties, uncertainties on the modeling of background processes, and theoretical uncertainties on the signal processes. In the statistical analysis each systematic uncertainty is treated as a nuisance parameter. The calculation of the experimental systematic uncertainties is done as follows. First, the four-lepton invariant mass ($m_{4\ell}$) distribution is considered using the standard weights and a nominal configuration of the NPs—the *nominal distribution*. Then, for each NP, the $m_{4\ell}$ distribution is made using a one sigma (σ) variation of the NP in question—the *modified distribution*. The variation is considered for the "up" and "down" configuration of the NP ($\pm 1\sigma$). For NPs that only affect the normalisation of the distribution, the relative change of the total event yield from the modified distribution is compared to that of the nominal distribution. For NPs that also affect the shape of the $m_{4\ell}$ distribution, the relative change to the mean and RMS of the modified distribution with respect to the nominal distribution is also calculated. These shape variations are used to construct an analytical variation to the distribution.

The signal and background predictions used in this study are affected by a variety of sources of experimental systematic uncertainty. The dominant experimental systematic uncertainties arise from the energy/momentum scales and reconstruction and identification efficiencies of the leptons and jets. Several sub-dominant systematic uncertainties are considered. The systematic uncertainties are calculated using the recommendations from the Combined Performance (CP) groups. The standard set of systematics is made of 96 nuisance parameters.

For simulated signal and backgrounds, theoretical modelling uncertainties associated with the PDFs, missing QCD higher-order corrections (via variations of factorisation and renormalisation scales), parton showering and electroweak higher-order correction are considered.

For the irreducible ZZ background, PDF and QCD scale uncertainties affect the overall normalisation, the shape of the $m_{4\ell}$ distribution and the acceptance originating from the event selection. For QCD scale uncertainties, these effects are studied with generated truth events by comparing weights corresponding to variations of the renormalization and factorization scale factors, up and down by a factor of two, envelop of different variations are used. PDF uncertainties include the standard deviation of 100 PDF replicas of NNPDF3.0 NNLO, and as well comparison to MMHT2014 NNLO, CT14 NNLO.

For signal hypotheses, the theoretical modelling uncertainties of missing QCD higher-order corrections and different PDF and parton shower variations are considered by using the method described above for backgrounds. The missing QCD higher-order corrections are accounted for by varying the scales in *MGMCatNLO* and are the largest uncertainties that affect the signal acceptance.

5.3.3 Results for the cut-based analysis

The results of cut-based analysis are presented in this section. Firstly the fit procedure is validated using Asimov data and then it is applied on the observed data. The expected and observed limits for both ggF and VBF production are calculated at 95% CL. Table 5.7 shows the expected and observed numbers of events for 139^{-1} of pp collision data in the four cut-based channels ($ggF_2e2\mu$, $ggF_4\mu$, ggF_4e, VBF_incl) .

Category	$q\bar{q} \to ZZ$	$q\bar{q} \to ZZ$ EW	$gg \to ZZ$	$Z + jets, t\bar{t}, WZ$	ttV, VVV	Expected	Observed
$2\mu 2e$	1352.6 ± 3.0	12.1 ± 0.1	169.9 ± 0.5	9.1 ± 0.8	26.8 ± 0.3	1570.5 ± 3.1	1656
$4e$	467.0 ± 2.0	4.4 ± 0.1	65.7 ± 0.3	3.5 ± 0.4	11.8 ± 0.2	552.4 ± 2.1	612
4μ	779.9 ± 2.6	6.9 ± 0.2	103.1 ± 0.4	3.0 ± 0.2	16.3 ± 0.2	909.2 ± 2.7	932
VBF	43.5 ± 0.6	10.9 ± 0.2	11.6 ± 0.1	0.6 ± 0.0	3.0 ± 0.1	69.6 ± 0.6	75
Total	2643.0 ± 4.5	34.3 ± 0.3	350.3 ± 0.7	16.2 ± 0.9	57.9 ± 0.4	3101.7 ± 4.7	3275

Table 5.7: Expected and observed numbers of events for $m_{4\ell} > 200$ GeV in the cut-based channels.

Fit Configuration

Limits on additional Higgs bosons are obtained using unbinned profile likelihood fits, using $m_{4\ell}$ as the discriminant. The likelihood function is a product of a Poisson term representing the probability for observing n events and a weighted sum of both signal and background probability distribution functions (PDFs) evaluated at all observed events.

$$\mathcal{L}(x_1..x_n|\sigma_{ggF}, \sigma_{VBF}) = \text{Pois}(n|S_{ggF} + S_{VBF} + B)\left[\prod_{i=1}^{n} \frac{S_{ggF} f_{\text{ggF}}(x_i) + S_{VBF} f_{\text{VBF}}(x_i) + B f_{\text{B}}(x_i)}{S_{ggF} + S_{VBF} + B}\right] \tag{5.19}$$

The terms f_{ggF}, f_{VBF}, and f_B are the PDFs describing the signal and background models. Implicit in this likelihood is the dependence of the pdfs (f_X) and normalizations (S_X and B) within the product on the analysis category of each event. Also implicit is that the factors B and $f_{\text{B}}(x_i)$ represent all different background contributions combined, each having different PDFs and yields.

The parameters of interest (POI) in the fit are σ_{ggF} (XS_ggF)and σ_{VBF} (XS_VBF). In setting a limit on one, the other is either fixed at 0, or profiled along with other nuisance parameters (except left unconstrained) during the minimization. These POI enter the likelihood inside the expected signal yields S_{ggF} and S_{VBF} as follows:

$$S_{ggF(VBF)} = \sigma_{ggF(VBF)} \times BR(S \to ZZ \to 4\ell) \times A \times C \times \int \mathcal{L}dt \tag{5.20}$$

where $A \times C$ is the signal acceptance and $\int \mathcal{L} = 139^{-1}$ is the integrated luminosity of the dataset.

The normalization of the major ZZ background is a free parameter in the fit (μ_{ZZ}) and it is profiled when fitting to the data. The advantage of floatting ZZ normalization in the fit is to reduce the dependence on theory prediction and associated uncertainties, especially given that the increased data luminosity would provide precise determination of the background rate. Thanks to the excellent discrimination power of $m_{4\ell}$ distribution between the SM background and the resonant signal, the floatting ZZ normalization in the fit would not affect the expected signal sensitivity. Two floating variables are used, one common for the ggF channels (muZZ_ggF) and one for the VBF channel (muZZ_VBF).

The dependence of the expected number of signal and background events and the shape of the PDFs on the systematic uncertainties is described by a set of nuisance parameters (NP) θ_i. Gaussian constraints are used to constrain the NPs to their nominal values within their estimated uncertainties.

The constraints are implemented via additional 'penalty' terms added to the likelihood which will increase the negative log-likelihood when any nuisance parameter is shifted from its nominal value. The final likelihood function $\mathcal{L}(\sigma_{ggF}, \sigma_{VBF}, m_H, \theta_i)$, is therefore a function of $\sigma_{ggF}, \sigma_{VBF}, m_H$, and θ_i. The fit includes all the theory and experimental systematic uncertainties as described in 5.3.2. It also includes uncertainties coming from the parametrization of the signal and ZZ backgrounds and from the DDE and smoothing of the Z+jets background. In addition to these uncertainties, there also exist systematic uncertainties related to the total integrated luminosity and trigger inefficiencies. The uncertainty in the combined 2015-2018 integrated luminosity is 1.7% [160]. A systematic uncertainty of 0.5% is considered for the μ trigger efficiency differences in the data and the simulation. These two normalization uncertainties are only applied to background or signal processes that are estimated by MC simulation. For the ZZ backgrounds these two normalization uncertainties are not applied as there are floating.

The upper limit for the cross-section $\sigma_{ggF(VBF)}$ at a given theorised Higgs-mass is obtained by setting the m_H parameter constant at the desired value and maximising the likelihood function with respect to nuisance parameters. The test statistics q_μ is used to set upper limits following [161]. In order to measure the compatibility of the data with the background-only hypothesis ($\sigma_{ggF} = \sigma_{VBF} = 0$), the test statistic q_0 is used. The CL_s [162] method is used to obtain exclusion limits.

Fit on Asimov data

To check the fit validity a signal+background scenario is simulated with Asimov data. The scenario is made with $m_H = 700$ GeV, XS_ggF=0.1, fb^{-1}, muZZ_VBF=1.0 and muZZ_ggF=1.1. The systematic uncertainties have been excluded for the Asimov data fits. The prefit background and signal models as well the Asimov data are drawn as shown if Figure 5.14. The excess of Asimov data coming from the signal (around 700 GeV) as well this coming from the normalization of ZZ_ggF (across full mass range) are obvious.

Firstly a test is performed to check if the correct background normalization can be achieved. Therefore it is performed by setting both the signal cross sections equal to 0. The background in the ggF channels fits the Asimov data yielding a MC/data ratio about 1 as shown in Figure 5.15. The narrow width of the signal allows the successful fit in such a case.

Then the complete fit is performed. All the four variables XS_ggF, XS_VBF, muZZ_VBF and muZZ_ggF are fitted simultaneously but the XS_ggF is assumed to be the parameter of interest. The signal model fits the excess of data around 700 GeV yielding XS_ggF=0.1 fb and XS_VBF=0. The excess of events in the VBF channel is correctly attributed to ggF migrated events. The ggF background normalization is again changes to fit excess of data in ggF channels. The after fit distributions are shown in Figure 5.16.

The likelihood function for the XS_ggF is shown in Figure 5.17(c). The minimum occurs for XS_ggF=0.1 fb as it is expected. Performing the fit by setting a different m_H the minimum occurs in smaller values as shown in Figures 5.17(a),5.17(b), 5.17(d) and 5.17(e). The expected and observed upper limits on the cross section times branching ratio around 700 GeV are shown in Figure 5.17(f). The discrepancy between the expected and observed limits indicates a signal- like excess in the data.

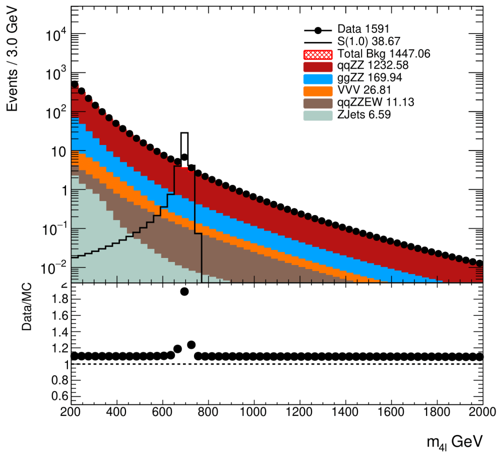

(a) $2e2\mu$

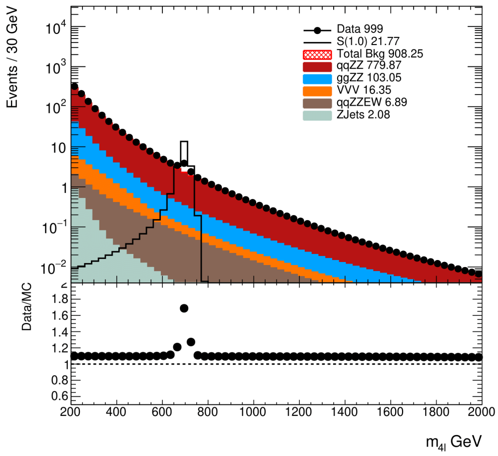

(b) 4μ

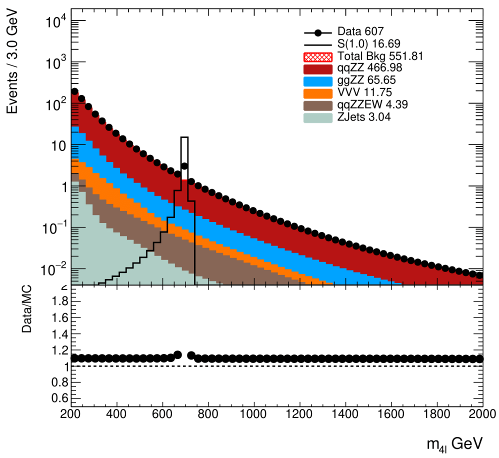

(c) $4e$

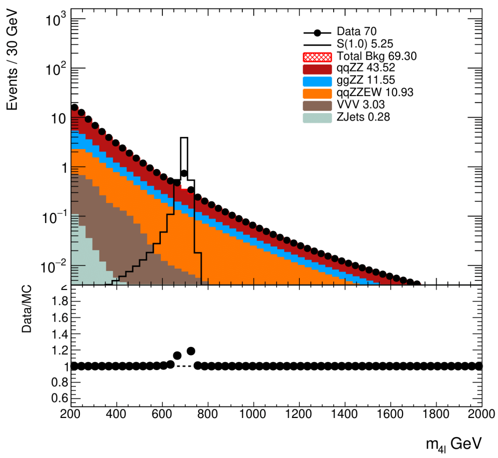

(d) VBF

Figure 5.14: Prefit distributions of m_4l and number of events in each analysis channel. Asimov data representing a signal + background scenario with $m_H = 700$ GeV, XS_ggF=0.1 fb, XS_VBF=0 fb, muZZ_VBF=1.0 and muZZ_ggF=1.1 are shown. A signal distribution of arbitrary cross section is also shown. The lower panel shows the ratio between data and background only hypothesis.

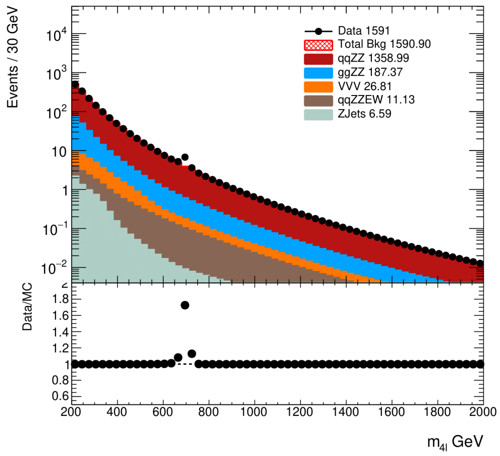

(a) $2e2\mu$

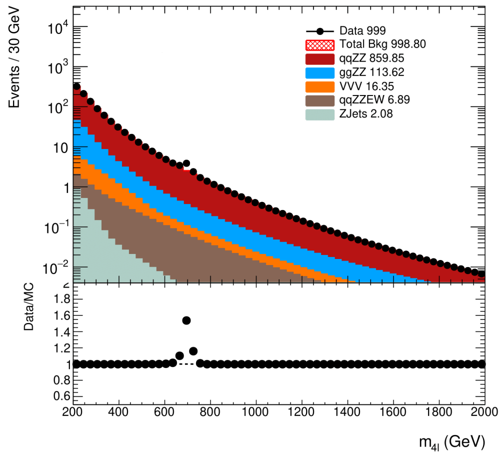

(b) 4μ

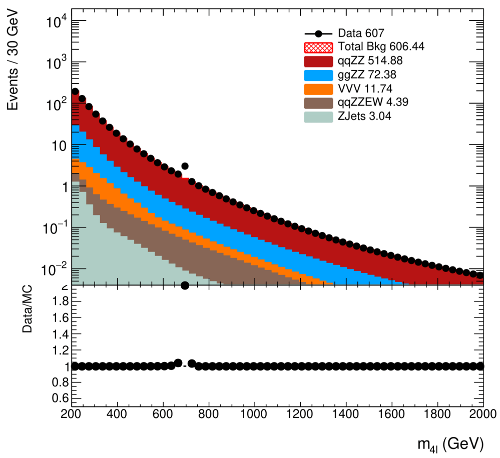

(c) $4e$

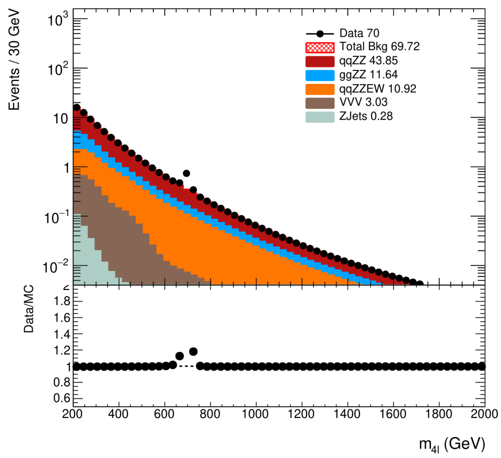

(d) VBF

Figure 5.15: Distributions of m_4l and number of events in each analysis channel after fitting the background only hypothesis. Asimov data representing a signal + background scenario with m_H = 700 GeV, XS_ggF=0.1 fb, XS_VBF=0 fb, muZZ_VBF=1.0 and muZZ_ggF=1.1 are also shown. Fit was performed by setting XS_ggF=0 add XS_VBF=0. Good agreement between the background model and the data is observed.The lower panel shows the ratio between data and background only hypothesis.

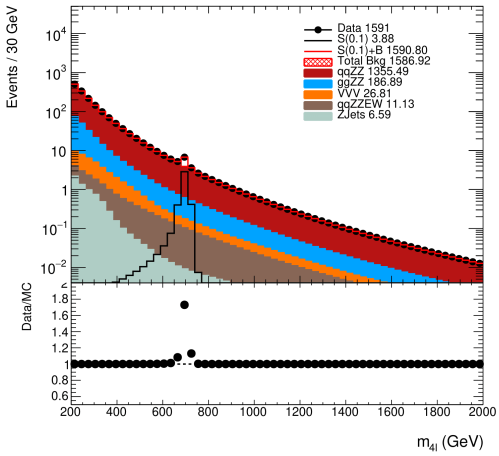

(a) $2e2\mu$

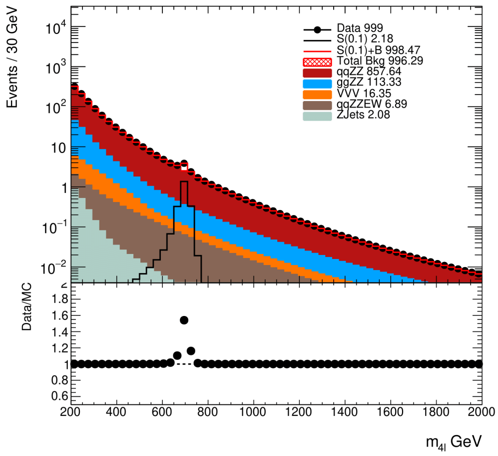

(b) 4μ

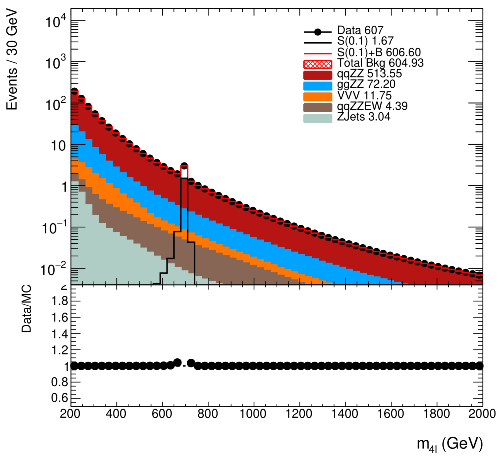

(c) $4e$

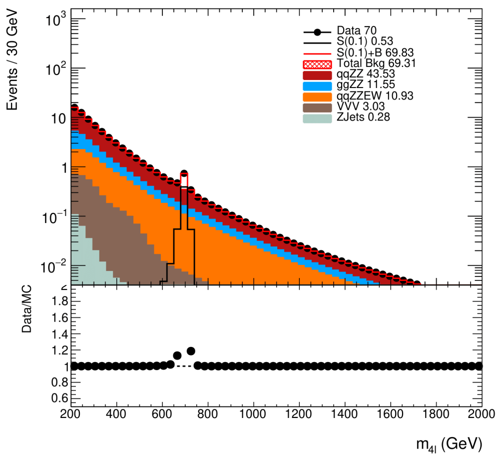

(d) VBF

Figure 5.16: Distributions of m_4l and number of events in each analysis channel after fitting the signal + background hypothesis. Asimov data representing a signal + background scenario with m_H = 700 GeV, XS_ggF=0.1 fb, XS_VBF=0 fb, muZZ_VBF=1.0 and muZZ_ggF=1.1 are also shown. Fit was performed by setting m_H = 700 GeV. Good agreement between the signal + background model and the data is observed.The lower panel shows the ratio between data and background only hypothesis.

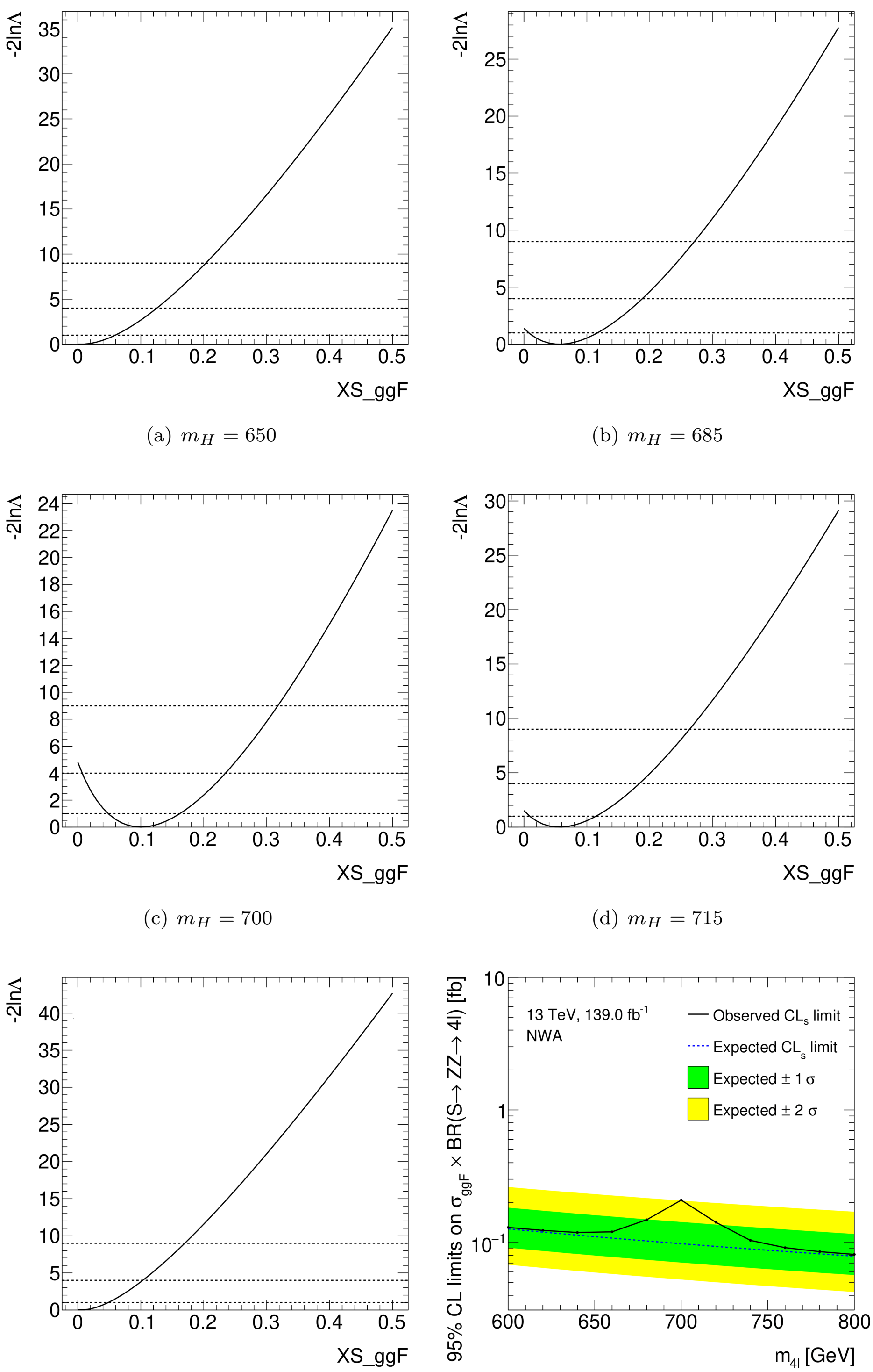

(a) $m_H = 650$

(b) $m_H = 685$

(c) $m_H = 700$

(d) $m_H = 715$

(e) $m_H = 750$

(f) *CL*

Figure 5.17: Likelihood functions for different mass points (a-e) and expected and observed limits (f). Fit was performed in Asimov data representing a signal + background scenario with $m_H = 700$ GeV, XS_ggF=0.1 fb, XS_VBF=0 fb, muZZ_VBF=1.0 and muZZ_ggF=1.1. For the hypothesised mass ($m_H = 700$ GeV) the expected XS_ggF=0.1 minimizes the likelihood function. The observed CL for this mass clearly exceeds the expected.

Fit on observed data and results

Lastly the fit is performed on the observed data. The normalization of the ZZ background is taken from data using two different normalization factors (muZZ) in ggF and VBF categories. Table 5.8 lists the value of ZZ normalization factors under a background only fit to observed data. The case for $m_H = 700$ is shown in Figure 5.18.

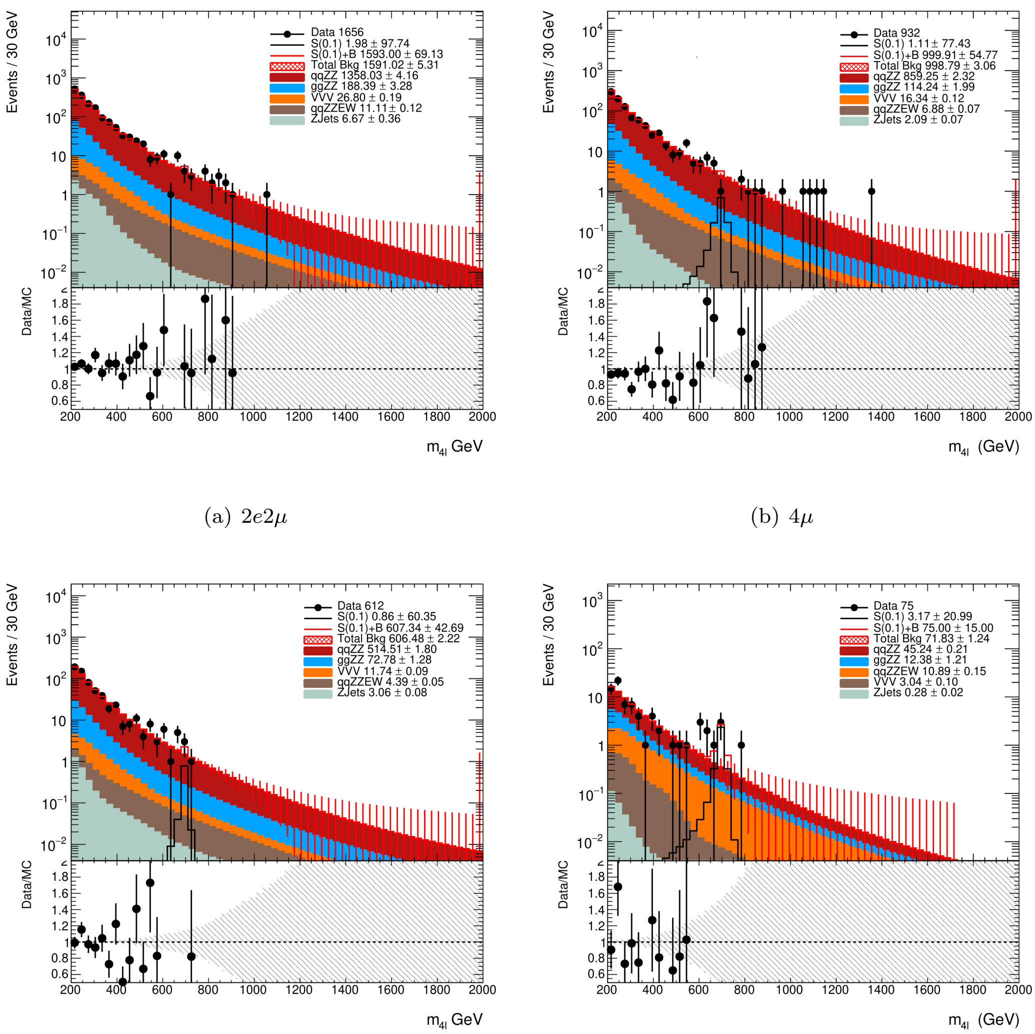

(a) $2e2\mu$

(b) 4μ

(c) $4e$

(d) VBF

Figure 5.18: Distributions of m_4l and number of events in each analysis channel after fitting the signal + background hypothesis on the observed data. Fit was performed by setting $m_H = 700$ GeV. No one significant excess of data is observed. The lower panel shows the ratio between data and background only hypothesis.

Upper limits on the cross section times branching ratio for a heavy resonance are obtained as a function of m_H with the CL_s procedure in the asymptotic approximation for the NWA scenarios. Figure 5.19 shows the expected and observed limit at 95% CL on $\sigma \times BR(S \to ZZ \to 4\ell)$ of a narrow scalar resonance for both the ggF and VBF production mode, with the integrated luminosity of the 2015-18 dataset, 139^{-1}.

To inspect the likelihood model, pulls and constraints of nuisance parameters (NP), as well as the

	Value	Error
muZZ_ggF	1.1031e+00	2.30e-02
muZZ_VBF	1.0950e+00	1.80e-01

Table 5.8: Values and errors of ZZ background normalization factors in different categories.

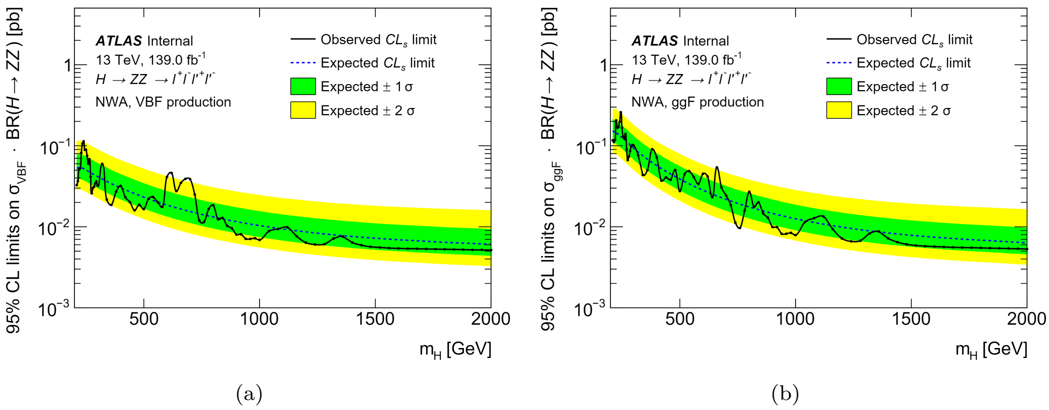

Figure 5.19: The expected and observed upper limits at 95% confidence level on $\sigma \times BR(S \to ZZ \to 4\ell)$ using the cut-based analysis for ggF (left) and VBF (right) production. The green and yellow bands represent the $\pm 1\sigma$ and $\pm 2\sigma$ uncertainties in the expected limits.

correlation matrix, are studied using both Asimov data and observed data. Figure 5.20 shows the NP pulls and constraints after a background only fit to Asimov data (top) and observed data (bottom). The correlation matrix is shown in Figure 5.21, only for the nuisances parameters with correlation larger than 0.1.

To check the impact of systematic uncertainties on expected signal sensitivity, a NP ranking study is performed using signal injected Asimov data, with injected signal cross-section close to the expected upper limit. The results are shown in Figure 5.22.

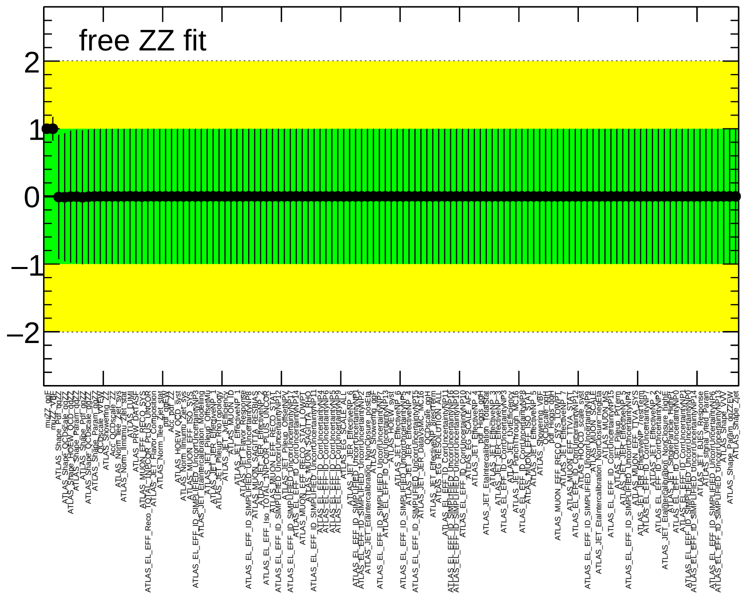

(a)

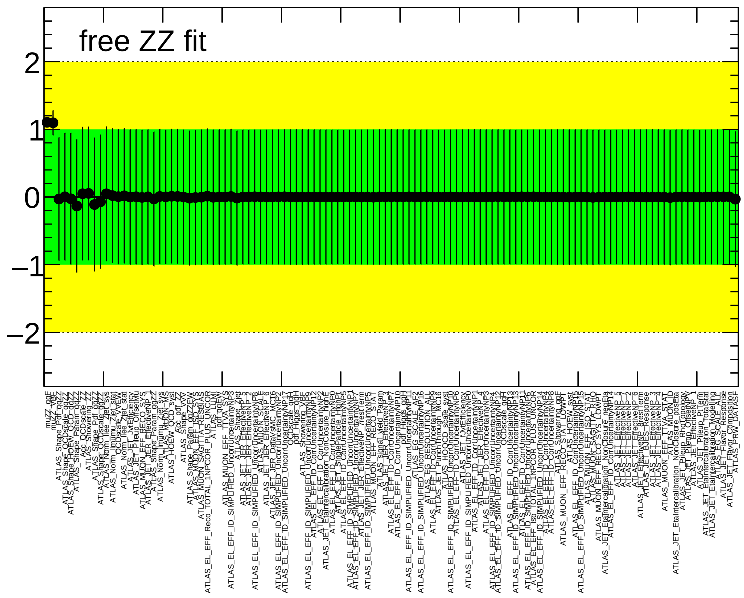

(b)

Figure 5.20: Pulls and constraints of nuisance parameters after a background only fit to (a) Asimov data and (b) observed data in the $\ell^+\ell^-\ell^+\ell^-$ channel. The Asimov data is generated with background data only, while the observed data includes datasets from 2015 to 2018.

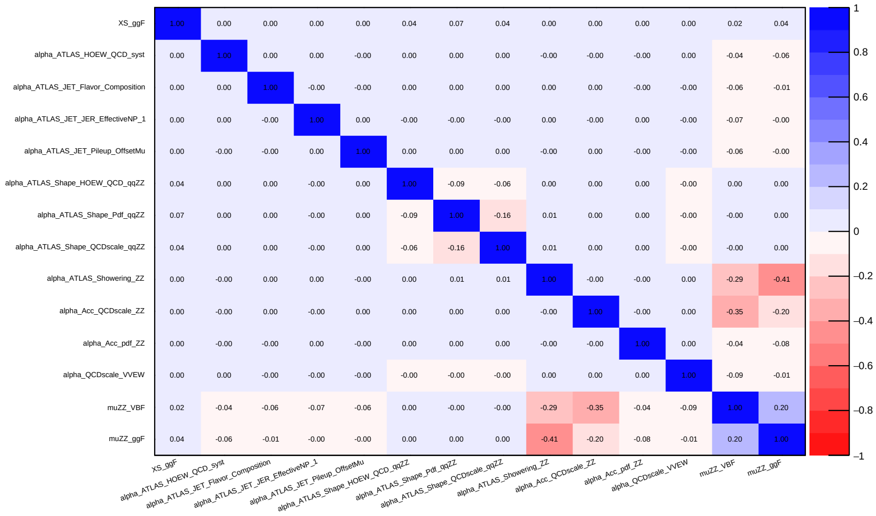

Figure 5.21: Correlation of nuisance parameters after a background only fit to Asimov data in the $\ell^+\ell^-\ell^+\ell^-$ channel. The Asimov data is generated with background data only.

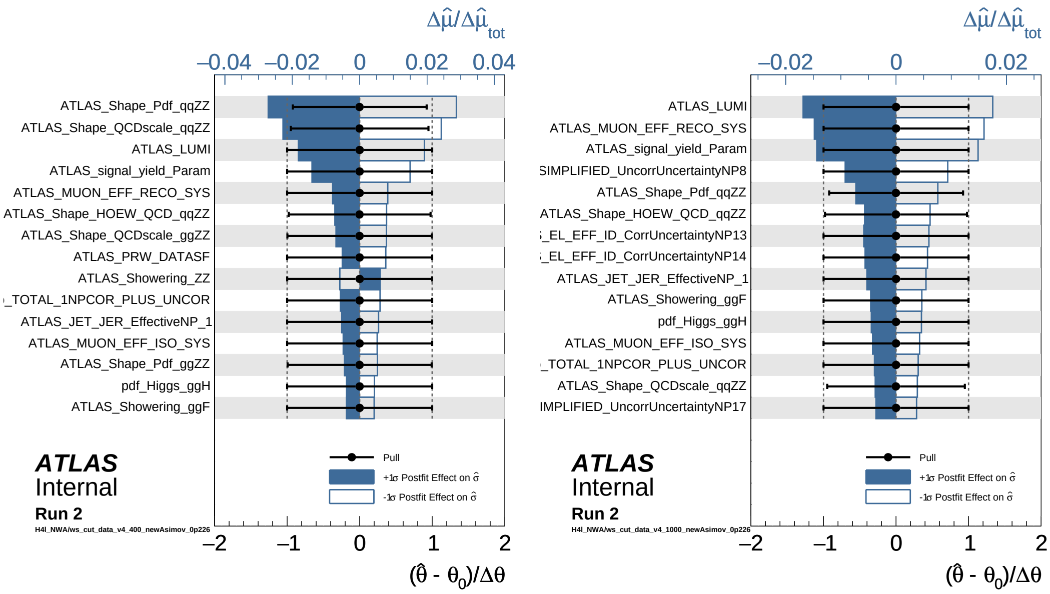

(a) (b)

Figure 5.22: NP ranking plot for the σ_{ggF} fit to Asimov data in the $\ell^+\ell^-\ell^+\ell^-$ channel. The Asimov data is injected with σ_{ggF} = 0.226 fb for $m_H = 400$ GeV (left) and σ_{ggF} = 0.050 fb for $m_H = 1000$ GeV (right).

6 Off-Shell Signal Strength Measurement

The observation of a new particle in the search for the Standard Model (SM) Higgs boson at the LHC, reported by the ATLAS [163] and CMS [164] collaborations, is a milestone in the quest to understand electroweak symmetry breaking. Precision measurements of the properties of the new boson are of critical importance. Efforts to measure the properties of the Higgs boson are primarily focused on on-shell production. However, above 125GeV off-shell production of the Higgs boson has a substantial cross section at the LHC, due to the increased phase space as the vector bosons (V=W, Z) and top quark decay products become on-shell with the increasing energy scale. This provides an opportunity to study the Higgs boson properties at higher energy scales. Off-shell production can provide sensitivity to new physics that alters the interactions between the Higgs boson and other fundamental particles in the high-mass region. The measurement of the decay width of Higgs boson is a major outcome of the off-shell study as shown in Section 1.4.

New physics can also enter in the decay of the Higgs boson, resulting in this case in a modification of the $\kappa^2_{V,\text{on-shell}}$ couplings. The study of the off-shell Higgs boson production will then also add information about the coupling structure of the Higgs boson particle. With the current sensitivity of the analysis, only an upper limit on the total width Γ_H can be determined, for which the weaker assumption

$$\kappa^2_{g,\text{on-shell}} \cdot \kappa^2_{V,\text{on-shell}} \leq \kappa^2_{g,\text{off-shell}} \cdot \kappa^2_{V,\text{off-shell}}\,, \tag{6.1}$$

that the on-shell couplings are no larger than the off-shell couplings, is sufficient. It is also assumed that any new physics which modifies the off-shell signal strength $\mu_{\text{off-shell}}$ and the off-shell couplings $\kappa_{i,\text{off-shell}}$ does not modify the predictions for the backgrounds. It is further assumed that there are no sizable kinematic modifications to the off-shell signal nor any new sizable signal in the search region of this analysis which is unrelated to an enhanced off-shell signal strength [165, 166].

Higher-order quantum chromodynamics (QCD) and electroweak (EW) corrections are known for the off-shell signal process $gg \to H^* \to ZZ$ [167]. Recently higher-order QCD corrections have became available also for the $gg \to ZZ$ background process [168, 169]. QCD corrections for the off-shell signal processes have only been calculated inclusively in the jet multiplicity or non-zero p_T(ZZ) values that are induced by the higher order QCD corrections, and may no longer be accurate if event selections which bias the jet multiplicity or transverse momentum p_T(ZZ) are applied. Consequently, the impact of any direct or indirect selections in jet multiplicity or p_T(ZZ), must be assessed by simulating the additional QCD activity with a parton shower MC to approximate the missing higher order matrix element contributions. This will lead to correspondingly larger acceptance uncertainties. The experimental analyses are therefore performed inclusively in jet observables and the event selections are designed to minimise the dependence on the boost of the ZZ system, which is sensitive to the jet multiplicity.

The above methodology should also apply to the Higgs boson production via vector-boson-fusion (VBF), except that the gluon-Higgs (ggH) coupling should be replaced with Higgs and vector-boson (HVV) coupling. Though the VBF Higgs production cross section is much smaller than the ggF process, the production and decay of the Higgs boson in VBF occurs at tree level, so that this process is sensitive to different theoretical systematics relative to the gluon fusion process. In particular it is not susceptible to loop effects that decouple in the off-shell region [40]. As pointed out in Ref. [170], the tail ($m_{ZZ} > 1$ TeV) of the Higgs-mediated diagrams is relatively more important for VBF than for ggF, compared to their respective peak cross sections. The differing fall off of the purely Higgs-mediated curves is due to the growth proportional to E^2 (E) of the underlying VBF (ggF) amplitudes. In this analysis, the off-shell Higgs boson via VBF is also considered. Given that we decide to do an inclusive analysis in jet observables, no specific VBF selection (like well separated forward tag jets) is used.

6.1 MC Simulation

The dominant processes contributing to the high-mass signal region in the $ZZ \to 4\ell$ final states are: the $gg \to H^* \to ZZ$ off-shell signal, the $gg \to ZZ$ background, the interference between them, ZZ production through VBF and VH-like production modes $pp \to ZZ + 2j$ (s-, t- and u-channel) and finally the dominant $q\bar{q} \to ZZ$ background. In the following a Higgs boson mass of $m_H = 125$ GeV is assumed for the signal processes. However, the expected value for the off-shell production rate is only very weakly dependent on the Higgs boson mass value.

Figure 6.1(a) shows the m_{4l} distribution for the $gg \to (H^* \to)ZZ \to 2e2\mu$ processes [1], after applying the event selection to the $ZZ \to 4\ell$ channel [172] on generator level quantities. The predictions with different off-shell Higgs couplings ($\mu_{\text{off-shell}} = 1, 5, 10$) are also shown for comparison. For low masses $m_{ZZ} < 2m_Z$ the off-shell signal is negligible, while it becomes comparable to the continuum $gg \to ZZ$ background for masses above the $2m_t$ threshold. The interference between the $gg \to H^* \to ZZ$ signal and the $gg \to ZZ$ background is always negative, as shown in Figure 6.1(b).

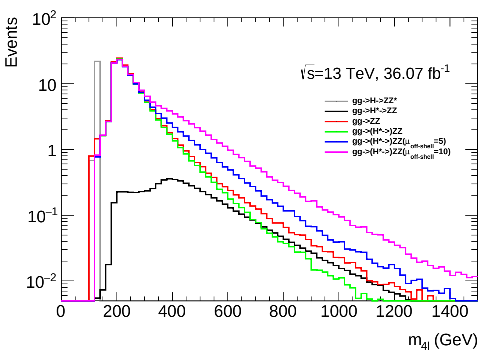

(a)

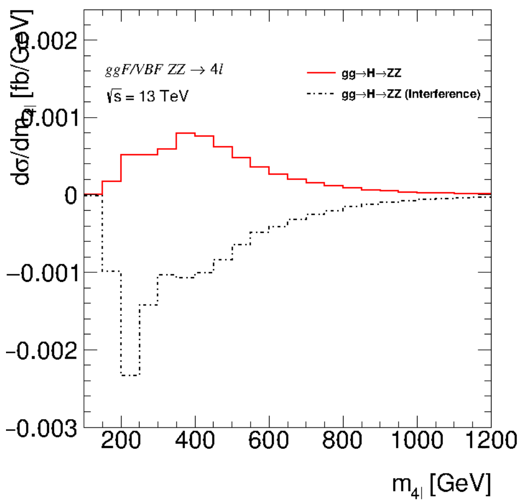

(b)

Figure 6.1: (a) Differential cross-sections for the $gg \to (H^* \to)ZZ \to 2e2\mu$ channel at the parton level, for the $gg \to H^* \to ZZ$ signal (red solid line), $gg \to ZZ$ continuum background (black line), $gg \to (H^* \to)ZZ$ with SM Higgs coupling (green line) and $gg \to (H^* \to)ZZ$ with $\mu_{\text{off-shell}} = 5$ (blue line). (b) $gg \to H^* \to ZZ \to 2e2\mu$ signal interference with the $gg \to ZZ \to 2e2\mu$ continuum background for the SM Higgs coupling (black) and with $\mu_{\text{off-shell}} = 5$ (red line).

[1] This illustration is valid for all four lepton final states ($2e2\mu$, $4e$ and 4μ), as final state interference effects from same lepton flavours are negligible in the high-mass region above 200 GeV, Fig. 4 of [171].

6.1.1 Samples and Theoretical Corrections

Monte Carlo (MC) samples of $gg \to (H^* \to)ZZ$ events, which include the SM Higgs boson signal, $gg \to H^* \to ZZ$, the continuum background, $gg \to ZZ$, and the signal–background interference contribution, were generated with the MC generator *SHERPA*-v2.2.2 + OpenLoops [173], [106], [108]. Matrix elements were calculated for zero jets and one jet at LO and merged with the Sherpa parton shower [109]. The NNPDF30NNLO [174] PDF set was used, and the QCD renormalisation and factorisation scales were set to $m_{ZZ}/2$.

The K-factor for the $gg \to H^* \to ZZ$process is known up to NNLO in QCD as a function of [46], [167] More recently, a NLO QCD calculation which includes the $gg \to ZZ$continuum process has become available [168], [169] allowing differential K-factors to be calculated with an expansion in the inverse top mass $(1/m_t)$ below $2m_t$, and assuming a massless-quark approximation above this threshold. This NLO QCD calculation was used to correct all three components with separate K-factors computed for the signal $gg \to (H^* \to)ZZ(K^S(m_{ZZ}))$, the background $gg \to ZZ(K^B(m_{ZZ}))$ and the interference $(K^I(m_{ZZ}))$. Since the NNLO QCD correction is only known differentially in m_{ZZ} for the $gg \to H^* \to ZZ$process and not for all three components in the off-shell region, an overall correction is applied by scaling the differential NLO QCD reweighted cross section by an additional factor of 1.2, which is assumed to be the same for the signal, background and interference. This additional constant scale factor is justified by the constant NNLO to NLO ratio of the QCD predictions over the data region considered in the analysis.

The electroweak $pp \to VV + 2j$ processes containing both the VBF-like events and events from associated Higgs production with vector bosons (VH), which includes on-shell Higgs boson production, were simulated using *MadGraph5_aMC@NLO* [99] with matrix elements calculated at LO. The QCD renormalisation and factorisation scales were set to m_W following the recommendation in Ref. [171] and the NNPDF23LO PDF set [175] was used. *PYTHIA* 8.186 [85] was used for parton showering and hadronisation, with the A14 set of tuned parameters for the underlying event. Due to the different dependence, the on-shell and off-shell Higgs boson production processes are separated when weighting MC events by requiring that the generated Higgs boson mass satisfy $|m_H^{gen.} - 125| < 1$ GeV. This requirement is fully efficient in selecting the on-shell VH process.

The $q\bar{q} \to ZZ$ background was simulated with *SHERPA* v2.2.2, using the NNPDF30NNLO PDF set for the hard-scattering process. NLO QCD accuracy is achieved in the matrix-element calculation for 0- and 1-jet final states and LO accuracy for 2- and 3-jet final states. The merging with the *SHERPA* parton shower was performed using the *MEPS@NLO* prescription. NLO EW corrections are applied as a function of the particle-level m_{ZZ} [111], [176].

The WZ background was simulated at NLO in QCD using the *POWHEG-BOX* v2 event generator [177] with the CT10NLO PDF set [178] and *PYTHIA* 8.186 for parton showering and hadronisation. The non-perturbative effects were modelled with the AZNLO set of tuned parameters [179].

Events containing a single Z boson with associated jets (Z + jets) were simulated using the *SHERPA* v2.2.1 event generator. Matrix elements were calculated for up to two partons at NLO and four partons at LO using the *COMIX* [107] and *OPENLOOPS* [108] matrix-element generators and merged with the *SHERPA* parton shower [109] using the *MEPS@NLO* prescription. The NNPDF30NNLO PDF set was used in conjunction with dedicated parton-shower tuning developed by the *SHERPA* authors. The Z + jets events are normalised using the NNLO cross sections [180].

The triboson backgrounds ZZZ, WZZ, and WWZ with fully leptonic decays and at least four prompt charged leptons were modelled using *SHERPA* v2.2.1. The contribution from triboson backgrounds with one W or Z boson decaying hadronically is not included in the simulation, but the impact on the analysis is found to be negligible. For the fully leptonic background, with four prompt charged leptons originating from the decays of the top quarks and Z boson, *MADGRAPH5_aMC@NLO* was used. The background, as well as the single-top and Wt production, were modelled using *POWHEG-BOX* v2 interfaced to *PYTHIA* 6.428 [181] with the Perugia 2012 [182] set of tuned parameters for parton showering, hadronisation and the underlying event, and to *EVTGEN* v1.2.0 [183] for properties of the bottom and charm hadron decays.

The particle-level events produced by each MC event generator were processed through the ATLAS detector simulation within the *GEANT* 4 framework [83, 184]. or the fast detector simulation package *Atlfast-II* [184]. Additional pp interactions in the same and nearby bunch crossings (pile-up) are included in the simulation. The pile-up events were generated using *PYTHIA* 8 with the A2 set of tuned parameters and the MSTW2008LO PDF set [185]. The simulation samples were weighted to reproduce the observed distribution of the mean number of interactions per bunch crossing in the data.

In table 6.1 the gluon-gluon fusion MCFM samples used in the analysis are reported, while the Sherpa gg samples are summarized in table 6.2. In table 6.3 the vector-boson-fusion samples are reported.

MCFM samples					
Process		DSID	Events	Filter efficiency	cross-section
$gg \to H^* \to ZZ$	ggH_ZZ_2e2mu_m4l130	344828	475000	1	0.107810 fb
	ggH_ZZ_4e_m4l130	344830	449000	1	0.053890 fb
	ggH_ZZ_4mu_m4l130	344832	453000	1	0.053884 fb
$gg \to ZZ$	gg_ZZ_2e2mu_m4l100	344833	494000	1	2.524 fb
	gg_ZZ_4e_m4l100	344834	497000	1	1.254 fb
	gg_ZZ_4mu_m4l100	344835	494000	1	1.254 fb
$gg \to (H^* \to)ZZ$	ggH_gg_ZZ_2e2mu_m4l130	344233	495000	1	2.288 fb
	ggH_gg_ZZ_4e_m4l130	344821	500000	1	1.139 fb
	ggH_gg_ZZ_4mu_m4l130	344823	50000	1	1.139 fb
$gg \to (H^* \to)ZZ(\mu_{\text{off-shell}} = 5)$	ggH_gg_ZZ_5SMW_2e2mu_m4l130	344824	496000	1	2.457 fb
	ggH_gg_ZZ_5SMW_4e_m4l130	344825	498000	1	1.224 fb
	ggH_gg_ZZ_5SMW_4mu_m4l130	344826	498000	1	1.224 fb
$gg \to (H^* \to)ZZ(\mu_{\text{off-shell}} = 10)$	ggH_gg_ZZ_10SMW_2e2mu_m4l130	344229	500000	1	2.802 fb
	ggH_gg_ZZ_10SMW_4e_m4l130	344230	500000	1	1.396 fb
	ggH_gg_ZZ_10SMW_4mu_m4l130	344231	500000	1	1.396 fb

Table 6.1: List of MCFM samples used in the 4ℓ analysis. For all the sample the events are generated with the ATLAS fast simulation but for $\Gamma_H = \Gamma_H^{SM}$ and $\Gamma_H = 10 \times \Gamma_H^{SM}$, for which only truth events are available. Only events with $m_{4\ell}$ ¿ 130(100) GeV are generated for $gg \to (H^* \to)ZZ \to 4\ell$ ($gg \to ZZ$) sample.

Sherpa samples					
Process		DSID	Events	Filter efficiency	cross-section
$gg \to H^* \to ZZ$	ggllllOnlyHiggs_130M4l	345712	49000	1	0.60 fb
$gg \to ZZ$	ggllllNoHiggs_130M4l	345709	499000	1	10.6 fb
$gg \to (H^* \to)ZZ$	ggllll_130M4l	345706	991400	1	10.0 fb

Table 6.2: List of Sherpa gg samples. Events are simulated with the ATLAS fast simulation.

MadGraph $qq \to ZZ \to 4\ell + jj$ samples				
Process	DSID	Events	Filter efficiency	cross-section
VBFH125_ZZ_4l_m4l130	345070	300000	1	0.125 fb
VBFH125_bkg_4l_m4l100	345276	299000	1	0.672 fb
VBFH125_sbi_4l_m4l130	345071	289000	1	0.636 fb
VBFH125_sbi5_4l_m4l130	345072	300000	1	0.775 fb
VBFH125_sbi10_4l_m4l130	345277	300000	1	1.002 fb

Table 6.3: List of $qq \to ZZ$ MadGraph samples used in the 4ℓ analysis. Events are simulated with the ATLAS fast simulation. Note that the cross section numbers are for one neutrino flavor and one needs to scale them up by a factor of three for proper normalisation.

6.1.2 Dependency of the off-shell signal and background interference on the signal strength

The known dependency of the off-shell Higgs boson signal process, the background process and the interference term on the off-shell signal strength $\mu_{\text{off-shell}}$ can be used to construct MC samples for arbitrary values of $\mu_{\text{off-shell}}$ from three basic samples generated at different fixed values of $\mu_{\text{off-shell}}$. An event sample ($\sigma_{gg\to(H^*\to)VV}(\mu_{\text{off-shell}})$) for the $gg \to (H^* \to)VV$ process with an arbitrary value of the off-shell Higgs boson signal strength $\mu_{\text{off-shell}}$, labelled as $SBIr$, can be constructed from the MC sample for the SM Higgs boson signal $gg \to H^* \to VV$ ($\sigma^{\text{SM}}_{gg\to H^*\to VV}$), labelled as S, the $gg \to VV$ continuum background MC sample ($\sigma_{gg\to VV,\,\text{cont}}$), labelled as B, and a full SM Higgs boson signal plus background $gg \to (H^* \to)VV$ MC sample ($\sigma^{\text{SM}}_{gg\to(H^*\to)VV}$), labelled as SBI.

At LO in QCD, the parametrization of SBI can be written as the following simple weighting function

$$
\begin{aligned}
\sigma_{gg\to(H^*\to)VV}(\mu_{\text{off-shell}}) &= \mu_{\text{off-shell}} \cdot \sigma^{\text{SM}}_{gg\to H^*\to VV} \\
&+ \sqrt{\mu_{\text{off-shell}}} \cdot \sigma^{\text{SM}}_{gg\to VV,\,\text{Interference}} \\
&+ \sigma_{gg\to VV,\,\text{cont}}\,,
\end{aligned} \tag{6.2}
$$

$$
\sigma^{\text{SM}}_{gg\to VV,\,\text{Interference}} = \sigma^{\text{SM}}_{gg\to(H^*\to)VV} - \sigma^{\text{SM}}_{gg\to H^*\to VV} - \sigma_{gg\to VV,\,\text{cont}}\,, \tag{6.3}
$$

This parametrisation is validated using the generated $gg \to (H^* \to) ZZ$ samples with $\mu_{\text{off-shell}} = 5$; the comparison with the reconstructed samples is shown in Figure 6.2. Truth events generated with MCFM and gg2VV with off-shell events are used. The generated $SBI5$ sample and the parameterized one are consistent within statistical uncertainty.

When the high order QCD corrections are applied, the $SBIr$ sample can be constructed using the following weighting function:

$$
\begin{aligned}
\sigma_{gg\to(H^*\to)VV}(\mu_{\text{off-shell}}) &= \mu_{\text{off-shell}} \cdot \mathrm{K}^S(m_{VV}) \cdot \sigma^{\text{SM}}_{gg\to H^*\to VV} \\
&+ \sqrt{\mu_{\text{off-shell}}} \cdot \mathrm{K}^I(m_{VV}) \cdot \sigma^{\text{SM}}_{gg\to VV,\,\text{Interference}} \\
&+ \mathrm{K}^{\mathrm{B}}(m_{VV}) \cdot \sigma_{gg\to VV,\,\text{cont}}\,,
\end{aligned} \tag{6.4}
$$

where the K-factors are calculated inclusively without any selections, and the interference sample is taken as the difference between $\sigma^{\text{SM}}_{gg\to(H^*\to)VV}$ and $\sigma^{\text{SM}}_{gg\to H^*\to VV} + \sigma_{gg\to VV,\,\text{cont}}$.

As a direct simulation of an interference MC sample is not possible, Eq. (6.3) is used to obtain:

$$
\begin{aligned}
\sigma_{gg\to(H^*\to)VV}(\mu_{\text{off-shell}}) &= \mu_{\text{off-shell}} \cdot \mathrm{K}^S(m_{VV}) \cdot \sigma^{\text{SM}}_{gg\to H^*\to VV} - \sqrt{\mu_{\text{off-shell}}} \cdot \mathrm{K}^I(m_{VV}) \cdot \sigma^{\text{SM}}_{gg\to H^*\to VV} \\
&+ \sqrt{\mu_{\text{off-shell}}} \cdot \mathrm{K}^I(m_{VV}) \cdot \sigma^{\text{SM}}_{gg\to(H^*\to)VV} \\
&+ \mathrm{K}^{\mathrm{B}}(m_{VV}) \cdot \sigma_{gg\to VV,\,\text{cont}} - \sqrt{\mu_{\text{off-shell}}} \cdot \mathrm{K}^I(m_{VV}) \cdot \sigma_{gg\to VV,\,\text{cont}}\,.
\end{aligned} \tag{6.5}
$$

In the above equation, the $SBIr$ sample is constructed from five individual samples:

- $\mathrm{K}^S(m_{VV}) \cdot \sigma^{\text{SM}}_{gg\to H^*\to VV}$: the signal sample with the high order corrections for the signal process applied;
- $\mathrm{K}^I(m_{VV}) \cdot \sigma^{\text{SM}}_{gg\to H^*\to VV}$: the signal sample with the high order corrections for the interference applied;
- $\mathrm{K}^{\mathrm{B}}(m_{VV}) \cdot \sigma_{gg\to VV,\,\text{cont}}$: the background sample with the high order corrections for the background process applied;
- $\mathrm{K}^I(m_{VV}) \cdot \sigma_{gg\to VV,\,\text{cont}}$: the background sample with the high order corrections for the interference applied;
- $\mathrm{K}^I(m_{VV}) \cdot \sigma^{\text{SM}}_{gg\to(H^*\to)VV}$: the SBI sample with the high order corrections for the interference applied.

In the final analysis, the NLO corrected Sherpa samples are used for the parametrization.
Similarly, a MC event sample for the EW $pp \to (H^* + 2j \to)ZZ + 2j$ process with an arbitrary value of the off-shell Higgs boson signal strength $\mu_{\text{off-shell}}$ can be constructed from a pure $pp \to ZZ + 2j$

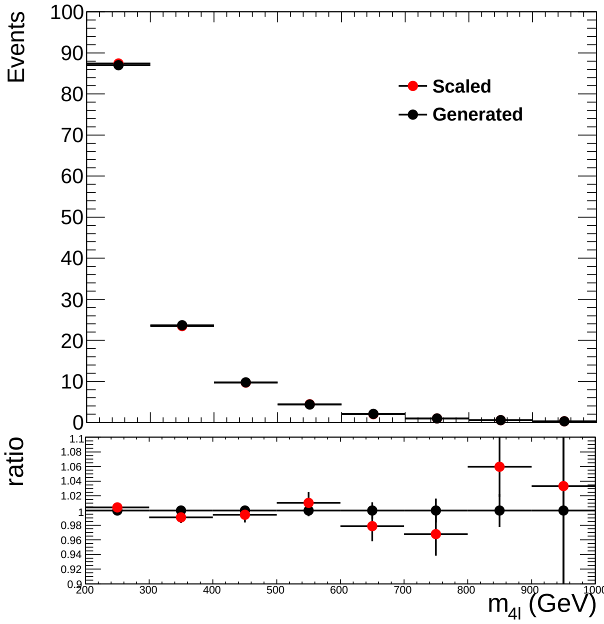

(a)

Figure 6.2: Comparison of the $m_{4\ell}$ distribution in $\ell^+\ell^-\ell^+\ell^-$ final state between the generated $gg \to (H^* \to) ZZ$ sample with $\mu_{off-shell} = 5$ and the sample reconstructed with the scaling procedure described in this section, using the generated sample of $gg \to H^* \to ZZ$ $gg \to ZZ$ and $gg \to (H^* \to) ZZ$. The distributions are normalized to the same luminosity.

continuum background MC sample, a full SM Higgs boson signal plus background $pp \to (H^* + 2j \to)ZZ + 2j$ MC sample and a third Higgs boson signal plus background $pp \to (H^* + 2j \to)ZZ + 2j$ MC sample with $\mu_{\text{off-shell}} = \kappa_V^4 = \Gamma_H/\Gamma_H^{\text{SM}} = 5$. Using $\Gamma_H/\Gamma_H^{\text{SM}} = 5$ for the last sample ensures that the on-shell VH events are generated with SM-like signal strength. Within the context of this analysis $\mu_{\text{off-shell}} = \kappa_V^2 \cdot \kappa_V^2 = \kappa_V^4$ is assumed for the sub-dominant VBF-like component.

The following weighting function is used:

$$\begin{aligned} \text{MC}_{pp\to(H^*+2j\to)ZZ+2j}(\mu_{\text{off-shell}}) &= \mu_{\text{off-shell}} \cdot \text{MC}^{\text{SM}}_{pp\to(H^*+2j\to)ZZ+2j} \\ &+ \sqrt{\mu_{\text{off-shell}}} \cdot \text{MC}^{\text{Interference}}_{pp\to ZZ+2j} \\ &+ \text{MC}^{\text{cont}}_{pp\to ZZ+2j}\,, \end{aligned} \tag{6.6}$$

where the signal and interference samples are implicitly defined through the SM $pp \to (H^* + 2j \to)ZZ + 2j$ MC sample

$$\text{MC}^{\text{SM}}_{pp\to(H^*+2j\to)ZZ+2j} = \text{MC}^{\text{SM}}_{pp\to H^*+2j\to ZZ+2j} + \text{MC}^{\text{Interference}}_{pp\to ZZ+2j} + \text{MC}^{\text{cont}}_{pp\to ZZ+2j} \tag{6.7}$$

and a $\mu_{\text{off-shell}} = 5$ MC sample:

$$\text{MC}^{\kappa_V^4=5}_{pp\to(H^*+2j\to)ZZ+2j} = 5 \cdot \text{MC}^{\text{SM}}_{pp\to H^*+2j\to ZZ+2j} + \sqrt{5} \cdot \text{MC}^{\text{Interference}}_{pp\to ZZ+2j} + \text{MC}^{\text{cont}}_{pp\to ZZ+2j}\,. \tag{6.8}$$

Solving for the generated MC samples yields:

$$\begin{aligned}
\mathrm{MC}_{pp\to(H^*+2j\to)ZZ+2j}(\mu_{\text{off-shell}}) &= \frac{\mu_{\text{off-shell}} - \sqrt{\mu_{\text{off-shell}}}}{5-\sqrt{5}}\mathrm{MC}^{\kappa_V^4=5}_{pp\to(H^*+2j\to)ZZ+2j} \\
&+ \frac{5\sqrt{\mu_{\text{off-shell}}} - \sqrt{5}\mu_{\text{off-shell}}}{5-\sqrt{5}}\mathrm{MC}^{\mathrm{SM}}_{pp\to(H^*+2j\to)ZZ+2j} \\
&+ \frac{(\sqrt{\mu_{\text{off-shell}}}-1)\cdot(\sqrt{\mu_{\text{off-shell}}}-\sqrt{5})}{\sqrt{5}}\mathrm{MC}^{\mathrm{cont}}_{pp\to ZZ+2j}.
\end{aligned} \tag{6.9}$$

Figure 6.3 shows the comparison of m_{ZZ} distribution for the generated $pp \to (H^* + 2j \to)ZZ + 2j$ sample with $\mu_{off-shell} = 5$ and for the sample reconstructed with the procedure described above. Truth events generated with MadGraph for both 4ℓ and $\ell\ell\nu\nu$ are used.

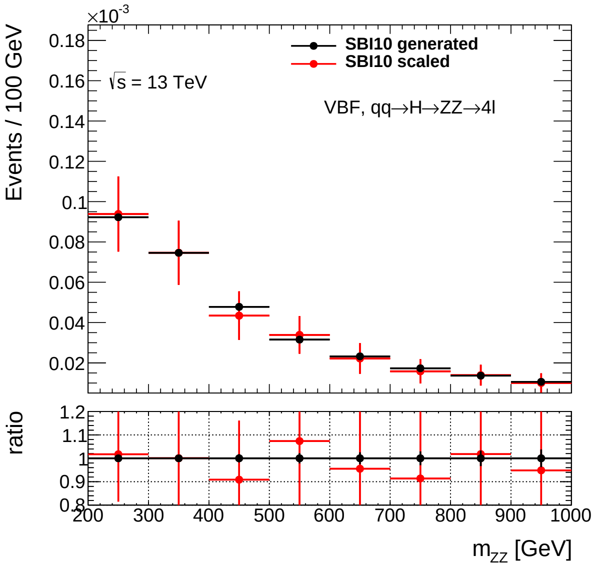

(a)

Figure 6.3: Comparison of the m_{ZZ} distribution between the generated $pp \to (H^* + 2j \to)ZZ + 2j$ sample with $\mu_{off-shell} = 5$ (black line) and the sample reconstructed with the scaling procedure described in this section (red curve).

6.1.3 Other MC samples

Other MC samples are used to model sub-leading backgrounds, mainly WZ, WW, $Z/\gamma^* + jets$, top-pairs production. A list of the additional samples used can be found in [186].

6.2 Analysis strategy in the $ZZ \to 4\ell$ channel

The analysis in the $ZZ \to 4\ell$ channel follows closely the Higgs boson measurements in the same final states in Ref. [186], with the same event selections in the off-peak region of 220 GeV $< m_{4\ell} <$ 2000 GeV. To avoid the dependence of the $gg \to ZZ$ kinematics on higher-order QCD effects, the analysis is performed inclusively, ignoring the number of jets in the events. The analysis is split into the same 4 lepton final states ($2\mu 2e$, $2e2\mu$, $4e$, 4μ) as in Ref. [186]. The same background estimation procedures are applied for the $q\bar{q} \to ZZ \to 4\ell$ and reducible backgrounds.

To enhance the sensitivity, a matrix element based kinematic discriminant (ME-based discriminant) is used, exploiting the full kinematics in the centre-of-mass frame of the 4ℓ system. For the nominal result, a binned maximum likelihood fit to the ME-based discriminant distribution is performed to benefit from the fully reconstructed final states. The additional use of initial state kinematics in a BDT discriminant provides only limited additional sensitivity at the cost of a non-inclusive analysis and is therefore not used as the baseline analysis.

6.2.1 Expected events and $m_{4\ell}$ distribution

Table 6.4 shows the expected number of events for the signal and background processes in the inclusive off-peak region and events with $220 < m_{4\ell} < 2000$ GeV are used to extract the results on $\mu_{\text{off-shell}}$. Figure 6.4 shows the $m_{4\ell}$ distributions of the expected signal and background processes. The dominant background comes from the $q\bar{q} \to ZZ$ process. The contribution of reducible backgrounds, such as Z+jets and top-quark production, is only about 0.5% of the total background in the full off-peak region and in the signal-enriched region. The contribution to the sensitivity on $\mu_{\text{off-shell}}$ is dominated by events in the high mass region ($m_{4\ell} > 400$ GeV) with higher signal-to-background ratio, as shown in Table 6.5.Events with $m_{4\ell} > 2000$ GeV are discarded, as no data event observed above this region. Such cutoff also avoids a phase space far away from the on-shell region, which might invalid the assumption of identical on-shell and off-shell Higgs couplings, and avoid possible unitarity violation [40]. In Table 6.4, the NLO K-factors are applied to the $gg \to ZZ$ processes, with an additional flat NNLO/NLO K-factor of 1.2 applied.

$220 < m_{4\ell} < 2000$ GeV				
Process	$4e$	4μ	$2e2\mu$	Total
$gg \to H^* \to ZZ$	$2.10 \pm 0.05 \pm 0.32$	$2.74 \pm 0.06 \pm 0.43$	$4.96 \pm 0.07 \pm 0.77$	$9.79 \pm 0.11 \pm 1.52$
$gg \to ZZ$	$20.33 \pm 0.22 \pm 3.28$	$30.29 \pm 0.26 \pm 4.76$	$50.71 \pm 0.35 \pm 8.39$	$101.33 \pm 0.49 \pm 16.43$
$gg \to (H^* \to)ZZ$	$18.72 \pm 0.37 \pm 3.01$	$29.28 \pm 0.44 \pm 4.61$	$48.11 \pm 0.58 \pm 7.51$	$96.11 \pm 0.82 \pm 15.13$
$gg \to (H^* \to)ZZ(\mu_{\text{off-shell}} = 5)$	$22.54 \pm 0.73 \pm 3.62$	$35.63 \pm 0.89 \pm 5.60$	$58.60 \pm 1.14 \pm 9.14$	$116.76 \pm 1.62 \pm 18.37$
$VBF\ H^* \to ZZ$	$0.36 \pm 0.01 \pm 0.02$	$0.47 \pm 0.02 \pm 0.02$	$0.84 \pm 0.02 \pm 0.03$	$1.68 \pm 0.03 \pm 0.06$
$VBF\ ZZ$	$2.02 \pm 0.01 \pm 0.11$	$2.90 \pm 0.02 \pm 0.13$	$4.96 \pm 0.02 \pm 0.17$	$9.88 \pm 0.03 \pm 0.41$
$VBF\ (H^* \to)ZZ$	$1.69 \pm 0.01 \pm 0.09$	$2.43 \pm 0.02 \pm 0.11$	$4.17 \pm 0.02 \pm 0.14$	$8.29 \pm 0.03 \pm 0.27$
$VBF\ (H^* \to)ZZ(\mu_{\text{off-shell}} = 5)$	$2.27 \pm 0.02 \pm 0.12$	$3.16 \pm 0.02 \pm 0.14$	$5.53 \pm 0.03 \pm 0.19$	$10.96 \pm 0.04 \pm 0.38$
$q\bar{q} \to ZZ$	$100.83 \pm 0.92 \pm 9.02$	$158.44 \pm 1.19 \pm 13.26$	$260.24 \pm 1.69 \pm 20.91$	$519.68 \pm 2.26 \pm 41.53$
Reducible backgrounds	1.14 ± 0.18	0.42 ± 0.04	1.49 ± 0.19	3.05 ± 0.41
Other backgrounds	$2.60 \pm 0.08 \pm 0.20$	$3.30 \pm 0.09 \pm 0.21$	$5.64 \pm 0.12 \pm 0.33$	$11.54 \pm 0.17 \pm 0.54$
Total Expected (SM)	$124.98 \pm 1.00 \pm 12.50$	$193.87 \pm 1.27 \pm 18.23$	$319.65 \pm 1.79 \pm 29.08$	$638.50 \pm 2.41 \pm 59.81$
Observed	157	220	327	704

Table 6.4: Expected and observed number of events in the $ZZ \to 4\ell$ channel. The reducible background includes contributions from the Z+jets and top quark processes. The "other background" includes contributions form ttV, VVV processes. The expected events for the $gg \to (H^* \to)ZZ$ and VBF $(H^* \to)ZZ$ processes, including the Higgs boson signal, background and interference, are reported for both the SM predictions and $\mu_{off\text{-}shell} = 5$. The NLO K-factors are applied to the $gg \to ZZ$ processes, with an additional flat NNLO/NLO K-factor of 1.2 applied. In the total expected event yields, for the $gg \to ZZ$ and $VBFVV \to ZZ$ processes, only the highlighted process are included. The uncertainties in the number of expected events include only the statistical uncertainties from MC samples and systematic uncertainties.

$400 < m_{4\ell} < 2000$ GeV				
Process	$4e$	4μ	$2e2\mu$	Total
$gg \to H^* \to ZZ$	$1.32 \pm 0.04 \pm 0.22$	$1.61 \pm 0.05 \pm 0.26$	$2.96 \pm 0.06 \pm 0.48$	$5.89 \pm 0.08 \pm 0.96$
$gg \to ZZ$	$2.46 \pm 0.07 \pm 0.47$	$3.38 \pm 0.08 \pm 0.64$	$5.93 \pm 0.11 \pm 1.10$	$11.77 \pm 0.15 \pm 2.21$
$gg \to (H^* \to)ZZ$	$2.17 \pm 0.12 \pm 0.42$	$3.10 \pm 0.14 \pm 0.59$	$5.38 \pm 0.18 \pm 1.00$	$10.64 \pm 0.26 \pm 2.00$
$gg \to (H^* \to)ZZ(\mu_{\text{off-shell}} = 5)$	$5.47 \pm 0.29 \pm 1.06$	$7.19 \pm 0.32 \pm 1.36$	$12.88 \pm 0.42 \pm 2.39$	$25.54 \pm 0.60 \pm 4.80$
$VBF\ H^* \to ZZ$	$0.25 \pm 0.01 \pm 0.01$	$0.31 \pm 0.01 \pm 0.01$	$0.58 \pm 0.01 \pm 0.02$	$1.14 \pm 0.02 \pm 0.04$
$VBF\ ZZ$	$0.87 \pm 0.01 \pm 0.04$	$1.21 \pm 0.01 \pm 0.05$	$2.09 \pm 0.01 \pm 0.08$	$4.16 \pm 0.02 \pm 0.18$
$VBF\ (H^* \to)ZZ(\mu_{\text{off-shell}} = 5)$	$1.02 \pm 0.01 \pm 0.06$	$1.38 \pm 0.01 \pm 0.07$	$2.45 \pm 0.02 \pm 0.09$	$4.85 \pm 0.02 \pm 0.19$
$VBF\ (H^* \to)ZZ$	$0.63 \pm 0.01 \pm 0.03$	$0.90 \pm 0.01 \pm 0.04$	$1.54 \pm 0.01 \pm 0.06$	$3.06 \pm 0.02 \pm 0.11$
$q\bar{q} \to ZZ$	$15.00 \pm 0.16 \pm 1.56$	$23.30 \pm 0.21 \pm 2.30$	$38.30 \pm 0.27 \pm 3.65$	$76.70 \pm 0.37 \pm 7.28$
Other backgrounds	$0.49 \pm 0.03 \pm 0.04$	$0.60 \pm 0.03 \pm 0.05$	$1.06 \pm 0.05 \pm 0.04$	$2.14 \pm 0.07 \pm 0.10$
Total Expected (SM)	$18.29 \pm 0.20 \pm 2.05$	$27.90 \pm 0.26 \pm 2.98$	$46.28 \pm 0.33 \pm 4.75$	$92.46 \pm 0.46 \pm 9.77$
Observed	19	36	59	114

Table 6.5: Expected and observed number of events in the $ZZ \to 4\ell$ channel, with $400 < m_{4\ell} < 2000$ GeV.

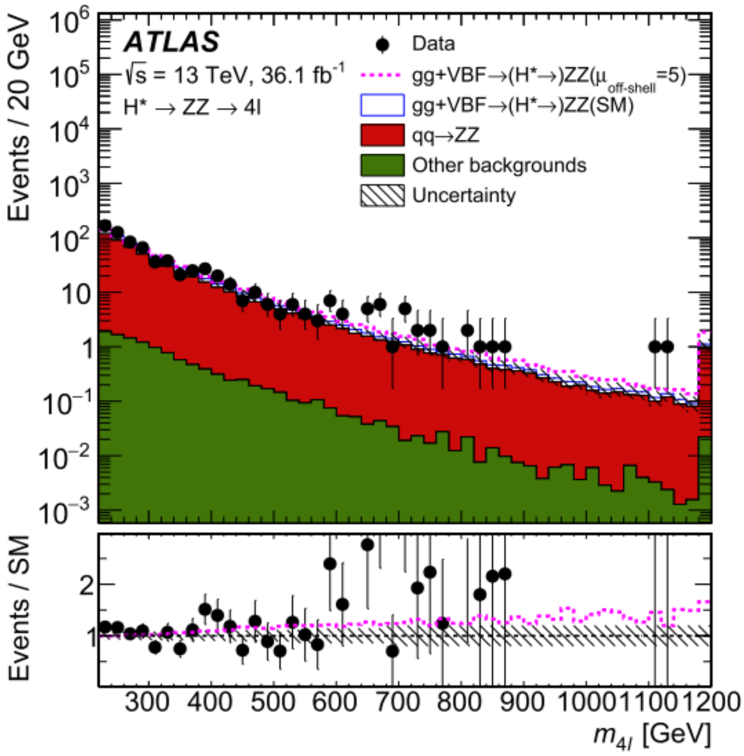

(a) $4e$

Figure 6.4: Observed distributions in the range 220 GeV < m_{4l} < 2000 GeV for the four-lepton invariant mass m_{4l} combining all lepton final states, compared to the expected contributions from the SM including the Higgs boson (stacked). Events with m_{4l} > 1200 GeV are included in the last bin of the m4 distribution. The hatched area shows the combined statistical and systematic uncertainties. The dashed line corresponds to the total expected event yield, including all backgrounds and the Higgs boson with $\mu_{off-shell} = 5$. The ratio plot shows the observed data yield divided by the SM prediction (black points) as well as the total expected event yield with $\mu_{off-shell} = 5$ divided by the SM prediction (dashed line) in each bin [187].

6.2.2 Matrix Element discriminant

As observed in table 6.4, the number of expected $H \to 4\ell$ events in the off-shell region is very small compared to the number of events expected for the irreducible $q\bar{q} \to ZZ$ and $gg \to ZZ$ backgrounds. To enhance the sensitivity to the $gg \to H^* \to ZZ$ signal a matrix element based discriminant is then constructed. It fully exploits the event kinematics in the centre-of-mass frame of the 4ℓ system, based on eight observables: $\{m_{4\ell}, m_{Z_1}, m_{Z_2}, \cos\theta_1, \cos\theta_2, \phi, \cos\theta^*, \phi_1\}$.

In a $ZZ^* \to 4l$ system the production and decay angles, shown in Figure 6.5, are defined in the following way

- θ_1, θ_2 are the angles between negative final state leptons and the direction of flight of their respective Z-bosons. The 4-vectors of the leptons are calculated in the rest frame of the corresponding Z-bosons.
- ϕ is the angle between the decay planes of the four final state leptons expressed in the rest frame of the four-leptons system
- ϕ_1 is the angle defined between the decay plane of the first lepton pair and a plane defined by the vector of Z1 in the rest frame of the four-leptons system and the positive direction of the collision axis.
- θ^* is the production angle of Z1 defined in the rest frame of the four-lepton system.

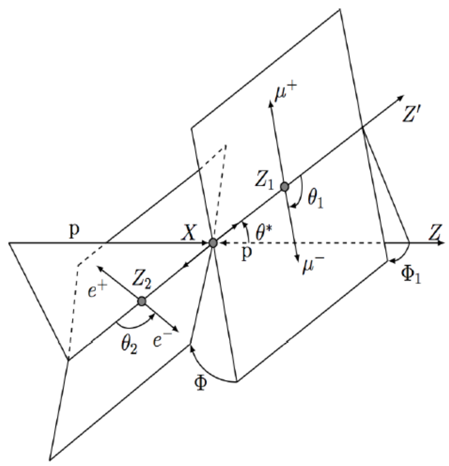

Figure 6.5: Production and decay angles in a $ZZ^* \to 4l$ system.

These observables are used to create the four-momenta of the leptons and incoming partons, which are then used to calculate matrix elements for different processes, provided by the MCFM program [38]. The following matrix elements are calculated for each event:

- $P_{q\bar{q}}$: matrix element for the $q\bar{q} \to ZZ \to 4\ell$ process,
- P_{gg}: matrix element for the $gg \to (H^* \to)ZZ \to 4\ell$ process including the Higgs boson ($m_H =$ 125.5 GeV) with SM couplings, continuum background and their interference,
- P_H: matrix element for for the $gg \to H^* \to ZZ \to 4\ell$ process ($m_H = 125.5$ GeV).

The kinematic discriminant is defined as in Ref. [38]:

$$\mathrm{ME} = \log_{10}\left(\frac{P_H}{P_{gg} + c \cdot P_{q\bar{q}}}\right), \tag{6.10}$$

where c is an empirical constant, chosen to be 0.1, to approximately balance the overall cross-sections of the $q\bar{q} \to ZZ$ and $gg \to (H^* \to)ZZ$ processes. The value of c has a very small effect on the overall sensitivity (Appendix **??**).

Figure 6.6 shows the shape comparisons of the input variables to the ME-based discriminant at reconstruction level,for the full off-peak region (220 GeV $< m_{4\ell} <$ 2000 GeV). Figure 6.7 shows the shape comparisons of the ME-based discriminant for the $gg \to H^* \to ZZ$ signal, $q\bar{q} \to ZZ$ background, $gg \to (H^* \to)ZZ$ with SM $\mu_{\text{off-shell}}$ and $gg \to (H^* \to)ZZ$ with $\mu_{\text{off-shell}} = 5$, for the full off-peak region (220 GeV $< m_{4\ell} <$ 2000 GeV) at reconstruction level. The $gg \to H^* \to ZZ$ signal events have on average larger ME-based discriminant values, compared to the $q\bar{q} \to ZZ$ background and the $gg \to ZZ$ background dominated $gg \to (H^* \to)ZZ$ events. The $gg \to (H^* \to)ZZ$ events with $\mu_{\text{off-shell}} = 5$ have a double-peak structure. The peak around -3 corresponds to the $gg \to ZZ$ background component, while the peak around -1 corresponds mainly to the $gg \to H^* \to ZZ$ component. Events with ME-based discriminant values between -4.5 and 0.5 are used in the final analysis. The ME discriminant is also used as the input for the likelihood fit.

BDT

In addition, an alternative multivariate discriminant based on a boosted decision tree (BDT) algorithm was studied to further separate the $gg \to H^* \to ZZ$ signal and the main $q\bar{q} \to ZZ$ background, by exploiting additional kinematic information (p_T and η) of the ZZ system. The BDT is trained using all the events with $m_{4\ell} >$ 220 GeV and using four discriminating variables: $m_{4\ell}$, $p_{T,4\ell}$, $\eta_{4\ell}$ and the ME discriminant. The signal and background shape comparison of these variables is given in figure 6.8. The resulting BDT distribution for signal and background is instead reported in figure 6.9, where a good separation is observed.

However, by training the BDT only against the $q\bar{q} \to ZZ$ background the analysis sensitivity improves very little (Appendix A.4) compared to the ME-based discriminant alone. Due to the dependence on the p_T of the ZZ system, the BDT-based discriminant introduces additional systematic uncertainties from the higher-order QCD corrections. For these reasons, the BDT-based discriminant is not used for the final result.

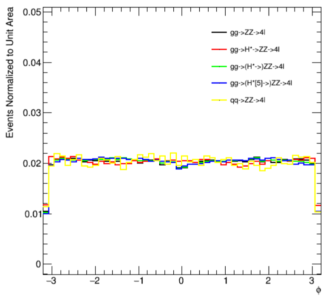

(a) ϕ

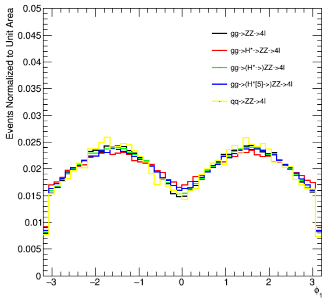

(b) ϕ_1

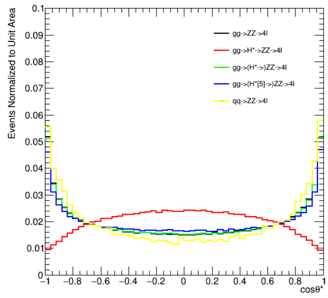

(c) $cos\theta^{*}$

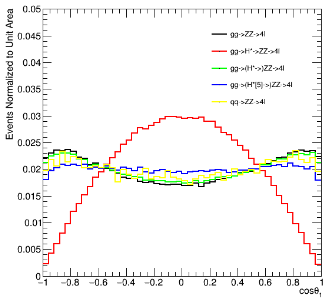

(d) $cos\theta_1$

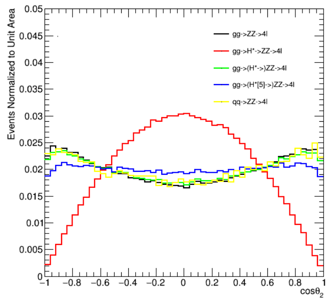

(e) $cos\theta_2$

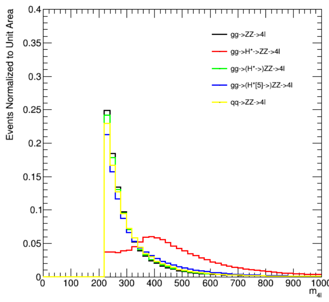

(f) m_{4l}

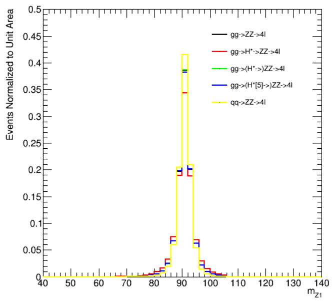

(g) m_{Z_1}

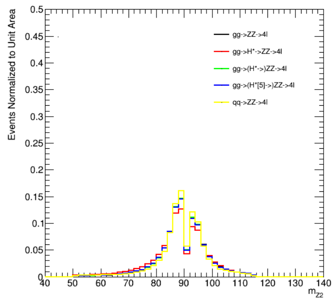

(h) m_{Z_2}

Figure 6.6: Distributions of the input variables to the ME-based discriminant, for all lepton final states combined, normalised to unit area for shape comparisons, for the full peak region ($220 < m_{4\ell} < 2000$ GeV). The yellow line represents the $q\bar{q} \rightarrow ZZ$ background, the black line the $gg \rightarrow ZZ$ background. The red line represents the $gg \rightarrow H^{*} \rightarrow ZZ$ signal with SM couplings, the light green the $gg \rightarrow (H^{*}) \rightarrow ZZ$ with $\mu_{off-shell} = 1$ and the blue line is the $gg \rightarrow (H^{*}) \rightarrow ZZ$ with $\mu_{off-shell}$ =5.

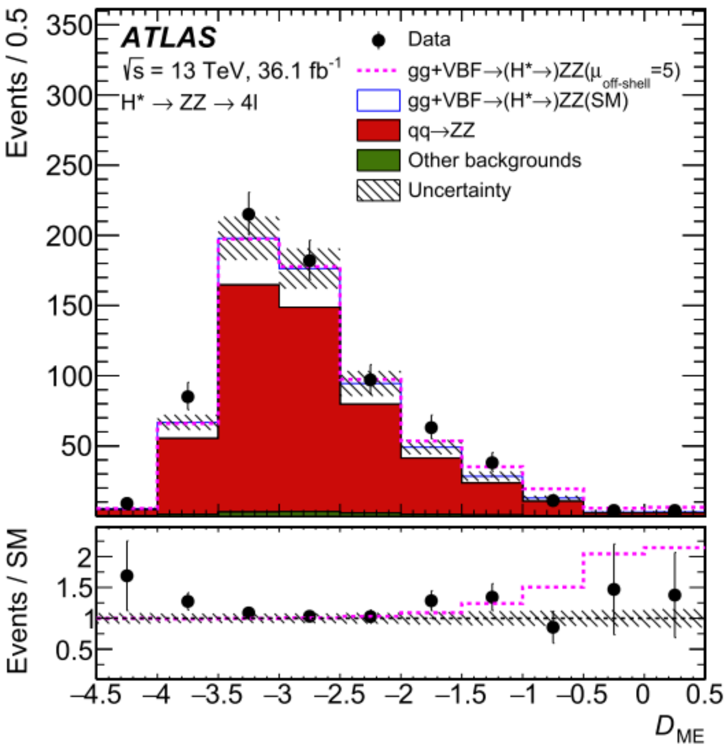

(a)

Figure 6.7: Observed distributions in the range 220 GeV < m_{4l} < 2000 GeV for the ME-based discriminant DME combining all lepton final states, compared to the expected contributions from the SM including the Higgs boson (stacked). The hatched area shows the combined statistical and systematic uncertainties. The dashed line corresponds to the total expected event yield, including all backgrounds and the Higgs boson with $\mu_{off-shell} = 5$. The ratio plot shows the observed data yield divided by the SM prediction (black points) as well as the total expected event yield with $\mu_{off-shell} = 5$ divided by the SM prediction (dashed line) in each bin [187].

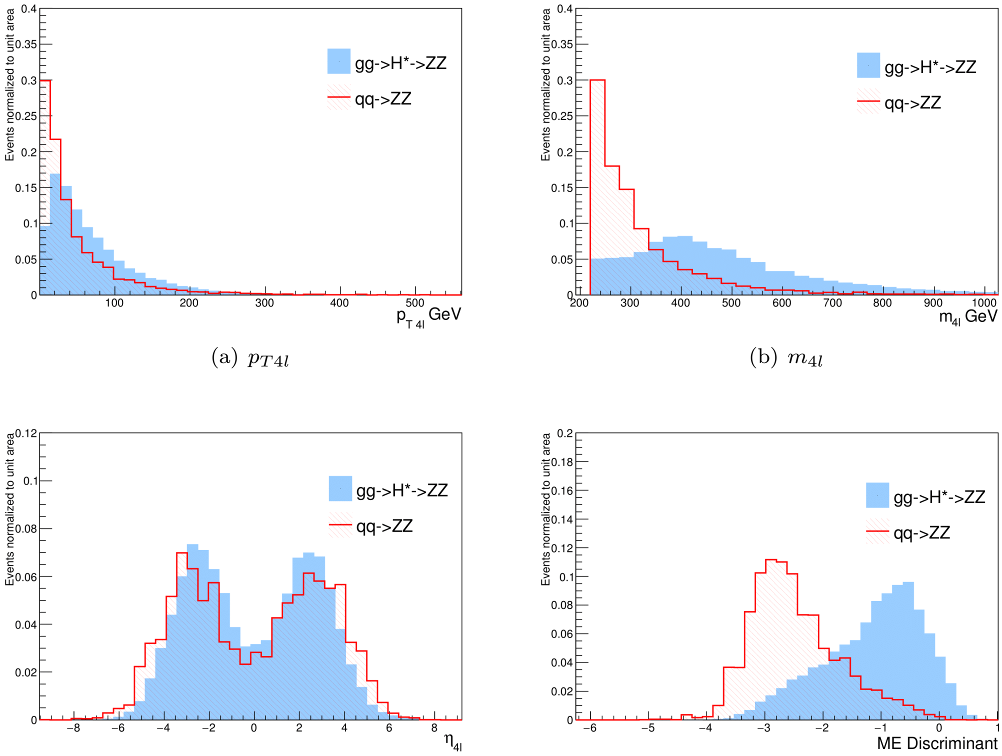

(a) p_{T4l} (b) m_{4l}

(c) η_{4l} (d) Matrix Element Discriminant

Figure 6.8: Distributions of the input variables to the BDT discriminant, for all lepton final states combined, normalised to unit area for shape comparisons, for the full peak region ($220 < m_{4\ell} < 2000$ GeV). The blue histogram represents the $gg \to H^* \to ZZ$ signal with SM couplings, while the red histogram the $q\bar{q} \to ZZ$ background against which the BDT is trained.

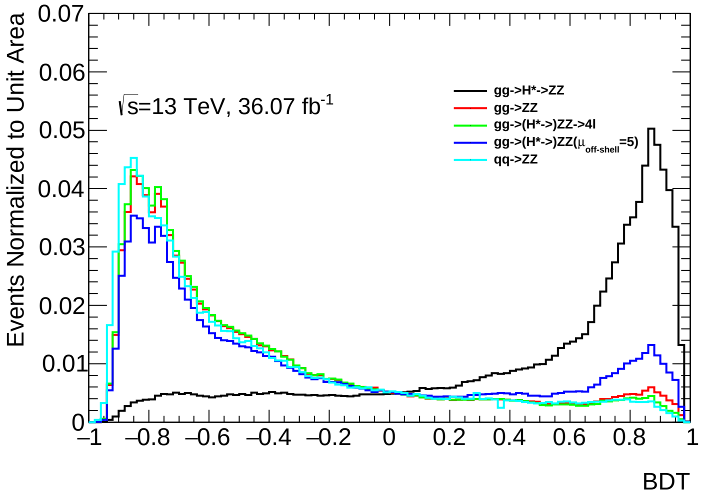

(a)

Figure 6.9: Distributions of the BDT-based discriminant in the four lepton final states normalised to unit area to show the shape comparisons, for the full peak region ($m_{4\ell} > 220$ GeV).

6.2.3 Reducible background estimation

Apart from the main irreducible background $pp \to ZZ^*$ production, additional sources of reducible background stem from Z+jets (comprised of both heavy- and light-flavour jets), the top-quark pair and WZ production. The data driven inclusive estimation of the contribution from each of these background components is described in [188]. Since they vary according to the flavour of the leptons of the subleading pair, the background analysis is performed separately for the $Z+\mu\mu$ and $Z+ee$ final states. Four categories of these background contributions are constructed. Two of them correspond to a subleading pair of muons and account for the contributions of Z+jets and $t\bar{t}$ productions. As it is explained in [188] the normalisation for these background sources is estimated with a simultaneous fit on specific control regions which are orthogonal to the signal region.

For this analysis, only events with the invariant mass of the four lepton system ($m_{4\ell}$) above 220 GeV are considered. In order to estimate the amount of events satisfying this requirement without depending significantly on particular Monte Carlo events with large weights, the $m_{4\ell}$ distributions are described by smoothed shapes obtained using the KEYS algorithm [137]. Figure 6.10 shows the raw and smoothed $m_{4\ell}$ distributions for the four background categories. Excellent consistency is observed in all categories. This is also reflected in the estimation of the number of events which pass the $m_{4\ell}$ requirement that presents marginal differences between raw and smoothed distributions, as shown in table 6.6. The KEYS algorithm is also used to smooth the ME-based discriminant distributions for the different background estimation categories. Figure 6.11 shows the corresponding raw and the smoothed distributions, along with their normalisation uncertainties.

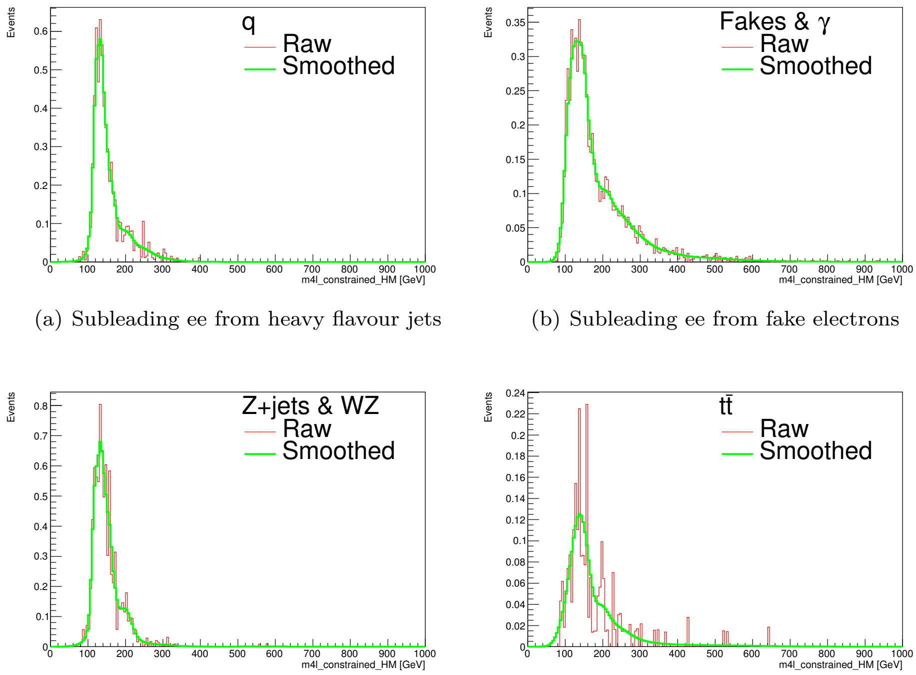

(a) Subleading ee from heavy flavour jets

(b) Subleading ee from fake electrons

(c) Subleading $\mu\mu$ from Z+jets

(d) Subleading $\mu\mu$ from $t\bar{t}$

Figure 6.10: Distributions of $m_{4\ell}$ invariant mass in the four reducible background categories. The raw distributions are presented in red, while the smoothed ones in green. (a) and (b) subleading pair of electrons from heavy flavour jets and fake electrons respectively. (c) and (d) subleading pair of muons from Z+jets and $t\bar{t}$ production respectively.

Background component	Total events	Events with $m_{4\ell}$ >220 GeV raw distribution	Events with $m_{4\ell}$ >220 GeV smoothed distribution
Fake+γ (electron)	7.02 ± 1.32	1.73	1.71 ± 0.32
heavy flavour (electron)	6.34 ± 1.93	0.56	0.58 ± 0.18
Z+jets, WZ (muon)	8.10 ± 1.11	0.34	0.37 ± 0.05
$t\bar{t}$ (muon)	2.29 ± 0.27	0.40	0.39 ± 0.05

Table 6.6: The number of expected events in each background category using the selection of the analysis, using either the raw or the smoothed $m_{4\ell}$ distribution. The error presented in the last column corresponds to the total statistical and systematic normalisation uncertainty.

Finally, the estimations of the four reducible background categories are divided into the three analysis channels according to the number of background events that contribute from each category to each final state. The estimation is performed using the flavour of the leading dilepton pair as in [188]. The resulting distributions are shown in figure 6.12 and the corresponding number of events in table 6.7. In total three events are expected in all the analysis channels, corresponding to about 0.5% of the main irreducible background. Moreover, the ME-based discriminant for these events is mainly distributed far from the area of interest, making their contribution to the final results even less significant.

Analysis channel	Estimated reducible background events
4e	1.14 ± 0.18
2e2μ	1.49 ± 0.19
4μ	0.42 ± 0.04

Table 6.7: The number of expected events in each background category using the selection of the analysis, using either the raw or the smoothed $m_{4\ell}$ distribution. The error presented in the last column corresponds to the total statistical and systematic normalisation uncertainty.

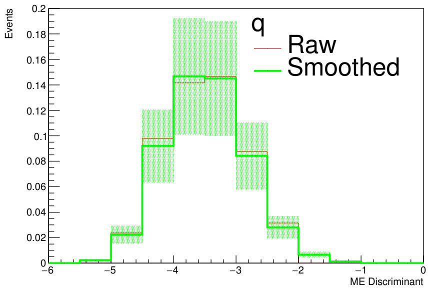

(a) Subleading ee from heavy flavour jets

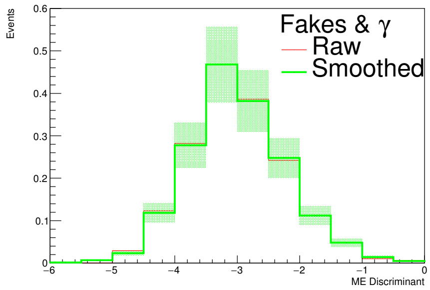

(b) Subleading ee from fake electrons

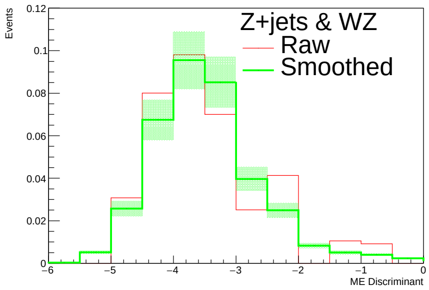

(c) Subleading $\mu\mu$ from Z+jets

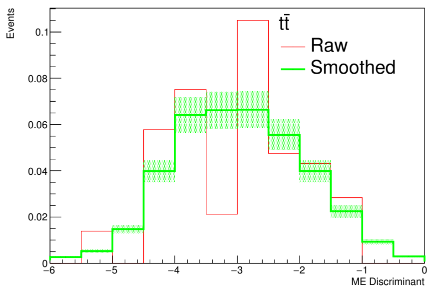

(d) Subleading $\mu\mu$ from $t\bar{t}$

Figure 6.11: Distributions of the ME-based discriminant in the four reducible background estimation categories. The raw distributions are presented in red, while the smoothed ones in green. The hatched area represents the normalisation uncertainty. (a) and (b) subleading pair of electrons from heavy flavour jets and fake electrons respectively. (c) and (d) subleading pair of muons from Z+jets and $t\bar{t}$ production respectively.

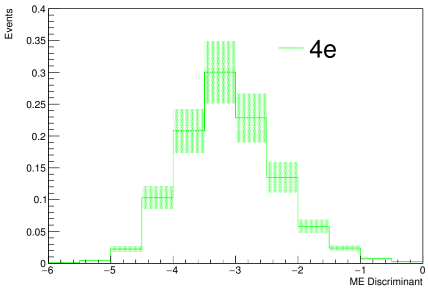

(a) 4e channel

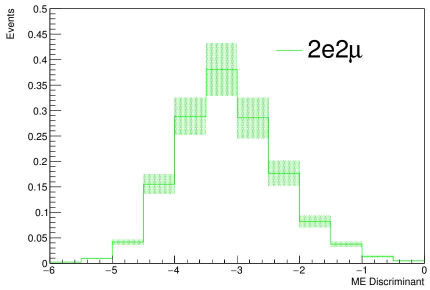

(b) 2e2μ channel

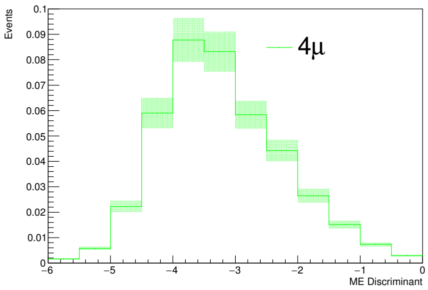

(c) 4μ channel

Figure 6.12: Distributions of the ME-based discriminant in the four analysis channels. The hatched area represents the normalisation uncertainty. (a) 4e channel, (b) 2e2μ channel and (c) 4μ channel.

6.3 Statistical Treatment and Results

In this section the results for the $ZZ \to 4\ell$ and $2\ell 2\nu$ channel analyses are combined and translated into limits on the off-shell signal strength $\mu_{\text{off-shell}}$ for the individual analyses and for its the combination.

6.3.1 Systematic Uncertainties

Systematic uncertainty sources impacting the analysis can be divided into two categories, uncertainties in the theoretical description of the signal and background processes and experimental uncertainties related to the detector or to the reconstruction algorithms. The largest systematic uncertainties arise from the theoretical uncertainties in the gg-initiated ZZ processes and the background process. The uncertainties from experimental measurements are generally small compared to the theoretical uncertainties in this analysis.

The theoretical uncertainties originate from the PDF choice, the missing higher-order corrections, and the parton-shower modelling. The PDF uncertainty corresponds to the 68% CL variations of the nominal PDF set NNPDF30NNLO for both $q\bar{q} \to ZZ$ and $gg \to (H^* \to)ZZ$ as well as the difference from alternative PDF sets. The alternative PDF sets used are CT10NNLO [189] and MMHT2014NNLO [190]. The uncertainty due to PDF is found to be about 3% in the high-mass region considered. The uncertainty due to higher-order QCD corrections (QCD scale uncertainty) is estimated by varying the renormalisation and factorisation scales independently, ranging from a factor of one-half to two. The uncertainty in the K-factors due to the NLO QCD scale uncertainty is 10–20% as a function of m_{ZZ} for the gg-initiated ZZ processes in the probed high-mass region, and ranges from 5% to 10% as a function of m_{ZZ} for the $q\bar{q} \to ZZ$ background. The QCD scale uncertainties are treated as correlated among the gg-initiated ZZ processes, and uncorrelated with the $q\bar{q}$-initiated ZZ process. In the region below $2m_t$, the higher-order corrections are computed with a maximum jet transverse momentum of 150 GeV to ensure a good description by the $1/m_t$ expansion. The default scale uncertainty is therefore doubled for events which have a jet with $p_T > 150$ GeV, corresponding to about 8% of the events in this region. The scale uncertainty is also increased by 50% around the m_t threshold, with a Gaussian-smoothed transition decreasing to the default uncertainty within 50 GeV of the threshold. This is intended to allow for possible effects on the K-factor which have not been estimated as the top quark moves on-shell. It is assumed that the 10–20% NLO QCD scale uncertainty for the gg-initiated ZZ processes covers the assumption of massless loops above the $2m_t$ threshold, and as well the uncertainties in the 1.2 scale factor estimated only for the NNLO/NLO signal correction but also applied to the background and interference components. These NLO QCD scale uncertainties are larger than those associated with the NNLO QCD signal uncertainties. The EW correction uncertainty for $q\bar{q} \to ZZ$ is evaluated using the same method as in Ref. [44] and its impact is estimated to be about 1%. The parton-shower uncertainty is evaluated by varying parameters in the parton-shower tunes according to Refs. [179] and found to be 2–3% in normalisation.

The theoretical uncertainties due to the missing higher-order corrections and PDF variations are small for VH-like and VBF-like processes $pp \to ZZ + 2j$; therefore, they are not included in the analysis.

The leading experimental systematic uncertainties are due to the electron and muon reconstruction and selection efficiency uncertainties, which are smaller than the uncertainties associated with the theoretical predictions. The same sources of experimental uncertainty as in Ref. [191] are evaluated.

The uncertainty in the combined 2015 and 2016 integrated luminosity is 2.1%, derived following a methodology similar to that detailed in Ref. [192], from a preliminary calibration of the luminosity scale using x–y beam-separation scans. This uncertainty is applied to the normalisation of the signal and also to background contributions whose normalisations are derived from MC simulations. A variation in the pile-up reweighting of MC events is included to cover the uncertainty in the ratio of the predicted and measured inelastic cross sections in Ref. [193].

6.3.2 Interpretations

It is useful to summarize the definitions of signal strength used in the on-shell and off-shell analyses. For on-shell analysis, the signal strength for the ggF and VBF [2] production can be written as:

$$\mu^{ggF}_{\text{on-shell}} \equiv \frac{\sigma^{gg\to H\to ZZ}_{\text{on-shell}}}{\sigma^{gg\to H\to ZZ}_{\text{on-shell, SM}}} = \frac{\kappa^2_{g,\text{on-shell}}\cdot\kappa^2_{V,\text{on-shell}}}{\Gamma_H/\Gamma^{\text{SM}}_H}, \tag{6.11}$$

$$\mu^{VBF}_{\text{on-shell}} \equiv \frac{\sigma^{VBF H\to ZZ}_{\text{on-shell}}}{\sigma^{VBF H\to ZZ}_{\text{on-shell, SM}}} = \frac{\kappa^4_{V,\text{on-shell}}}{\Gamma_H/\Gamma^{\text{SM}}_H} \tag{6.12}$$

For off-shell analysis, the signal strength for the ggF and VBF production can be written as:

$$\mu^{ggF}_{\text{off-shell}} \equiv \frac{\sigma^{gg\to H\to ZZ}_{\text{off-shell}}}{\sigma^{gg\to H\to ZZ}_{\text{off-shell, SM}}} = \kappa^2_{g,\text{off-shell}}\cdot\kappa^2_{V,\text{off-shell}}, \tag{6.13}$$

$$\mu^{VBF}_{\text{off-shell}} \equiv \frac{\sigma^{VBF H\to ZZ}_{\text{off-shell}}}{\sigma^{VBF H\to ZZ}_{\text{off-shell, SM}}} = \kappa^4_{V,\text{off-shell}} \tag{6.14}$$

And the coupling ratios are defined as ,

$$R_{gg} \equiv \kappa^2_{g,\text{off-shell}}/\kappa^2_{g,\text{on-shell}}, \tag{6.15}$$

$$R_{VV} \equiv \kappa^2_{V,\text{off-shell}}/\kappa^2_{V,\text{on-shell}} \tag{6.16}$$

Thus the on-shell signal strengths and off-shell signal strengths have the following relationship:

$$\mu^{ggF}_{\text{off-shell}} = R_{gg}\cdot R_{VV}\cdot\mu^{ggF}_{\text{on-shell}}\cdot\Gamma_H/\Gamma^{\text{SM}}_H \tag{6.17}$$

$$\mu^{VBF}_{\text{off-shell}} = R^2_{VV}\cdot\mu^{VBF}_{\text{on-shell}}\cdot\Gamma_H/\Gamma^{\text{SM}}_H \tag{6.18}$$

Since the off-shell analysis is performed inclusively, without categorization for the ggF and VBF production modes, it does not have sensitivity to individually constrain the off-shell signal strength for the ggF and VBF production modes. Thus, the signal strength $\mu_{\text{off-shell}}$ is determined by fixing the ratio of the signal strength in $gg\to H^*$ and VBF to the SM prediction, namely $\frac{\mu^{ggF}_{\text{off-shell}}}{\mu^{VBF}_{\text{off-shell}}} = 1$. The combination with the on-shell analyses is performed under some assumptions.

Since there are few free parameters in equation 6.18 and 6.18, the following interpretation is considered. The assumptions are summarized in Table 6.8.

- The $\Gamma_H/\Gamma^{\text{SM}}_H$ is determined when profiling a common coupling scale factor $\kappa = \kappa_g = \kappa_V$ associated with the on- and off-shell $gg\to H^{(*)}$ and VBF production and the $H^{(*)}\to VV$ decay, assuming $\kappa_{g,\text{on-shell}} = \kappa_{g,\text{off-shell}}$ and $\kappa_{V,\text{on-shell}} = \kappa_{V,\text{off-shell}}$. Thus for on-shell measurement there is only one overall signal strenght.

POI	Profiling	Assumptions
$\Gamma_H/\Gamma^{\text{SM}}_H$	$\mu_{\text{on-shell}}$	$\kappa_{g,\text{on-shell}} = \kappa_{g,\text{off-shell}} = \kappa_{V,\text{on-shell}} = \kappa_{V,\text{off-shell}}$, thus R_{gg}=1, R_{VV}=1, $\mu^{ggF}_{\text{on-shell}} = \mu^{VBF}_{\text{on-shell}}$

Table 6.8: On-shell and Off-shell combined fit configurations for the various interpretations.

[2] In all results the signal strength for VH associated production is assumed to scale with VBF production while the $b\bar{b}H$ and $t\bar{t}H$ processes scale with the $gg\to H$ process. These additional production modes are expected to give negligible contributions to the off-shell measurements, but have small contributions to the on-shell signal yields.

6.3.3 Statistical analysis

In the $ZZ \rightarrow 4\ell$ channel, a binned maximum-likelihood fit to the ME-based discriminant distribution is performed to extract the limits on the off-shell Higgs boson signal strength. The fit model accounts for signal and background processes, including $gg \rightarrow (H^* \rightarrow)ZZ$, VBF$(H^* \rightarrow)ZZ$ and $q\bar{q} \rightarrow ZZ$. The probability density functions (pdf) of the signal-related processes $gg \rightarrow (H^* \rightarrow)ZZ$ and VBF $(H^* \rightarrow)ZZ$ are parametrised as a function of both the off-shell Higgs boson signal strength $\mu_{\text{off-shell}}$ as given in Eqs. (6.5) and (6.9). Normalisation and shape systematic uncertainties on the signal and background processes are taken into account as described in Sect. 6.3.1, with correlations between different components and processes as indicated therein.

In the $ZZ \rightarrow 2\ell 2\nu$ channel, a similar maximum-likelihood fit to the transverse mass (m_{T}^{ZZ}) is performed, comparing the event yield in the signal-enriched region in data with the predictions. The fit model accounts for the signal and all background processes mentioned in Table 6.4. The modelling of the dominant signal and background processes is the same as in the $ZZ \rightarrow 4\ell$ channel.

The likelihood is a function of a parameter of interest μ and nuisance parameters $\vec{\theta}$. Hypothesis testing and confidence intervals are based on the profile likelihood ratio [194]. The parameters of interest are different in the various tests, while the remaining parameters are profiled. Hypothesised values for a parameter of interest μ are tested with a statistic

$$\Lambda(\mu) = \frac{L\big(\mu, \hat{\hat{\vec{\theta}}}(\mu)\big)}{L(\hat{\mu}, \hat{\vec{\theta}})} \quad , \tag{6.19}$$

where the single circumflex denotes the unconditional maximum-likelihood estimate of a parameter and the double circumflex (e.g. $\hat{\hat{\vec{\theta}}}(\mu)$) denotes the conditional maximum-likelihood estimate (e.g. of $\vec{\theta}$) for given fixed values of μ. This test statistic extracts the information on the parameters of interest from the full likelihood function.

Apart from the simple likelihood scan method, all 95% confidence level (CL) upper limits are also derived using the CLs method [156], based on the following ratio of one-sided p-values: $\mathrm{CLs}(\mu) = p_\mu/(1-p_1)$ where p_μ is the p-value for testing a given $\mu = \mu_{\text{off-shell}}$ or $\mu = \Gamma_H/\Gamma_H^{\mathrm{SM}}$ (the non-SM hypothesis) and p_1 is the p-value derived from the same test statistic under the SM hypothesis of $\mu_{\text{off-shell}} = 1$ in the first case and $\Gamma_H/\Gamma_H^{\mathrm{SM}} = \mu_{\text{on-shell}} = 1$ in the second case.[3] The 95% CLs upper limit is found by solving for $\mathrm{CLs}(\mu^{95\%}) = 5\%$. Values $\mu > \mu^{95\%}$ are regarded as excluded at 95% CL. A detailed description of the implementation of the CLs procedure can be found in Ref. [195].

The results presented rely on the asymptotic approximation [194] for the test statistic $\Lambda(\mu)$. This approximation was cross-checked with Monte Carlo ensemble tests that confirm its validity in the range of the parameters for which the 95% CL limits are derived. Deviations appear close to the boundary of $\mu_{\text{off-shell}} \geq 0$ imposed by Eq. (6.4) and hence the 1σ uncertainties can only be seen as approximate.

The combination results are obtained with the NLO K-factors for the $gg \rightarrow ZZ$ processes in the off-shell analyses, with an additional flat NNLO/NLO K-factor of 1.2 applied.

6.3.4 Off-shell signal strength

The $4l$ and $2l2\nu$ analyses are combined to obtain a limit on $\mu_{\text{off-shell}}$. In combining the off-shell results the main systematic uncertainties related to the theory uncertainties on the $gg \rightarrow (H^* \rightarrow)ZZ$ (including signal and interference contributions) and $q\bar{q} \rightarrow ZZ$ processes are treated as correlated between the different channels. Where appropriate, the experimental systematic uncertainties are also treated as correlated. However, they are found to have a very small impact on the final combined limit.

[3] In the context of this analysis the alternative hypothesis is given by the SM value(s) for all relevant parameters of the fit model.

The scan of the negative log-likelihood, $-2\ln\Lambda$, as a function of $\mu_{\text{off-shell}}$ for data and the expected curve obtained when fitting an Asimov dataset for a SM Higgs boson and data are shown in Fig. 6.13, with the signal strength parameters in both $gg \to H^*$ and VBF fixed to the SM prediction.

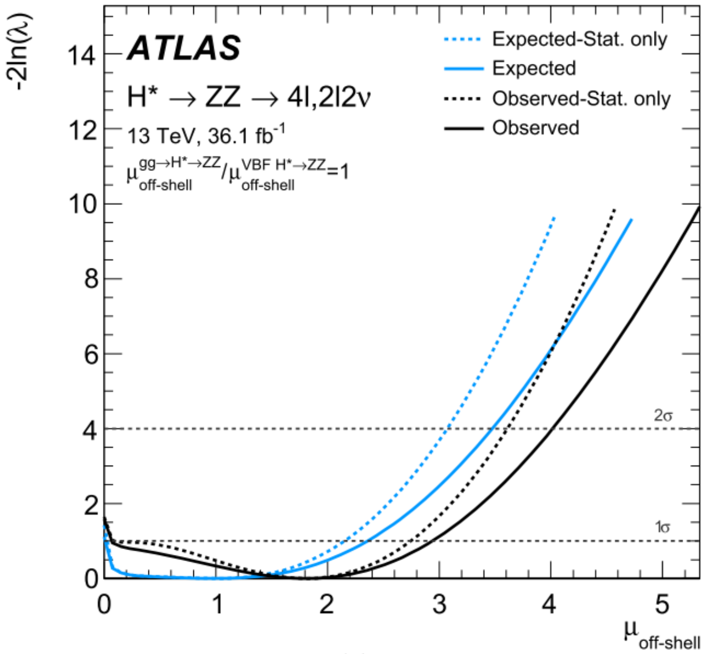

Figure 6.13: Scan of the negative log-likelihood, -2lnΛ, for the off-shell signal strength, for data (black) and simulation (blue) with the $ZZ \to 4\ell$ and $ZZ \to 2\ell\,2\nu$ off-shell analyses combined. The m_{ZZ} dependent NLO K-factors and an additional flat NNLO/NLO K-factor of 1.2 are applied each individual $gg \to ZZ$ process [187].

6.3.5 Higgs total width

To extract the final result on Higgs total width constraint, the off-shell analyses of both $ZZ \to 4\ell$ and $ZZ \to \ell^+\ell^-\nu\bar{\nu}$ are combined with the on-shell $ZZ \to 4\ell$ analysis. In combining the on-shell results, the experimental uncertainties and the theory uncertainties are properly considered in the combination. Especially the QCD scale uncertainties for the gg processes are treated as uncorrelated between the on-shell and off-shell analyes, given the different high-order QCD corrections. The QCD scale uncertainties for the $q\bar{q} \to ZZ$ process are treated as correlated. Where appropriate, the experimental systematic uncertainties are also treated as correlated. However, they are found to have a very small impact on the final combined limit.

The negative log-likelihood scan on $\Gamma_H/\Gamma_H^{\text{SM}}$ is shown in figure 6.14 with data and Asimov data, assuming the off-shell signal strength parameters in both $gg \to H^*$ and VBF fixed to the SM prediction. The best fit signal strength for the on-shell Higgs ($\mu_{\text{on-shell}}$) is found to be 1.24, slightly different than the measurement in the coupling analysis [196], which is 1.29. The difference is caused by the correlation of the nuisance parameters in the combined fit. The observed upper limit on $\Gamma_H/\Gamma_H^{\text{SM}}$ is slightly smaller than the expected, due to the fact that the observed $\mu_{\text{on-shell}}$ is larger than 1.

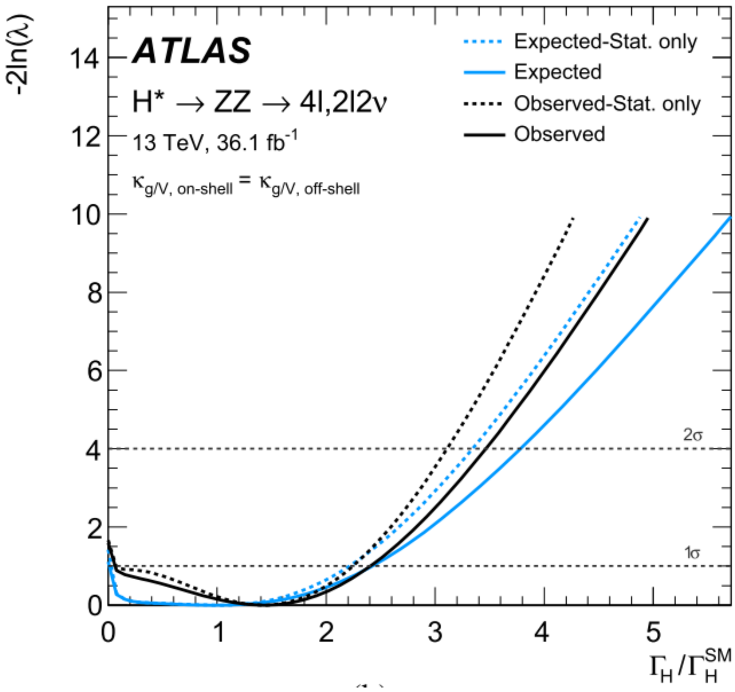

(a)

Figure 6.14: Scan of the negative log-likelihood, -2lnΛ, for data (black) and simulation (blue) for the Γ_H/Γ_H^{SM} ratio, with the on-shell and the $ZZ \to 4\ell$, $ZZ \to 2\ell\,2\nu$ off-shell analyses combined. The m_{ZZ} dependent NLO K-factors and an additional flat NNLO/NLO K-factor of 1.2 are applied to the $gg \to ZZ$ process for the off-shell analysis [187].

6.3.6 Summary

The fit results on $\mu_{\text{off-shell}}$ and $\Gamma_H/\Gamma_H^{\text{SM}}$ are summarized in Table 6.9. Results from both the likelihood scan and the CL$_s$ method are presented. For the CLs method, the SM prediction ($\mu_{\text{off-shell}} = 1$ and $\Gamma_H/\Gamma_H^{\text{SM}} = 1$) is used as the alternative hypothesis. Table 6.10 shows the impact the systematic uncertainties on the fit results of $\mu_{\text{off-shell}}$ and $\Gamma_H/\Gamma_H^{\text{SM}}$ using the likelihood scan method. The results are obtained with the NLO K-factors and an additional flat NNLO/NLO K-factor of 1.2.

Fit configuration	POI	CLs				NLL	
		Median expected	Obs.	[-1σ,+1σ]	[-2σ,+2σ]	Expected	Observed
Off-Shell 4ℓ	$\mu_{\text{off-shell}}$	4.25	4.49	3.34 - 5.43	2.74 - 7.06	4.36	4.65
Off-Shell $\ell^+\ell^-\nu\bar{\nu}$	$\mu_{\text{off-shell}}$	4.37	5.31	3.43 - 5.51	2.81 - 7.01	4.47	5.68
Off-Shell 4ℓ + $\ell^+\ell^-\nu\bar{\nu}$	$\mu_{\text{off-shell}}$	3.41	3.81	2.73 - 4.21	2.29 - 5.26	3.48	4.02
Off-Shell 4ℓ + $\ell^+\ell^-\nu\bar{\nu}$ + On-Shell	$\Gamma_H/\Gamma_H^{\text{SM}}$	3.68	3.50	2.94 - 4.79	2.44 - 6.50	3.78	3.46

Table 6.9: Summary of the fit results on $\mu_{\textit{off-shell}}$ and Γ_H/Γ_H^{SM} . Results obtained from both the likelihood scan and the CL$_s$ method are shown for comparison. The results are obtained with the NLO K-factors and an additional flat NNLO/NLO K-factor of 1.2. The ratio of the ggF and VBF processes is assumed to be as in the SM.

Fit configuration	POI	NLL	
		Stat. only	All syst.
Off-Shell 4ℓ	$\mu_{\text{off-shell}}$	4.40	4.65
Off-Shell $\ell^+\ell^-\nu\bar{\nu}$	$\mu_{\text{off-shell}}$	4.80	5.68
Off-Shell 4ℓ + $\ell^+\ell^-\nu\bar{\nu}$	$\mu_{\text{off-shell}}$	3.61	4.02
Off-Shell 4ℓ + $\ell^+\ell^-\nu\bar{\nu}$ + On-Shell 4ℓ	$\Gamma_H/\Gamma_H^{\text{SM}}$	3.11	3.46

Table 6.10: Impact of systematic uncertainties on $\mu_{\textit{off-shell}}$ and Γ_H/Γ_H^{SM} . Observed results are obtained with the likelihood scan method.

7 Summary

During Run II (2015-2018) the ATLAS experiment collected data corresponding to about 140 fb^{-1}. Its capability to maintain the excellent performance depends on a series of upgrades.

During Upgrade Phase II a new Inner Tracker will be installed allowing for a great improvement of the electron identification in the forward region, as it was shown in Chapter 3. By combining cluster-track matching criteria, machine learning methods and isolation variables an about 83% efficiency can be achieved yielding to a fake rate of about 2%. This study was included in publication [197].

The ATLAS experiment contributes significantly on Higgs boson studies. One of the best channels for these studies is the decay of Higgs boson to ZZ* and afterwards to 4 leptons. The estimation of the reducible background in this channel is driven by the real data, as presented in Chapter 4. The results are used for several Higgs studies. Two of them, need a differential estimation of the background are already published ([198] and [199]).

Some BSM models predict more Higgs-like bosons. The study described in Chapter 5 is a search for a new heavy ZZ resonance. It was performed with the full data of Run II. The existence of a new resonance is excluded using the CLs method. The expected upper limit on cross section times branching ratio for the ggF production is a function of the mass, decreasing from 150 fb at 200 GeV to about 6 fb at 2 TeV. The VBF production limits have similar behaviour, decreasing from 50 fb at 200 GeV to 6 pb at 2 TeV. The statistical analysis yielded to some small excesses (roughly 2σ) for 3 mass points in the CLs. The sensitivity of the experiment using the Neural Network based categorization and the combination with the $\ell\ell\nu\nu$ is expected to be improved. The study including these improvements will be published soon . Also the collection of more data during Run III will allow the exclusion limits to become even deeper and possible excesses will be revealed. In the previous study of this search, made using integrated luminosity of 36 fb^{-1} [200], the ggF production limits, using only the 4ℓ channel, had been calculated decreasing from 300 fb at 200 GeV to about 30 fb at 2 TeV and for the VBF production decreasing from 150 fb at 200 GeV to about 30 fb at 2 TeV.

Lastly, the off-shell Higgs boson cross section was measured in Chapter 6 allowing to set limits on the decay width. Combining the results with the $ll\nu\nu$ channels, the extracted limit on Γ_H/Γ_H^{SM} at 95% CL is 3.46 times the SM prediction. This measurement was performed using only 2015-1016 data, corresponding to about 70 fb $^{-1}$, and it was published in 2018 [187]. The analysis of the full Run II dataset as well as the improvement of the analysis methodology will probably allow for a precise measurement of the width for the first time. The previous study of this subject [201] was made using data of 20 fb^{-1} integrated luminosity collected at $\sqrt{s} = 8$ TeV. In this case the data yielded an observed (expected) 95% CL upper limit on the width in the range 4.5–7.5 (6.5–11.2).

A Appendices

A.1 Forward Electron Identification

A.1.1 Track-cluster matching criteria p_T dependency

$\lvert\eta\rvert$	2.5-3.2	3.2-3.35	3.35-4.0
Single e 20GeV	92.3±0.1	89.9±0.4	90.7±0.1
Single e 45GeV	96.46±0.07	95.6±0.2	95.41±0.08
Single e 100GeV	98.38±0.09	97.8±0.3	97.3±0.1
Single e with pile-up 20GeV	91.5±0.7	84±3	90.3±0.8
Single e with pile-up 45GeV	94.6±0.6	93±2	94.4±0.6
Single e with pile-up 100GeV	97.9±0.6	94±2	96.8±0.7

Table A.1: Matching criteria efficiency-fake rate(%). Only statistical errors included.

A.1.2 Intermediate region cluster shapes

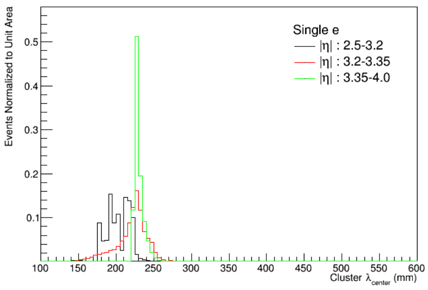

(a)

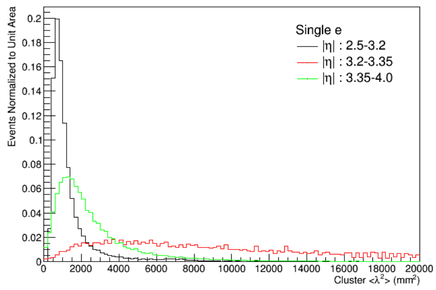

(b)

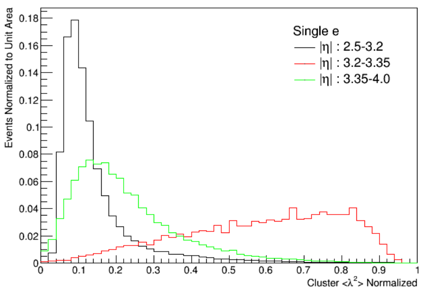

(c)

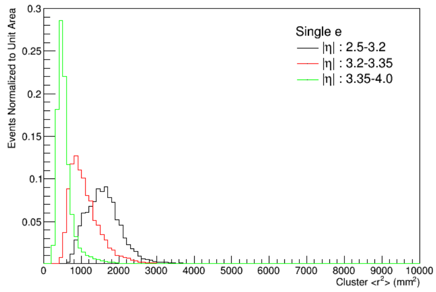

(d)

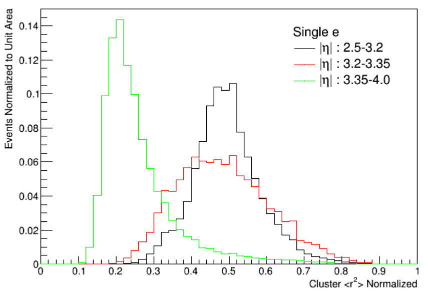

(e)

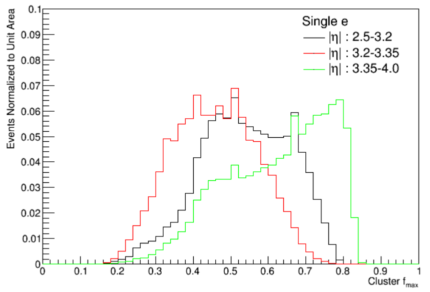

(f)

Figure A.1: Cluster shape variables in different η regions

A.1.3 Cluster shapes p_T dependency

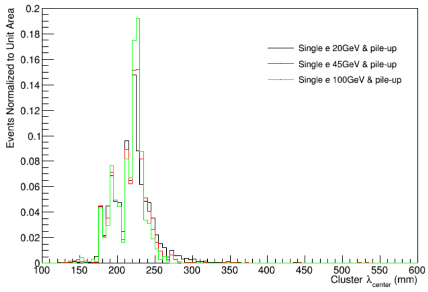

(a)

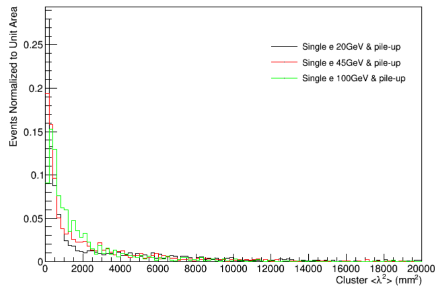

(b)

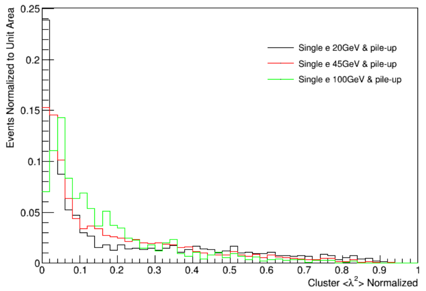

(c)

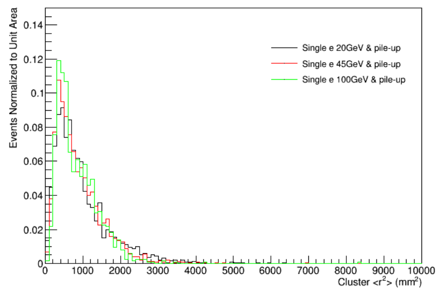

(d)

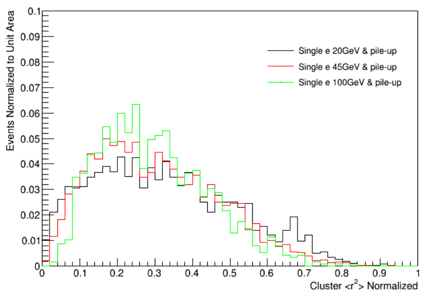

(e)

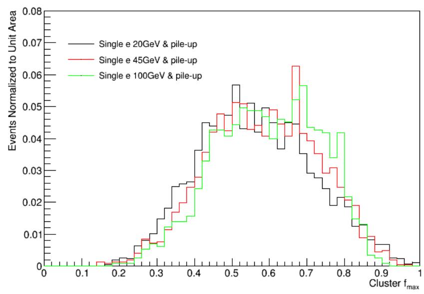

(f)

Figure A.2: Cluster shapes variables for different momenta

A.1.4 BDT performance

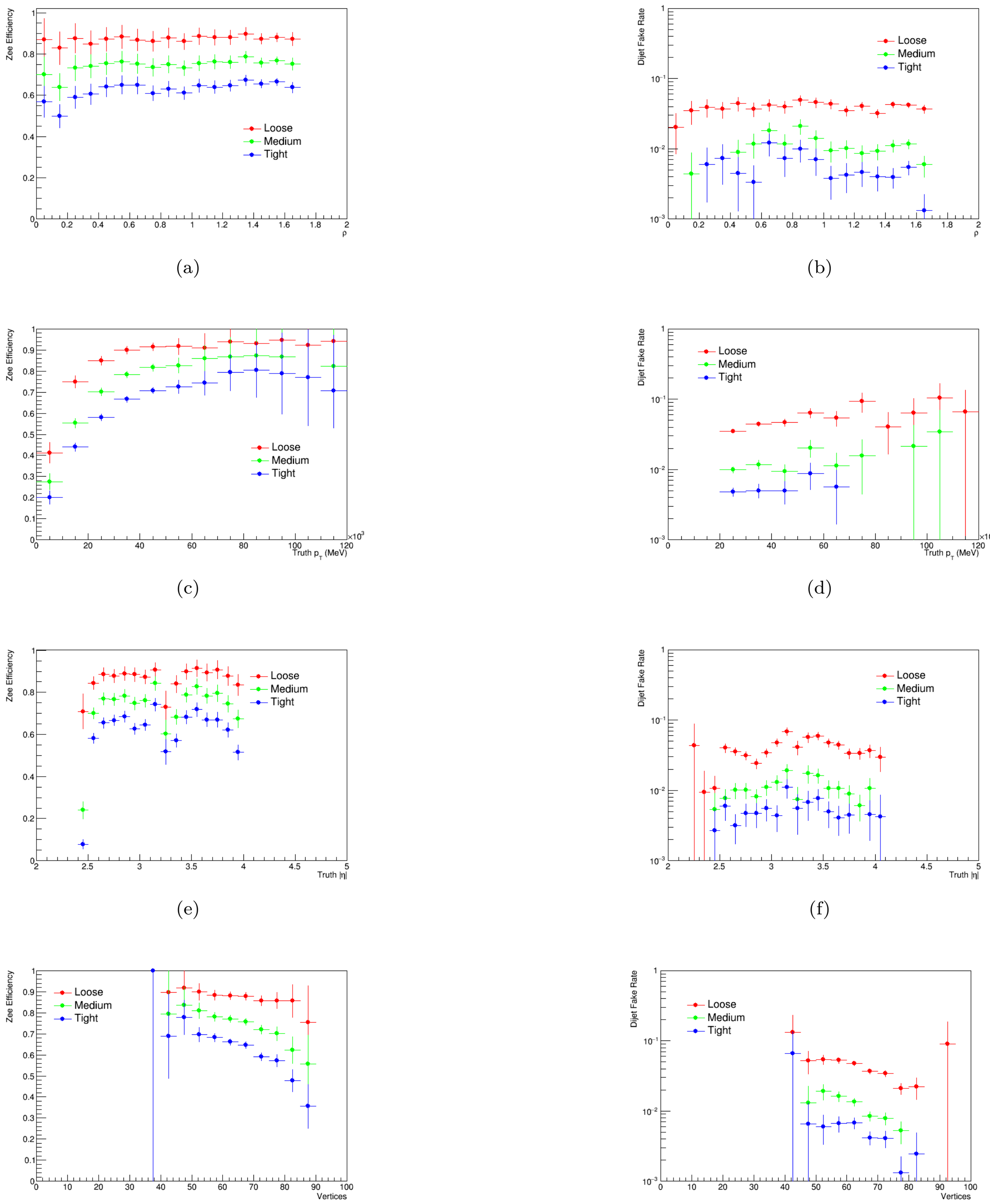

(a) (b)

(c) (d)

(e) (f)

(g) (h)

Figure A.3: BDT method efficiency and fake rate

A.1.5 Isolation

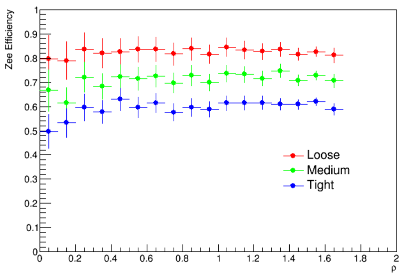

(a)

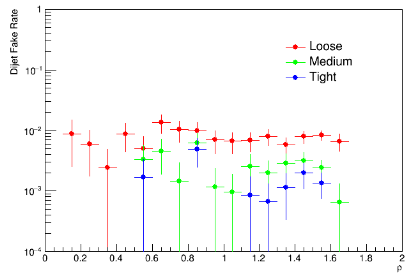

(b)

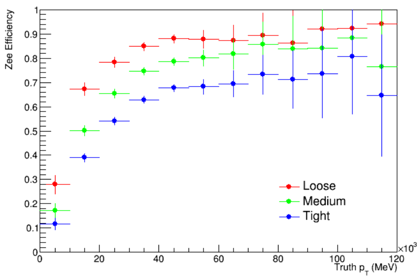

(c)

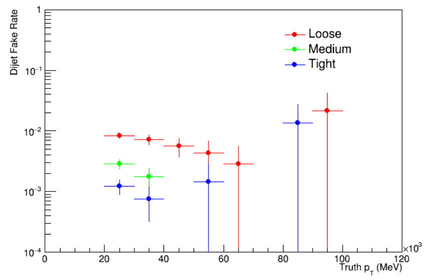

(d)

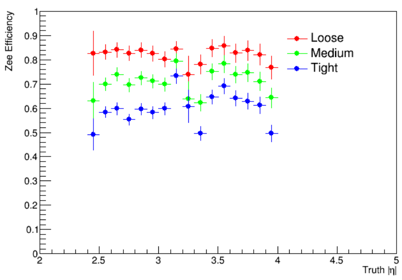

(e)

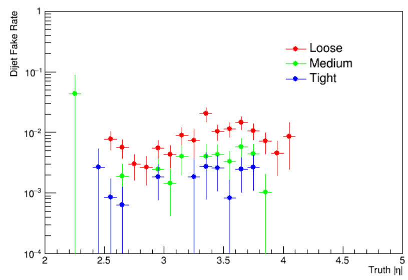

(f)

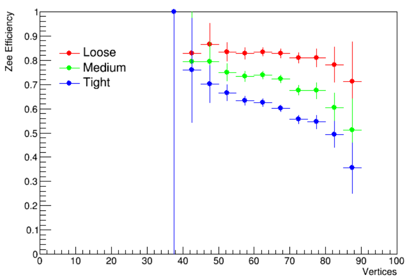

(g)

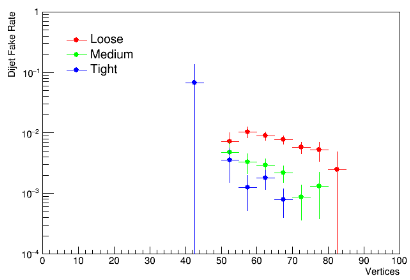

(h)

Figure A.4: Efficiency and fake rate after isolation cut application

A.2 Calculated SM Higgs boson production cross sections (σ)

m_H GeV	$\sigma\,(gg \to H)$ [pb]	$\sigma\,(qq' \to Hqq')$ [pb]	$\sigma\,(q\bar{q} \to WH)$ [pb]	$\sigma\,(pp \to ZH)$ [pb]
124.0	$49.27\ ^{+4.6\%}_{-6.8\%}\ ^{+3.2\%}_{-3.2\%}$	$3.812\ ^{+0.4\%}_{-0.3\%}\ ^{+2.1\%}_{-2.1\%}$	$1.408\ ^{+0.6\%}_{-0.6\%}\ ^{+1.9\%}_{-1.9\%}$	$0.9051\ ^{+3.6\%}_{-3.1\%}\ ^{+1.6\%}_{-1.6\%}$
124.5	$48.92\ ^{+4.6\%}_{-6.7\%}\ ^{+3.2\%}_{-3.2\%}$	$3.798\ ^{+0.4\%}_{-0.3\%}\ ^{+2.1\%}_{-2.1\%}$	$1.390\ ^{+0.6\%}_{-0.6\%}\ ^{+1.9\%}_{-1.9\%}$	$0.8943\ ^{+3.8\%}_{-3.0\%}\ ^{+1.6\%}_{-1.6\%}$
125.0	$48.58\ ^{+4.6\%}_{-6.7\%}\ ^{+3.2\%}_{-3.2\%}$	$3.782\ ^{+0.4\%}_{-0.3\%}\ ^{+2.1\%}_{-2.1\%}$	$1.373\ ^{+0.5\%}_{-0.7\%}\ ^{+1.9\%}_{-1.9\%}$	$0.8839\ ^{+3.8\%}_{-3.1\%}\ ^{+1.6\%}_{-1.6\%}$
125.09	$48.52\ ^{+4.6\%}_{-6.7\%}\ ^{+3.2\%}_{-3.2\%}$	$3.779\ ^{+0.4\%}_{-0.3\%}\ ^{+2.1\%}_{-2.1\%}$	$1.369\ ^{+0.5\%}_{-0.7\%}\ ^{+1.9\%}_{-1.9\%}$	$0.8824\ ^{+3.8\%}_{-3.0\%}\ ^{+1.6\%}_{-1.6\%}$
125.5	$48.23\ ^{+4.6\%}_{-6.7\%}\ ^{+3.2\%}_{-3.2\%}$	$3.767\ ^{+0.4\%}_{-0.3\%}\ ^{+2.1\%}_{-2.1\%}$	$1.355\ ^{+0.5\%}_{-0.7\%}\ ^{+1.9\%}_{-1.9\%}$	$0.8744\ ^{+3.7\%}_{-3.1\%}\ ^{+1.6\%}_{-1.6\%}$
126.0	$47.89\ ^{+4.5\%}_{-6.7\%}\ ^{+3.2\%}_{-3.2\%}$	$3.752\ ^{+0.4\%}_{-0.3\%}\ ^{+2.1\%}_{-2.1\%}$	$1.337\ ^{+0.6\%}_{-0.8\%}\ ^{+1.9\%}_{-1.9\%}$	$0.8649\ ^{+3.8\%}_{-3.1\%}\ ^{+1.6\%}_{-1.6\%}$
m_H GeV	$\sigma\,(gg \to ZH)$ [pb]	$\sigma\,\left(q\bar{q}/gg \to t\bar{t}H\right)$ [pb]	$\sigma\,\left(q\bar{q}/gg \to b\bar{b}H\right)$ [pb]	$B\ (H \to ZZ^* \to 4\ell)$ $[10^{-3}]$
124.0	$0.1242\ ^{+25.1\%}_{-18.9\%}\ ^{+2.4\%}_{-2.4\%}$	$0.5193\ ^{+5.9\%}_{-9.2\%}\ ^{+3.6\%}_{-3.6\%}$	$0.4999\ ^{+20.1\%}_{-24.0\%}$	$0.1131 \pm 2.24\%$
124.5	$0.1235\ ^{+25.1\%}_{-18.9\%}\ ^{+2.4\%}_{-2.4\%}$	$0.5132\ ^{+5.8\%}_{-9.2\%}\ ^{+3.6\%}_{-3.6\%}$	$0.4930\ ^{+20.0\%}_{-23.9\%}$	$0.1185 \pm 2.21\%$
125.0	$0.1227\ ^{+25.1\%}_{-18.9\%}\ ^{+2.4\%}_{-2.4\%}$	$0.5071\ ^{+5.8\%}_{-9.2\%}\ ^{+3.6\%}_{-3.6\%}$	$0.4880\ ^{+20.2\%}_{-23.9\%}$	$0.1240 \pm 2.18\%$
125.09	$0.1227\ ^{+25.1\%}_{-18.9\%}\ ^{+2.4\%}_{-2.4\%}$	$0.5065\ ^{+5.7\%}_{-9.3\%}\ ^{+3.6\%}_{-3.6\%}$	$0.4863\ ^{+20.1\%}_{-23.9\%}$	$0.1251 \pm 2.16\%$
125.5	$0.1221\ ^{+25.1\%}_{-18.9\%}\ ^{+2.4\%}_{-2.4\%}$	$0.5023\ ^{+5.7\%}_{-9.3\%}\ ^{+3.6\%}_{-3.6\%}$	$0.4809\ ^{+20.1\%}_{-23.8\%}$	$0.1297 \pm 2.14\%$
126.0	$0.1218\ ^{+25.1\%}_{-18.9\%}\ ^{+2.4\%}_{-2.4\%}$	$0.4964\ ^{+5.7\%}_{-9.3\%}\ ^{+3.6\%}_{-3.6\%}$	$0.4760\ ^{+20.2\%}_{-24.0\%}$	$0.1355 \pm 2.12\%$

Table A.2: Calculated SM Higgs boson production cross sections (σ) for gluon fusion, vector-boson fusion and associated production with a W or Z boson or with a $b\bar{b}$ or $t\bar{t}$ pair in pp collisions at $\sqrt{s} = 13$ TeV. The first and second quoted uncertainties correspond to the theoretical systematic uncertainties calculated by adding in quadrature the QCD scale and PDF+α_s uncertainties, respectively. The decay branching ratio (B) for $H \to 4\ell$ with $\ell = e, \mu$, is reported in the last column.

A.3 List of Monte Carlo simulation samples

A.3.1 Signal samples

Sample	Generator	Tune	PDF	σ	Filter efficiency	K-factor
MC16.341471.PowhegPythia8EvtGen_CT10_AZNLOCTEQ6L1_ggH125_ZZ4lep	Powheg+Pythia8+EvtGen	AZNLO_CTEQ6L1	NULL	30.2	1.0	1.0
MC16.341504.PowhegPythia8EvtGen_CT10_AZNLOCTEQ6L1_ggH124_ZZ4lep_noTau	Powheg+Pythia8+EvtGen	AZNLO_CTEQ6L1	NULL	30.6	1	1
MC16.341505.PowhegPythia8EvtGen_CT10_AZNLOCTEQ6L1_ggH125_ZZ4lep_noTau	Powheg+Pythia8+EvtGen	AZNLO_CTEQ6L1	NULL	30.2	1.0	1.0
MC16.341506.PowhegPythia8EvtGen_CT10_AZNLOCTEQ6L1_ggH126_ZZ4lep_noTau	Powheg+Pythia8+EvtGen	AZNLO_CTEQ6L1	NULL	29.8	1	1
MC16.341508.PowhegPythia8EvtGen_CT10_AZNLOCTEQ6L1_ggH128_ZZ4lep_noTau	Powheg+Pythia8+EvtGen	AZNLO_CTEQ6L1	NULL	29.0	1	1
MC16.345060.PowhegPythia8EvtGen_NNLOPS_nnlo_30_ggH125_ZZ4l	Powheg+Pythia8+EvtGen	AZNLO_CTEQ6L1	NULL	28.3	1	1
MC16.342282.PowhegPythia8EvtGen_CT10_AZNLOCTEQ6L1_ggH125_inc	Powheg+Pythia8+EvtGen	AZNLO_CTEQ6L1	NULL	48.6	1	1
MC16_13TeV.345576.PowhegPythia8EvtGen_NNLOPS_nnlo_30_ggH123_ZZ4l	Powheg+Pythia8+EvtGen	AZNLO_CTEQ6L1	NULL	29.5	1	1
MC16_13TeV.345577.PowhegPythia8EvtGen_NNLOPS_nnlo_30_ggH124_ZZ4l	Powheg+Pythia8+EvtGen	AZNLO_CTEQ6L1	NULL	29.1	1	1
MC16_13TeV.345578.PowhegPythia8EvtGen_NNLOPS_nnlo_30_ggH126_ZZ4l	Powheg+Pythia8+EvtGen	AZNLO_CTEQ6L1	NULL	28.3	1	1
MC16_13TeV.345579.PowhegPythia8EvtGen_NNLOPS_nnlo_30_ggH127_ZZ4l	Powheg+Pythia8+EvtGen	AZNLO_CTEQ6L1	NULL	27.9	1	1
MC16_13TeV.345581.PowhegPythia8EvtGen_NNLOPS_nnlo_30_ggH123p5_ZZ4l	Powheg+Pythia8+EvtGen	AZNLO_CTEQ6L1	NULL	29.3	1	1
MC16_13TeV.345582.PowhegPythia8EvtGen_NNLOPS_nnlo_30_ggH124p5_ZZ4l	Powheg+Pythia8+EvtGen	AZNLO_CTEQ6L1	NULL	28.9	1	1
MC16_13TeV.345583.PowhegPythia8EvtGen_NNLOPS_nnlo_30_ggH125p5_ZZ4l	Powheg+Pythia8+EvtGen	AZNLO_CTEQ6L1	NULL	28.5	1	1

Table A.3: Signal low-mass MC ggF. All p-tags are p3387 unless otherwise noted.

Sample	Generator	Tune	PDF	σ	Filter efficiency	K-factor
MC16.341488.PowhegPythia8EvtGen_CT10_AZNLOCTEQ6L1_VBFH125_ZZ4lep	Powheg+Pythia8+EvtGen	AZNLO_CTEQ6L1	NULL	3.83	1	0.979
MC16.344235.PowhegPy8EG_NNPDF30_AZNLOCTEQ6L1_VBFH125_ZZ4lep_notau	Powheg+Pythia8+EvtGen	AZNLO_CTEQ6L1	NULL	3.74	1	1
MC16.342283.PowhegPythia8EvtGen_CT10_AZNLOCTEQ6L1_VBFH125_inc	Powheg+Pythia8+EvtGen	AZNLO_CTEQ6L1	NULL	3.83	1	0.9781

Table A.4: Signal low-mass MC VBF.

Sample	Generator	Tune	PDF	σ	Filter efficiency	K-factor
MC16.341947.Pythia8EvtGen_A14NNPDF23LO_ZH125_ZZ4l	Pythia8+EvtGen	A14_NNPDF23LO	NULL	0.0158	0.0103	1
MC16.341975.Pythia8EvtGen_A14NNPDF23LO_ZllH125_ZZ4l	Pythia8+EvtGen	A14_NNPDF23LO	NULL	1.6e-05	1	1
MC16.345038.PowhegPythia8EvtGen_NNPDF30_AZNLO_ZH125J_Zincl_MINLO	Powheg+Pythia8+EvtGen	AZNLO_CTEQ6L1	NULL	0.761	1	1

Table A.5: Signal low-mass MC ZH.

Sample	Generator	Tune	PDF	σ	Filter efficiency	K-factor
MC16.345066.PowhegPythia8EvtGen_NNPDF3_AZNLO_ggZH125_ZZ4lepZinc	Powheg+Pythia8+EvtGen	AZNLO_CTEQ6L1	NULL	0.057	1	1

Table A.6: Signal low-mass MC ggZH (e5931_e5984_s3126).

Sample	Generator	Tune	PDF	σ	Filter efficiency	K-factor
MC16.341964.Pythia8EvtGen_A14NNPDF23LO_WH125_ZZ4l	Pythia8+EvtGen	A14_NNPDF23LO	NULL	0.000291	1	1.0
MC16.345039.PowhegPythia8EvtGen_NNPDF30_AZNLO_WpH125J_Wincl_MINLO	Powheg+Pythia8+EvtGen	AZNLO_CTEQ6L1	NULL	0.862	1	1
MC16.345040.PowhegPythia8EvtGen_NNPDF30_AZNLO_WmH125J_Wincl_MINLO	Powheg+Pythia8+EvtGen	AZNLO_CTEQ6L1	NULL	0.54	1	1

Table A.7: Signal low-mass MC WH.

Sample	Generator	Tune	PDF	σ	Filter efficiency	K-factor
MC16.342561.aMcAtNloHerwigppEvtGen_UEEE5_CTEQ6L1_CT10ME_ttH125_4l	aMcAtNlo+Herwigpp+EvtGen	CTEQ6L1-UE-EE-5	CT10(ME);cteq6l1(shower/MPI)	0.446	1.0	1.0
MC16.345936.PowhegPy8EG_A14NNPDF23_NNPDF30ME_ttH125_ZZ4l_allhad_Winc	Powheg+Pythia8+EvtGen	A14 NNPDF23LO	NULL	0.325	1	1
MC16.345047.PowhegPythia8EvtGen_A14NNPDF23_NNPDF30ME_ttH125_ZZ4l_semilep	Powheg+Pythia8+EvtGen	A14 NNPDF23LO	NULL	0.627	1	1
MC16.345048.PowhegPythia8EvtGen_A14NNPDF23_NNPDF30ME_ttH125_ZZ4l_dilep	Powheg+Pythia8+EvtGen	A14 NNPDF23LO	NULL	0.052	1	1

Table A.8: Signal low-mass MC ttH.

Sample	Generator	Tune	PDF	σ	Filter efficiency	K-fac
MC16.345966.aMcAtNloHppEG_UEEE5_CTEQ6L1_CT10ME_tWH125_ZZ4l_yt_plus1	MadGraph5_aMC@NLO+Herwigpp+EvtGen	CTEQ6L1-UE-EE-5	CT10 (ME); cteq6l1 (shower/MPI)		1	1
MC16.345967.MadGraphPythia8EvtGen_A14_CT10ME_tHjb125_ZZ4l	MadGraph5_aMC@NLO+Pythia8+EvtGen+Photospp	A14 NNPDF23LO	NULL	0.054	1	1
MC16.342001.aMcAtNloHppEG_UEEE5_CTEQ6L1_CT10ME_tWH125_lep_yt_plus1	MadGraph5_aMC@NLO+Herwigpp)+EvtGen	CTEQ6L1-UE-EE-5	CT10 (ME); cteq6l1 (shower/MPI)		1	1
MC16.343273.MadGraphPythia8EvtGen_A14_CT10ME_tHjb125_lep	MadGraph5_aMC@NLO+Pythia8+EvtGen+Photospp	A14 NNPDF23LO	NULL	0.054	1	1

Table A.9: Signal low-mass MC tH.

Sample	Generator	Tune	PDF	σ	Filter efficiency	K-factor
MC16.344973.aMcAtNloPythia8EvtGen_A14NNPDF23LO_bbH125_yb2_ZZ4lep_noTau	aMcAtNlo+Pythia8+EvtGen	A14_NNPDF23LO	NULL	0.426	1	1
MC16.344974.aMcAtNloPythia8EvtGen_A14NNPDF23LO_bbH125_ybyt_ZZ4lep_noTau	aMcAtNlo+Pythia8+EvtGen	A14_NNPDF23LO	NULL		1	1

Table A.10: Signal low-mass MC bbH.

A.3.2 ZZ background samples

Sample	Generator	Tune	PDF	σ	Filter efficiency	K-factor
MC16.361603.PowhegPy8EG_CT10nloME_AZNLOCTEQ6L1_ZZllll_mll4	Powheg+Pythia8+EvtGen	AZNLO_CTEQ6L1	NULL	1.27	1	1
MC16.342556.PowhegPy8EG_CT10nloME_AZNLOCTEQ6L1_ZZllll_mll4_m4l_100_150	Powheg+Pythia8+EvtGen	AZNLO_CTEQ6L1	NULL	1.28	0.0325	1
MC16.343232.PowhegPy8EG_CT10nloME_AZNLOCTEQ6L1_ZZllll_mll4_m4l_500_13000	Powheg+Pythia8+EvtGen	AZNLO_CTEQ6L1	NULL	1.27	0.00368	1

Table A.11: Powheg $q\bar{q} \to ZZ$ background samples.

Sample	Generator	Tune	PDF	σ	Filter efficiency	K-factor
MC16.343212.Powheggg2vvPythia8EvtGen_gg_ZZ_bkg_2e2mu_13TeV	Powheg+gg2vv+Pythia8+EvtGen	A14_NNPDF23LO	NULL	0.00275	1	1
MC16.343213.Powheggg2vvPythia8EvtGen_gg_ZZ_bkg_4l_noTau_13TeV	Powheg+gg2vv+Pythia8+EvtGen	A14_NNPDF23LO	NULL	0.0027	1	1

Table A.12: gg2vv $gg \to ZZ$ samples.

Sample	Generator	Tune	PDF	σ	Filter efficiency	K-factor
MC16.364250.Sherpa_222_NNPDF30NNLO_llll	Sherpa 2.2.2	NNPDF3.0 NNLO	NNPDF30NNLO	1.25	1	1
MC16.364251.Sherpa_222_NNPDF30NNLO_llll_m4l100_300_filt100_150	Sherpa 2.2.2	NNPDF3.0 NNLO	NNPDF30NNLO	0.35	0.13	1
MC16.364252.Sherpa_222_NNPDF30NNLO_llll_m4l300	Sherpa 2.2.2	NNPDF3.0 NNLO	NNPDF30NNLO	0.062	1	1
MC16.364283.Sherpa_222_NNPDF30NNLO_lllljj_EW6	Sherpa 2.2.2	NNPDF3.0 NNLO	NNPDF30NNLO	0.011	1	1
MC16.364364.Sherpa_222_NNPDF30NNLO_lllljj_EW6_noHiggs	Sherpa 2.2.2	NNPDF3.0 NNLO	NNPDF30NNLO			

Table A.13: Sherpa $qq \to ZZ$ samples.

Sample	Generator	Tune	PDF	σ	Filter efficiency	K-factor
MC16.345706.Sherpa_222_NNPDF30NNLO_ggllll_130M4l	Sherpa+OpenLoops	NNPDF3.0 NNLO	NNPDF30NNLO	0.010	1	1
MC16.345707.Sherpa_222_NNPDF30NNLO_ggllll_130M4l_5gamma	Sherpa+OpenLoops	NNPDF3.0 NNLO	NNPDF30NNLO			
MC16.345709.Sherpa_222_NNPDF30NNLO_ggllllNoHiggs_130M4l	Sherpa+OpenLoops	NNPDF3.0 NNLO	NNPDF30NNLO	0.011	1	1
MC16.345712.Sherpa_222_NNPDF30NNLO_ggllllOnlyHiggs_130M4l	Sherpa+OpenLoops	NNPDF3.0 NNLO	NNPDF30NNLO	6.0e-4	1	1

Table A.14: Sherpa $gg \to ZZ$ samples (p2879).

A.3.3 Reducible background samples

Sample	Generator	Tune	PDF	σ	Filter efficiency	K-factor
MC16.361601.PowhegPy8EG_CT10nloME_AZNLOCTEQ6L1_WZlvll_mll4	Powheg+Pythia8+EvtGen	AZNLO_CTEQ6L1	NULL	4.51	1	1

Table A.15: WZ samples.

Sample	Generator	Tune	PDF	σ	Filter efficiency	K-factor
MC16.410470.PhPy8EG_A14_ttbar_hdamp258p75_nonallhad	Powheg+Pythia8+EvtGen	A14 NNPDF23LO	NULL	730	0.544	1.14
MC16.410472.PhPy8EG_A14_ttbar_hdamp258p75_dil	Powheg+Pythia+EvtGen	A14 NNPDF23LO	NULL	730	0.105	1.14
MC16.410289.PhPy8EG_A14_ttbar_hdamp258p75_4lMFilt_40_8	Powheg+Pythia+EvtGen	A14 NNPDF23LO	NULL	730	5.5e-3	1.14

Table A.16: $t\bar{t}$ samples.

Sample	Generator	Tune	PDF	σ	Filter efficiency	K-factor
MC16.364100.Sherpa_221_NNPDF30NNLO_Zmumu_MAXHTPTV0_70_CVetoBVeto	Sherpa	NNPDF3.0_NNLO	NNPDF30NNLO	1.98e+03	0.822	0.975
MC16.364101.Sherpa_221_NNPDF30NNLO_Zmumu_MAXHTPTV0_70_CFilterBVeto	Sherpa	NNPDF3.0_NNLO	NNPDF30NNLO	1.98e+03	0.113	0.975
MC16.364102.Sherpa_221_NNPDF30NNLO_Zmumu_MAXHTPTV0_70_BFilter	Sherpa	NNPDF3.0_NNLO	NNPDF30NNLO	1.98e+03	0.0642	0.975
MC16.364103.Sherpa_221_NNPDF30NNLO_Zmumu_MAXHTPTV70_140_CVetoBVeto	Sherpa	NNPDF3.0_NNLO	NNPDF30NNLO	109	0.689	0.975
MC16.364104.Sherpa_221_NNPDF30NNLO_Zmumu_MAXHTPTV70_140_CFilterBVeto	Sherpa	NNPDF3.0_NNLO	NNPDF30NNLO	109	0.186	0.975
MC16.364105.Sherpa_221_NNPDF30NNLO_Zmumu_MAXHTPTV70_140_BFilter	Sherpa	NNPDF3.0_NNLO	NNPDF30NNLO	109	0.114	0.975
MC16.364106.Sherpa_221_NNPDF30NNLO_Zmumu_MAXHTPTV140_280_CVetoBVeto	Sherpa	NNPDF3.0_NNLO	NNPDF30NNLO	39.9	0.609	0.975
MC16.364107.Sherpa_221_NNPDF30NNLO_Zmumu_MAXHTPTV140_280_CFilterBVeto	Sherpa	NNPDF3.0_NNLO	NNPDF30NNLO	39.8	0.233	0.975
MC16.364108.Sherpa_221_NNPDF30NNLO_Zmumu_MAXHTPTV140_280_BFilter	Sherpa	NNPDF3.0_NNLO	NNPDF30NNLO	39.9	0.146	0.975
MC16.364109.Sherpa_221_NNPDF30NNLO_Zmumu_MAXHTPTV280_500_CVetoBVeto	Sherpa	NNPDF3.0_NNLO	NNPDF30NNLO	8.54	0.559	0.975
MC16.364110.Sherpa_221_NNPDF30NNLO_Zmumu_MAXHTPTV280_500_CFilterBVeto	Sherpa	NNPDF3.0_NNLO	NNPDF30NNLO	8.54	0.265	0.975
MC16.364111.Sherpa_221_NNPDF30NNLO_Zmumu_MAXHTPTV280_500_BFilter	Sherpa	NNPDF3.0_NNLO	NNPDF30NNLO	8.49	0.176	0.975
MC16.364112.Sherpa_221_NNPDF30NNLO_Zmumu_MAXHTPTV500_1000	Sherpa	NNPDF3.0_NNLO	NNPDF30NNLO	1.79	1	0.975
MC16.364113.Sherpa_221_NNPDF30NNLO_Zmumu_MAXHTPTV1000_E_CMS	Sherpa	NNPDF3.0_NNLO	NNPDF30NNLO	0.148	1	0.975
MC16.364114.Sherpa_221_NNPDF30NNLO_Zee_MAXHTPTV0_70_CVetoBVeto	Sherpa	NNPDF3.0_NNLO	NNPDF30NNLO	1.98e+03	0.821	0.975
MC16.364115.Sherpa_221_NNPDF30NNLO_Zee_MAXHTPTV0_70_CFilterBVeto	Sherpa	NNPDF3.0_NNLO	NNPDF30NNLO	1.98e+03	0.113	0.975
MC16.364116.Sherpa_221_NNPDF30NNLO_Zee_MAXHTPTV0_70_BFilter	Sherpa	NNPDF3.0_NNLO	NNPDF30NNLO	1.98e+03	0.0638	0.975
MC16.364117.Sherpa_221_NNPDF30NNLO_Zee_MAXHTPTV70_140_CVetoBVeto	Sherpa	NNPDF3.0_NNLO	NNPDF30NNLO	110	0.69	0.975
MC16.364118.Sherpa_221_NNPDF30NNLO_Zee_MAXHTPTV70_140_CFilterBVeto	Sherpa	NNPDF3.0_NNLO	NNPDF30NNLO	111	0.184	0.975
MC16.364119.Sherpa_221_NNPDF30NNLO_Zee_MAXHTPTV70_140_BFilter	Sherpa	NNPDF3.0_NNLO	NNPDF30NNLO	110	0.114	0.975
MC16.364120.Sherpa_221_NNPDF30NNLO_Zee_MAXHTPTV140_280_CVetoBVeto	Sherpa	NNPDF3.0_NNLO	NNPDF30NNLO	40.7	0.615	0.975
MC16.364121.Sherpa_221_NNPDF30NNLO_Zee_MAXHTPTV140_280_CFilterBVeto	Sherpa	NNPDF3.0_NNLO	NNPDF30NNLO	40.7	0.23	0.975
MC16.364122.Sherpa_221_NNPDF30NNLO_Zee_MAXHTPTV140_280_BFilter	Sherpa	NNPDF3.0_NNLO	NNPDF30NNLO	40.7	0.149	0.975
MC16.364123.Sherpa_221_NNPDF30NNLO_Zee_MAXHTPTV280_500_CVetoBVeto	Sherpa	NNPDF3.0_NNLO	NNPDF30NNLO	8.67	0.561	0.975
MC16.364124.Sherpa_221_NNPDF30NNLO_Zee_MAXHTPTV280_500_CFilterBVeto	Sherpa	NNPDF3.0_NNLO	NNPDF30NNLO	8.67	0.263	0.975
MC16.364125.Sherpa_221_NNPDF30NNLO_Zee_MAXHTPTV280_500_BFilter	Sherpa	NNPDF3.0_NNLO	NNPDF30NNLO	8.68	0.172	0.975
MC16.364126.Sherpa_221_NNPDF30NNLO_Zee_MAXHTPTV500_1000	Sherpa	NNPDF3.0_NNLO	NNPDF30NNLO	1.81	1	0.975
MC16.364127.Sherpa_221_NNPDF30NNLO_Zee_MAXHTPTV1000_E_CMS	Sherpa	NNPDF3.0_NNLO	NNPDF30NNLO	0.149	1	0.975
MC16.364128.Sherpa_221_NNPDF30NNLO_Ztautau_MAXHTPTV0_70_CVetoBVeto	Sherpa	NNPDF3.0_NNLO	NNPDF30NNLO	1.98e+03	0.821	0.975
MC16.364129.Sherpa_221_NNPDF30NNLO_Ztautau_MAXHTPTV0_70_CFilterBVeto	Sherpa	NNPDF3.0_NNLO	NNPDF30NNLO	1.98e+03	0.113	0.975
MC16.364130.Sherpa_221_NNPDF30NNLO_Ztautau_MAXHTPTV0_70_BFilter	Sherpa	NNPDF3.0_NNLO	NNPDF30NNLO	1.98e+03	0.0645	0.975
MC16.364131.Sherpa_221_NNPDF30NNLO_Ztautau_MAXHTPTV70_140_CVetoBVeto	Sherpa	NNPDF3.0_NNLO	NNPDF30NNLO	110	0.689	0.975
MC16.364132.Sherpa_221_NNPDF30NNLO_Ztautau_MAXHTPTV70_140_CFilterBVeto	Sherpa	NNPDF3.0_NNLO	NNPDF30NNLO	111	0.183	0.975
MC16.364133.Sherpa_221_NNPDF30NNLO_Ztautau_MAXHTPTV70_140_BFilter	Sherpa	NNPDF3.0_NNLO	NNPDF30NNLO	111	0.111	0.975
MC16.364134.Sherpa_221_NNPDF30NNLO_Ztautau_MAXHTPTV140_280_CVetoBVeto	Sherpa	NNPDF3.0_NNLO	NNPDF30NNLO	40.8	0.608	0.975
MC16.364135.Sherpa_221_NNPDF30NNLO_Ztautau_MAXHTPTV140_280_CFilterBVeto	Sherpa	NNPDF3.0_NNLO	NNPDF30NNLO	40.7	0.229	0.975
MC16.364136.Sherpa_221_NNPDF30NNLO_Ztautau_MAXHTPTV140_280_BFilter	Sherpa	NNPDF3.0_NNLO	NNPDF30NNLO	40.8	0.134	0.975
MC16.364137.Sherpa_221_NNPDF30NNLO_Ztautau_MAXHTPTV280_500_CVetoBVeto	Sherpa	NNPDF3.0_NNLO	NNPDF30NNLO	8.55	0.56	0.975
MC16.364138.Sherpa_221_NNPDF30NNLO_Ztautau_MAXHTPTV280_500_CFilterBVeto	Sherpa	NNPDF3.0_NNLO	NNPDF30NNLO	8.67	0.262	0.975
MC16.364139.Sherpa_221_NNPDF30NNLO_Ztautau_MAXHTPTV280_500_BFilter	Sherpa	NNPDF3.0_NNLO	NNPDF30NNLO	8.68	0.173	0.975
MC16.364140.Sherpa_221_NNPDF30NNLO_Ztautau_MAXHTPTV500_1000	Sherpa	NNPDF3.0_NNLO	NNPDF30NNLO	1.81	1	0.975
MC16.364141.Sherpa_221_NNPDF30NNLO_Ztautau_MAXHTPTV1000_E_CMS	Sherpa	NNPDF3.0_NNLO	NNPDF30NNLO	0.148	1	0.975

Table A.17: Sherpa 2.2.1 unfiltered Z+jets samples.

Sample	Generator	Tune	PDF	σ	Filter efficiency	K-factor
MC16.344295.Sherpa_NNPDF30NNLO_Zee_4lMassFilter40GeV8GeV	Sherpa	NNPDF3.0_NNLO	NNPDF	2.07e+03	0.000601	1
MC16.344296.Sherpa_NNPDF30NNLO_Zmumu_4lMassFilter40GeV8GeV	Sherpa	NNPDF3.0_NNLO	NNPDF	2.06e+03	0.00061	1
MC16.344297.Sherpa_NNPDF30NNLO_Zee_3lPtFilter4GeV_4lMassVeto40GeV8GeV	Sherpa	NNPDF3.0_NNLO	NNPDF	2.07e+03	0.0133	1
MC16.344298.Sherpa_NNPDF30NNLO_Zmumu_3lPtFilter4GeV_4lMassVeto40GeV8GeV	Sherpa	NNPDF3.0_NNLO	NNPDF	2.07e+03	0.0133	1

Table A.18: Filtered Sherpa 2.2.1 Z+jets samples, either accepting $m\_\ell\ell, 1 > 40$ GeV and $m\_\ell\ell, 2 > 8$ GeV or vetoing $m\_\ell\ell, 1 > 40$ GeV and $m\_\ell\ell, 2 > 8$ GeV.

Sample	Generator	Tune	PDF	σ	Filter efficiency	K-factor	Tag (mc16a)	N_{events} mc16a	Tag (mc16d)	N_{ev}
MC16.361106.PowhegPythia8EvtGen_AZNLOCTEQ6L1_Zee	Powheg+Pythia8+EvtGen+Photospp	AZNLO_CTEQ6L1	NULL	1.9e+03	1	1.03				
MC16.361107.PowhegPythia8EvtGen_AZNLOCTEQ6L1_Zmumu	Powheg+Pythia8+EvtGen+Photospp	AZNLO_CTEQ6L1	NULL	1.9e+03	1	1.03				
MC16.361108.PowhegPythia8EvtGen_AZNLOCTEQ6L1_Ztautau	Powheg+Pythia8+EvtGen+Photospp	AZNLO_CTEQ6L1	NULL	1.9e+03	1	1.03				

Table A.19: Powheg Z+jets samples.

Sample	Generator	Tune	PDF	σ	Filter efficiency	K-factor
MC16.364500.Sherpa_222_NNPDF30NNLO_eegamma_pty_7_15	Sherpa 2.2.2	NNPDF3.0 NNLO	NNPDF30NNLO	57.6	1	1
MC16.3645001.Sherpa_222_NNPDF30NNLO_eegamma_pty_15_35	Sherpa 2.2.2	NNPDF3.0 NNLO	NNPDF30NNLO	57.6	1	1
MC16.364502.Sherpa_222_NNPDF30NNLO_eegamma_pty_35_70	Sherpa 2.2.2	NNPDF3.0 NNLO	NNPDF30NNLO	57.6	1	1
MC16.364503.Sherpa_222_NNPDF30NNLO_eegamma_pty_70_140	Sherpa 2.2.2	NNPDF3.0 NNLO	NNPDF30NNLO	57.6	1	1
MC16.364504.Sherpa_222_NNPDF30NNLO_eegamma_pty_140_E_CMS	Sherpa 2.2.2	NNPDF3.0 NNLO	NNPDF30NNLO	57.6	1	1
MC16.364505.Sherpa_222_NNPDF30NNLO_eegamma_pty_7_15	Sherpa 2.2.2	NNPDF3.0 NNLO	NNPDF30NNLO	57.6	1	1
MC16.364506.Sherpa_222_NNPDF30NNLO_eegamma_pty_15_35	Sherpa 2.2.2	NNPDF3.0 NNLO	NNPDF30NNLO	57.6	1	1
MC16.364507.Sherpa_222_NNPDF30NNLO_eegamma_pty_35_70	Sherpa 2.2.2	NNPDF3.0 NNLO	NNPDF30NNLO	57.6	1	1
MC16.364508.Sherpa_222_NNPDF30NNLO_eegamma_pty_70_140	Sherpa 2.2.2	NNPDF3.0 NNLO	NNPDF30NNLO	57.6	1	1
MC16.364509.Sherpa_222_NNPDF30NNLO_eegamma_pty_140_E_CMS	Sherpa 2.2.2	NNPDF3.0 NNLO	NNPDF30NNLO	57.6	1	1

Table A.20: Sherpa $Z + \gamma$

A.3.4 Tribosons and $t\bar{t}$+V

Sample	Generator	Tune	PDF	σ	Filter efficiency	K-factor
MC16.410144.Sherpa_NNPDF30NNLO_ttW	Sherpa	NNPDF3.0_NNLO	NNPDF	0.577	1	1.12
MC16.410142.Sherpa_NNPDF30NNLO_ttll_mll5	Sherpa	NNPDF3.0_NNLO	NNPDF	0.113	1	1.09
MC16.410155.aMcAtNloPythia8EvtGen_MEN30NLO_A14N23LO_ttW	MadGraph5_aMC@NLO+Pythia8+EvtGen	A14 NNPDF23LO	NULL	0.5483	1	1.1
MC16.410218.aMcAtNloPythia8EvtGen_MEN30NLO_A14N23LO_ttee	MadGraph5_aMC@NLO+Pythia8+EvtGen	A14 NNPDF23LO	NULL	0.037	1	1.1
MC16.410219.aMcAtNloPythia8EvtGen_MEN30NLO_A14N23LO_ttmumu	MadGraph5_aMC@NLO+Pythia8+EvtGen	A14 NNPDF23LO	NULL	0.037	1	1.1
MC16.364243.Sherpa_222_NNPDF30NNLO_WWZ_4l2v_EW6	Sherpa 2.2.2	NNPDF3.0 NNLO	NNPDF30NNLO	1.8e-3	1	1
MC16.364245.Sherpa_222_NNPDF30NNLO_WZZ_5l1v_EW6	Sherpa 2.2.2	NNPDF3.0 NNLO	NNPDF30NNLO	1.9e-4	1	1
MC16.364247.Sherpa_222_NNPDF30NNLO_ZZZ_6l0v_EW6	Sherpa 2.2.2	NNPDF3.0 NNLO	NNPDF30NNLO	1.5e-5	1	1
MC16.364248.Sherpa_222_NNPDF30NNLO_ZZZ_4l2v_EW6	Sherpa 2.2.2	NNPDF3.0 NNLO	NNPDF30NNLO	3.9e-4	0.22	1

Table A.21: Sherpa tribosons and $t\bar{t}+V$.

A.4 Sensitivity comparison by using BDT discriminant and ME discriminant

In $\ell^+\ell^-\ell^+\ell^-$ analysis, two shape based discriminants are studied, ME discriminant (6.2.2) and BDT discriminant (6.2.2). The sensitivity on $\mu_{\text{off-shell}}$ from these two discriminants is compared by using the likelihood scan. The result is shown in Figure A.5. For this comparison, no systematic uncertainty is considered. The 95% CL upper limits from the likelihood scan are summarized in Table A.22. One can see that the improvement of using BDT is about 2%.

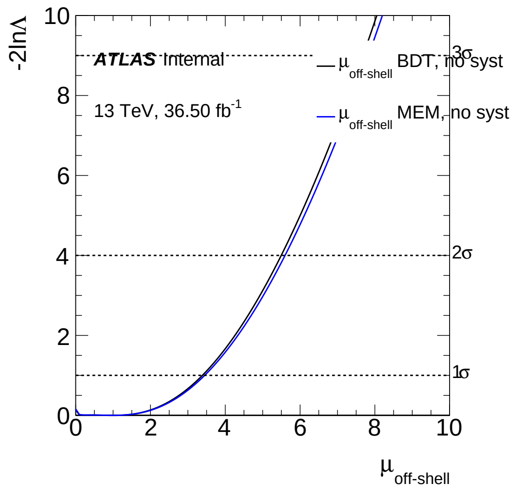

Figure A.5: Distributions of the likelihood scan on $\mu_{\text{off-shell}}$ for using two different discriminant shapes: BDT (black) and matrix element discriminant (blue).

Discriminant	Limit on $\mu_{\text{off-shell}}$
BDT	5.5
ME	5.6

Table A.22: 95% CL upper limits on $\mu_{\text{off-shell}}$ from the likelihood scan.

References

[1] Steven Weinberg. "The Making of the standard model". In: *Eur. Phys. J.* C34 (2004). [,99(2005)], pp. 5–13. DOI: 10.1142/9789812567147_0005,10.1140/epjc/s2004-01761-1. arXiv: hep-ph/0401010 [hep-ph].

[2] David Griffiths. *Introduction to elementary particles*. 2008. ISBN: 9783527406012.

[3] Mark Thomson. *Modern particle physics*. New York: Cambridge University Press, 2013. ISBN: 9781107034266.

[4] F. Halzen and Alan D. Martin. *QUARKS AND LEPTONS: AN INTRODUCTORY COURSE IN MODERN PARTICLE PHYSICS*. 1984. ISBN: 0471887412, 9780471887416.

[5] Emmy Noether. "Invariant variation problems". In: *Transport Theory and Statistical Physics* 1.3 (1971), 186–207. ISSN: 1532-2424. DOI: 10.1080/00411457108231446. URL: http://dx.doi.org/10.1080/00411457108231446.

[6] Katherine Brading and Harvey R. Brown. *Noether's Theorems and Gauge Symmetries*. 2000. arXiv: hep-th/0009058 [hep-th].

[7] F. Englert and R. Brout. "Broken Symmetry and the Mass of Gauge Vector Mesons". In: *Phys. Rev. Lett.* 13 (9 1964), pp. 321–323. DOI: 10.1103/PhysRevLett.13.321. URL: https://link.aps.org/doi/10.1103/PhysRevLett.13.321.

[8] Peter W. Higgs. "Broken Symmetries and the Masses of Gauge Bosons". In: *Phys. Rev. Lett.* 13 (16 1964), pp. 508–509. DOI: 10.1103/PhysRevLett.13.508. URL: https://link.aps.org/doi/10.1103/PhysRevLett.13.508.

[9] Sheldon L. Glashow. "The renormalizability of vector meson interactions". In: *Nucl. Phys.* 10 (1959), pp. 107–117. DOI: 10.1016/0029-5582(59)90196-8.

[10] Steven Weinberg. "A Model of Leptons". In: *Phys. Rev. Lett.* 19 (21 1967), pp. 1264–1266. DOI: 10.1103/PhysRevLett.19.1264. URL: https://link.aps.org/doi/10.1103/PhysRevLett.19.1264.

[11] Julia Woithe, Gerfried J Wiener, and Frederik F Van der Veken. "Let's have a coffee with the Standard Model of particle physics!" In: *Physics Education* 52.3 (2017), p. 034001. DOI: 10.1088/1361-6552/aa5b25. URL: https://doi.org/10.1088%2F1361-6552%2Faa5b25.

[12] H.E. Haber and G.L. Kane. "The search for supersymmetry: Probing physics beyond the standard model". In: *Physics Reports* 117.2 (1985), pp. 75 –263. ISSN: 0370-1573. DOI: https://doi.org/10.1016/0370-1573(85)90051-1. URL: http://www.sciencedirect.com/science/article/pii/0370157385900511.

[13] Nima Arkani–Hamed, Savas Dimopoulos, and Gia Dvali. "The hierarchy problem and new dimensions at a millimeter". In: *Physics Letters B* 429.3-4 (1998), 263–272. ISSN: 0370-2693. DOI: 10.1016/s0370-2693(98)00466-3. URL: http://dx.doi.org/10.1016/S0370-2693(98)00466-3.

[14] Gian Francesco Giudice. "Naturally Speaking: The Naturalness Criterion and Physics at the LHC". In: *Perspectives on LHC Physics* (2008), 155–178. DOI: 10.1142/9789812779762_0010. URL: http://dx.doi.org/10.1142/9789812779762_0010.

[15] G.C. Branco et al. "Theory and phenomenology of two-Higgs-doublet models". In: *Physics Reports* 516.1-2 (2012), 1–102. ISSN: 0370-1573. DOI: 10.1016/j.physrep.2012.02.002. URL: http://dx.doi.org/10.1016/j.physrep.2012.02.002.

[16] A. Hill and J. J. van der Bij. "Strongly interacting singlet-doublet Higgs model". In: *Phys. Rev. D* 36 (11 1987), pp. 3463–3473. DOI: 10.1103/PhysRevD.36.3463. URL: https://link.aps.org/doi/10.1103/PhysRevD.36.3463.

[17] Jihn E. Kim. "Light Pseudoscalars, Particle Physics and Cosmology". In: *Phys. Rept.* 150 (1987), pp. 1–177. DOI: 10.1016/0370-1573(87)90017-2.

[18] R. D. Peccei and Helen R. Quinn. "CP Conservation in the Presence of Pseudoparticles". In: *Phys. Rev. Lett.* 38 (25 1977), pp. 1440–1443. DOI: 10.1103/PhysRevLett.38.1440. URL: https://link.aps.org/doi/10.1103/PhysRevLett.38.1440.

[19] Mark Trodden. *Electroweak Baryogenesis: A Brief Review*. 1998. arXiv: hep-ph/9805252 [hep-ph].

[20] G. Aad et al. "Observation of a new particle in the search for the Standard Model Higgs boson with the ATLAS detector at the LHC". In: *Physics Letters B* 716.1 (2012), 1–29. ISSN: 0370-2693. DOI: 10.1016/j.physletb.2012.08.020. URL: http://dx.doi.org/10.1016/j.physletb.2012.08.020.

[21] S. Chatrchyan et al. "Observation of a new boson at a mass of 125 GeV with the CMS experiment at the LHC". In: *Physics Letters B* 716.1 (2012), 30–61. ISSN: 0370-2693. DOI: 10.1016/j.physletb.2012.08.021. URL: http://dx.doi.org/10.1016/j.physletb.2012.08.021.

[22] C. Mariotti G. Passarino R. Tanaka (Eds.) LHC Higgs Cross Section Working Group S. Dittmaier. *Handbook of LHC Higgs Cross Sections: 1. Inclusive Observables*. 2011. arXiv: 1101.0593 [hep-ph].

[23] C. Mariotti G. Passarino R. Tanaka (Eds.) LHC Higgs Cross Section Working Group S. Dittmaier. *Handbook of LHC Higgs Cross Sections: 2. Differential Distributions*. 2012. arXiv: 1201.3084 [hep-ph].

[24] C. Mariotti G. Passarino R. Tanaka (Eds.) The LHC Higgs Cross Section Working Group S. Heinemeyer. *Handbook of LHC Higgs Cross Sections: 3. Higgs Properties*. 2013. arXiv: 1307.1347 [hep-ph].

[25] C. Grojean F. Maltoni C. Mariotti A. Nikitenko M. Pieri P. Savard M. Schumacher R. Tanaka (Eds.) The LHC Higgs Cross Section Working Group D. de Florian. *Handbook of LHC Higgs Cross Sections: 4. Deciphering the Nature of the Higgs Sector*. 2016. arXiv: 1610.07922 [hep-ph].

[26] Abdelhak Djouadi et al. "HDECAY: Twenty++ years after". In: *Computer Physics Communications* 238 (2019), 214–231. ISSN: 0010-4655. DOI: 10.1016/j.cpc.2018.12.010. URL: http://dx.doi.org/10.1016/j.cpc.2018.12.010.

[27] A. Bredenstein et al. "Precise predictions for the Higgs-boson decay $H \to WW/ZZ \to 4$ leptons". In: *Phys. Rev. D* 74 (1 2006), p. 013004. DOI: 10.1103/PhysRevD.74.013004. URL: https://link.aps.org/doi/10.1103/PhysRevD.74.013004.

[28] Axel Bredenstein et al. "Radiative corrections to the semileptonic and hadronic Higgs-boson decays $H \to WW/ZZ \to 4$ fermions". In: *Journal of High Energy Physics* 2007.02 (2007), 080–080. ISSN: 1029-8479. DOI: 10.1088/1126-6708/2007/02/080. URL: http://dx.doi.org/10.1088/1126-6708/2007/02/080.

[29] M. Tanabashi et al. "Review of Particle Physics". In: *Phys. Rev.* D98.3 (2018), p. 030001. DOI: 10.1103/PhysRevD.98.030001.

[30] G. Aad et al. “Combined Measurement of the Higgs Boson Mass in pp Collisions at $\sqrt{s}$=7 and 8 TeV with the ATLAS and CMS Experiments”. In: *Physical Review Letters* 114.19 (2015). ISSN: 1079-7114. DOI: 10.1103/physrevlett.114.191803. URL: http://dx.doi.org/10.1103/PhysRevLett.114.191803.

[31] G. Aad et al. “Measurement of the Higgs boson mass from the $H \to \gamma\gamma$ and $H \to ZZ^* \to 4\ell$ channels in pp collisions at center of mass energies of 7 and 8 TeV with the ATLAS detector”. In: *Physical Review D* 90.5 (2014). ISSN: 1550-2368. DOI: 10.1103/physrevd.90.052004. URL: http://dx.doi.org/10.1103/PhysRevD.90.052004.

[32] V. Khachatryan et al. “Precise determination of the mass of the Higgs boson and tests of compatibility of its couplings with the standard model predictions using proton collisions at 7 and 8 TeV”. In: *The European Physical Journal C* 75.5 (2015). ISSN: 1434-6052. DOI: 10.1140/epjc/s10052-015-3351-7. URL: http://dx.doi.org/10.1140/epjc/s10052-015-3351-7.

[33] Morad Aaboud et al. “Measurement of the Higgs boson mass in the $H \to ZZ^* \to 4\ell$ and $H \to \gamma\gamma$ channels with $\sqrt{s} = 13$ TeV pp collisions using the ATLAS detector”. In: *Phys. Lett. B* 784 (2018), pp. 345–366. DOI: 10.1016/j.physletb.2018.07.050. arXiv: 1806.00242 [hep-ex].

[34] G. Aad et al. “Study of the spin and parity of the Higgs boson in diboson decays with the ATLAS detector”. In: *The European Physical Journal C* 75.10 (2015). ISSN: 1434-6052. DOI: 10.1140/epjc/s10052-015-3685-1. URL: http://dx.doi.org/10.1140/epjc/s10052-015-3685-1.

[35] “Combined measurements of Higgs boson production and decay using up to 80 fb^{-1} of proton-proton collision data at $\sqrt{s} = 13$ TeV collected with the ATLAS experiment”. In: *Phys. Rev. D* 101 (1 2020), p. 012002. DOI: 10.1103/PhysRevD.101.012002. URL: https://link.aps.org/doi/10.1103/PhysRevD.101.012002.

[36] Nikolas Kauer and Giampiero Passarino. “Inadequacy of zero-width approximation for a light Higgs boson signal”. In: *JHEP* 08 (2012), p. 116. DOI: 10.1007/JHEP08(2012)116. arXiv: 1206.4803 [hep-ph].

[37] Fabrizio Caola and Kirill Melnikov. “Constraining the Higgs boson width with ZZ production at the LHC”. In: *Phys.Rev.* D 88 (2013), p. 054024. DOI: 10.1103/PhysRevD.88.054024. arXiv: 1307.4935 [hep-ph].

[38] John M. Campbell, R. Keith Ellis, and Ciaran Williams. “Bounding the Higgs width at the LHC using full analytic results for $gg \to e^- e^+ \mu^- \mu^+$”. In: *JHEP* 04 (2014), p. 060. DOI: 10.1007/JHEP04(2014)060. arXiv: 1311.3589 [hep-ph].

[39] John M. Campbell, R. Keith Ellis, and Ciaran Williams. “Bounding the Higgs width at the LHC: complementary results from $H \to WW$”. In: *Phys.Rev.* D 89 (2014), p. 053011. DOI: 10.1103/PhysRevD.89.053011. arXiv: 1312.1628 [hep-ph].

[40] Christoph Englert and Michael Spannowsky. “Limitations and Opportunities of Off-Shell Coupling Measurements”. In: (2014). arXiv: 1405.0285 [hep-ph].

[41] Giacomo Cacciapaglia et al. “Higgs couplings: disentangling New Physics with off-shell measurements”. In: (2014). arXiv: 1406.1757 [hep-ph].

[42] Aleksandr Azatov et al. “Taming the off-shell Higgs boson”. In: (2014). arXiv: 1406.6338 [hep-ph].

[43] Margherita Ghezzi, Giampiero Passarino, and Sandro Uccirati. “Bounding the Higgs Width Using Effective Field Theory”. In: (2014). arXiv: 1405.1925 [hep-ph].

[44] “Constraints on the off-shell Higgs boson signal strength in the high-mass ZZ and WW final states with the ATLAS detector”. In: *Eur. Phys. J. C* 75 (2015), p. 335. DOI: 10.1140/epjc/s10052-015-3542-2. arXiv: 1503.01060 [hep-ex].

[45] "Constraints on the Higgs boson width from off-shell production and decay to Z-boson pairs". In: (2014). arXiv: 1405.3455 [hep-ex].

[46] LHC Higgs Cross Section Working Group et al. "Handbook of LHC Higgs Cross Sections: 4. Deciphering the Nature of the Higgs Sector". In: (2016). arXiv: 1610.07922 [hep-ph].

[47] *ATLAS: letter of intent for a general-purpose pp experiment at the large hadron collider at CERN*. Letter of Intent. Geneva: CERN, 1992. URL: https://cds.cern.ch/record/291061.

[48] *ATLAS: technical proposal for a general-purpose pp experiment at the Large Hadron Collider at CERN*. LHC Tech. Proposal. Geneva: CERN, 1994. URL: https://cds.cern.ch/record/290968.

[49] *Design study of the Large Hadron Collider (LHC): a multiparticle collider in the LEP tunnel*. The report is replaced by CERN/AC/95-05(LHC). Geneva: CERN, 1991. URL: https://cds.cern.ch/record/220493.

[50] Thomas Sven Pettersson and P Lefèvre. *The Large Hadron Collider: conceptual design*. Tech. rep. CERN-AC-95-05-LHC. 1995. URL: https://cds.cern.ch/record/291782.

[51] Oliver Sim Brüning et al. *LHC Design Report*. Geneva: CERN, 2004. URL: https://cds.cern.ch/record/782076.

[52] Oliver Sim Brüning et al. *LHC Design Report*. Geneva: CERN, 2004. URL: https://cds.cern.ch/record/815187.

[53] Michael Benedikt et al. *LHC Design Report*. Geneva: CERN, 2004. URL: https://cds.cern.ch/record/823808.

[54] *ATLAS technical coordination: Technical Design Report*. Technical Design Report ATLAS. Geneva: CERN, 1999. URL: https://cds.cern.ch/record/385482.

[55] Airapetian et al. *ATLAS detector and physics performance: Technical Design Report, 1*. Technical Design Report ATLAS. Geneva: CERN, 1999. URL: https://cds.cern.ch/record/391176.

[56] Airapetian et al. *ATLAS detector and physics performance: Technical Design Report, 2*. Technical Design Report ATLAS. Geneva: CERN, 1999. URL: https://cds.cern.ch/record/391177.

[57] *ATLAS inner detector: Technical Design Report, 1*. Technical Design Report ATLAS. Geneva: CERN, 1997. URL: https://cds.cern.ch/record/331063.

[58] S Haywood et al. *ATLAS inner detector: Technical Design Report, 2*. Technical Design Report ATLAS. Geneva: CERN, 1997. URL: https://cds.cern.ch/record/331064.

[59] Norbert Wermes and G Hallewel. *ATLAS pixel detector: Technical Design Report*. Technical Design Report ATLAS. Geneva: CERN, 1998. URL: https://cds.cern.ch/record/381263.

[60] M Capeans et al. *ATLAS Insertable B-Layer Technical Design Report*. Tech. rep. CERN-LHCC-2010-013. ATLAS-TDR-19. 2010. URL: https://cds.cern.ch/record/1291633.

[61] *ATLAS calorimeter performance: Technical Design Report*. Technical Design Report ATLAS. Geneva: CERN, 1996. URL: https://cds.cern.ch/record/331059.

[62] *ATLAS liquid-argon calorimeter: Technical Design Report*. Technical Design Report ATLAS. Geneva: CERN, 1996. URL: https://cds.cern.ch/record/331061.

[63] *ATLAS tile calorimeter: Technical Design Report*. Technical Design Report ATLAS. Geneva: CERN, 1996. URL: https://cds.cern.ch/record/331062.

[64] *ATLAS muon spectrometer: Technical Design Report*. Technical Design Report ATLAS. Geneva: CERN, 1997. URL: https://cds.cern.ch/record/331068.

[65] *ATLAS magnet system: Technical Design Report, 1*. Technical Design Report ATLAS. Geneva: CERN, 1997. URL: https://cds.cern.ch/record/338080.

[66] *ATLAS central solenoid: Technical Design Report*. Technical Design Report ATLAS. Electronic version not available. Geneva: CERN, 1997. URL: https://cds.cern.ch/record/331067.

[67] *ATLAS end-cap toroids: Technical Design Report*. Technical Design Report ATLAS. Electronic version not available. Geneva: CERN, 1997. URL: https://cds.cern.ch/record/331066.

[68] "The ATLAS Data Acquisition and High Level Trigger system". In: *Journal of Instrumentation* 11.06 (2016), P06008–P06008. DOI: 10.1088/1748-0221/11/06/p06008. URL: https://doi.org/10.1088%2F1748-0221%2F11%2F06%2Fp06008.

[69] *ATLAS level-1 trigger: Technical Design Report*. Technical Design Report ATLAS. Geneva: CERN, 1998. URL: https://cds.cern.ch/record/381429.

[70] Peter Jenni et al. *ATLAS high-level trigger, data-acquisition and controls: Technical Design Report*. Technical Design Report ATLAS. Geneva: CERN, 2003. URL: https://cds.cern.ch/record/616089.

[71] *ATLAS Computing: technical design report*. Technical Design Report ATLAS. Geneva: CERN, 2005. URL: https://cds.cern.ch/record/837738.

[72] Peter Vankov and ATLAS Collaboration. *ATLAS Future Upgrade*. Tech. rep. ATL-UPGRADE-PROC-2016-003. Geneva: CERN, 2016. URL: https://cds.cern.ch/record/2195333.

[73] *Letter of Intent for the Phase-I Upgrade of the ATLAS Experiment*. Tech. rep. CERN-LHCC-2011-012. LHCC-I-020. Geneva: CERN, 2011. URL: https://cds.cern.ch/record/1402470.

[74] T Kawamoto et al. *New Small Wheel Technical Design Report*. Tech. rep. CERN-LHCC-2013-006. ATLAS-TDR-020. ATLAS New Small Wheel Technical Design Report. 2013. URL: https://cds.cern.ch/record/1552862.

[75] Collaboration ATLAS. *Letter of Intent for the Phase-II Upgrade of the ATLAS Experiment*. Tech. rep. CERN-LHCC-2012-022. LHCC-I-023. Draft version for comments. Geneva: CERN, 2012. URL: http://cds.cern.ch/record/1502664.

[76] *ATLAS Phase-II Upgrade Scoping Document*. Tech. rep. CERN-LHCC-2015-020. LHCC-G-166. Geneva: CERN, 2015. URL: https://cds.cern.ch/record/2055248.

[77] ATLAS Collaboration. *Technical Design Report for the ATLAS Inner Tracker Pixel Detector*. Tech. rep. CERN-LHCC-2017-021. ATLAS-TDR-030. Geneva: CERN, 2017. URL: https://cds.cern.ch/record/2285585.

[78] ATLAS Collaboration. *Technical Design Report for the ATLAS Inner Tracker Strip Detector*. Tech. rep. CERN-LHCC-2017-005. ATLAS-TDR-025. Geneva: CERN, 2017. URL: https://cds.cern.ch/record/2257755.

[79] M (CERN) Aleksa et al. *ATLAS Liquid Argon Calorimeter Phase-I Upgrade Technical Design Report*. Tech. rep. CERN-LHCC-2013-017. ATLAS-TDR-022. Final version presented to December 2013 LHCC. 2013. URL: https://cds.cern.ch/record/1602230.

[80] C Zimmermann. *Optimized electron identification with the forward calorimeters of the ATLAS detector for the 2012 data*. Tech. rep. ATL-COM-PHYS-2013-1589. Geneva: CERN, 2013. URL: https://cds.cern.ch/record/1633158.

[81] A. Hoecker et al. "TMVA - Toolkit for Multivariate Data Analysis". In: *ArXiv Physics e-prints* (Mar. 2007). eprint: physics/0703039.

[82] ATLAS Collaboration. "The ATLAS simulation Infrastructure". In: *Eur. Phys. J.* C 70 (2010), pp. 823–874. arXiv: 1005.4568 [physics.ins-det].

[83] S. Agostinelli et al. "GEANT4: A simulation toolkit". In: *Nucl. Instrum. Meth.* A 506 (2003), pp. 250–303.

[84] Torbjorn Sjostrand, Stephen Mrenna, and Peter Z. Skands. "PYTHIA 6.4 Physics and Manual". In: *JHEP* 05 (2006), p. 026. arXiv: hep-ph/0603175.

[85] Torbjorn Sjostrand, Stephen Mrenna, and Peter Z. Skands. "A Brief Introduction to PYTHIA 8.1". In: *Comput. Phys. Commun.* 178 (2008), pp. 852–867. DOI: 10.1016/j.cpc.2008.01.036. arXiv: 0710.3820 [hep-ph].

[86] D. J. Lange. "The EvtGen particle decay simulation package". In: *Nucl. Instrum. Meth.* A462 (2001), pp. 152–155. DOI: 10.1016/S0168-9002(01)00089-4.

[87] M. Bahr et al. "Herwig++ Physics and Manual". In: *Eur. Phys. J.* C58 (2008), pp. 639–707. DOI: 10.1140/epjc/s10052-008-0798-9. arXiv: 0803.0883 [hep-ph].

[88] J. Bellm et al. "Herwig++ 2.7 Release Note". In: (2013). arXiv: 1310.6877 [hep-ph].

[89] Paolo Nason. "A New method for combining NLO QCD with shower Monte Carlo algorithms". In: *JHEP* 11 (2004), p. 040. DOI: 10.1088/1126-6708/2004/11/040. arXiv: hep-ph/0409146.

[90] Stefano Frixione, Paolo Nason, and Carlo Oleari. "Matching NLO QCD computations with parton shower simulations: the POWHEG method". In: *JHEP* 11 (2007), p. 070. DOI: 10.1088/1126-6708/2007/11/070. arXiv: 0709.2092 [hep-ph].

[91] Simone Alioli et al. "A general framework for implementing NLO calculations in shower Monte Carlo programs: the POWHEG BOX". In: *JHEP* 06 (2010), p. 043. DOI: 10.1007/JHEP06(2010)043. arXiv: 1002.2581 [hep-ph].

[92] John M. Campbell et al. "NLO Higgs Boson Production Plus One and Two Jets Using the POWHEG BOX, MadGraph4 and MCFM". In: *JHEP* 07 (2012), p. 092. DOI: 10.1007/JHEP07(2012)092. arXiv: 1202.5475 [hep-ph].

[93] Keith Hamilton et al. "NNLOPS simulation of Higgs boson production". In: *JHEP* 10 (2013), p. 222. DOI: 10.1007/JHEP10(2013)222. arXiv: 1309.0017 [hep-ph].

[94] Jon Butterworth et al. "PDF4LHC recommendations for LHC Run II". In: *J. Phys.* G43 (2016), p. 023001. DOI: 10.1088/0954-3899/43/2/023001. arXiv: 1510.03865 [hep-ph].

[95] Giuseppe Bozzi et al. "Transverse-momentum resummation and the spectrum of the Higgs boson at the LHC". In: *Nucl. Phys.* B737 (2006), pp. 73–120. DOI: 10.1016/j.nuclphysb.2005.12.022. arXiv: hep-ph/0508068 [hep-ph].

[96] Daniel de Florian et al. "Transverse-momentum resummation: Higgs boson production at the Tevatron and the LHC". In: *JHEP* 11 (2011), p. 064. arXiv: 1109.2109 [hep-ph].

[97] Paolo Nason and Carlo Oleari. "NLO Higgs boson production via vector-boson fusion matched with shower in POWHEG". In: *JHEP* 02 (2010), p. 037. arXiv: 0911.5299 [hep-ph].

[98] Gionata Luisoni et al. "$HW^{\pm}$/HZ + 0 and 1 jet at NLO with the POWHEG BOX interfaced to GoSam and their merging within MiNLO". In: *JHEP* 10 (2013), p. 083. DOI: 10.1007/JHEP10(2013)083. arXiv: 1306.2542 [hep-ph].

[99] J. Alwall et al. "The automated computation of tree-level and next-to-leading order differential cross sections, and their matching to parton shower simulations". In: *JHEP* 07 (2014), p. 079. DOI: 10.1007/JHEP07(2014)079. arXiv: 1405.0301 [hep-ph].

[100] M. Wiesemann et al. "Higgs production in association with bottom quarks". In: *JHEP* 02 (2015), p. 132. DOI: 10.1007/JHEP02(2015)132. arXiv: 1409.5301 [hep-ph].

[101] R. D. Ball et al. "Parton distributions with LHC data". In: *Nucl. Phys. B* 867 (2013), pp. 244–289. DOI: 10.1016/j.nuclphysb.2012.10.003. arXiv: 1207.1303 [hep-ph].

[102] A. Djouadi, J. Kalinowski, and M. Spira. "HDECAY: A program for Higgs boson decays in the standard model and its supersymmetric extension". In: *Comput. Phys. Commun.* 108 (1998), pp. 56–74. arXiv: hep-ph/9704448.

[103] A. Bredenstein et al. "Precise predictions for the Higgs-boson decay $H \to WW/ZZ \to$ 4leptons". In: *Phys. Rev.* D 74 (2006), p. 013004. arXiv: hep-ph/0604011.

[104] A. Bredenstein et al. "Radiative corrections to the semileptonic and hadronic Higgs-boson decays $H \to WW/ZZ \to 4$ fermions". In: *JHEP* 02 (2007), p. 080. arXiv: hep-ph/0611234.

[105] D. de Florian et al. "Handbook of LHC Higgs Cross Sections: 4. Deciphering the Nature of the Higgs Sector". In: (2016). arXiv: 1610.07922 [hep-ph].

[106] T. Gleisberg et al. "Event generation with SHERPA 1.1". In: *JHEP* 02 (2009), p. 007. DOI: 10.1088/1126-6708/2009/02/007. arXiv: 0811.4622 [hep-ph].

[107] Tanju Gleisberg and Stefan Höche. "Comix, a new matrix element generator". In: *JHEP* 12 (2008), p. 039. DOI: 10.1088/1126-6708/2008/12/039. arXiv: 0808.3674 [hep-ph].

[108] Fabio Cascioli, Philipp Maierhofer, and Stefano Pozzorini. "Scattering Amplitudes with Open Loops". In: *Phys. Rev. Lett.* 108 (2012), p. 111601. DOI: 10.1103/PhysRevLett.108.111601. arXiv: 1111.5206 [hep-ph].

[109] Steffen Schumann and Frank Krauss. "A Parton shower algorithm based on Catani-Seymour dipole factorisation". In: *JHEP* 03 (2008), p. 038. DOI: 10.1088/1126-6708/2008/03/038. arXiv: 0709.1027 [hep-ph].

[110] Stefan Höche et al. "QCD matrix elements + parton showers: The NLO case". In: *JHEP* 04 (2013), p. 027. DOI: 10.1007/JHEP04(2013)027. arXiv: 1207.5030 [hep-ph].

[111] B. Biedermann et al. "Electroweak corrections to $pp \to \mu^+\mu^-e^+e^- + X$ at the LHC: a Higgs background study". In: *Phys. Rev. Lett.* 116.16 (2016), p. 161803. DOI: 10.1103/PhysRevLett.116.161803. arXiv: 1601.07787 [hep-ph].

[112] Benedikt Biedermann et al. "Next-to-leading-order electroweak corrections to the production of four charged leptons at the LHC". In: *JHEP* 01 (2017), p. 033. DOI: 10.1007/JHEP01(2017)033. arXiv: 1611.05338 [hep-ph].

[113] ATLAS Collaboration. "Measurement of the Z/γ^* boson transverse momentum distribution in pp collisions at $\sqrt{s} = 7$ TeV with the ATLAS detector". In: *JHEP* 09 (2014), p. 145. DOI: 10.1007/JHEP09(2014)145. arXiv: 1406.3660 [hep-ex].

[114] F. Cascioli et al. "ZZ production at hadron colliders in NNLO QCD". In: *Phys. Lett.* B735 (2014), pp. 311–313. DOI: 10.1016/j.physletb.2014.06.056. arXiv: 1405.2219 [hep-ph].

[115] Massimiliano Grazzini, Stefan Kallweit, and Dirk Rathlev. "ZZ production at the LHC: fiducial cross sections and distributions in NNLO QCD". In: *Phys. Lett.* B750 (2015), pp. 407–410. DOI: 10.1016/j.physletb.2015.09.055. arXiv: 1507.06257 [hep-ph].

[116] LHC Higgs Cross Section Working Group et al. "Handbook of LHC Higgs Cross Sections: 2. Differential Distributions". In: *CERN-2012-002* (CERN, Geneva, 2012). arXiv: 1201.3084 [hep-ph].

[117] Johan Alwall et al. "MadGraph 5 : Going Beyond". In: *JHEP* 06 (2011), p. 128. DOI: 10.1007/JHEP06(2011)128. arXiv: 1106.0522 [hep-ph].

[118] N. Davidson, T. Przedzinski, and Z. Was. "PHOTOS Interface in C++: Technical and Physics Documentation". In: (2010). arXiv: 1011.0937 [hep-ph].

[119] H4l Group. *Common supporting note for the $H \to 4\ell$ channel: Event selection, background estimates, performance studies, etc.* Tech. rep. ATL-COM-PHYS-2015-1277. The authors are the members of the HZZ H4l analysis team. This will be corrected as soon as possible. Geneva: CERN, 2015. URL: https://cds.cern.ch/record/2058249.

[120] ATLAS Collaboration. *Electron and photon reconstruction and performance in ATLAS using a dynamical, topological cell clustering-based approach*. ATL-PHYS-PUB-2017-022. 2017. URL: https://cds.cern.ch/record/2298955.

[121] ATLAS Collaboration. *Electron efficiency measurements with the ATLAS detector using the 2012 LHC proton–proton collision data*. ATLAS-CONF-2014-032. 2014. URL: https://cds.cern.ch/record/1706245.

[122] ATLAS Collaboration. *Electron efficiency measurements with the ATLAS detector using the 2015 LHC proton–proton collision data*. ATLAS-CONF-2016-024. 2016. URL: https://cds.cern.ch/record/2157687.

[123] ATLAS Collaboration. "Electron and photon energy calibration with the ATLAS detector using LHC Run 1 data". In: *Eur. Phys. J. C* 74 (2014), p. 3071. DOI: 10.1140/epjc/s10052-014-3071-4. arXiv: 1407.5063 [hep-ex].

[124] ATLAS Collaboration. "Muon reconstruction performance of the ATLAS detector in proton–proton collision data at $\sqrt{s} = 13$ TeV". In: *Eur. Phys. J. C* 76 (2016), p. 292. DOI: 10.1140/epjc/s10052-016-4120-y. arXiv: 1603.05598 [hep-ex].

[125] ATLAS Collaboration. "Measurements of Higgs boson production and couplings in the four-lepton channel in *pp* collisions at center-of-mass energies of 7 and 8 TeV with the ATLAS detector". In: *Phys. Rev. D* 91 (2015), p. 012006. DOI: 10.1103/PhysRevD.91.012006. arXiv: 1408.5191 [hep-ex].

[126] ATLAS Collaboration. "Jet reconstruction and performance using particle flow with the ATLAS Detector". In: *Eur. Phys. J. C* 77 (2017), p. 466. DOI: 10.1140/epjc/s10052-017-5031-2. arXiv: 1703.10485 [hep-ex].

[127] ATLAS Collaboration. "Jet energy scale measurements and their systematic uncertainties in proton–proton collisions at $\sqrt{s} = 13$ TeV with the ATLAS detector". In: *Phys. Rev. D* 96 (2017), p. 072002. DOI: 10.1103/PhysRevD.96.072002. arXiv: 1703.09665 [hep-ex].

[128] ATLAS Collaboration. "Performance of b-jet identification in the ATLAS experiment". In: *JINST* 11 (2016), P04008. DOI: 10.1088/1748-0221/11/04/P04008. arXiv: 1512.01094 [hep-ex].

[129] ATLAS Collaboration. *Optimisation and performance studies of the ATLAS b-tagging algorithms for the 2017-18 LHC run*. ATL-PHYS-PUB-2017-013. 2017. URL: https://cds.cern.ch/record/2273281.

[130] ATLAS Collaboration. *Measurement of b-tagging efficiency of c-jets in $t\bar{t}$ events using a likelihood approach wth the ATLAS detector*. ATLAS-CONF-2018-001. 2018. URL: https://cds.cern.ch/record/2306649.

[131] H4l Team. *Event selection and background estimation in the $H \to ZZ^{(*)} \to 4\ell$ channel at $\sqrt{s} = 13$ - Moriond 2017 Analysis*. Geneva, 2016. URL: https://cds.cern.ch/record/2231576.

[132] J. De Vivie De Regie et al. *ATLAS electron, photon and muon isolation in Run 2*. Tech. rep. ATL-COM-PHYS-2015-071. Geneva: CERN, 2015. URL: https://cds.cern.ch/record/2256658.

[133] T. Skwarnicki. "Ph.D. thesis". In: *DESY-F31-86-02* (1986), Appendix E.

[134] M. Oreglia. "Ph.D. thesis". In: *SLAC-R-0236* (1980), Appendix D.

[135] Syed Haider Abidi et al. *Measurement of the fiducial, differential and total Higgs production cross sections in the $H \to ZZ^* \to \ell^+\ell^-\ell^+\ell^-$ final state from proton–proton collisions at $\sqrt{s} = 13$ TeV with 2015-2018 data*. Tech. rep. ATL-COM-PHYS-2019-930. Geneva: CERN, 2019. URL: https://cds.cern.ch/record/2683860.

[136] Syed Haider Abidi et al. *Couplings and simplified cross section studies in the $H \to ZZ^* \to \ell^+\ell^-\ell^+\ell^-$ channel and their EFT interpretation*. Tech. rep. ATL-COM-PHYS-2019-929. Geneva: CERN, 2019. URL: https://cds.cern.ch/record/2683853.

[137] Kyle S. Cranmer. "Kernel estimation in high-energy physics". In: *Comput. Phys. Commun.* 136 (2001), pp. 198–207. DOI: 10.1016/S0010-4655(00)00243-5. arXiv: hep-ex/0011057 [hep-ex].

[138] ATLAS Collaboration. *Measurements of the Higgs boson inclusive and differential fiducial cross sections in the 4ℓ decay channel at $\sqrt{s} = 13$ TeV*. 2020. arXiv: 2004.03969 [hep-ex].

[139] ATLAS Collaboration. "Observation of a new particle in the search for the Standard Model Higgs boson with the ATLAS detector at the LHC". In: *Phys. Lett. B* 716 (2012), p. 1. DOI: 10.1016/j.physletb.2012.08.020. arXiv: 1207.7214 [hep-ex].

[140] CMS Collaboration. "Observation of a new boson at a mass of 125 GeV with the CMS experiment at the LHC". In: *Phys. Lett. B* 716 (2012), p. 30. DOI: 10.1016/j.physletb.2012.08.021. arXiv: 1207.7235 [hep-ex].

[141] ATLAS Collaboration. "Measurements of the Higgs boson production and decay rates and coupling strengths using pp collision data at $\sqrt{s} = 7$ and 8 TeV in the ATLAS experiment". In: *Eur. Phys. J. C* 76 (2016), p. 6. DOI: 10.1140/epjc/s10052-015-3769-y. arXiv: 1507.04548 [hep-ex].

[142] ATLAS Collaboration. "Study of the spin and parity of the Higgs boson in diboson decays with the ATLAS detector". In: *Eur. Phys. J. C* 75 (2015), p. 476. DOI: 10.1140/epjc/s10052-015-3685-1. arXiv: 1506.05669 [hep-ex].

[143] CMS Collaboration. "Precise determination of the mass of the Higgs boson and tests of compatibility of its couplings with the standard model predictions using proton collisions at 7 and 8 TeV". In: *Eur. Phys. J. C* 75 (2015), p. 212. DOI: 10.1140/epjc/s10052-015-3351-7. arXiv: 1412.8662 [hep-ex].

[144] CMS Collaboration. "Constraints on the spin-parity and anomalous HVV couplings of the Higgs boson in proton collisions at 7 and 8 TeV". In: *Phys. Rev. D* 92 (2015), p. 012004. DOI: 10.1103/PhysRevD.92.012004. arXiv: 1411.3441 [hep-ex].

[145] Lisa Randall and Raman Sundrum. "A Large mass hierarchy from a small extra dimension". In: *Phys. Rev. Lett.* 83 (1999), pp. 3370–3373. DOI: 10.1103/PhysRevLett.83.3370. arXiv: hep-ph/9905221.

[146] H. Davoudiasl, J. L. Hewett, and T. G. Rizzo. "Bulk gauge fields in the Randall-Sundrum model". In: *Phys. Lett. B* 473 (2000), pp. 43–49. DOI: 10.1016/S0370-2693(99)01430-6. arXiv: hep-ph/9911262.

[147] Simone Alioli et al. "NLO Higgs boson production via gluon fusion matched with shower in POWHEG". In: *JHEP* 04 (2009), p. 002. arXiv: 0812.0578 [hep-ph].

[148] Rikkert Frederix and Stefano Frixione. "Merging meets matching in MC@NLO". In: *JHEP* 12 (2012), p. 061. DOI: 10.1007/JHEP12(2012)061. arXiv: 1209.6215 [hep-ph].

[149] J. Alwall et al. "The automated computation of tree-level and next-to-leading order differential cross sections, and their matching to parton shower simulations". In: (). arXiv: 1405.0301 [hep-ph].

[150] Pierre Artoisenet et al. "Automatic spin-entangled decays of heavy resonances in Monte Carlo simulations". In: *Journal of High Energy Physics* 2013.3 (2013), p. 15. ISSN: 1029-8479. DOI: 10.1007/JHEP03(2013)015. arXiv: 1212.3460 [hep-ph]. URL: http://dx.doi.org/10.1007/JHEP03(2013)015.

[151] ATLAS Collaboration. "The ATLAS Simulation Infrastructure". In: *Eur. Phys. J. C* 70 (2010), p. 823. DOI: 10.1140/epjc/s10052-010-1429-9. arXiv: 1005.4568 [physics.ins-det].

[152] ATLAS Collaboration. *The simulation principle and performance of the ATLAS fast calorimeter simulation FastCaloSim*. ATL-PHYS-PUB-2010-013. 2010. URL: https://cds.cern.ch/record/1300517.

[153] Wouter Verkerke and David P. Kirkby. "The RooFit toolkit for data modeling". In: *eConf* C0303241 (2003). Ed. by L. Lyons and Muge Karagoz, MOLT007. arXiv: physics/0306116.

[154] Lorenzo Moneta et al. "The RooStats Project". In: *PoS* ACAT2010 (2010). Ed. by T. Speer et al., p. 057. DOI: 10.22323/1.093.0057. arXiv: 1009.1003 [physics.data-an].

[155] Glen Cowan et al. "Asymptotic formulae for likelihood-based tests of new physics". In: *The European Physical Journal C* 71.2 (2011). ISSN: 1434-6052. DOI: 10.1140/epjc/s10052-011-1554-0. URL: http://dx.doi.org/10.1140/epjc/s10052-011-1554-0.

[156] Alexander L. Read. “Presentation of search results: The CL(s) technique”. In: *J. Phys. G* 28 (2002). Ed. by M.R. Whalley and L. Lyons, pp. 2693–2704. DOI: 10.1088/0954-3899/28/10/313.

[157] M. Aaboud et al. “Search for four-top-quark production in the single-lepton and opposite-sign dilepton final states in pp collisions at $\sqrt{s} = 13$ TeV with the ATLAS detector”. In: *Phys. Rev. D* 99 (5 2019), p. 052009. DOI: 10.1103/PhysRevD.99.052009. URL: https://link.aps.org/doi/10.1103/PhysRevD.99.052009.

[158] Gioacchino Ranucci. “The profile likelihood ratio and the look elsewhere effect in high energy physics”. In: *Nuclear Instruments and Methods in Physics Research Section A: Accelerators, Spectrometers, Detectors and Associated Equipment* 661.1 (2012), 77–85. ISSN: 0168-9002. DOI: 10.1016/j.nima.2011.09.047. URL: http://dx.doi.org/10.1016/j.nima.2011.09.047.

[159] Eilam Gross and Ofer Vitells. “Trial factors for the look elsewhere effect in high energy physics”. In: *Eur. Phys. J.* C 70 (2010), p. 525. DOI: 10.1140/epjc/s10052-010-1470-8.

[160] ATLAS Collaboration. *Luminosity determination in pp collisions at $\sqrt{s} = 13$ TeV using the ATLAS Detector at the LHC*. ATLAS-CONF-2019-021. 2019. URL: https://cds.cern.ch/record/2677054.

[161] G Cowan et al. “Asymptotic formulae for likelihood-based tests of new physics”. In: *Eur. Phys. J.* C 71 (2011), p. 1554. arXiv: 1007.1727 [physics.data-an].

[162] Alexander L. Read. “Presentation of search results: The CL_s technique”. In: *J. Phys. G* 28 (2002), p. 2693.

[163] “Observation of a new particle in the search for the Standard Model Higgs boson with the ATLAS detector at the LHC”. In: *Phys. Lett.* B 716 (2012), p. 1. DOI: 10.1016/j.physletb.2012.08.020. arXiv: 1207.7214 [hep-ex].

[164] “Observation of a new boson at a mass of 125 GeV with the CMS experiment at the LHC”. In: *Phys. Lett.* B 716 (2012), p. 30. DOI: 10.1016/j.physletb.2012.08.021. arXiv: 1207.7235 [hep-ex].

[165] Christoph Englert, Yotam Soreq, and Michael Spannowsky. “Off-Shell Higgs Coupling Measurements in BSM scenarios”. In: (2014). arXiv: 1410.5440 [hep-ph].

[166] Heather E. Logan. “Hiding a Higgs width enhancement from off-shell gg ($\to$ h*) $\to$ ZZ measurements”. In: (2014). arXiv: 1412.7577 [hep-ph].

[167] Giampiero Passarino. “Higgs CAT”. In: *Eur. Phys. J.* C 74 (2014), p. 2866. DOI: 10.1140/epjc/s10052-014-2866-7. arXiv: 1312.2397 [hep-ph].

[168] F. Caola et al. “QCD corrections to ZZ production in gluon fusion at the LHC”. In: *Phys. Rev.* D 92 (2015), p. 18. DOI: 10.1103/PhysRevD.92.094028. arXiv: 1509.06734 [hep-ph].

[169] F. Caola et al. “QCD corrections to vector boson pair production in gluon fusion including interference effects with off-shell Higgs at the LHC”. In: *JHEP* 087 (2016), p. 23. DOI: 10.1007/JHEP07(2016)087. arXiv: 1605.04610 [hep-ph].

[170] John M. Campbell and R. Keith Ellis. “Higgs Constraints from Vector Boson Fusion and Scattering”. In: *JHEP* 04 (2015), p. 030. DOI: 10.1007/JHEP04(2015)030. arXiv: 1502.02990 [hep-ph].

[171] LHC Higgs Cross Section Working Group et al. “Handbook of LHC Higgs Cross Sections: 2. Differential distributions”. In: *CERN-2012-002* (CERN, Geneva, 2012). arXiv: 1201.3084 [hep-ph].

[172] Syed Haider Abidi et al. *Event selection and background estimation in the $H \to ZZ^{(*)} \to 4\ell$ channel at $\sqrt{s} = 13$ - Moriond 2017 Analysis*. Tech. rep. ATL-COM-PHYS-2016-1599. Geneva: CERN, 2016. URL: https://cds.cern.ch/record/2231576.

[173] F. Cascioli et al. “Precise Higgs-background predictions: merging NLO QCD and squared quark-loop corrections to four-lepton + 0,1 jet production”. In: *JHEP* 01 (2014), p. 046. DOI: 10.1007/JHEP01(2014)046. arXiv: 1309.0500 [hep-ph].

[174] Richard D. Ball et al. “Parton distributions for the LHC Run II”. In: *JHEP* 04 (2015), p. 040. DOI: 10.1007/JHEP04(2015)040. arXiv: 1410.8849 [hep-ph].

[175] Richard D. Ball et al. “Parton distributions with LHC data”. In: *Nuclear Physics B* 867.2 (2013), pp. 244 –289. ISSN: 0550-3213. DOI: https://doi.org/10.1016/j.nuclphysb.2012.10.003. URL: http://www.sciencedirect.com/science/article/pii/S0550321312005500.

[176] Benedikt Biedermann et al. “Next-to-leading-order electroweak corrections to the production of four charged leptons at the LHC”. In: *Journal of High Energy Physics* 2017.1 (2017). ISSN: 1029-8479. DOI: 10.1007/jhep01(2017)033. URL: http://dx.doi.org/10.1007/JHEP01(2017)033.

[177] Paolo Nason and Giulia Zanderighi. “W^+W^- W + W - , WZ W Z and ZZ Z Z production in the POWHEG-BOX-V2”. In: *The European Physical Journal C* 74.1 (2014). ISSN: 1434-6052. DOI: 10.1140/epjc/s10052-013-2702-5. URL: http://dx.doi.org/10.1140/epjc/s10052-013-2702-5.

[178] H.-L. Lai et al. “New parton distributions for collider physics”. In: *Phys. Rev. D* 82 (2010), p. 074024. DOI: 10.1103/PhysRevD.82.074024. arXiv: 1007.2241 [hep-ph].

[179] ATLAS Collaboration. “Measurement of the Z/γ^* boson transverse momentum distribution in pp collisions at $\sqrt{s} = 7$ TeV with the ATLAS detector”. In: *JHEP* 09 (2014), p. 145. DOI: 10.1007/JHEP09(2014)145. arXiv: 1406.3660 [hep-ex].

[180] Ryan Gavin et al. “FEWZ 2.0: A code for hadronic Z production at next-to-next-to-leading order”. In: *Computer Physics Communications* 182.11 (2011), 2388–2403. ISSN: 0010-4655. DOI: 10.1016/j.cpc.2011.06.008. URL: http://dx.doi.org/10.1016/j.cpc.2011.06.008.

[181] Torbjorn Sjostrand, Stephen Mrenna, and Peter Z. Skands. “PYTHIA 6.4 physics and manual”. In: *JHEP* 05 (2006), p. 026.

[182] Peter Z. Skands. “Tuning Monte Carlo generators: The Perugia tunes”. In: *Physical Review D* 82.7 (2010). ISSN: 1550-2368. DOI: 10.1103/physrevd.82.074018. URL: http://dx.doi.org/10.1103/PhysRevD.82.074018.

[183] David J. Lange. “The EvtGen particle decay simulation package”. In: *Nuclear Instruments and Methods in Physics Research Section A: Accelerators, Spectrometers, Detectors and Associated Equipment* 462.1 (2001). BEAUTY2000, Proceedings of the 7th Int. Conf. on B-Physics at Hadron Machines, pp. 152 –155. ISSN: 0168-9002. DOI: https://doi.org/10.1016/S0168-9002(01)00089-4. URL: http://www.sciencedirect.com/science/article/pii/S0168900201000894.

[184] “The ATLAS simulation infrastructure”. In: *Eur. Phys. J.* C 70 (3 2010), p. 823. ISSN: 1434-6044. arXiv: 1005.4568 [hep-ph].

[185] A.D. Martin et al. “Parton distributions for the LHC”. In: *Eur.Phys.J.* C 63 (2009), pp. 189–285. DOI: 10.1140/epjc/s10052-009-1072-5. arXiv: 0901.0002 [hep-ph].

[186] ATLAS. *Event selection and background estimation in the $H \to 4\ell$ channel at $\sqrt{s}$=13- Moriond 2017 Analysis*. Tech. rep. ATL-COM-PHYS-2016-1599. Authors: The HZZ group. Geneva: CERN, 2017. URL: https://cds.cern.ch/record/2231576.

[187] M. Aaboud andothers. “Constraints on off-shell Higgs boson production and the Higgs boson total width in $ZZ \to 4\ell$ and $ZZ \to 2\ell 2\nu$ final states with the ATLAS detector”. In: *Physics Letters B* 786 (2018), pp. 223 –244. ISSN: 0370-2693. DOI: https://doi.org/10.1016/j.physletb.2018.09.048. URL: http://www.sciencedirect.com/science/article/pii/S0370269318307494.

[188] HSG2. *Event selection and background estimation in the $H \to 4\ell$ channel at $\sqrt{s} = 13$ - Moriond 2017 Analysis.* URL: https://cds.cern.ch/record/2231576.

[189] Jun Gao et al. "The CT10 NNLO Global Analysis of QCD". In: *Phys.Rev.* D 89 (2014), p. 033009. DOI: 10.1103/PhysRevD.89.033009. arXiv: 1302.6246 [hep-ph].

[190] L. A. Harland-Lang et al. "Parton distributions in the LHC era: MMHT 2014 PDFs". In: *The European Physical Journal C* 75.5 (2015). ISSN: 1434-6052. DOI: 10.1140/epjc/s10052-015-3397-6. URL: http://dx.doi.org/10.1140/epjc/s10052-015-3397-6.

[191] M. Aaboud et al. "Measurement of inclusive and differential cross sections in the $H \to ZZ^* \to 4$ decay channel in pp collisions at $\sqrt{s} = 13$ TeV with the ATLAS detector". In: *Journal of High Energy Physics* 2017.10 (2017). ISSN: 1029-8479. DOI: 10.1007/jhep10(2017)132. URL: http://dx.doi.org/10.1007/JHEP10(2017)132.

[192] M. Aaboud et al. "Luminosity determination in pp collisions at $\sqrt{s}$ s = 8 TeV using the ATLAS detector at the LHC". In: *The European Physical Journal C* 76.12 (2016). ISSN: 1434-6052. DOI: 10.1140/epjc/s10052-016-4466-1. URL: http://dx.doi.org/10.1140/epjc/s10052-016-4466-1.

[193] A. M. Sirunyan et al. "Measurement of the inelastic proton - proton cross section at s = 13 $\sqrt{s} = 13$ TeV". In: *Journal of High Energy Physics* 2018.7 (2018). ISSN: 1029-8479. DOI: 10.1007/jhep07(2018)161. URL: http://dx.doi.org/10.1007/JHEP07(2018)161.

[194] G. Cowan, K. Cranmer, E. Gross, and O. Vitells. "Asymptotic formulae for likelihood-based tests of new physics". In: *Eur. Phys. J.* C 71 (2011), p. 1554. DOI: 10.1140/epjc/s10052-011-1554-0. arXiv: 1007.1727 [physics.data-an].

[195] "Combined search for the Standard Model Higgs boson in *pp* collisions at $\sqrt{s}$=7 TeV with the ATLAS detector". In: *Phys. Rev.* D 86 (2012), p. 032003. arXiv: 1207.0319 [hep-ex].

[196] Morad Aaboud et al. "Measurement of the Higgs boson coupling properties in the $H \to ZZ^* \to 4\ell$ decay channel at $\sqrt{s} = 13$ TeV with the ATLAS detector". In: (2017). arXiv: 1712.02304 [hep-ex].

[197] *Expected performance of the ATLAS detector at the High-Luminosity LHC.* Tech. rep. ATL-PHYS-PUB-2019-005. Geneva: CERN, 2019. URL: https://cds.cern.ch/record/2655304.

[198] Georges Aad et al. "Measurements of the Higgs boson inclusive and differential fiducial cross sections in the 4ℓ decay channel at $\sqrt{s} = 13$ TeV". In: (Apr. 2020). arXiv: 2004.03969 [hep-ex].

[199] Georges Aad et al. "Higgs boson production cross-section measurements and their EFT interpretation in the 4ℓ decay channel at $\sqrt{s} = 13$ TeV with the ATLAS detector". In: (Apr. 2020). arXiv: 2004.03447 [hep-ex].

[200] M. Aaboud et al. "Search for heavy ZZ resonances in the $\ell^+\ell^-\ell^+\ell^-$ and $\ell^+\ell^-\nu\bar{\nu}$ final states using proton–proton collisions at $\sqrt{s} = 13$ TeV with the ATLAS detector". In: *Eur. Phys. J. C* 78.4 (2018), p. 293. DOI: 10.1140/epjc/s10052-018-5686-3. arXiv: 1712.06386 [hep-ex].

[201] G. Aad et al. "Constraints on the off-shell Higgs boson signal strength in the high-mass ZZ and WW final states with the ATLAS detector". In: *The European Physical Journal C* 75.7 (2015). ISSN: 1434-6052. DOI: 10.1140/epjc/s10052-015-3542-2. URL: http://dx.doi.org/10.1140/epjc/s10052-015-3542-2.